Reference particles for field-flow fractionation

Dissertation
zur Erlangung des Grades
des Doktors der Naturwissenschaften
der Naturwissenschaftlich-Technischen Fakultät
der Universität des Saarlandes

von
Aljosha-Rakim Jochem

Saarbrücken, Juni 2017

Tag des Kolloquiums:	13. Oktober 2017
Dekan:	Prof. Dr. Guido Kickelbick
Berichterstatter:	Prof. Dr. Tobias Kraus
	Priv.-Doz. Dr. Ralf Kautenburger
Vorsitzender:	Prof. Dr. Uli Kazmaier
Akad. Mitarbeiter:	Dr. Bernd Morgenstern

Dedicated to my family

for their faith, patience, encouragement, and love.

“Impossible is just a word thrown around by small men who find it easier to live in the world they've been given than to explore the power they have to change it. Impossible is not a fact. It's an opinion. Impossible is potential. Impossible is temporary. Impossible is nothing.”

– Muhammad Ali –

Acknowledgements

First and foremost, I would like to thank Prof. Eduard Arzt for his ongoing support, the temporary supervision of this thesis and for giving me the opportunity to perform this research at the INM - Leibniz-Institute for New Materials. My deepest and sincerest gratitude goes to Prof. Tobias Kraus, an extraordinary mentor, who supervised and guided me during this study. I am very thankful for his patience during numerous abstract iterations, the fruitful discussions, the faith in me and my research, the wide-spread responsibilities but also freedom I was able to enjoy, and the attempt to teach me a more logically way of thinking.

This thesis would not have been possible without the support of my prestigious colleagues of the structure formation group of which many has become good friends: Dr. Ioannis Kanelidis, Johannes H. M. Maurer, Beate Reiser, Dr. Lola Gonzáles-García, Sebastian Beck, Jona Engel, Thilo Grammes, Jonas Hubertus, Indra Backes, Dr. Sebastian Mörz, Dr. Peng Zhang, Juraj Drzic, Robert Strahl, Dr. Daniel Brodoceanou, Dr. Johann Lacava, Dr. David Doblas Jiménez, Ronja Anton, Andrea Pyttlik, Dr. Alberto Escudero, Dr. Thibaut Thai, and Dr. Genesis Ngwa Ankah. I really enjoyed the inspiring discussions in and outside of the lab, our funny group excursions, and the plenty official and unofficial group meetings.

I would like to especially thank my long-term colleagues, Thomas Kister with his unbelievable practical hands-on-mentality, Andreas Hegetschweiler with his sincere and true manner, and his scientific and sporting collaboration, and Dr. Dominik Gerstner for his manifold advices, the great time in the office, introducing me to synchrotron and swimming sessions, and for sharing his programming skills with me.

I am indebted to many of my colleagues who supported me with the experimental work and always had my back: Anika Kleemann, Anika Schwarz, Sarah Schmidt, Kathrin Alt, and the outstanding students Anna Zimmermann, Lars-Arne Meyer, and Christopher Scherrer. I would have not succeeded without these motivated and helpful colleagues. Thank you for your great effort and commitment; I could not have dreamed of a better team.

Particular thanks go to the external collaborators and colleagues for their support in this research: Prof. Uli Jonas, Dr. Ralf Kautenburger, Dr. Christoph Johann, Dr. Ulrich Rösch, and particularly Stephan Elsenberg who never hesitated answering the countless technical requests. I would also like to thank the Wyatt and Superon team for technical assistance, and the GradUs program (Saarland University) and the Federal Ministry of Economic Affairs and Energy (BMWi) for financial support.

I would like to show my gratitude to all the colleagues at INM for their support not only during my time as a PhD student, in particular Dr. Markus Koch, Andrea Jung, Dr. Henrike Peuschel, Dr. Thomas Ruckelshausen, Dr. Yuliya Silina, Dr. Isabella Tavernaro, Dr. Claudia-Fink Straube, Herbert Beerman, Christian Ersfeld, and Robert Drumm.

I would like to express my very great appreciation to all the former colleagues and research groups who influenced me along the way: Prof. Hegetschweiler and his research group at Saarland University (especially Bernd Morgenstern for supervising my Master thesis and for scientific discussion concerning this thesis), Dr. Annette Kraegeloh and the nano cell interactions group at INM (especially Dr. Christian Cavelius for his long-term supervision and mentoring), and Prof. Galen D. Stucky and his research group at the University of California, Santa Barbara.

Finally, I owe my deepest gratitude to my beloved family: my mom for her unlimited and selfless support; Ines for her incredible encouragement, patience, and her phenomenal job raising our wonderful children, Marlin and Philine. They truly blessed me with a magnificent life outside the lab. I cannot express how much you have contributed to this long journey, thank you from the bottom of my heart.

Statement on contributions

I analyzed the data, developed the synthesis protocols, and drew the figures in this dissertation using the cited references. The synthesis, characterization and field-flow fractionation experiments were supported by co-workers and collaborators as explained in the following. The work on PEGylated gold nanoparticles by Aljosha-Rakim Jochem, Genesis Ankah, Lars-Arne Meyer, Stephan Elsenberg, Christoph Johann, and Tobias Kraus has been previously published in *Analytical Chemistry* **2016**, 88, 10065-10073.

Reference nanoparticles

All nanoparticles syntheses and characterization measurements were performed by me or under my supervision. Synthesis, modification, and characterization of gold nanoparticles were partially carried out by Anika Kleemann and Anna Zimmermann. Synthesis of silica nanoparticles were supported by Anika Schwarz, Kathrin Alt, and Anika Kleemann. Metal-labeled silica nanoparticles syntheses were partially performed by Christopher Scherrer. The synthesis, modification, and batch characterization of PEGylated gold nanoparticles has been carried out by me.

Field-flow fractionation

Asymmetrical flow field-flow fractionation was performed by me or by Lars-Arne Meyer and Anna Zimmermann under my supervision. Dr. Tobias Kraus, Stephan Elsenberg, and Dr. Christoph Johann contributed to the design of the study on PEGylated gold nanoparticles. Characterization of the separation membrane was performed by Dr. Genesis Ankah.

Abstract

Nanoparticles with properties that deviate from the bulk are the basis of many innovations in nanotechnology. Analytical techniques for the reliable characterization of nanoparticles are gaining importance as nanoparticle fabrication and their use increase in research and industry. Field-flow fractionation is capable of analyzing particulate samples from different materials that have complex size distributions. Good analytical performances have been reported for field-flow fractionation of inorganic nanoparticles, but large particle losses have so far hampered its application.

This thesis studies reference particles to identify and overcome particle loss mechanisms during field-flow fractionation. Silica and gold nanoparticles were synthesized as model particle cores, and their size was systematically varied. Different labeling strategies were tested to make the particles easy to identify. The particles surfaces were modified to tune colloidal behavior and adsorption properties. Losses of different reference particles during field-flow fractionation were then studied and correlated with the particles' structure and colloidal stability. Particle losses due to destabilization of particles with loosely attached ligands or polymer-mediated bridging adsorption on the separation membrane were identified. Reference particles were tested in a complex matrix.

Zusammenfassung

Nanopartikel deren Eigenschaften sich von Bulkmaterialien unterscheiden sind die Grundlage weitreichender Innovationen der Nanotechnologie. Zuverlässige Nanopartikelanalyse-verfahren gewinnen zunehmend an Bedeutung auf Grund der fortschreitenden Entwicklung und Anwendung von Nanopartikeln in Forschung und Industrie. Feldflussfraktionierung eignet sich für die Analyse partikulärer Proben unterschiedlicher Materialien mit komplexer Größenverteilung. Starke Partikelverluste behindern bislang die gute analytische Leistungsfähigkeit der Feldflussfraktionierung anorganischer Nanopartikel.

Diese Arbeit beschäftigt sich mit Referenzpartikeln zur Aufklärung und Überwindung von Partikelverlustmechanismen während der Feldflussfraktionierung. Silica- und Gold-Nanopartikel wurden als Modellpartikel in unterschiedlichen Größen hergestellt. Verschiedene Markierungsstrategien wurden getestet um eine möglichst einfache Identifizierung der Partikel zu gewährleisten. Die Partikeloberflächen wurden modifiziert, um das kolloidale Verhalten und die Adsorptionseigenschaften anzupassen. Der Verlust verschiedener Referenzpartikel während der Feldflussfraktionierung wurde untersucht und mit der Partikelstruktur und der kolloidalen Stabilität korreliert. Dabei wurden die Destabilisierung von Partikeln mit schwach gebundenen Liganden und die polymerinduzierte Adsorption auf der Trennmembran als Verlustmechanismen identifiziert. Die Referenzpartikel wurden in einer komplexen Matrix getestet.

Table of contents

List of abbreviations

AF4 ..... *Asymmetrical flow field-flow fractionation*
AU ..... *Absorption Units*
BAM ..... *Bundesanstalt für Materialforschung und -prüfung*
CA ..... *Cellulose acetate*
CRM ..... *Certified reference material*
DAD ..... *Diode array detector*
DLS ..... *Dynamic light scattering*
DTAB ..... *Dodecyltrimethylammonium bromide*
EC ..... *European Commission*
EDTA ..... *Ethylenediaminetriacetic acid*
EFTEM ..... *Energy-filtered transmission electron microscopy*
ENP ..... *Engineered nanoparticle*
FFF ..... *Field-flow fractionation*
HPLC ..... *High performance liquid chromatography*
HSAB ..... *Hard and soft (Lewis) acids and bases*
ICP-MS ..... *Inductively coupled plasma mass spectroscopy*
ICP-OES ..... *Inductively coupled plasma optical emission spectroscopy*
IRMM ..... *Institute for Reference Materials and Measurements*
LS ..... *Light scattering*
LSPR ..... *Localized surface plasmon resonance*
LU ..... *Luminescence Units*
MALS ..... *Multi angle light scattering*
NFP ..... *Normalized Flocculation Parameter*
NIST ..... *National Institute of Standards and Technology*
NOM ..... *Natural organic matter*
NP ..... *Nanoparticle*
OHP ..... *Outer Helmholtz Plane*
PDI ..... *Polydispersity index*
PEEK ..... *Polyetheretherketone*
PEG ..... *Polyethylene glycol*
PES ..... *Polyethersulfone*
PS ..... *Polystyrene*
PVA ..... *Poly(vinyl alcohol)*

PVDF.....*Polyvinylidene difluoride*
QELS.....*Quasi-elastic light scattering*
RC.....*Regenerated cellulose*
RM.....*Reference material*
SDS.....*Sodium dodecyl sulfate*
SEM.....*Scanning electron microscopy*
TEM.....*Transmission electron microscopy*
TEOS.....*Tetraethylorthosilicate*
TMS-EDTA.....*N-(trimethoxysilylpropyl) ethylenediaminetriacetic acid*
UV-Vis.....*Ultraviolet-Visible*
VWD.....*Variable wavelength detector*

List of symbols

$|u_0|$ ..... *Cross-flow density*

A ..... *Hamaker constant*

c ..... *Concentration*

c_0 ..... *Sample concentration at membrane*

D ..... *Diffusion coefficient*

$D_{AF4\text{-}DLS}$ ..... *Hydrodynamic diameter determined using online DLS*

$D_{Batch\text{-}DLS}$ ..... *Hydrodynamic diameter determined in batch-mode*

D_h ..... *Hydrodynamic diameter*

D_T ..... *Thermal diffusion coefficient*

D_{TEM} ..... *Particle diameter determined by TEM*

H ..... *Separation distance*

I ..... *Ionic strength*

l ..... *Mean layer thickness*

M ..... *Molar mass*

n ..... *Amount of substance*

r ..... *Particle radius*

R ..... *Retention ratio*

t_0 ..... *Void time*

t_r ..... *Retention time*

V ..... *Volume*

V^0 ..... *Void volume*

V_c ..... *Cross-flow rate*

x ..... *Distance from membrane*

Z ..... *Interaction constant*

β ..... *Mass concentration*

κ^{-1} ..... *Debye length*

λ ..... *Retention parameter*

ω ..... *Effective channel thickness*

1. Introduction

1.1. Preliminary

Nanoparticle metrology, the characterization of nanoparticles (in particular their size distribution), is a readily growing and demanding scientific area. It is becoming more important due to steadily rising applications of nanoparticles in everyday-life products (cosmetics and food). Yet, there are ongoing discussions about legislative regulations concerning the definition and characterization of nanoparticles. The cosmetics industry is already subject to a European Commission (EC) regulation that makes it mandatory to declare "nano" ingredients (http://data.europa.eu/eli/reg/2009/1223/oj). The EC defines "nanomaterial", as a "material containing particles, in an unbound state or as an aggregate or as an agglomerate and where, for 50 % or more of the particles in the number size distribution, one or more external dimensions is in the size range 1 nm - 100 nm" [1]. Thorough NP characterization techniques must therefore provide qualitative and quantitative measures.

Current nanoparticle (NP) characterization methods can be divided into different categories. Ensemble methods, such as laser diffraction or dynamic light scattering (DLS), detect the particles all at once [2]. They are characterized by lower size resolution since the detection signal strongly depends on particle sizes as in the case of larger particles when using DLS, for example. On the other hand, classifying methods first separate the particles into different size classes prior to detection which enables higher resolution and accuracy. Analytical ultracentrifugation [3], hydrodynamic chromatography [4], and field-flow fractionation (FFF) [5] have proven to be suitable for the characterization of polydisperse samples. Counting methods (e.g. microscopy, particle tracking) and classifying counting methods (electrospray-differential mobility analysis) are a third class of particle characterization techniques, useful for the determination of number based particle populations due to their high resolution. However, they are often limited by the presence of complex matrices which may introduce artefacts. Details about the advantages and limitations of the aforementioned techniques can be found in several articles and books [2,6].

Asymmetrical flow field-flow fractionation (AF4) has been employed for the size determination of NP samples even in complex matrices in the past 20 years [7]. It provides fast

and automatable measurements and is a candidate to become a standardized measurement technique for NP characterization. However, sample losses of NPs during AF4 are greater for polymers or proteins than for particles, they can lead to biased results [8,9,10].

The development of AF4 for standardized size determination requires reliable reference particles and strategies that minimize particles loss-based errors. Reference particles are interesting for size calibration, method development, and quality assurance of the setup. Reference particles with distinctive properties such as characteristic optical behavior or elemental composition can be used as tracer particles to spike complex samples.

The requirements of reference or tracer particles in AF4 include:

- reliable particle identification with standard setups and detectors,
- similar properties (size, surface chemistry, charge) as engineered nanoparticles (ENPs) to ensure comparable behavior during sample preparation and fractionation,
- uniform and narrow size distribution for size determination via retention times (channel calibration),
- and minimal losses at various conditions to reduce setup contamination and danger of distorted analysis.

These requirements lead to the central objectives of my thesis:

1) Synthesis of tracer particles: I developed inorganic nanoparticles that can be used as reference particles for AF4 analysis. Nanoparticles with narrow size distribution were tuned by core and surface modification. By incorporation of metals or a fluorescent dye, NPs with specific optical behavior and elemental compositions were obtained, which can be potentially used as tracer particles. Surface modification introduced a broad variety of functionalities in order to match the surface properties of ENPs.
2) Identification of particle loss mechanisms: I investigated whether agglomeration, adsorption, or both mechanisms are responsible for particle losses within the analysis system and how they are connected. This should lead to a better understanding of flow field-flow driven particle losses and enable their minimization. Suitable NPs with reduced particle losses were identified and used for spiking a real sample.

The following section introduces the mechanisms and effects of particle losses of AF4.

1.2. Field-flow fractionation

1.2.1. FFF principle

Field-flow fractionation is a hypernym for a family of field-driven separation techniques. Their common principle is the fractionation of the sample through the action of an external force field [11, pp. 4-5]. This force field acts perpendicular to a laminar flow in the so-called separation channel (Figure 1.1). In contrast to chromatographic separation, FFF fractionates samples without a stationary phase; thus, interactions between the sample and the channel components are unnecessary and undesired.

Classical FFF separation channels consist of an inlet and outlet port and, in some cases, an additional port for sample injection. When the sample enters the channel, an applied field pushes the sample against the "accumulation wall" (Figure 1.1). Sample components will move away from the accumulation wall and reach different wall distances depending on their response to the applied field (opposing force). This step is referred to as "relaxation" [11, p. 18]. An equilibrium distribution is formed due to the balancing between the applied force field and the opposing force field. A laminar flow with a parabolic flow profile (different velocities at different channel heights) enables separation of the sample components with different equilibrium distributions. This combination of an external field and the parabolic flow profile is the defining feature of field-flow fractionation [11, p. 5].

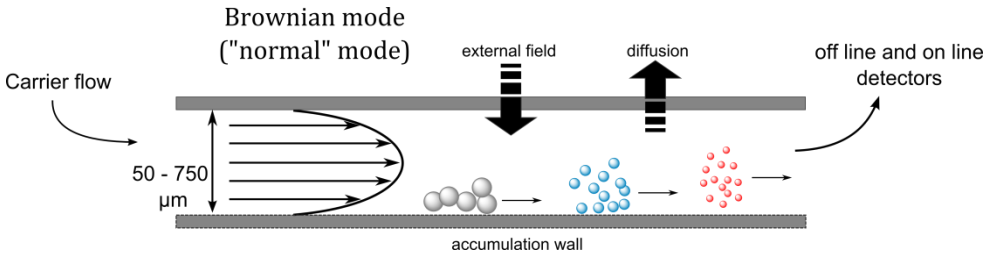

Figure 1.1: Cross section of a typical FFF channel displaying the size separation in Brownian mode.

The nature of the opposing force determines the formation of the equilibrium distributions and consequently the different operating modes in FFF [11, p. 18]. "Brownian mode" or "normal mode" applies when the external field is balanced by the analytes' diffusion [11, pp. 18-19]. Since diffusion increases with decreasing particle sizes, smaller particles elute before larger particles (normal elution order). Brownian mode is by far the most widely implemented operating mode and applicable for particles with diameters up to 1 µm.

Larger particles elute either by the so-called “steric mode” or more complex modes, such as “lift-hyperlayer mode”, for example. For larger particles, the diffusion as opposing force can be neglected [11, p. 20]. Repulsive forces preventing the penetration of the particles into the accumulation wall are the only opposing force in steric mode. As a result, a thin layer of particles is formed at the wall. In lift-hyperlayer mode, additional flow-induced hydrodynamic lift forces are the opposing forces, which will cause formation of the thin particle layer above (more than two radii) the accumulation wall [11, pp. 20-21]. In both cases, larger particles will form thicker layers, reach faster flow streams, and will elute before smaller particles (inverted elution order) [11, p. 20]. All particles in this thesis have diameters < 150 nm and are separated in the Brownian mode.

The FFF techniques can be categorized according to the applied field (Table 1.1). In thermal FFF, for example, a temperature gradient causes separation according to the thermal diffusion coefficient D_T. This technique is often applied for polymers that usually have large solvent dependent variations of D_T [12]. On the other hand, sedimentation FFF is applied for the separation of particles according to their density and is characterized by a high selectivity [12].

Table 1.1: Selection of the most important external FFF fields and the corresponding techniques [11, p. 8].

Field	Technique
Sedimentation	Sedimentation FFF (SdFFF)
	Centrifugal FFF
	Gravitational FFF
Thermal (temperature gradient) (Th)	Thermal FFF (ThFFF)
Cross-flow (Fl)	Flow FFF (FlFFF)
Electrical (El)	Electrical FFF (ElFFF)
Magnetic	Magnetic FFF (MgFFF)
Dielectric (Dl)	Dielectric FFF (DlFFF)

1.2.2. Asymmetrical flow field-flow fractionation

Asymmetrical flow field-flow fractionation is the most applied FFF method since it separates particles by their size (often requested), can be operated with aqueous as well as non-aqueous solvents, and is close to standard HPLC systems. The method is based on a flow field (cross-flow) that drives particles towards the accumulation wall, a semi-permeable ultrafiltration membrane (Figure 1.2). The size-dependent diffusivity of particles leads to different positions inside the channel: small, highly diffusive particles can

diffuse further from the accumulation wall than large particles. The parabolic flow profile therefore elutes smaller particles before larger particles (Figure 1.2).

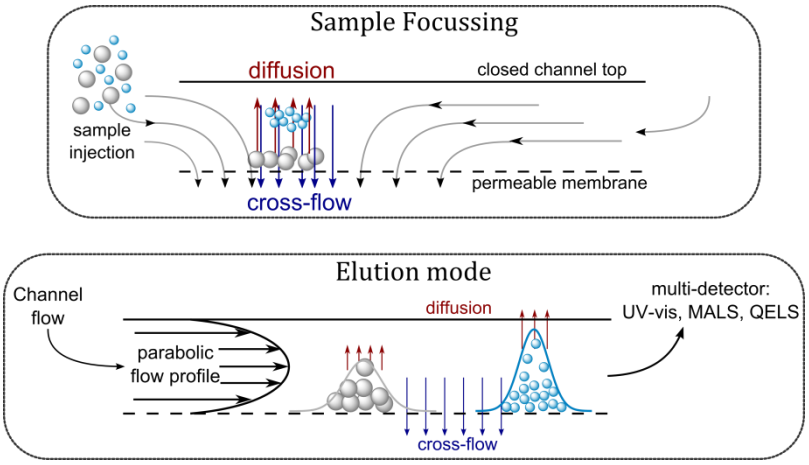

Figure 1.2: Illustration of the separation mechanism: (I) Sample equilibration (relaxation) during focusing process and (II) consequent sample elution.

The separation process has two subsequent steps: After injection, sample relaxation and focusing is carried out in order to reach the equilibrium distribution and to narrow the width of the sample zone. The sample is confined at a thin band close to the accumulation wall (focusing area) by two opposing flows that concentrates the sample by orders of magnitude (Figure 1.2, top) [13]. In the next step, the flow direction of the channel outlet is switched and the particles elute (Figure 1.2, bottom). Particles of different sizes separate in the stable cross-flow field that is perpendicular to the parabolic flow profile.

A typical AF4 fractogram of gold nanoparticles is presented in Figure 1.3. The main sample peak at an elution time of around 11 minutes (corresponding to a net retention time of ~ 6 minutes) is often accompanied by a void peak and a release peak. The void peak consists of unretained particles which were not properly relaxed during the focusing step. Particles with strong attractive particle-membrane interactions are over-retained and elute in the release peak after the cross-flow field was turned off (at 20 minutes in Figure 1.3).

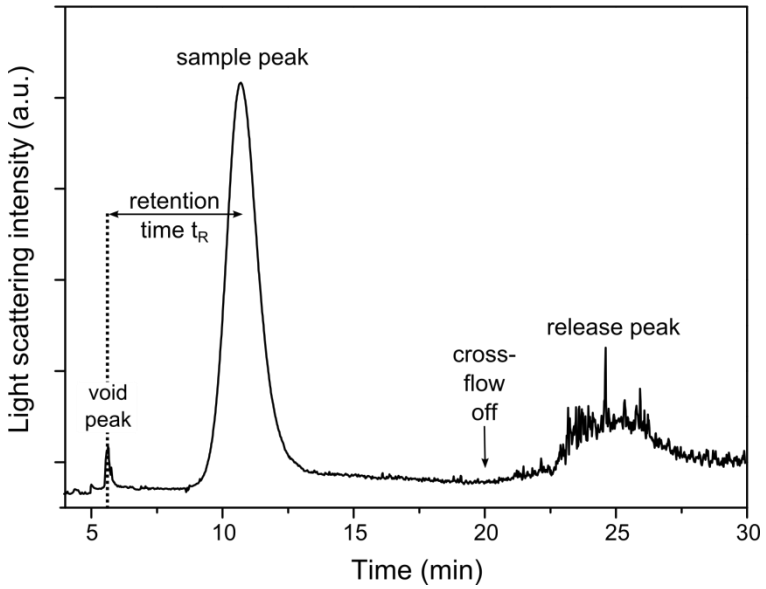

Figure 1.3: Typical AF4 fractogram of AuNPs showing a void peak (un-retained NPs), a sample peak (proper fractionation), and a release peak (over-retained NPs).

The theoretical description of AF4 is based on fundamental work of Prof. Calvin Giddings, who invented the FFF technique in the 1970s [14]. Detailed descriptions of the theory can be found in the *Field-Flow Fractionation Handbook* [11]. I give a brief summary of the theoretical aspects and important parameters in the following.

The retention ratio R describes the velocity of the eluting sample compared to the average fluid velocity and can be determined by the ratio of the retention time of the void peak, t_0, to the retention time of the sample, t_r. A dimensionless retention parameter λ is often defined as $R = 6\,\lambda$. The relation between retention time and the diffusion coefficient in AF4 is given by:

$$\lambda = \frac{V^0 D}{\dot{V}_c \omega^2} \qquad (1)$$

where V^0 is the void volume, D the analyte diffusion coefficient, V_c the cross-flow rate, and ω the effective channel thickness. Thus, for known ω, the retention time can directly be converted into diffusion coefficients, and the hydrodynamic diameter follows from the Stokes-Einstein relation [15]. Determination of ω is usually achieved by calibration with well-defined size standards that do not interact with the membrane.

The evolution of the analyte's concentration along the channel in "Brownian mode" is given by:

$$c(x) = c_0 e^{-x/l} \tag{2}$$

where c_0 represents the sample concentration of the analyte at the membrane ($x = 0$). The parameter l is the mean layer thickness and represents the mean distance between the analyte and the accumulation wall:

$$l = \frac{D}{|u_0|} \tag{3}$$

where $|u_0|$ is the applied cross-flow density (cross-flow rate per area). Equation (2) shows that the highest sample concentration is always at the accumulation wall ($x = 0$).

The model above assumes ideal behavior and neglects particle-particle or particle-membrane interactions, for example. It has been shown that these interactions can lead to significant particle losses, retention time shifts, and are insufficient to describe the fractionation according to theory in many cases [8,10,16,17]. This limits the use of AF4 for standardized particle characterization.

A major drawback is increased sample losses of NPs during AF4 fractionation. Size-, type-, and material-dependent NP losses can lead to biased results which are unacceptable for any reliable analytical method [10]. Yet, the dependence of the particles properties and the particle loss mechanisms are still under discussion and are subject of ongoing research.

Finally, the lack of proper reference particles is a weak point in AF4. Reference particles are important for many aspects like size calibration (determination of effective channel thickness) [18] or as an internal standard to spike real samples [19]. It has been shown that particle-membrane interactions can alter the retention time and generate distorted size determinations [10,16,20]. Therefore, the size determination without the use of a complementary sizing detector is susceptible to improper size calculation when particle-membrane interactions are present. A time-consuming method development of a large number of parameters and settings is often required in order to minimize the particle losses and assure elution according to theory [7]. For particulate samples, the colloidal stabilization mechanism, particle shapes, and surface chemistry are key parameters influencing the elution behavior but may not be known in advance. The essential properties have to be

determined beforehand to ensure proper choice of the measurement conditions. The availability of suitable reference particles with defined properties would allow a systematic investigation of the interactions leading to deviations and distorted results. Yet, there are only few suitable reference nanoparticles available.

The following chapter will report on existing applications of reference nanoparticles used in FFF for sample spiking and method development after which the reported mechanisms of nanoparticle losses will be summarized in chapter 1.4.

1.3. Nanoparticle standards in AF4

Reference materials in general can be divided in different categories. Certified reference materials (CRM) are materials "accompanied by documentation issued by an authoritative body and providing one or more specified property values with associated uncertainties and traceabilities, using valid procedures" [21, p. 51]. CRM particles in the nanometer range are available with polystyrene (NIST), silica (IRMM), and silver (BAM) cores.

There are also reference materials (RM) available which are not issued by an authoritative body. Such reference materials are defined as "material sufficiently homogeneous and stable with reference to specified properties, which has been established to be fit for its intended use in measurement or in examination of nominal properties" [21, p. 50]. Several companies provide particles with different size classes and cores. Commonly employed CRMs and RMs are summarized in Tsuzuki *et al.* [22, pp. 295-296].

Field-flow fractionation often requires reference particles as size-calibration standards to determine the effective channel thickness and the calculation of particle sizes via the retention time. This requires particles with a narrow size distribution and minimized particle-membrane interactions. Besides size-calibration, reference particles in AF4 (CRMs, RMs or other) ideally have multiple functions. They might be used for method development or system quality assurance. Furthermore, standards with unique and characteristic properties could also be used for spiking the sample during sample preparation. The currently available nanoparticle standards are often only used for size calibration and method development in AF4.

The most commonly materials used are gold and polystyrene (PS) particles [13,15,20,23,24,25]. Gold nanoparticles standards are available as RMs from NIST and are often used when metallic nanoparticles are investigated in AF4 [26]. Three sizes are

available (10 nm, 30 nm, and 60 nm) and sufficient for size calibration in most cases. Polystyrene particles are often recommended because they are believed to be less prone to particle losses through membrane interactions. The particle-membrane interactions are a central issue and will therefore be studied in this thesis in more detail.

In order to assess the effect of complex matrices on particles in real samples, sample spiking using labeled (tracer) nanoparticles is of great interest [27]. AF4 is frequently used in the environmental sciences, where the fate and quantification of ENPs, and the differentiation between ENPs and geogenic NPs are central topics. An interesting way to quantify and simultaneously spike samples is the use of isotopically labeled NPs [19]. Stable isotopes exist for most of the elements of which ENPs are composed of [19]. Isotopic sample spiking allows unambiguous identification of ENPs and quantification at low concentrations by the so-called "isotopic dilution method" [19,28]. Here, isotopically enriched analyte substances are used as an internal standard to quantify analyte concentrations. The use of sample spiking with isotopically enriched ENPs for FFF analysis of nanoparticles is still very limited. Gigault and Hackley reported the synthesis and AF4 characterization of ^{109}Ag-enriched silver nanoparticles [29]. They were able to detect the isotopic signature of AgNPs (without pre-digestion) and used AgNPs to differentiate between isotopically enriched tracers and naturally occurring species. Recently, Palmai *et al.* published the synthesis of ^{29}Si-enriched SiO_2 nanoparticles [30]. The synthesis included the preparation of a ^{29}Si-enriched precursor, ^{29}Si tetraethyl orthosilicate (^{29}Si-TEOS), and subsequent sol-gel particle synthesis. Another approach was published by Meermann *et al.*, who synthesized isotopically enriched ^{57}Fe nanoparticles coated with a SiO_2 shell and successfully modified and spiked a river matrix sediment using a reverse post-channel on-line isotope dilution AF4/ICP-SFMS method [19].

The major disadvantage of isotopic labeling is the limited availability and especially the associated higher costs for the preparation of precursors used for NP synthesis [31]. Labeling of nanoparticles can also be performed by the incorporation or attachment of fluorophores [32] or other metal ions [33], for example. In this thesis, ENPs are labeled with different metals or metal ions in ENPs: (i) silver-labeled gold nanoparticles, which can be differentiated by their gold/silver ratio and their corresponding optical properties, and (ii) metal-labeled silica nanoparticles with different metal ratios.

To further optimize the properties of labeled nanoparticles for FFF analysis, it is necessary to overcome existing limitations such as particle-dependent retention time shifts and NP losses [13,17]. The current understanding of NP losses in AF4 is reviewed in the following section.

1.4. Nanoparticle losses in AF4

Sample recovery in FFF has been discussed in many publications [8,10,17,20,26]. Possible loss mechanisms include agglomeration and adsorption [7,15,34]. They are affected by particle and sample properties such as the composition of the particle core and surface charges, and also depend on system parameters, for example, the eluent composition and flow rates.

1.4.1. Sample Recovery: Definitions and methods

Sample recovery (or losses) can be divided into absolute and relative losses. The percentage of an injected sample that is recovered after passing through the entire separation system is its *absolute recovery* [11, p. 326]. The absolute recovery is important if quantitative information of the analyte in the sample is necessary, which is often the case in NP characterization. The *proportional recovery* describes the recovery of "several different components in amounts that are proportional to (but not necessarily equal to) their levels in the original sample" [11, p. 327]. Proportional recovery is critical because regulating bodies such as the EU define nanomaterials using number-based criteria.

Relative recovery represents the percentage of the injected sample that is recovered normalized to a reference or calibration run [10,11, p. 327,35,36]. The relative recovery is often used in literature to evaluate and compare different method parameters. There is no correlation between the absolute recovery and the relative recovery.

Recovery values can be determined using two strategies. Bypassing strategies [11, p. 328] use online detection (UV-Vis, fluorescence, refractive index) of a "reference" or "calibration" run that bypasses the separation channel. The detector signal of the fractionation run is then divided by the signal of the calibration run, which is set to 100 %. This on-line procedure is generally used for the determination of relative recoveries in AF4 in dependence of different method parameters (cross-flow field, eluent composition). The bypassing strategy can also be used for the determination of absolute recoveries under the as-

sumption that particle losses on internal surfaces can be neglected. This assumption has to be checked for each measurement condition and strongly depends on the analytes' properties.

The second strategy for recovery measurements is based on the collection of fractionated samples and subsequent off-line concentration determination [11, p. 328]. The original sample concentration in the sample vial and the concentration of the collected fractions are determined. Elementary analysis, such as inductively coupled plasma optical emission spectroscopy (ICP-OES) or mass spectrometry (ICP-MS), is often used because of its low detection limit. Although this "collect and measure" approach is more time-consuming, it allows reliable statements about absolute and relative recoveries without additional assumptions.

1.4.2. Colloidal interactions in agglomeration and adsorption

Colloidal interactions (particle-particle and particle-surface) affect particle losses during fractionation because they set the amount of agglomeration and adsorption [7]. For electrostatically stabilized nanoparticles in aqueous samples, which are frequently investigated using AF4, electrostatic and van der Waals interactions are considered as the most important interactions affecting stability. They are described by DLVO theory [37, pp. 409-412]. Polymers cause additional interactions, the so-called Non-DLVO interactions such as hydrophobic and steric interactions [38, pp. 50-58].

1.4.2.1. Van der Waals interactions

Interactions caused by intermolecular long-ranged forces due to fluctuating electromagnetic fields between two closely separated surfaces are called van der Waals interactions [38, p. 43]. Van der Waals forces can be divided into different types, where London-dispersion forces (also called dispersion forces) are often considered most important for colloidal stability [39, p. 55]. They act between particles and are generally attractive. The Hamaker constant A is a material-dependent constant that describes the material-dependent magnitude of the van der Waals attraction for a given geometry [40, p. 253].

The van der Waals interaction energy between two equal spheres in the case of small separation distances, $U_{VDW,ss}$, is given by:

$$U_{VDW,ss} = -A\frac{r}{12H} \quad (4)$$

where r is the particle radius and H is the separation distance between the two particles [38, p. 45]. When describing colloidal stability, the effective Hamaker constant for macroscopic bodies interacting through a medium has to be applied. The effective Hamaker constant can be calculated from A of the material itself and A of the solvent [38, p. 45].

The van der Waals interaction energy between a sphere and a flat surface (plate) [40, p. 254] is described by:

$$U_{VDW,sp} = -A\frac{r}{6H} \quad (5).$$

Thus, the van der Waals attraction between the sphere and a plat is twice as large as between two spheres if the particles and the surface are composed of the same material. As a consequence, particle adsorption on a wall can be induced before particle agglomeration [41].

1.4.2.2. Electrostatic interactions

Particles in aqueous media are generally charged and subject to long-ranged electrostatic interactions [40, p. 291]. Surface charges often arise from preferential solution of surface ions, ionization of functional groups on the surface or specific ion adsorption [39, p. 79]. Charged surfaces attract opposite counterions, forming the so-called *electrical double-layer* (EDL) [38, p. 10]. In general, the electrical double-layer consists of three parts: the charged surface, the surface-bound counterions, and a more loosely attached ion layer (Figure 1.4) [40, p. 307]. Particles with like charges will repel when they approach each other and the diffuse double layers overlap. The length scale of interaction is the Debye screening length κ^{-1} [37, p. 225].

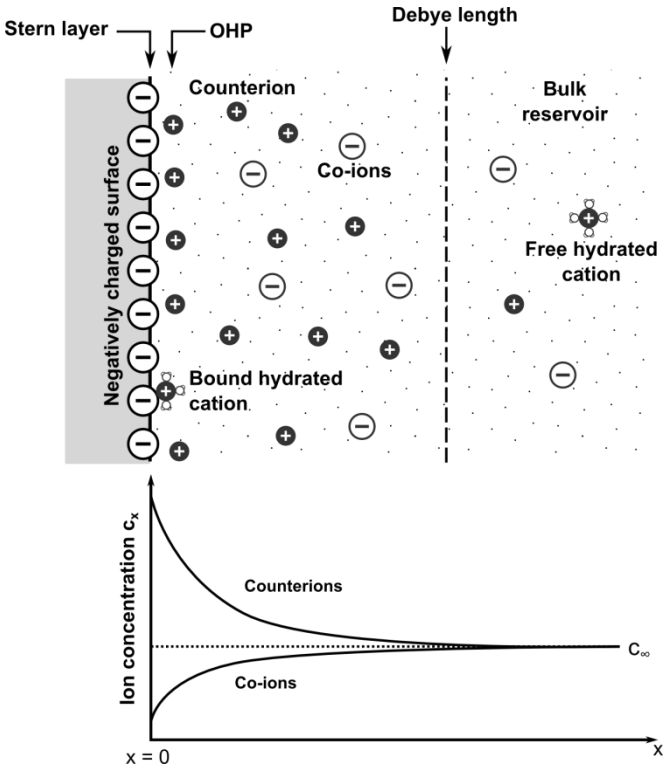

Figure 1.4: Distance depending charge distribution of a flat surface displaying the relation between the Stern layer, Outer Helmholtz Plane (OHP), and Debye length according to [40, p. 307].

At a given temperature, the interaction between two charged surfaces in aqueous solution greatly depends on the nature and concentration of the electrolyte [38, p. 10]. The repulsive interaction energy due to the overlap of two EDLs can be expressed by:

$$U_E = \frac{1}{2} RZe^{-\kappa H} \tag{6}$$

where Z is an interaction constant that depends solely on the properties of the surface and can be seen analogues to the Hamaker constant [40, pp. 317-318].

Sphere-plate interactions between a particle and a wall are again twice as large as the interactions between equal spheres for identical charge densities.

1.4.2.3. Hydrophobic and steric interactions

Interactions beyond DLVO occur if particles and surfaces carry adsorbed fluid layers or polymers [38, p. 50]. This may cause reversible agglomeration or high colloidal stability at elevated ionic strength. The additional ‘structural forces’ can be divided into hydration interactions, hydrophobic interactions, and steric interactions [38, p. 50]. Since particles

with adsorbed polymer layers were investigated for this thesis, a concise description will be given here.

Hydration forces are short-ranged forces that cause extra repulsion between two approaching, hydrated surfaces. Approach of such surfaces would require dehydration and cause an increase of free energy [38, p. 52]. Additionally, repulsive steric interactions arise when particles with adsorbed polymer layers approach each other. Close contact of the polymer chains would impede configurational freedom of the polymers, which would lead to a decrease of the configurational entropy [37, p. 276]. Thus, interpenetration of the approaching polymers is prevented. This so-called 'steric stabilization' is the governing stabilization mechanism of polymeric-grafted nanoparticles enabling stable particle dispersions at high ionic strengths [38, p. 55].

Attractive hydrophobic interactions act between two hydrophobic surfaces in an aqueous system [37, p. 39]. The approach of two hydrophobic surfaces is favored since it supports water molecules to migrate out of the gap, which allow the formation of hydrogen-bonded water clusters (not possible between approaching surfaces) leading to a lower free energy. This interaction is especially important when particles with hydrophobic surfaces are dispersed in aqueous solution.

1.4.3. Empirically established parameters influencing NP losses

Taking a closer look on flow field-flow fractionation, many interactions and forces come into play besides double-layer repulsion and van der Waals attraction (Figure 1.5). For small particles (Brownian mode), the most important forces remain double-layer repulsion, van der Waals attraction, and – depending on the constitution – steric/hydrophobic interactions. It is generally accepted that decreased particles recoveries are dominated by these interactions which cause agglomeration and adsorption [8,10,15,34].

Agglomeration and adsorption occur when the repulsive energy barriers are sufficiently lowered so that the attractive interactions can overcome them. Energy barriers may be reduced by changing surface properties (e.g. increasing/decreasing surface charges) or the composition of the surrounding medium (e.g. changing polarity).

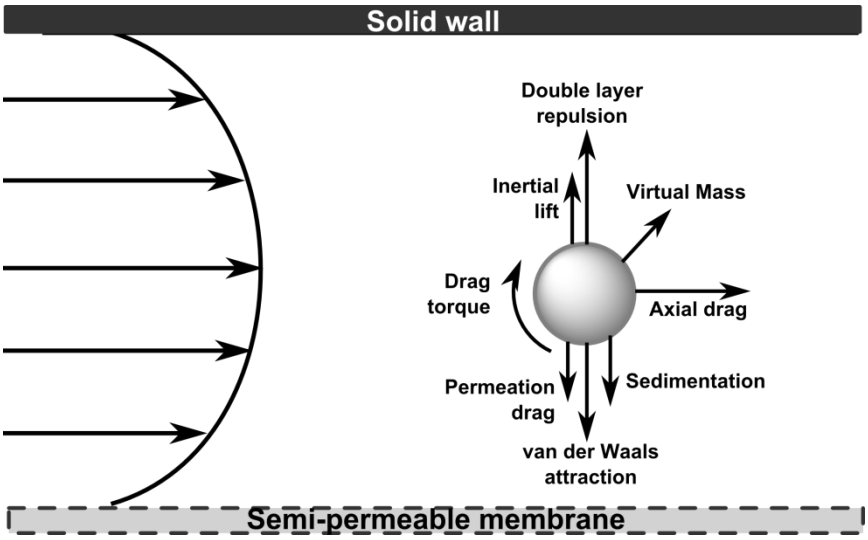

Figure 1.5: Schematic illustration of forces acting on a particle during tangential flow filtration according to [42].

Both cases may occur during FFF characterization. On the one hand, particles come into contact with different materials inside the setup which may vary in their surface properties. On the other hand, the eluent composition is often adjusted by the addition of surfactants or salts, which adsorb on surfaces and lower the screening length κ^{-1}, respectively. It then strongly depends on the sample and surface properties if particle-particle interactions will lead to agglomeration or if adsorption will be induced by particle-membrane interactions [43]. Thus, adsorption and agglomeration are closely linked phenomena and can be induced by similar external adjustment (addition of destabilizing agent).

A classification of the factors that influence the particle-particle and particle-membrane interactions is illustrated in Figure 1.6. In literature, several studies investigated the influence of these factors on particles losses. A summary of the current state on particle losses during AF4, together with a classification of the key properties determining losses, is provided in the next chapter.

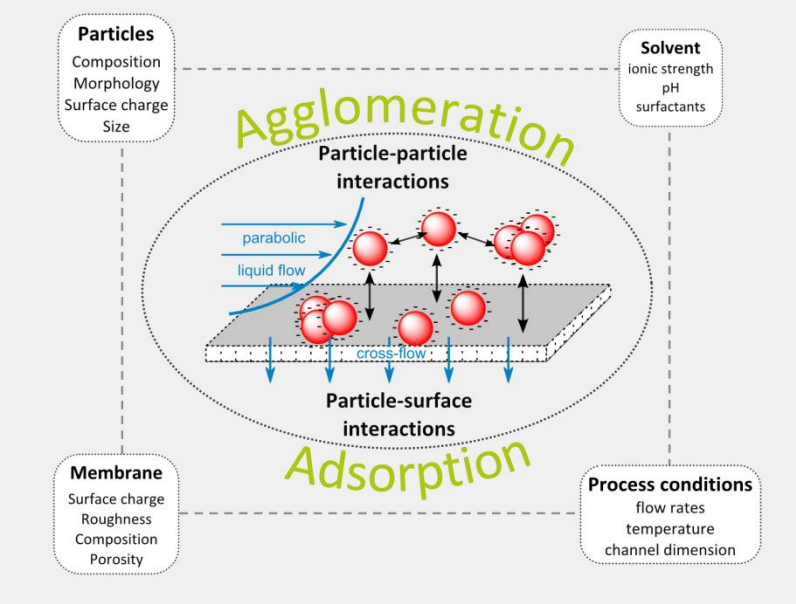

Figure 1.6: Influencing factors in AF4 contributing to particles losses by agglomeration or adsorption.

1.4.3.1. Processing parameters

Particle losses can be affected by processing parameters such as the focusing time, the channel flow, and the cross-flow rate [34,44]. Both affect the duration and the forces acting on the particle during fractionation.

Sample focusing is a critical step in AF4 since the particles are concentrated into a narrow band. Increasing concentration might induce agglomeration which may lead to increased particle mass and reinforce adsorption probability [45]. To minimize sample losses, a short focusing time is recommended [15]. The cross-flow rate determines the strength of the flow field pushing the particles against the accumulation wall and impact the number of particle-membrane collisions, as well as shear forces. Work on macromolecular samples has shown that increasing cross-flow rates are usually associated with decreasing sample recovery due to sample adhesion on the membrane [15,45,46,47], a frequent observation in AF4 which also applied to particles. Studies on flow rate dependent nanoparticle losses are discussed in the following.

Hagendorfer *et al.* observed particle losses of citrate-stabilized gold nanoparticles due to immobilization on the membrane with increasing cross-flow-densities (highest cross-flow rate 1.5 mL/min) [17]. Focusing times above 5 minutes were less favorable due to particle immobilization. The variation of cross-flow rates for the fractionation of citrate-stabilized gold nanoparticles (30 nm and 60 nm) showed that higher cross-flow rates induce ag-

glomeration as indicated by the formation of a shoulder in the fractogram of 30 nm sized particles [5]. The appearance of this additional peak was related to sample aggregation caused by the higher flow rate. However, this behavior did not occur for the larger particles. Variation of the cross-flow and the focusing time was studied by Bolea *et al.* using silver nanoparticles [48]. The relative recoveries dropped by 15 % when the cross-flow was increased from 0.5 mL/min to 1.0 mL/min during the focusing step. However, the lower cross-flow increased the number of particles not properly focused that were eluted in the void peak and might explain the lower relative recovery detected. Zattoni *et al.* observed decreasing radii of gyration for polymerically stabilized quantum dots when increasing the cross-flow densities [24]. The authors assume that higher cross-flow densities lead to higher shear stress because the particle-membrane distance is decreased. This might lead to desorption of the physisorbed polymer, reduce colloidal stability, and cause higher losses by adsorption processes [24].

A somewhat different observation was made by Loeschner *et al.*, who analyzed PVA-stabilized silver nanoparticles [49]. They observed peak broadening at higher cross-flow rates and explained them by increasing particle-membrane interactions. The effect of the cross-flow rate, the focus time and the sample concentration on the relative recoveries was negligible. Similar behavior was shown by Barahona *et al.* who detected peak tailing for SiO_2 nanoparticles at higher cross-flow rates (1.5 mL/min) indicating nanoparticle-membrane interactions [18]. However, no statements about particle losses were made. Isaacson *et al.* did not observe decreasing recoveries when increasing the cross-flow from 1 to 4 mL/min during the analysis of aqueous C_{60} fullerene aggregates [50].

Clearly, there exists an optimum of the cross-flow rate and the focusing time at which particles are fractionated with a proper resolution in a reasonable amount of time. Hence, a careful variation of the different method parameters should always be made regarding the desired tasks (optimized resolution, measurement time, recovery). The next chapters will discuss the effects of solvent composition, membrane, and particle properties on particle losses.

1.4.3.2. Solvent composition

The eluent composition influences charge distributions, screening lengths, and solubility. The composition of the eluent and the sample solvent in AF4 is often different because the eluent composition has to be adjusted to achieve a proper fractionation. Thus, particle

injection into the separation system is often accompanied by a change of solvent. The first contact with the carrier liquid occurs in the sample loop, after which the sample is concentrated up to 100 times in a very thin zone during the focusing process [7]. The solvent strongly affects colloidal stability.

In aqueous AF4, the relaxation of the sample close to the membrane is sometimes hindered by the presence of electrostatic interactions. In order to screen these interactions, the adjustment of the ionic strength or the pH is often recommended or necessary [13]. However, high ionic strengths or a change in the pH can lead to numerous deviations, such as agglomeration due to enhanced screening of the electrostatic repulsion or charge neutralization [51, p. 208]. The eluent composition not only influences agglomeration but also adsorption by changing the interactions between the NPs and the internal surfaces, especially during focusing. In literature, there is an ongoing debate about the optimization and the effects of the eluent composition on particle losses.

Loeschner *et al.* reported on slightly decreasing relative recoveries with increasing $(NH_4)_2CO_3$ concentration (pH 9) for PVA-stabilized silver nanoparticles [49]. In a study on citrate-stabilized AgNPs, a major effect of the pH was determined [52]. Water adjusted with NaOH to a pH of 9.2 was superior with respect to sample recovery and peak broadening compared to lower pH values and the use of ammonium carbonate buffer. Decreased relative recoveries (5-10 %) when using ammonium carbonate were attributed to increasing particle-membrane interactions leading to particle adsorption. Particle losses of citrate-stabilized AgNPs covered with humic substances depended on the ionic strength and the pH. Particle losses were observed when increasing the ionic strength from 1 mM to 10 mM at pH 5, but not at pH 8 [53]. The authors claim that the charge reduction presumably is insufficient to induce agglomeration. The optimal mobile phase for commercial TiO_2 nanoparticles was determined by Bendixen *et al.* and consisted of 1 mM hexametaphosphate. In this study, both, the surface charges of the membrane and the particles were taken into account and optimized through the eluent composition to bear sufficiently negative charges in order to achieve high colloidal stability and reduce the probability of sample adsorption [10].

Surfactants can have significant effects on particle recovery and retention behavior. Surfactants are commonly recommended in order to properly disperse particles and facilitate the wetting of hydrophobic particles [11, pp. 189-198]. In the case of cationic nanoparticles, the use of a cationic surfactant is necessary to achieve reasonable recovery by over-

coming the attractive interaction between the positively charged particles and the negatively charged membrane [54,55]. However, controversial effects of surfactants during AF4 have been reported which are not fully understood.

In the analysis of commercial AgNPs, relative recoveries in ultrapure water (0-72 %) and ultrapure water adjusted to pH 8 (62-85 %) were low [48]. The use of the non-ionic surfactant Tween 20 caused size independent particle elution which the authors explain by enhanced particle-membrane repulsion that prevented the particles from approaching the membrane close enough. The best recoveries were determined using a 0.01 % sodium dodecyl sulfate (SDS) solution adjusted to pH 8, which led to relative recoveries for AgNP standards of 90-100 % with good repeatability [48]. Similarly high recoveries of 88-98 % for the analysis of citrate-stabilized AgNPs were achieved when using 0.025 % NaN_3 and 0.025 % FL-70 mixtures as solvent [56].

Particle losses due to adhesion on internal surfaces can be improved by the addition of surfactants as shown by Schmidt *et al.* [23]. The addition of SDS improved the analysis and decreased particle loss caused by adhesion to the instrument surfaces. However, precipitation of the gold calibrant solution disturbed the ICP-MS calibration when SDS was added. This example already reveals some contradictory effects when using surfactants during AF4. Citrate-stabilized gold nanoparticles characterized using AF4 with a PVDF membrane were completely lost at an ionic strength of 1 mM (NaCl) [17]. Whereas the high losses during fractionation could not be improved by the addition of anionic (SDS) or cationic surfactants (dodecyltrimethylammonium bromide (DTAB)), detected system losses due to adsorption on internal surfaces were improved when using DTAB. Analogous trends were observed for commercial AgNPs (electrostatically and sterically stabilized), where the addition of the surfactants SDS and DTAB led to increased relative particle losses of up to 90 % [57]. Hence, the authors recommended water without any additives as an eluent and achieved relative recoveries up to 100 %.

Other researchers recommend low ionic strengths only to avoid possible interactions caused by surfactants [5]. A higher background noise at low concentrations of SDS (0.05 %) was reported compared to the use of an ammonium carbonate buffer (0.25 mM). The authors favored the use of the buffer since it is more advantageous for online AF4-ICP-MS coupling due to its greater volatility [18].

In summary, the effects of different solvent composition on particle losses are not clear yet. An increase of the ionic strength generally leads to increased particle losses. This has been explained by the loss of colloidal stability causing particle agglomeration or increased particle adsorption on internal surfaces, especially the membrane. The use of surfactants is controversial since increased and decreased particle losses were observed in similar studies. The above mentioned observations may result from the use different membrane materials that influence particle-membrane interactions.

1.4.3.3. Membrane

The membrane material controls particle-membrane interactions. Since the sample concentration is the highest at the membrane surface (Equation 2) and the sample has longer residence times at the membrane than at other surfaces, particle-membrane interactions leading to particle adsorption are accounted for particle losses. The most important membrane surface properties which influence the particle-membrane interactions were identified to be the hydrophobicity/hydrophilicity, roughness, and charge distribution [10].

The most common membranes used in AF4 for nanoparticle fractionation are regenerated cellulose (RC), polyethersulfone (PES), and polyvinyldifluoride (PVDF) ultrafiltration membranes [10]. A general observation is a saturation of the membrane which is characterized by a gradual increase in the recovery with increasing numbers of sample injections [15,17,23,26,48,49,53,57]. Due to this effect, it is sometimes recommended to perform a so-called “conditioning” with multiple sample injections before analysis [53]. Predictions about the proper membrane which should be used for nanoparticle analysis can hardly be made as discussed in several publications [13,58].

As shown by Cho *et al.*, successful fractionation of gold nanoparticles can be achieved using the rather hydrophobic PVDF membrane with DI water only, while addition of salt was necessary for proper fractionation with RC membranes [5]. The authors still recommend the use of RC membranes because a) there are only limited cut-off sizes for PVDF membranes available, b) increased fouling or degradation occurred for PVDF membranes, and c) the performance in the separation of multiple components in a mixture was poor.

In a comprehensive study, Hagendorfer *et al.* compared several nano- and ultrafiltration membranes for the fractionation of citrate-stabilized gold nanoparticles [17]. Conditioning effects were observed for all tested membranes. The authors found evidence that the recovery and separation characteristics strongly depend on charge and hydrophobicity.

Low surface charge and increasing hydrophobicity were accompanied by higher relative recoveries. The authors obtained the highest relative recoveries when using PVDF and RC membranes along with ultrapure water as eluent for AF4 analysis of citrate-stabilized gold and commercial silver nanoparticles [17,57]. In contrast, Loeschner *et al.* could not separate similar particles (PVA-stabilized AgNPs) using PVDF membranes with ultrapure water [49]. Complete particle loss with only small signals in the release peak were observed in 0.5 mM ammonium carbonate buffer. The authors recommend using PES membranes (10 kDa) and low buffer concentrations. The use of RC membranes in combination with a buffer led to similar results.

On the other hand, Bolea *et al.* reported higher recoveries for the fractionation of commercial AgNPs when using PES instead of RC membranes (cut-off 1 kDa) [48]. Similarly, larger peak areas were detected with PES (10 kDa) rather than with RC membranes for citrate-stabilized gold nanoparticles as presented by Schmidt *et al.* [23]. The authors further presented scanning electron microscopy (SEM) images of AuNPs immobilized on the separation membrane but also report on possible losses due to surface adhesion on internal surfaces.

Recently, more studies have focused on particle-membrane interactions. Bendixen *et al.* performed a detailed study on the particle-membrane interactions of commercial TiO_2 nanoparticles by varying the membrane materials and the mobile phase [10]. Retention time shifts depending on the type of the used membrane impeded particle size determination based on classical AF4 theory. Interestingly, retention time shifts and particle losses were not correlated with zeta potentials of the various membrane materials (RC, PES, PVDF) and pore sizes. Similar results were found by Mudalige *et al.* who detected varying losses for RC membranes (5 and 30 kDa) and PES membranes for citrate-stabilized gold nanoparticles [26]. The losses could not be explained by zeta potential measurements. Both groups believe that other properties such as the roughness, van der Waals, and hydrophobic interactions are probably contributing to the losses. To facilitate the method optimization, Gigault and Hackley recommend the use of PES membranes, which have broad compatibility with NPs and polymers and are applicable in a broad pH range (negatively charged at pH 3-11) [13]. Further adjustment of particle-membrane interactions should then be made by the optimization of the eluent composition.

Membranes effects are not exclusive to nanoparticles but also occur for proteins and other macromolecules [15,47,58]. Particle-membrane interactions strongly contribute to particle losses by adsorption phenomena, where surface charges and hydrophobicity of the membrane have been identified as the key properties. However, the strength of particle-membrane interactions is also influenced by the particles properties themselves which will be reviewed in the following section.

1.4.3.4. Particle properties

Colloidal interactions during AF4 (particle-particle and particle-membrane) strongly depend on the particles' core properties, such as the size and material composition, and their interfacial properties, such as the surface charge and surface functionalities. In literature, some attempts have been made to correlate the particles' properties with their losses and elution behavior during fractionation.

Size-independent retention time shifts that depended on the nanoparticle material (Au, Ag, Se, PSL) were detected by Gigault *et al.* [16]. Particles with larger Hamaker constants exhibited an increase in retention time, which is believed to be caused by increased van der Waals interactions between the membrane and the particles. Detected losses of < 12 % were attributed to membrane adsorption during fractionation. Although no further statements about material-dependent losses were given, this study emphasizes the influence of the particle core on particle-membrane and particle-particles interactions during AF4 analysis.

Some research groups report size-dependent losses. In the case of SiO_2 nanoparticles, size-dependent absolute recoveries of 53-76 % were observed, where recovery increased with decreasing NP size [18]. Relative recoveries of citrate-stabilized AgNPs ranging from 70-98 % with an increased loss of large AgNPs (100 nm) were found by Geiss *et al.* [52]. The same observations were reported for commercial TiO_2 NPs [10] and citrate-stabilized AuNPs [26]. The behavior was frequently explained by the higher probability of larger particles to adsorb on the membrane since they accumulate closer to the membrane.

In contrast, Schmidt *et al.* determined varying particle losses for citrate-stabilized AuNPs that did not follow a distinct trend [23]. The lowest recoveries were determined for 10 nm and 59 nm mean diameter particles with an absolute recovery of 50 % and 67 %, respectively. Particles with a diameter of 20 nm showed excellent recovery of 95 %. In addition,

citrate-stabilized AuNPs with different diameters showed similar recoveries, where only small particles exhibited lower recoveries [17]. The lower recoveries were caused by particle adsorption inside the system which was minimized by surfactant addition. Comparable results have been reported for commercial AgNPs [57]. Likewise, size-independent absolute recoveries of citrate-stabilized AgNPs (10 nm, 40 nm, and 70 nm) of 88-98 % were reported [56].

The contradictory results suggest that particle size may not be the only determining sample property. Different method parameters, like surfactant addition and varying membrane materials, impede a detailed comparison. Particle surfaces bearing different functionalities, which might modify hydrophobicity and hydrophilicity, contribute to particle losses. For example, it is known from environmental studies that surface modification of colloids by the addition of natural substances, such as humic acids and natural organic matter can alter the stability and behavior during FFF [29,59,60,61]. However, the effect of the particle surface on particle losses has scarcely been investigated yet.

Meisterjahn *et al.* examined the AF4 analysis of commercial AuNPs and natural nanoparticles in the presence of natural organic matter [36]. The addition of natural nanoparticles and natural organic matter (NOM) to the citrate-stabilized AuNPs resulted in decreased particle losses. This is probably due to adsorption of the NOM on the nanoparticle surface, increasing colloidal stability, and decreasing the adsorption probability. Based on the AF4 investigation of differently stabilized particles (citrate- and PVA-stabilized AgNPs and poly-acrylate stabilized TiO_2 nanoparticles), Ulrich *et al.* suggested a theory for particle-particle and particle-membrane interactions [8]. The authors state that van der Waals and electrostatic interactions are responsible for the observed retention time shifts of differently charged particles. They observed that highly charged particles reach higher flow streams compared to less charge particles due to enhanced repulsion between the particles and similarly charged membranes. This should also influence the particle recovery, which was not the main focus of this study [8]. Recently, Mudalige *et al.* studied particle losses of surface-modified AuNPs and proposed a correlation between the affinity of adsorbed surface ligands and particle losses [26]. Whereas citrate-stabilized AuNPs suffered significant losses, particles with tannic acid or bis(*p*-sulfonatophenyl)-phenylphosphine showed high relative recoveries. It is not yet clear which mechanisms are responsible for the improved recoveries.

Clearly, particle properties are strongly correlated to particle losses. Modifying the properties can be used to adjust particle-membrane and particle-particle interactions in order to minimize losses. In the following, the current approaches to overcome particle losses will briefly be discussed.

1.5. Strategies to overcome particle losses in AF4

Sample losses during AF4 have been recognized as a critical limitation of the method and an effort has been made to improve recoveries using two approaches: 1) modification of the analyzing system by adjustment of the solvent composition and membrane properties, and 2) modification of the sample during sample preparation.

Approach 1) includes an informed choice of the membrane and the carrier solution which is possible when basic knowledge about the sample composition exists. The addition of surfactants often increases recovery by adsorbing on the membrane and increasing electrostatic or steric repulsion [13]. Also, unspecific surfactant adsorption on the particles is likely and may significantly modify the original sample properties. Another way to increase sample recovery by minimizing particle adsorption on the membrane is membrane modification. This can either be achieved by physisorption of polymers [26,62] or covalent grafting. Physisorption of polymers is a straight-forward way to modify the entire internal setup by injecting the respective polymer solution before the actual sample. This strategy was recently applied by Mudalige *et al.* who injected polystyrene sulfonate before sample analysis [26].

The second approach, specific modification of the sample properties during sample preparation, was recently applied. Here, the addition of particle-specific ligands represents a promising concept. Mudalige *et al.* modified the surface of gold nanoparticles before characterization and minimized particle losses when combined with in-situ modifications of the internal setup [26]. A high colloidal stability seems to be a key requirement for low losses, thus increasing the colloidal stability of the sample beforehand is an important requirement for high recoveries.

However, both strategies have the disadvantage that the analytes might be modified, alter the behavior during FFF characterization, and do not represent the original sample property. It is therefore not always possible to overcome sample losses without modifying the sample itself. An alternative strategy to account analyte losses in analytical investigations

is the use of internal standards which is a common method in analytical chemistry [63, pp. 46-48]. Internal standards are substances, of which a defined amount is added to the sample (sample spiking) in order to assure qualification and quantification of the analyte [63, pp. 46-48]. There are several requirements for internal standards, such as similar physicochemical properties as the analyte. Further requirements are that the standard should not be present in the original sample and that it does not cause matrix effects itself [63]. Under the assumption that the analyte and the standard are subject to the same physicochemical influences, the recovery rate of the standard can be used for the correction of the analytical result of the analyte.

In order to transfer this general concept of internal standards to nanoparticle characterization with AF4, the development of such nanoparticles with well-defined properties is necessary. The development of suitable nanoparticles is hindered by a lack of understanding the relationship between particle loss mechanisms and particles properties. A systematic investigation of the particle properties on particle losses is therefore the main focus of this thesis.

The remaining sections are briefly summarized in the following. First, the synthesis, modification, and characterization of gold and silica nanoparticles are presented in chapter 2. This includes the investigation of labeling strategies, modification of the particle surface, and AF4 characterization. In chapter 3, particle loss mechanisms during FFF analysis of the various nanoparticles are investigated in detail. Particles losses of NPs with different surface functionalities are detected and relationships between the particle properties and the loss mechanisms are determined. Finally, spiking of river water using modified gold nanoparticles demonstrates the importance of nanoparticle surface modification on particle losses.

2. Reference nanoparticles

Nanoparticles used as internal standards should possess well-defined properties and distinct identification in order to be suitable for the determination of nanoparticle losses in real samples after sample spiking. Such "reference" or "tracer" NPs can also be used for the systematic investigation of particle losses during FFF characterization and might also be relevant for the development of FFF methods. A systematic investigation of NP characterization using FFF requires the availability of well-defined nanoparticle systems with narrow size dispersion, good detectability, and easy identification. Furthermore, these nanoparticles should possess a high stability in different media to enable a reliable characterization also when added to complex and challenging matrices as an internal standard.

Two NPs systems were applied as representative models for tracer nanoparticles in this study: silica and gold nanoparticles. Reliable synthesis protocols in a wide size range are available for both types, their surface modification is straight-forward, and they are intrinsically non-toxic [64,65].

Silica nanoparticles are used in many research fields, such as bioimaging [66] or drug delivery [65], and have widespread industrial applications, for example in the food industry [67]. The synthesis of SiO_2 nanoparticles was carried out using the well-investigated sol-gel synthesis which has been often described in literature with numerous synthesis procedures [65]. SiO_2 NPs can be modified with a variety of surface functionalities via covalent attachment with a broad range of functional silanes [68]. However, SiO_2 nanoparticles exhibit no significant optical absorption or fluorescence that would facilitate identification. Labeling techniques, such as dye labeling with fluorescent markers, are required to detect and clearly identify them.

Gold nanoparticles which were used as representative metal nanoparticles have some common features. The first aqueous synthesis protocols were developed by Turkevich [69] and Frens [70] after which various attempts have been made to further improve the quality of synthesized particles. Up to know, there are several fabrication protocols in aqueous as well as in non-aqueous media available [71]. Surface modification is usually carried out exploiting the high gold-sulfur affinity with thiolated ligands that easily bind to the particle surface [71]. The benefit of using gold nanoparticles for AF4 studies is the

characteristic optical absorption caused by the localized surface plasmon resonance (LSPR) [5]. The LSPR is not only size-dependent but also depends on the attached ligand and the surrounding media [71]. This optical property allows differentiation from other nanoparticles.

This chapter presents the synthesis, modification, and characterization of silica and gold nanoparticles in a size range of 5-105 nm. Standard synthesis routes were optimized and further developed. The obtained NPs were thoroughly characterized off-line in batch and using AF4. The goal was to achieve different particle systems with well-defined properties and a high stability in various media. This chapter has been divided into three parts: the synthesis of silica nanoparticles, synthesis and modification of gold nanoparticles, and the colloidal stability testing in batch.

The first part deals with the synthesis and characterization of silica nanoparticles including fluorescent labeling and metal labeling strategies to enhance detectability and differentiation. NP labeling was carried out during synthesis by the development and adjustment of existing synthesis protocols. AF4 characterization of silica nanoparticles was in agreement with AF4 theory and comparable TEM and DLS measurements. Fluorescent labeling was suitable for enabling a distinct differentiation. A new synthesis protocol enables the synthesis of monodispersed silica nanoparticles that contain different metal ions incorporated. The second part presents the synthesis of gold nanoparticles and their surface modification using different stabilizing ligands. Surface modification of gold NPs using thiolated ligands yielded nanoparticles with different surface properties. Growth of different silver-containing shells onto gold nanoparticles modified the optical properties yielding in unique and specific absorption properties. Surface modification of these particles resulted in shell degradation depending on the used ligand. Finally, the colloidal stability of gold and silica nanoparticles was tested using dynamic light scattering and UV-Vis absorption spectroscopy in different media. Colloidal stability testing revealed a strong ligand dependence on the agglomeration behavior of gold nanoparticles. Silica nanoparticles were stable at higher ionic strength compared to gold nanoparticles.

2.1. Silica nanoparticles

2.1.1. Biphasic sol-gel synthesis of silica nanoparticles

The synthesis of silica nanoparticles is based on the sol-gel process, which involves the hydrolysis of a silica precursor under alkaline conditions, and further polycondensation to form the so-called silica sol [72, pp. 174-176]. The well-known method by Stöber *et al.* uses ammonia in an alcoholic solution to hydrolyze tetraethylorthosilicate (TEOS) to form SiO_2 NPs within a broad size range [73]. Many protocols for the synthesis of silica nanoparticles are available but there is still ongoing research to optimize the sol-gel method in order to achieve better control over particle properties such as the morphology and surface characteristics [65].

The method described by Hartlen *et al.* was applied for the synthesis of unlabeled silica nanoparticles [74]. It can produce particles with a narrow size distribution for particles below 20 nm that the traditional Stöber method cannot. The Hartlen method uses L-Arginine as a basic catalyst in a biphasic system. Here, TEOS as the precursor is present in the organic layer on top of the alkaline amino acid solution. This allows a more precise control over the hydrolysis, which only takes place at the liquid-liquid interface. In contrast to the Stöber method, the Hartlen process uses seeding growth of the primarily synthesized SiO_2 NPs for the formation of larger NPs (Figure 2.1). This multistep process retains a narrow size distribution with homogenous particle morphology [74].

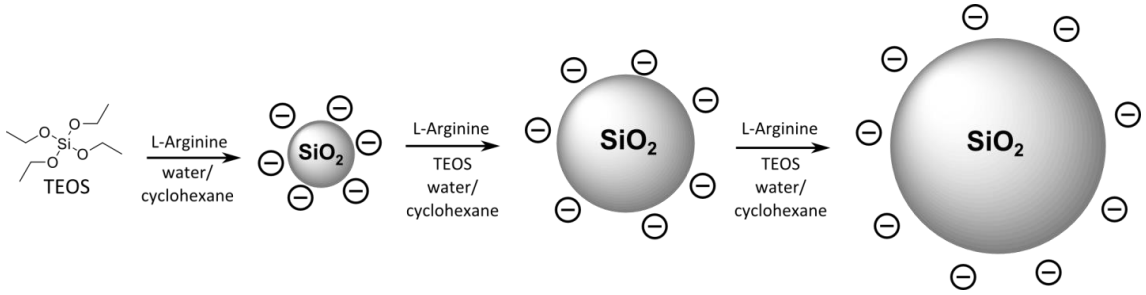

Figure 2.1: Biphasic synthesis procedure of silica nanoparticles prepared by the Hartlen method.

The particle formation process using basic amino acids in the biphasic synthesis protocol has been studied [75,76]. It is believed to follow a La-Mer like particle mechanism combined with a densification step [76]. The main characteristics can be summarized as follows:

1. The hydrolysis of TEOS at the liquid-liquid interface leads to an accumulation and an increase of soluble silicate species in the aqueous solution until a critical concentration is reached. The time required to reach this concentration is called the lag time (at the applied conditions ~100-140 min).
2. Nucleation is triggered above a critical concentration (supersaturation) leading to small silica nanoparticles. A transition of fractal gel-like particles into dense spheres occurs simultaneously.
3. Further nanoparticle growth and densification takes place, and the supersaturation slowly reaches an equilibrium value. The growth is then limited by the diffusion-controlled addition of monomer species (formed by TEOS hydrolysis) onto primary particles.

The most important parameters influencing the particle formation are the L-Arginine concentration, the pH, and the synthesis temperature [74]. The as-synthesized nanoparticles were characterized using AF4 and compared to DLS and TEM measurements. Furthermore, the elution behavior during AF4 was assessed.

2.1.1.1. Experimental procedures

The synthesis protocol of Hartlen *et al.* with seed formation and seeding growth was used without further modification [74]. For the synthesis of the primary seed particles (SiO_2-NP25) with a mean core diameters in the range of 15-25 nm, 91 mg (0.52 mmol) L-Arginine was dissolved in 69 mL ultrapure water and topped with 4.5 mL cyclohexane. The solution was heated to 60 °C under mild stirring after which 5.5 mL (24.8 mmol) TEOS was added to the top layer and the liquid was slowly stirred for 20 hours.

Silica nanoparticles with a mean core diameter of 13 nm (SiO_2-NP13) were synthesized using a similar procedure but using $NaHCO_3$ instead of L-Arginine as catalyst. Briefly, 131 mg $NaHCO_3$ were dissolved in 207 mL water and heated to 40 °C. The solution was topped with 15 mL cyclohexane, after which 16.5 mL (7.5 mmol) TEOS was added and stirred (90 rpm) for 20 hours.

After the reaction time, the dispersions were purified by dialysis against ultrapure water using a 100 kDa RC membrane for at least 24 hours and repeated (usually 3-5 times) water exchange. Finally, the dispersions were filtered through a 0.2 µm PES syringe filter.

Seeding growth was performed by dissolving 14 mg (0.08 mmol) L-Arginine in 26 mL ultrapure water to which 10 mL of the seed particle dispersion was added. The alkaline SiO_2 dispersion was then topped with 5 mL cyclohexane and heated to 60 °C. Addition of 3.52 mL (15.9 mmol) TEOS and moderate stirring at 60 °C for 20 hours completed particle growth. Purification was again performed by dialysis and filtration as mentioned above. The obtained nanoparticles were labeled as SiO_2-NP30, SiO_2-NP51, and SiO_2-NP93.

Dynamic light scattering, elementary analysis, transmission electron microscopy, and zeta potential measurements were performed for batch NP characterization. Different dynamic light scattering instruments were used in this thesis. The instrumental details and procedures for DLS and TEM characterization are given in chapter 5.2. The synthesized silica nanoparticles in this section were characterized using DLS setup 2.

AF4 characterization was performed using a 10 kDa PES membrane and 0.05 % (w/v) SDS as eluent. Two different cross-flow fields were applied in order to remain a moderate retention time and high resolution for different sized particles. SiO_2-NP13 particles were fractionated using a cross-flow of 1.5 mL/min, whereas the larger particle samples (> 13 nm) were analyzed using a cross-flow of 1.0 mL/min as summarized in Figure 2.2. The detailed flow program is listed in Table 5.3 (chapter 5).

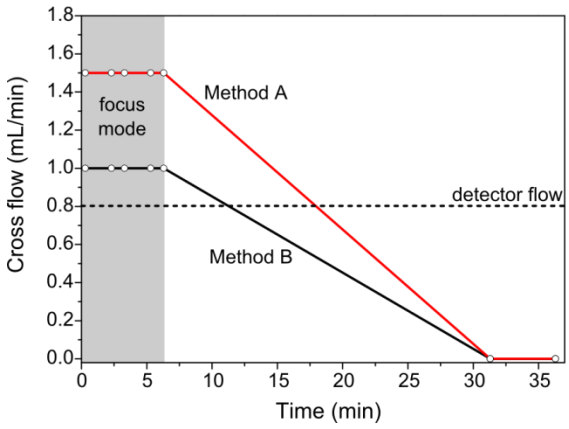

Figure 2.2: Flow programs used for the separation of silica nanoparticles. SiO2-NP13 particles were fractionated using Method A. Larger NPs were fractionated using Method B.

2.1.1.2. Results

The TEM images of the synthesized silica nanoparticles are presented in Figure 2.3. The Hartlen method yielded primary SiO_2 nanoparticles with a mean core diameter of 13 nm (reaction temperature 40 °C) and 25 nm (reaction temperature 60 °C). A threefold seeding

growth using the 25 nm sized particles as seeds resulted in particles with a mean core size of 30 nm, 51 nm, and 92 nm in subsequent growth steps. All synthesized particles showed a homogenous spherical morphology and narrow size distribution (polydispersity ≤ 15 %).

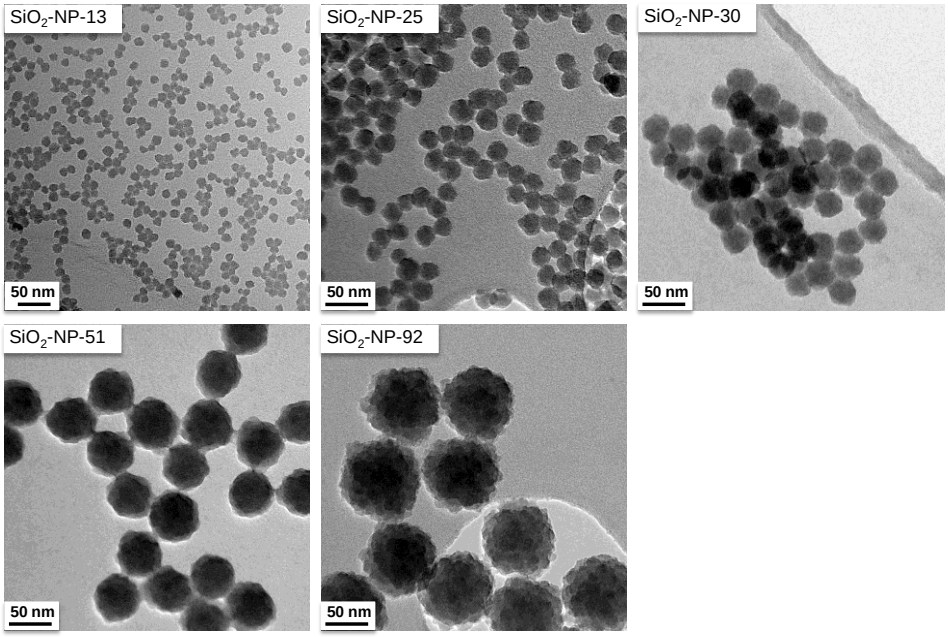

Figure 2.3: TEM images of silica nanoparticles obtained using the Hartlen method.

Table 2.1 summarizes the determined properties of the synthesized nanoparticles. The particles were negatively charged with zeta potential values ranging from -72 to -28 mV (measured in ultrapure water). Offline (batch DLS) and online DLS (AF4-DLS) measurements confirmed a narrow size distribution for all synthesized particles. Except for SiO2-NP92 particles, which showed a lower hydrodynamic diameter in online DLS, the results of the batch-mode and online DLS were in good agreement.

Table 2.1: Colloidal characterization of nanoparticles synthesized using the Hartlen method.

	$D_{TEM/SEM}$ (nm)	$D_{Batch-DLS}$ (nm)	$D_{AF4-DLS}$ (nm)	Zeta potential (mV)
SiO2-NP13	12.5 ± 1.9	14.0 ± 4.0	15.2 ± 2.0	-28
SiO2-NP25	25.1 ± 2.8	26.6 ± 1.5	28.8 ± 3.5	-72
SiO2-NP30	29.9 ± 2.8	34.4 ± 1.8	36.9 ± 1.9	-60
SiO2-NP51	51.4 ± 2.4	60.8 ± 4.0	58.4 ± 2.4	-50
SiO2-NP92	91.9 ± 3.7	95.6 ± 5.2	82.3 ± 3.6	-52

The AF4 fractograms of the synthesized nanoparticles are presented in Figure 2.4.

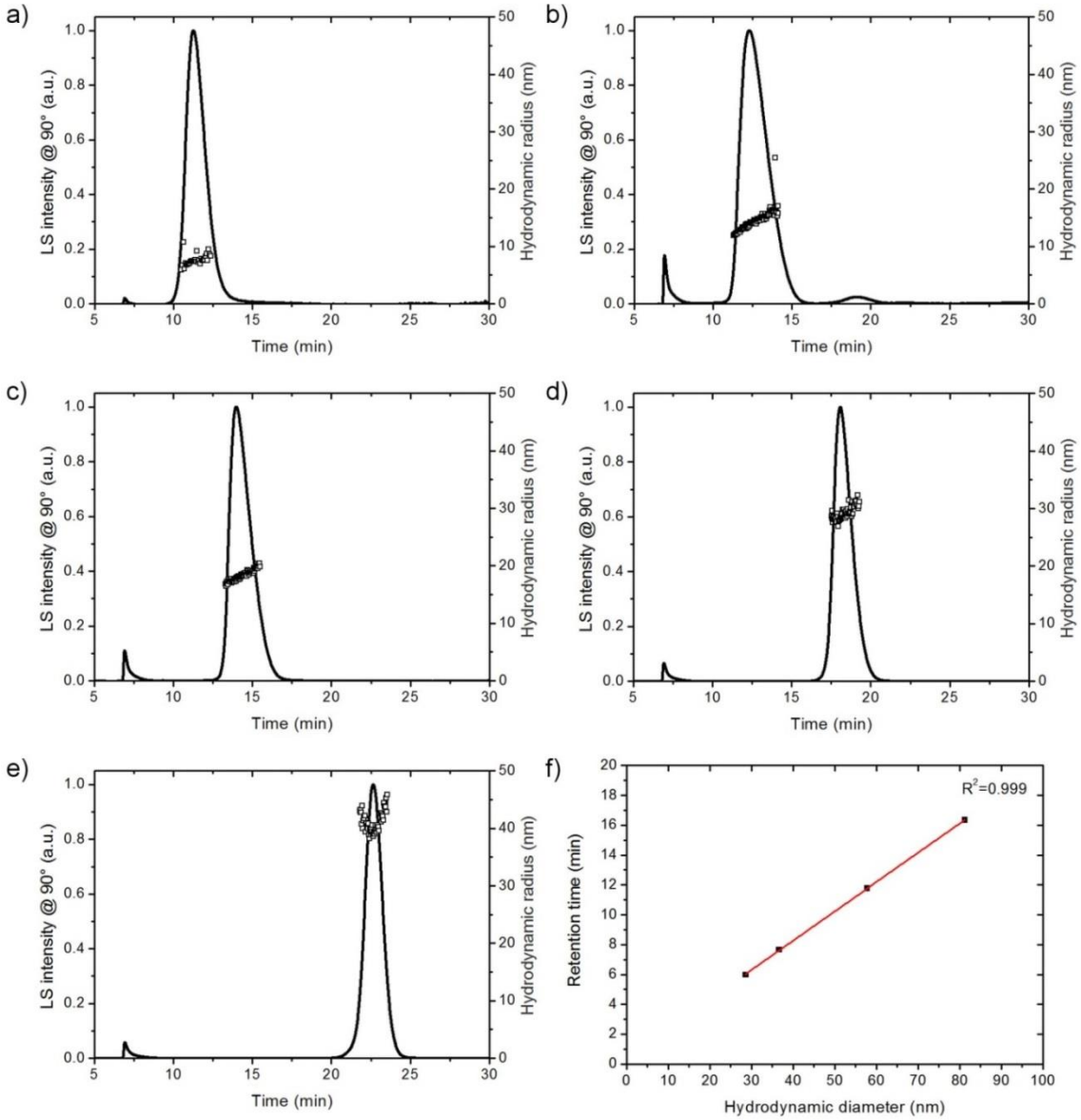

Figure 2.4: a-e) AF4 fractograms (solid line) and hydrodynamic diameters (squares) of synthesized silica nanoparticles with a mean core diameter of a) 13 nm, b) 25 nm, c) 30 nm, d) 51 nm, and e) 92 nm. f) Linear relationship between hydrodynamic diameter (from online DLS) and the retention time was detected. Fractionation was performed using a 10 kDa PES membrane and 0.005 % SDS solution as eluent.

All fractograms show a void peak at an elution time of 6.9 min and the main sample peak with a Gaussian-like peak shape. In the case of SiO2-NP25, a second small peak was observed at an elution time of about 18 min. However, this peak steadily decreased in subsequent runs and therefore might be caused by desorption of previously adsorbed particles. Except for SiO_2-NP92, the detected hydrodynamic diameters increased with increasing retention time as expected. Plotting the determined hydrodynamic diameter versus the retention time revealed a linear relationship (Figure 2.4, f).The results show that the syn-

thesized monodispersed silica nanoparticles were successfully fractionated using AF4. Sizing of the NPs were achieved using online DLS measurements which showed a good agreement with the batch DLS and TEM measurements except for the largest NPs (Figure 2.5).

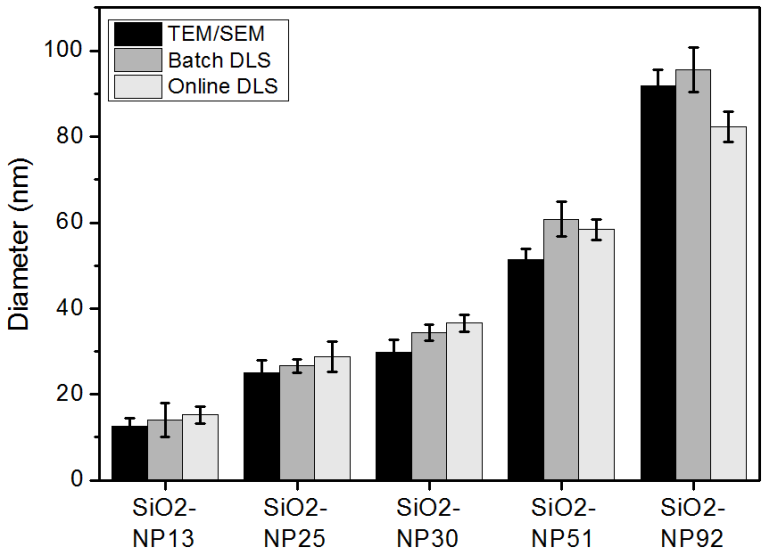

Figure 2.5: Summary of determined nanoparticle sizes using electron microscopy (black), batch DLS (dark grey), and online DLS from AF4 characterization (light grey). Error bar represent one standard deviation.

2.1.1.3. Discussion

Monodisperse silica nanoparticles with mean core diameters of 13-92 nm were synthesized using the Hartlen method. The biphasic synthesis protocol proves to be suitable for the fabrication of nanoparticles in a broad size range. A narrow size distribution (polydispersity ≤ 15 %) was confirmed for synthesized particles with batch DLS, AF4 measurements including online DLS, and TEM measurements, except for the smallest particles synthesized (polydispersity of 29 % with batch DLS).

The AF4 characterization of the synthesized nanoparticles yielded results that were in accordance with theory, except for the largest NP tested. The characterization results using TEM and batch DLS were consistent with the online DLS results obtained during AF4 analysis, except for the largest nanoparticles synthesized. For these particles, online DLS showed significantly smaller diameters. The reasons for this deviation are unclear but may include concentration effects leading to multiple scattering or too low residence times. The expected linear relationship between the retention time and the hydrodynamic diameter confirmed an ideal elution behavior. This allows the use of these particles to be

used as calibration standards in the tested eluent. The results fit to the report of Barahona *et al.* who also reported ideal behavior of purchased silica nanoparticles using 0.05 % SDS and ammonium carbonate buffer (0.25 mM) as eluent [18]. Thus, the investigated NP system presents a relevant basis for the development of tracer nanoparticles for AF4.

2.1.2. Fluorescently labeled silica nanoparticles

Fluorescence labeling provides a specific feature for the distinct identification of the silica nanoparticles. Dye labeling of SiO_2 nanoparticles is a common strategy to enhance their detectability and use them for different imaging techniques, such as fluorescent microscopy in life science applications. To obtain fluorescently labeled SiO_2 NPs, fluorescent dyes can be incorporated into the particles [77] or attached to the particle surface [78]. Rhodamine dyes are frequently employed for biological imaging and nanoparticle labeling due to their high absorption coefficients and photostability [79].

In this thesis, Rhodamine B was used as labeling dye, which was previously used for particle labeling of silica nanoparticles [80]. I have chosen dye incorporation into the NPs because it ensures low dye leaching rate and provides surface functionality for further modification [81]. Both, the Hartlen method and the Stöber method were modified with the introduction of the dye similar to Tavernaro *et al.* [82]. The size distribution, morphologies, and AF4 characterization of the synthesized particles were compared in order to test their use as reference and tracer particles.

2.1.2.1. Experimental procedures

The covalent incorporation of the dye was achieved by coupling the isothiocayanate functionalized dye with the amine containing silane linker (3-aminopropyl)triethoxysilane [83, p. 410]. The primary amine and the isothiocyanate react to form a thiourea linkage as shown in Figure 2.6. The precursor was prepared by dissolving 9 mg (0.017 mmol) Rhodamine B isothiocyanate in 2 mL DMSO. Then, 13 µL (0.055 mmol) of (3-aminopropyl)triethoxysilane was added and the mixture was shaken at 60 °C for 24 hours. The silane modified dye was then employed for the in-situ modification during particle formation. Two approaches were used for particle synthesis.

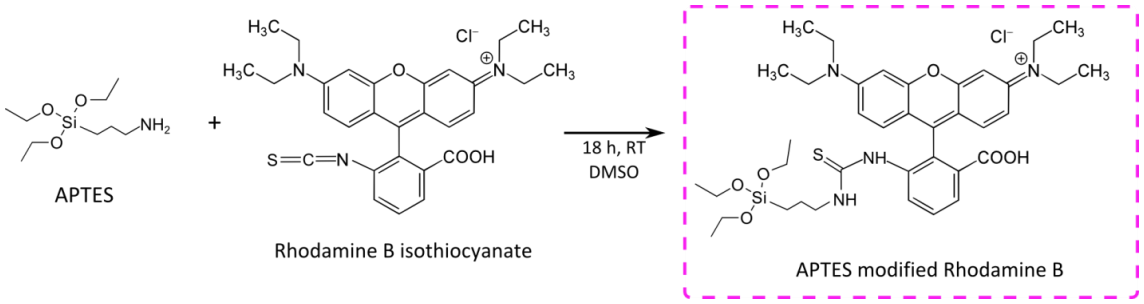

Figure 2.6: APTES coupling of Rhodamine B isothiocyanate.

The previously described Hartlen method was modified for the synthesis of Rhodamine-labeled particles by addition of Rhodamine dye into the reaction mixture. The growth for larger particles was performed with the addition of Rhodamine-APTES for sufficient dye loading (Figure 2.7).

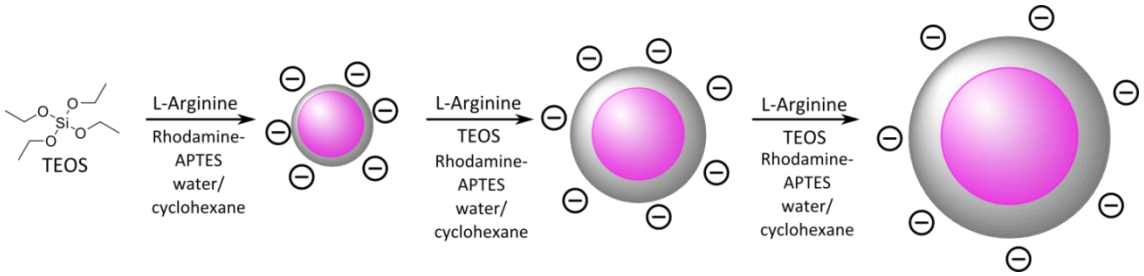

Figure 2.7: Synthesis of Rhodamine-labeled SiO_2 nanoparticles using the Hartlen method.

Primary particles were synthesized by dissolving 91 mg (0.52 mmol) L-Arginine in 69 mL ultrapure water, addition of 4.5 mL cyclohexane, and heating to 60 °C. Then, 5.5 mL (24.8 mmol) TEOS was added to the top layer. After 30 minutes, 200 µL of the APTES-Rhodamine solution was added and the solution was stirred for 20 hours. The dispersion was purified by dialysis against ultrapure water using a 100 kDa RC membrane for at least 24 hour and multiple water exchange. Finally, the dispersion was filtered through a 0.2 µm PES syringe filter.

Seeding growth was performed by dissolving 14 mg (0.08 mmol) L-Arginine in 26 mL ultrapure water to which 10 mL of the former synthesized nanoparticle dispersion was added. The alkaline SiO_2 dispersion was then topped with 5 mL cyclohexane and heated to 60 °C. Addition of 3.52 mL (15.9 mmol) TEOS was followed by addition of 200 µL of the APTES-Rhodamine solution 30 minutes after TEOS addition. Moderate stirring at 60 °C was maintained for 20 hours to complete particle growth. Purification was again performed by dialysis and filtration as mentioned above. The particles synthesized using

this approach are labeled SiO2-Ha-Rhod-27, SiO2-Ha-Rhod-38, SiO2-Ha-Rhod-65, and SiO2-Ha-Rhod-105.

The second route to achieve Rhodamine-labeled SiO_2 nanoparticles used the Stöber method according to Figure 2.8. Addition of Rhodamine-APTES at the beginning of the reaction yielded fluorescently labeled silica nanoparticles, too.

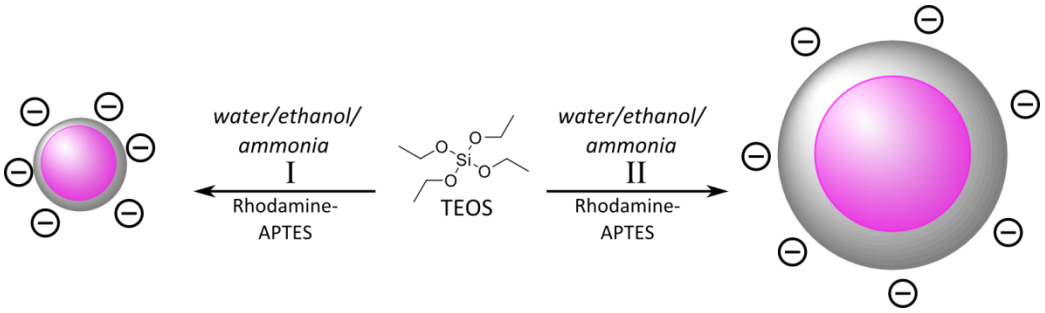

Figure 2.8: Synthesis of Rhodamine-labeled SiO_2 nanoparticles using the Stöber process.

Synthesis of Rhodamine-labeled silica nanoparticles via the Stöber process was performed by mixing the respective amounts of water, ethanol, and ammonia after which TEOS was added (Table 2.2). The reaction mixture was stirred for 30 minutes and then, 500 µL of the APTES-Rhodamine mixture was added. After a reaction time of 24 hours, the suspension was dialyzed against ultrapure water using a 100 kDa RC membrane for at least 24 hours and multiple water exchange. Finally, the dispersion was filtered through a 5 µm CA syringe filter and a 0.2 µm PES syringe filter. The obtained particles were labeled as SiO_2-Stö-Rhod-19 and SiO_2-Stö-Rhod-66.

Table 2.2: Applied concentrations for the synthesis of Rhodamine-labeled silica nanoparticles using the Stöber method.

Sample	Water (µL)	Ethanol (g)	Ammonia (g)	TEOS (mL)
SiO_2-Stö-Rhod-19	822	37.23	0.95	1.11
SiO_2-Stö-Rhod-66	822	35.60	1.88	2.11

Dye leaching was tested by centrifuging 500 µL of the Rhodamine-labeled nanoparticles using a centrifuge filter device (100 kDa PES) and collecting the filtrate. The ratio in percent of the fluorescence intensity of the filtrate and the neat dispersion (both 100x diluted with ultrapure water) represents the amount of free Rhodamine dye.

AF4 characterization was performed using a 10 kDa PES membrane and a 0.005 % SDS with 1 mM NH_4NO_3 solution as eluent. Flow program C with a linear decreasing cross-flow of 1 mL/min was used. The detailed flow program is listed in Table 5.5 (chapter 5).

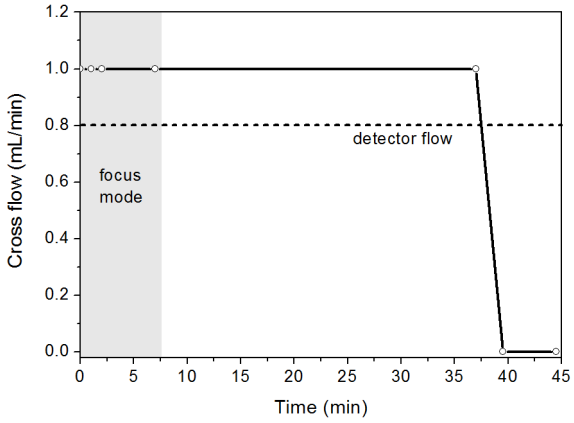

Figure 2.9: Flow program used for the separation of Rhodamine-labeled silica nanoparticles (Flow method C).

2.1.2.2. Results

The TEM images of the Rhodamine-labeled silica nanoparticles are presented in Figure 2.10.

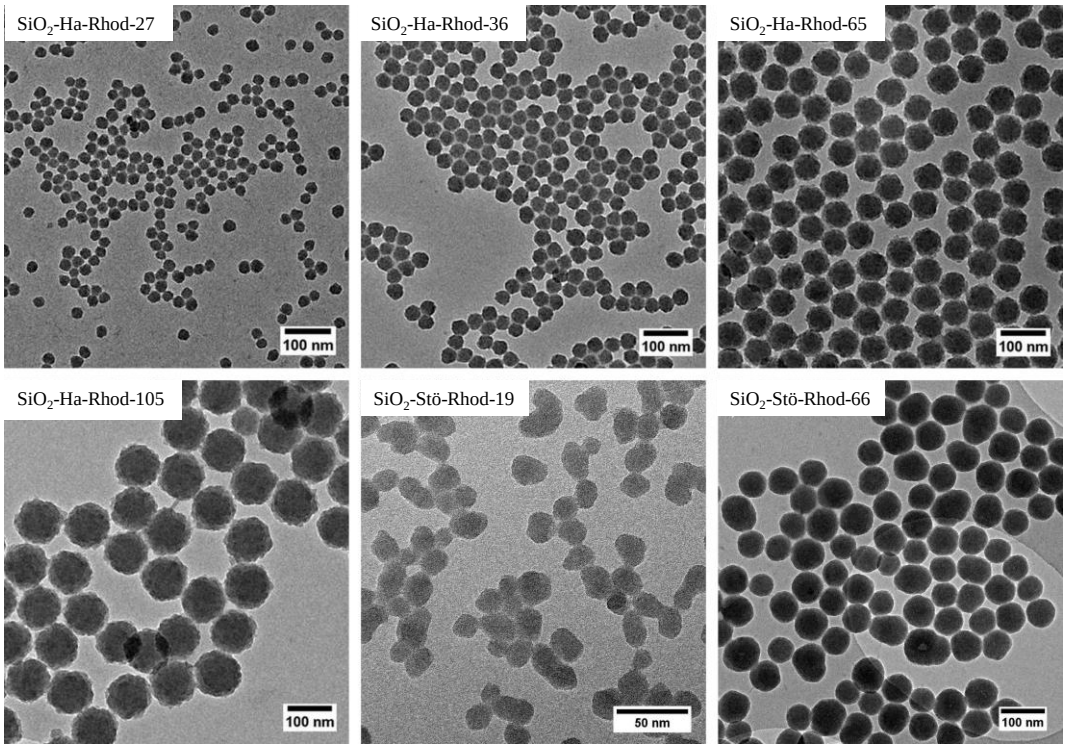

Figure 2.10: TEM images of synthesized Rhodamine-labeled silica nanoparticles using the Hartlen (SiO_2-Ha-Rhod-27, -38, -65, -105) and the Stöber method (SiO_2-Stö-Rhod-19, -66).

The TEM images confirm the high monodispersity and uniform morphology of the silica nanoparticles prepared by the Hartlen method similar to the presented unlabeled SiO_2 NPs in the previous section. Nanoparticles prepared by the Stöber method varied in morphology and size distribution.

The properties of the Rhodamine-labeled silica nanoparticles are summarized in Table 2.3. The incorporation of the silane-modified Rhodamine dye using the Hartlen method yielded fluorescent SiO_2 nanoparticles with mean core diameters of 27 nm, 38 nm, 65 nm, and 105 nm. Using the Stöber method, fluorescent silica nanoparticles with mean core diameters of 19 nm and 66 nm were obtained.

Table 2.3: Colloidal characterization of Rhodamine-labeled silica nanoparticles.

Sample	D_{TEM} (nm)	$D_{Batch\text{-}DLS}$ (nm)	$D_{AF4\text{-}DLS}$ (nm)	Zeta potential (mV)	Dye leaching (%)
SiO_2-Ha-Rhod-27	26.6 ± 2.5	24.2 ± 2.8	29.2 ± 1.2	-26	0.89
SiO_2-Ha-Rhod-38	37.6 ± 2.2	38.4 ± 3.1	39.2 ± 1.2	-28	0.69
SiO_2-Ha-Rhod-65	65.4 ± 2.6	66.8 ± 5.2	66.2 ± 1.7	-31	1.81
SiO_2-Ha-Rhod-105	104.7 ± 4.6	110.8 ± 5.0	104.6 ± 3.9	-36	0.86
SiO_2-Stö-Rhod-19	18.6 ± 2.2	26.4 ± 2.0	27.1 ± 3.2	-24	0.49
SiO_2-Stö-Rhod-66	65.7 ± 8.7	80.2 ± 4.8	77.5 ± 5.8	-29	2.04

A narrow size distribution was determined by all three sizing techniques for all synthesized nanoparticles. The particles were all negatively charged with zeta potential values ranging from -24 to -36 mV. Leaching of the fluorescent dye was less or equal than 2 % for all synthesized particles. Figure 2.11 presents the relative absorption and fluorescence spectra of 27 nm sized labeled SiO_2 NPs with a Stokes shift of 20 nm. AF4 fractograms of the Rhodamine-labeled silica nanoparticles and a plot of the retention time vs. the hydrodynamic diameter are presented in Figure 2.12.

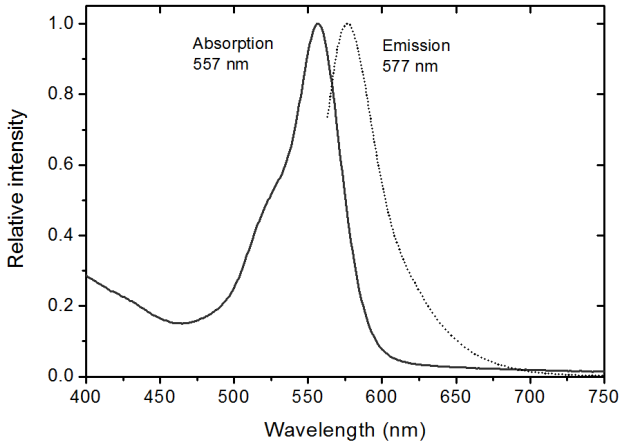

Figure 2.11: Relative absorption (closed) and fluorescence (dotted) spectra of SiO_2-Ha-Rhod-27 NPs.

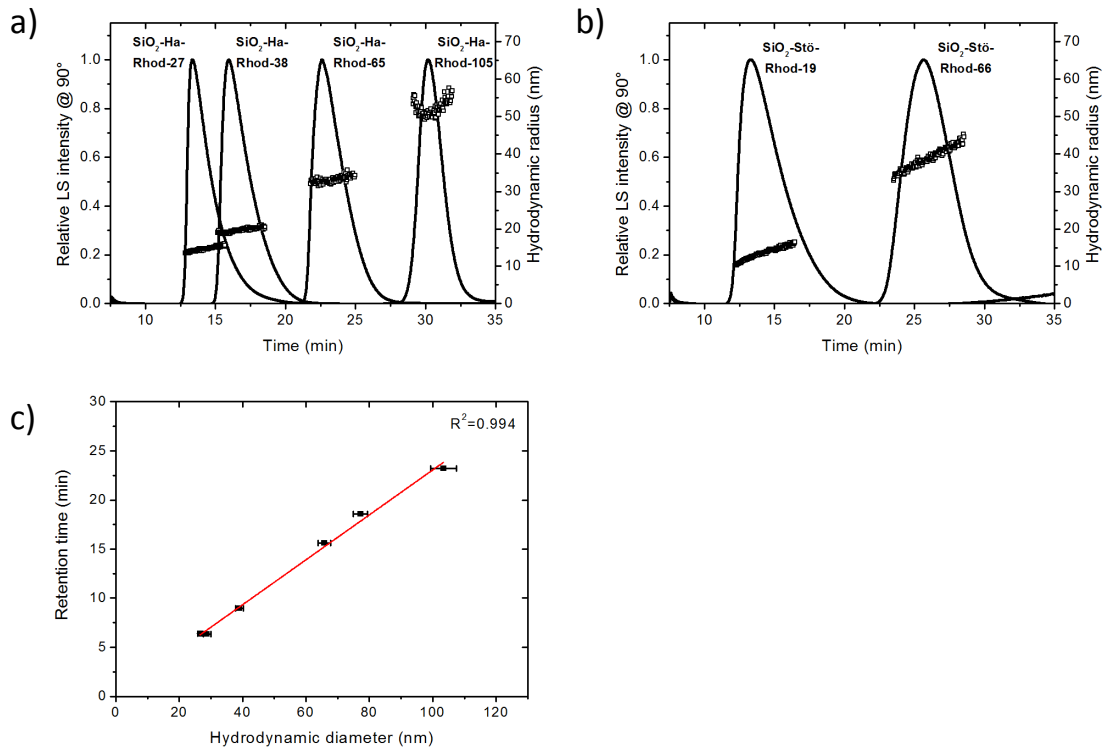

Figure 2.12: AF4 fractograms (solid line) and hydrodynamic diameter (squares) of the Rhodamine-labeled silica nanoparticles prepared using the Hartlen method (a) and the Stöber method (b). (c) A linear relationship between the retention time and the determined online D_h indicate proper elution (error bar represents standard deviation of the particle size distribution).

The AF4 fractograms reveals a broader size distribution for the particles synthesized via the Stöber method as indicated by the broader peak width. The same behavior as for the SiO_2-NP92 particles was observed for the largest fluorescently labeled NPs (SiO_2-Ha-Rhod-105). The detected hydrodynamic diameters did not increase with increasing reten-

tion time (Figure 2.12 a). A linear correlation between the retention time and the hydrodynamic diameter verified proper elution according to AF4 theory (Figure 2.12 c).

Figure 2.13 presents the iso-absorbance plot of Rhodamine-labeled silica nanoparticles and unlabeled silica nanoparticles. A fluorescence signal of the Rhodamine-labeled NPs was detected at an elution time of 12.6-16.6 min. In contrast, the unlabeled silica nanoparticles did not show a significant fluorescence signal (elution time of 10-15.5 minutes).

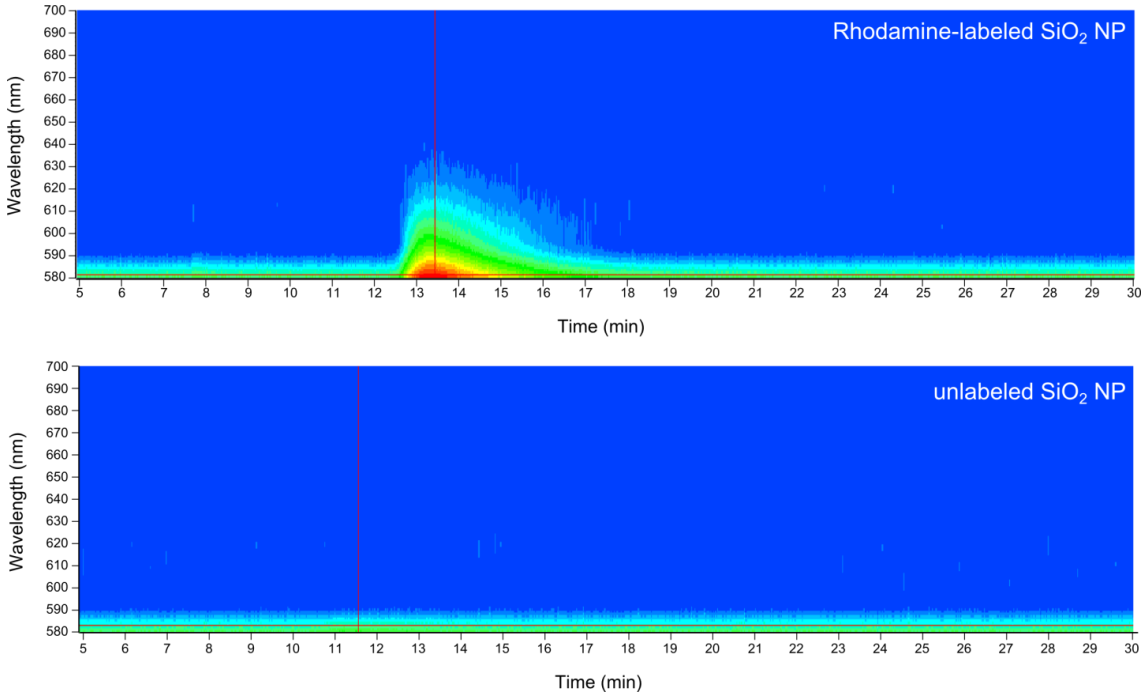

Figure 2.13: Iso-absorbance plots of the fractograms of Rhodamine-labeled SiO_2 NPs (SiO_2-Ha-Rhod-27) (top) and unlabeled silica nanoparticles (D_h = 16.8 nm) (bottom). The red line indicates the position of the sample peaks' mode. The excitation wavelength was set to 553 nm.

2.1.2.3. Discussion

Fluorescence labeling of SiO_2 NPs was successfully achieved with two different sol-gel methods. The Stöber and the Hartlen method were used for the synthesis of dye-labeled NPs. Synthesis using the biphasic Hartlen approach yielded in particles with a narrower size distribution compared to the Stöber process. The reason for the narrower size distribution is likely the controlled and slow nucleation, which is responsible for a more homogenous size distribution [74]. NPs obtained by both methods exhibited only minimal dye leaching ($\leq$ 2 %) which confirms a robust covalent attachment of the dye and a passivation of the surrounding silica shell. Reliable dye incorporation is necessary to ensure a

uniform behavior during fractionation without substantial deviations of the fluorescence signal.

Deviations between different sizing methods were detected for more polydispersed samples. One interesting finding is the discrepancy between the number based size distribution determined by TEM and the intensity based size distribution determined by DLS for the SiO_2 nanoparticles using the Stöber method. It is expected for DLS to determine larger sizes compared to TEM, since the D_h includes the core diameter (equivalent to D_{TEM}) plus the attached hydration shell. A further aspect adds to the detected deviation. The detection signal in DLS, the scattered light intensity, is very sensitive to different particle sizes since the scattering intensity of a particles is proportional to the sixth power of its diameter [23]. Therefore, the intensity based size distribution may be shifted to larger sizes in the case of polydispersed samples. The discrepancy between these two measurements increases with wider size distribution [84]. A conversion of the intensity weighted size distribution into a volume or number based size distribution will likely overcome this issue [84].

Fluorescence detection allows differentiation between labeled and unlabeled silica nanoparticles. The results of this study showed that Rhodamine-labeled silica nanoparticles can be differentiated using online fluorescence detection. By comparison of the iso-absorbance plots of unlabeled and Rhodamine-labeled silica nanoparticles, identification of the labeled particles was achieved. A further benefit of fluorescence-labeling is the possibility of particle quantification using online fluorescence detection.

2.1.3. Metal-labeled silica nanoparticles

A growing number of AF4 is coupled to ICP-MS/OES, especially for natural colloids and ENPs investigations [27]. Tracer NPs with a distinctive elemental composition enable sample spiking and differentiation using AF4 in combination with elementary analysis. The synthesis of such particles requires a controlled loading with different metal ions to ensure homogenous distribution.

There are two approaches for the synthesis of such particles: introduction of the metal ions during synthesis or post-synthesis adsorption of metal ions onto the surface. The latter is investigated in many research fields such as contrast agents in biomedical imaging [85] or waste-removal in environmental studies [86]. In many cases, the strategy involves

surface modification prior to subsequent adsorption of metal ions. Surface modification introduces functional groups (in most cases chelates) which then can strongly bind the metal ions [87]. In addition, unspecific adsorption of metal ions onto SiO_2 NP surface was shown recently [88]. The main disadvantages of metal ion adsorption on surface-modified NPs are possible alteration of their colloidal stability and increased matrix effects. The second strategy introduces the metal ions during NP synthesis, which enables a homogenous distribution inside the particles. This method was used for the development of isotopically labeled NPs for AF4 [19,29,30]. The artificial isotope relations are then used to identify the modified NPs. Isotope labeling during synthesis require precursors from costly artificial isotopes.

Based on the Hartlen method, I have developed a synthesis protocol for the incorporation of different metals into silica nanoparticles. Similar to fluorescent labeling, a precursor (metal-chelator) complex was prepared and introduced into the reaction mixtures. This method was used for the synthesis of primary SiO_2 nanoparticles with different incorporated metal ions. In addition, metal-labeling of unmodified nanoparticles by incorporation of the metal-chelator complex into the silica shell was achieved.

2.1.3.1. Experimental procedures

The precursor was formed by mixing an aqueous metal salt with an ethylenediaminetriacetic acid (EDTA) functionalized silane, N-(trimethoxysilylpropyl) ethylenediaminetriacetic acid (TMS-EDTA), either in an L-Arginine solution (0.22-1.36 mg/mL) or without dilution (Figure 2.14). The precursor mixture was mixed freshly before each synthesis step (at least 30 minutes in advance). A 10-fold amount of TMS-EDTA compared to the metal ion was used unless otherwise stated.

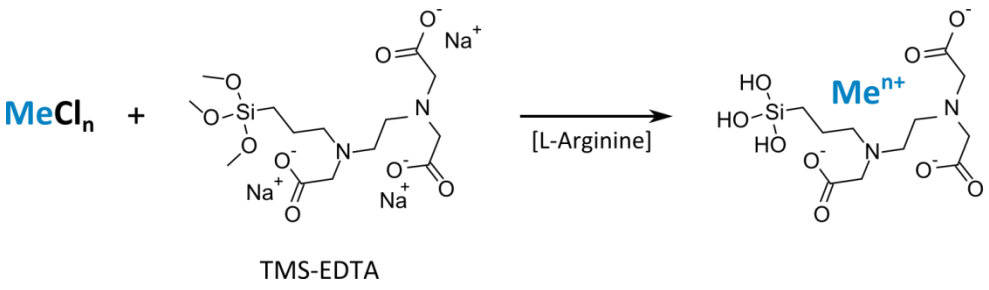

Figure 2.14: Formation of metal-TMS-EDTA precursor mixture.

The synthesis of primary silica nanoparticles was investigated by variation of the precursor concentration and used metal ions. A standard synthesis was performed as follows.

1.36 mg/mL L-Arginine solution was topped with cyclohexane, slowly stirred (90 rpm), and heated to 60 °C after which TEOS was added to the top layer. The TEOS concentration in the top layer was kept constant at 1.36 mol/L. After a reaction time of 15 minutes, the precursor mixture was injected into the aqueous phase. Stirring at 60 °C was remained for 20 hours after which purification via dialysis against water (100 kDa RC membrane) and final filtering through a 0.2 µm PES syringe filter was performed.

The influences of the metal concentration and metal/TMS-EDTA ratio on particle formation and labeling efficiency were investigated by preparation of different precursor mixtures (Cu(II) as cation). Table 2.4 summarizes the details of the different batches. Two different parameters were varied: either the Cu(II) concentration was kept constant and the TMS-EDTA concentration was adjusted (batch A-D) or vice versa (batch D-F). Syntheses of all six batches were performed parallel using a six fold heating system (Carousel 6 Plus Reaction Station, Radleys, England). The obtained particles were labeled as SiO_2-Cu-EDTA-A to -F.

Table 2.4: Copper and TMS-EDTA concentrations used for the synthesis of Cu-labeled primary silica nanoparticles.

Sample	*c*(TMS-EDTA) (mM)	*c*(Cu(II)) (mM)	*c*(TMS-EDTA) /*c*(Cu)
SiO_2-Cu-EDTA-A	0	10	--
SiO_2-Cu-EDTA-B	25	10	2.5
SiO_2-Cu-EDTA-C	50	10	5
SiO_2-Cu-EDTA-D	100	10	10
SiO_2-Cu-EDTA-E	100	20	5
SiO_2-Cu-EDTA-F	100	40	2.5

The influence of different metal cations on particle formation was investigated using Cu(II), Co(II), Ce(III), Fe(II), and Fe(III). The precursor solutions were mixed immediately before synthesis and added 15 minutes after TEOS addition (fixed TMS-EDTA/metal ratio of 10). The precursor mixture was prepared by dissolving 225 µL TMS-EDTA in 2.25 mL L-Arginine (1.36 mg/mL) solution and addition of 275 µL of the respective metal salt (100 mM). Except for Ce(III), clear solutions were formed when mixing the respective metal salt with TMS-EDTA. In the case of Ce(III), the formation of white flakes were observed which dissolved after a few seconds. Similar observations

were made when Gd(III) was used as metal cation. The synthesized NPs were labeled as SiO_2-Me-EDTA where "Me" stands for the respective metal cation.

Seeding growth of labeled nanoparticles as well as unlabeled nanoparticles was tested with and without addition of the precursor mixture. The standard procedure of the Hartlen method was modified as follows. In a first investigation, seeding growth with addition of a precursor solution was performed by diluting 5 mL of unlabeled seed particles ($D_{\text{Batch-DLS}}$ = 32 nm, β(Si) = 337.8 mg/L) and adjusting the L-Arginine concentration to 0.22 mg/mL to obtain a final volume of 23 mL. The dispersion was then topped with 2.25 mL cyclohexane and heated to 60 °C. Then, 112 µL (0.136 mmol) TMS-EDTA was added to modify the nanoparticle surface in-situ. Different amounts of a 100 mM $CuCl_2$ solution were added after different reaction times (Table 2.5). After further 30 minutes, 1.76 mL (7.94 mmol) TEOS was added to initiate shell formation. The obtained NPs were labeled as SiO_2-Cu-EDTA-II-A to -F.

Table 2.5: Copper TMS-EDTA concentrations and addition times applied for the seeding growth of silica nanoparticles.

Sample	$c(CuCl_2)$ (mM)	c(TMS-EDTA) /c(Cu)	Addition $CuCl_2$	Addition TEOS
SiO_2-Cu-EDTA-II-A	0	--	--	60 min
SiO_2-Cu-EDTA-II-B	0.043	136	30 min	60 min
SiO_2-Cu-EDTA-II-C	0.216	27	30 min	60 min
SiO_2-Cu-EDTA-II-D	0.649	9	30 min	60 min
SiO_2-Cu-EDTA-II-E	0.649	9	15 min	45 min
SiO_2-Cu-EDTA-II-F	0.649	9	direct	30 min

In a second batch the influence of the precursor addition was tested using a syringe pump for the addition of a premixed precursor solution. 5 mL of seed particles ($D_{\text{Batch-DLS}}$ = 17.6 ± 1.6 nm, β(Si) = 992 mg/L) were diluted in L-Arginine solution (0.22 mg/mL) to obtain a final volume of 23 mL. The dispersion was then topped with 2.25 mL cyclohexane and heated to 60 °C. In the meantime, the precursor solution was prepared by addition of 280 µL (0.341 mmol) TMS-EDTA in 5 mL L-Arginine solution (0.22 mg/mL) and final addition of 375 µL (0.038 mmol) of the respective metal salt solution (100 mM). Precursor solutions were mixed using the copper(II), cobalt(II), gadolinium(III), and europium(III) salts. Addition of 1.76 mL (7.94 mmol) TEOS was followed by addition of

2 mL precursor solution in 2 hours (labeled as SiO_2-"Me"-EDTA-II-2h) or 8 hours (SiO_2-Cu-EDTA-II-8h) during shell formation. As comparison, a synthesis batch was performed with direct addition of the Cu-TMS-EDTA mixture at the same time as TEOS addition (SiO_2-Cu-EDTA-II-0h). Silicon and metal concentrations were measured using ICP-OES. The aqueous particle dispersions were diluted with ultrapure water beforehand depending on the expected concentration (usually factor 100 or 1000). No further treatment of the particles dispersions was performed.

Asymmetrical flow-field flow fractionation was performed using a 10 kDa PES membrane and a 1 mM $NaNO_3$ solution as eluent. Flow method A (Table 5.2) was adapted by increasing the Focus+Inject time by 2 minutes. The flow profile is illustrated in Figure 2.15.

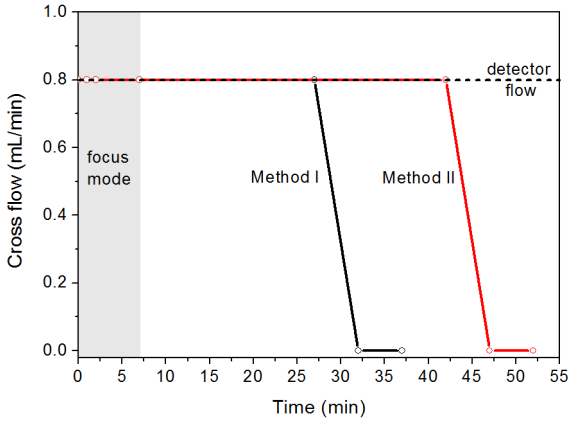

Figure 2.15: Flow program used for AF4 characterization of metal-labeled primary silica nanoparticles (Method I) and NPs prepared by seeding growth (Method II).

2.1.3.2. Results

Precursor formation

Precursor formation was tested using Cu(II) as metal ion. Mixing copper(II) chloride solution and different amounts of TMS-EDTA in an 1.36 mg/mL L-Arginine solution led to the formation of a clear, blue solution for all tested ratios (Figure 2.16). The UV-Vis absorption spectra of different metal and chelator mixtures are presented in Figure 2.16.

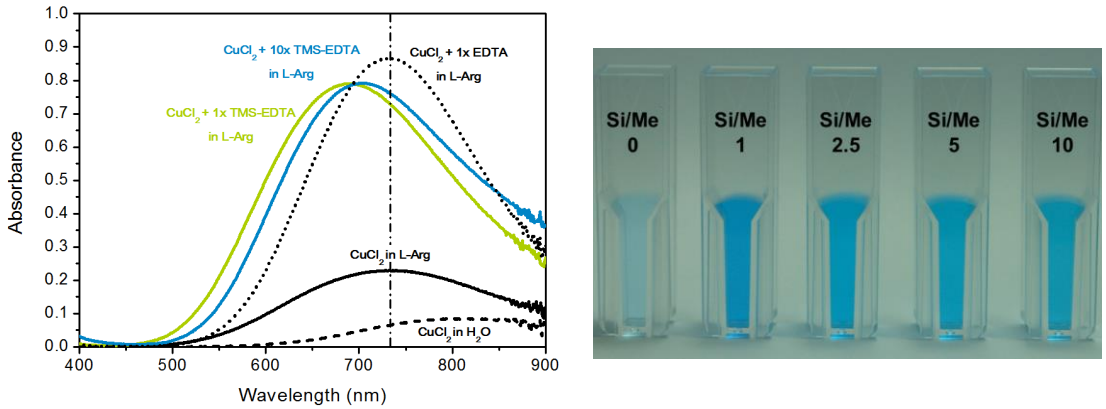

Figure 2.16: UV-Vis absorption spectra (left) and optical images (right) of different precursor mixtures (10 mM Cu(II)).

In all cases, the Cu(II) concentration was kept constant (10 mM). A low absorption intensity of aqueous $CuCl_2$ with an absorption maximum at 812 nm was observed. An increase in the absorption intensity and a blue shift to 735 nm was observed for the Cu(II) salt in L-Arginine solution. Addition of an equimolar amount of EDTA led to a further increase of the absorption but identical peak position. Mixing Cu(II) and an equimolar amount of TMS-EDTA in L-Arginine solution led to a blue shift to a peak maximum of 690 nm, whereas a 10-fold amount of TMS-EDTA was associated with a peak shift to 705 nm.

Synthesis of primary particles

The results of the synthesis of primary silica NPs using different copper and TMS-EDTA concentrations are summarized in Table 2.6.

Table 2.6: Colloidal characterization of primary Cu-labeled silica nanoparticles using different copper and TMS-EDTA concentrations.

Sample	$D_{\text{Batch-DLS}}$ (nm)	$D_{\text{AF4-DLS}}$ (nm)	β(Cu) (mg/L)	β(Si) (mg/L)	Cu/Si (at. %)	Cu(II) yield (%)
SiO_2-Cu-EDTA-A	n.a.	n.a.	0.23	227.2	0.04	0.5
SiO_2-Cu-EDTA-B	27.4 ± 4.3	21.8 ± 4.5	11.92	1169.3	0.45	23.7
SiO_2-Cu-EDTA-C	16.6 ± 1.4	15.9 ± 2.0	13.61	167.5	3.59	27.1
SiO_2-Cu-EDTA-D	13.4 ± 1.3	11.7 ± 3.1	8.68	139	2.76	17.3
SiO_2-Cu-EDTA-E	13.6 ± 3.2	n.a.	15.02	119	5.58	14.9
SiO_2-Cu-EDTA-F	12.4	n.a.	25.46	62.5	18.00	12.7

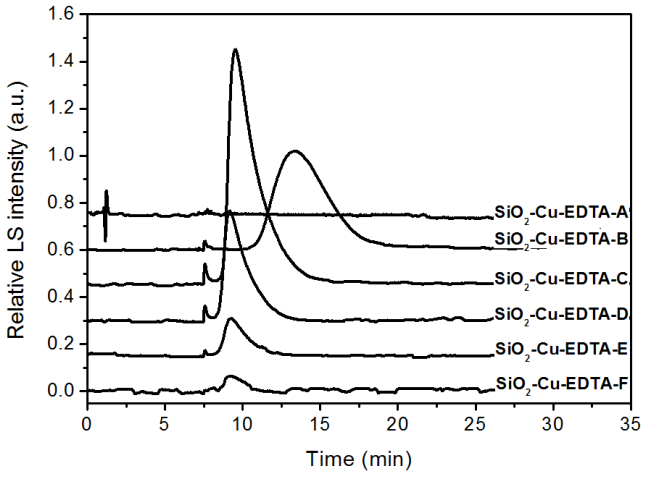

Figure 2.17: AF4 fractogram of Cu-labeled (primary) silica nanoparticles.

For the NP synthesis batch without the addition of TMS-EDTA in the precursor solution (SiO_2-Cu-EDTA-A), no particles could be detected using DLS and AF4 (Figure 2.17) although a relatively low silicon amount was detected using ICP-OES.

Variation of the TMS-EDTA concentration in the precursor mixture while keeping the copper concentration identical led to decreasing mean particle sizes and Si concentrations (corresponding to the number of particles formed) with increasing TMS-EDTA concentration (batches B-D). The detected amount of incorporated Cu was in the range of 8.7-13.6 mg/L with no clear trend observed. Comparing SiO_2-Cu-EDTA-B and SiO_2-Cu-EDTA-C, a significant increase of Cu relative to Si was observed that indicates higher copper loading.

Keeping a constant TMS-EDTA concentration and increasing the Cu(II) concentration in the precursor mixtures led to a further decrease of the total Si concentration. A slight decrease in the hydrodynamic diameter was observed with broader size distributions determined by DLS. In the case of SiO_2-Cu-EDTA-F with the highest amount of added copper, significantly less and broadly distributed particles (lowest Si-concentration) with the highest amount of incorporated copper per particle formed.

The formation of silica nanoparticles using other metals was tested, too. The results are summarized in Table 2.7. The corresponding AF4 fractograms are presented in Figure 2.18.

Table 2.7: Colloidal characterization of primary silica nanoparticles using different cations.

Sample	$D_{\text{Batch-DLS}}$ (nm)	$D_{\text{AF4-DLS}}$ (nm)	β(Me) (mg/L)	β(Si) (mg/L)	Me/Si (at %)	Me yield (%)
SiO_2-Co-EDTA	15.6 ± 1.0	17.7 ± 1.5	18.89	1542.6	0.58	40.5
SiO_2-Cu-EDTA	15.6 ± 0.9	18.5 ± 1.4	20.41	880.7	1.02	40.6
SiO_2-Ce-EDTA	11.4 ± 1.7	13.9 ± 1.2	5.86	1551.8	0.08	5.3
SiO_2-FeII-EDTA	15.8 ± 1.5	19.1 ± 2.1	24.86	1738.1	0.72	56.3
SiO_2-FeIII-EDTA	15.8 ± 1.4	18.0 ± 2.2	22.30	1390.7	0.81	50.5

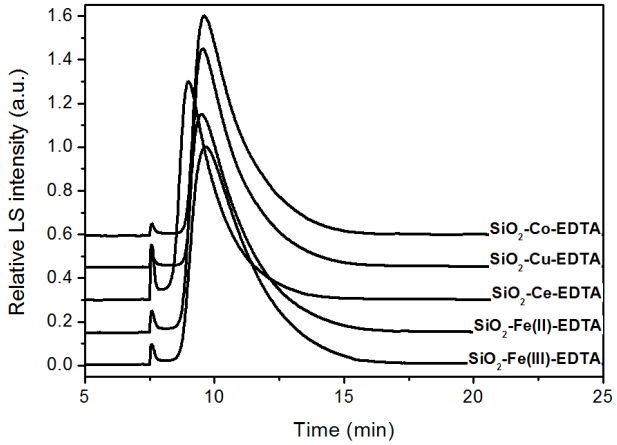

Figure 2.18. AF4 fractograms of metal-labeled silica nanoparticles.

The hydrodynamic diameter for Co(II), Cu(II), Fe(II), and Fe(III) labeled particles are in the same range of around 16 nm. The amounts of incorporated metal ions, the labeling yield, was 41 % for copper and cobalt, and 51-56 % in the case of iron. In contrast, SiO_2 NPs formed in the presence of the Ce(III)-TMS-EDTA precursor mixture had a smaller hydrodynamic diameter of only 11.4 nm. A very low metal amount for the Ce(III) labeled NPs was detected where only 5 % of the added Ce(III) was recovered after dialysis.

Seeding growth

The results of the nanoparticle seeding growth of unmodified silica nanoparticles using different addition times of the precursor mixture are summarized in Table 2.8.

Table 2.8: Colloidal characterization of copper-labeled silica nanoparticles prepared by seeding growth.

Sample	$D_{\text{Batch-DLS}}$ (nm)	$D_{\text{AF4-DLS}}$ (nm) Peak 1	Peak 2	β(Cu) (mg/L)	β(Si) (mg/L)	Cu/Si (at %)
SiO_2-seed-I	31.6 ± 1.9	34.1 ± 4.7		n.a.	337.8	0
SiO_2-Cu-EDTA-II-A	50.8 ± 2.2	n.a.[a]	54.8 ± 2.9	0.08	1360.9	0.00
SiO_2-Cu-EDTA-II-B	47.8 ± 2.8	24.7 ± 3.3	53.1 ± 2.3	1.103	1322.5	0.04
SiO_2-Cu-EDTA-II-C	44.8 ± 3.0	22.6 ± 2.5	50.4 ± 2.5	4.864	1356.7	0.16
SiO_2-Cu-EDTA-II-D	44.6 ± 3.2	24.7 ± 2.2	53.0 ± 2.4	13.681	1465.3	0.41
SiO_2-Cu-EDTA-II-E	47.4 ± 4.1	25.3 ± 2.4	53.6 ± 2.2	13.571	1453.4	0.41
SiO_2-Cu-EDTA-II-F	49.6 ± 3.3	n.a.[a]	54.1 ± 3.3	10.675	1142.1	0.41

[a]Lower particle size of bimodal size distribution could not be determined due to low signal intensity.

Batch DLS characterization yielded hydrodynamic diameter with a narrow size distribution in the range of 45-50 nm. The hydrodynamic diameter decreased with increasing copper amount. Copper loading (amount of Cu/Si) increased with increasing amount of copper added to the reaction mixture. No differences between the direct addition of copper (batch F), addition after 15 min (batch E), and 30 minutes (batch D) were observed.

Figure 2.19 displays the fractograms of the copper-labeled silica nanoparticles prepared by seeding growth.

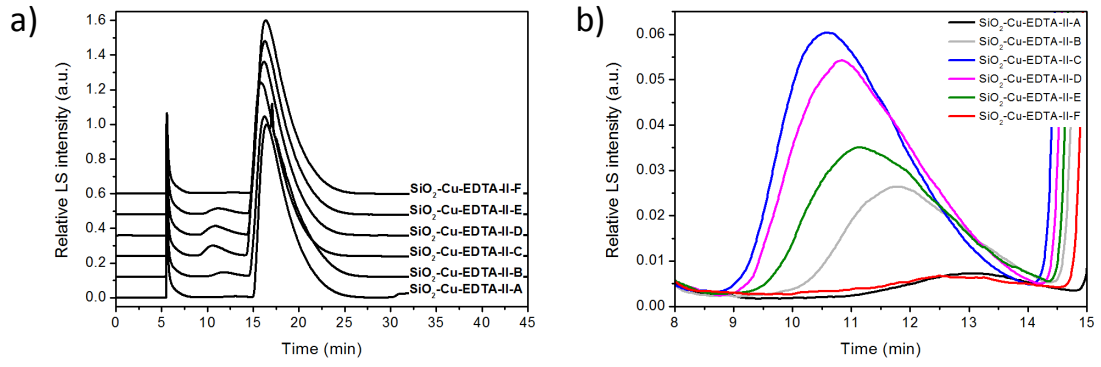

Figure 2.19: (a) AF4 fractograms of copper-labeled silica nanoparticles prepared by seeding growth. (b) Comparative AF4 fractograms of the peak at elution times ranging from 9-14 min indicate a bimodal distribution.

AF4 investigations revealed a bimodal distribution in all cases as shown by the presence of two peaks. The main sample peak occurred at elution times between 16-18 minutes, the second peak at 10.5-13.5 minutes (Figure 2.19). The main peak corresponds to a D_h of 49-53 nm as determined via online DLS. For silica nanoparticles synthesized in the absence of copper chloride (batch A) and simultaneous addition of copper chloride and

TMS-EDTA (batch F), the first peak representing the smaller nanoparticles was the lowest. The low scattering signal did not allow online DLS characterization. In the other cases, the second population consisted of nanoparticles with hydrodynamic diameter of 23-25 nm (online DLS).

In order to reduce a second particle size population, the precursor mixture was slowly added with a syringe pump. The results are summarized in Table 2.9.

Table 2.9: Colloidal characterization of seed NPs and metal- (Cu, Co, Gd, Eu) labeled silica NPs prepared by seeding growth using different addition times.

Sample	$D_{\text{Batch-DLS}}$ (nm)	$D_{\text{AF4-DLS}}$ (nm) Peak 1	Peak 2	β(Me) (mg/L)	β(Si) (mg/L)	Me/Si (%)
SiO_2-seed-II	17.6 ± 1.7	23.8 ± 1.9		--	992	0
SiO_2-Cu-EDTA-II-0h	41.3 ± 2.8	n.a.[a]	47.2 ± 1.9	8.51	1022	0.37
SiO_2-Cu-EDTA-II-2h	33.2 ± 1.4	35.3 ± 1.6		4.59	405	0.50
SiO_2-Cu-EDTA-II-8h	37.4 ± 1.5	39.8 ± 2.2		7.81	638	0.54
SiO_2-Co-EDTA-II-2h	52.8 ± 2.4	57.8 ± 1.0		8.92	4169	0.095
SiO_2-Gd-EDTA-II-2h	27.8 ± 6.6	n.a.[a]	32.7 ± 2.8	51.21	3609	0.25
SiO_2-Eu-EDTA-II-2h	41.2 ± 9.6	15.6 ± 4.0	42.8 ± 7.7	17.12	1579	0.20

[a]Lower particle size of bimodal size distribution could not be determined due to low signal intensity.

Batch DLS measurements of particles synthesized via direct addition of the precursor mixtures at beginning of the reaction (SiO_2-Cu-EDTA-II-0h) determined a mean D_h of 41 nm. A copper amount of 8.51 mg/L was determined leading to a lower copper/silicon ratio of 0.37. Continuous addition of the same amount of Cu-TMS-EDTA complex during 2 hours and 8 hours resulted in particles with a $D_{\text{Batch-DLS}}$ of 33 nm and 37 nm, respectively. The silicon concentrations decreased and the Cu/Si ratio increased.

Nanoparticles synthesized with Co-, Gd-, and Eu-labeled precursor mixtures showed lower labeling rates. Silicon concentrations were significantly larger compared to the copper-labeled particles. Batch DLS of SiO_2-Gd-EDTA-II-2h and SiO_2-Eu-EDTA-II-2h NPs showed a braod particle size distribution. TEM (Figure 2.20) and AF4 characterization (Figure 2.21) revealed the formation of different particle species.

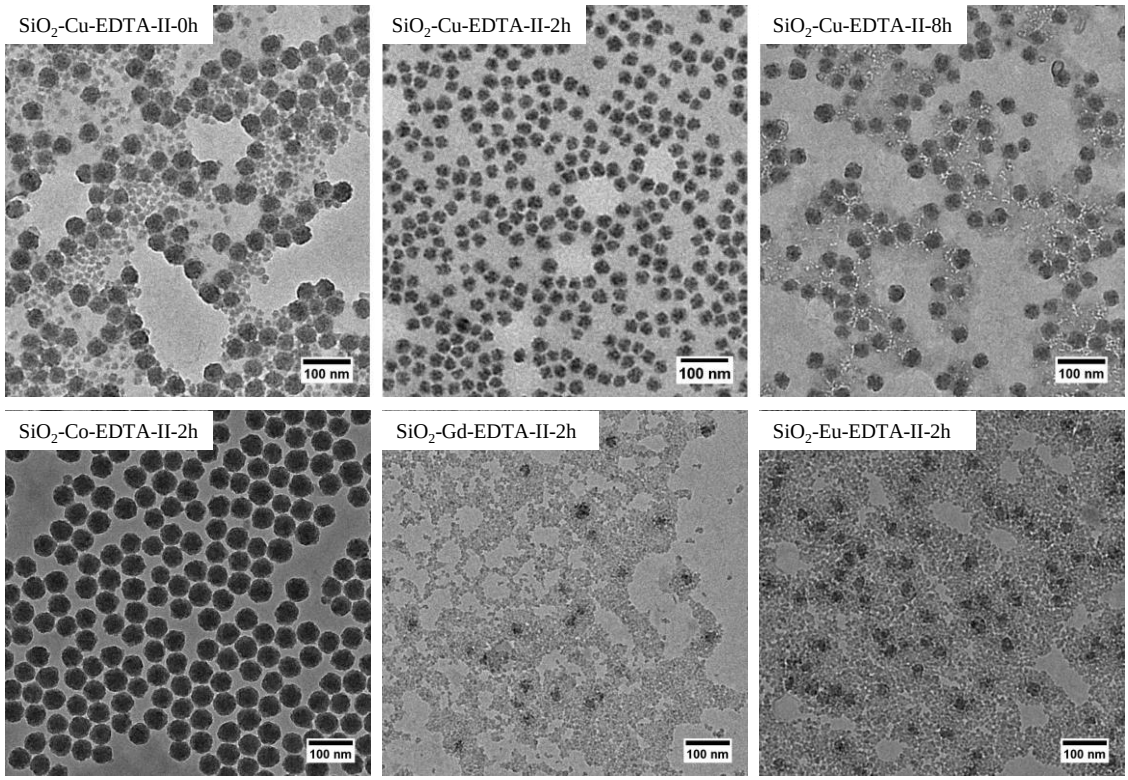

Figure 2.20: TEM images of silica nanoparticles prepared by seeding growth of unlabeled silica NPs using different metal ions and precursor addition rate.

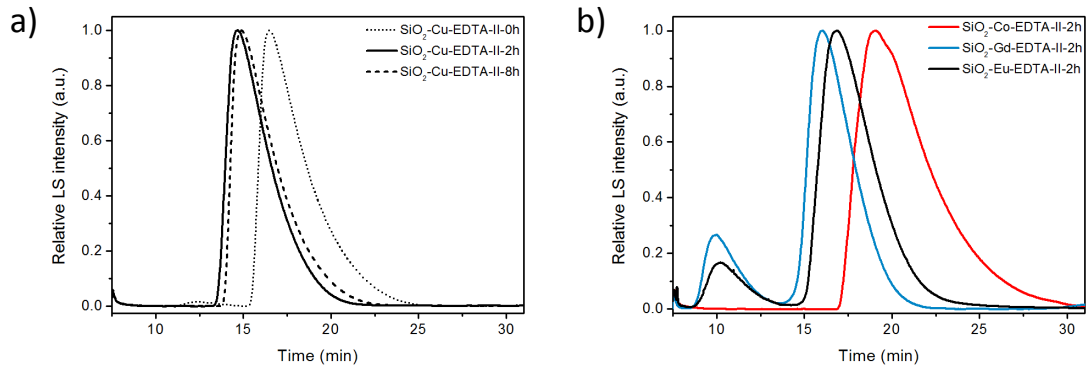

Figure 2.21: AF4 fractograms of copper-labeled (a) and Co- (red), Eu-(black) and Gd-(blue) labeled silica nanoparticles (b). Direct addition of the copper precursor (a, dotted), and Eu- and Gd-labeling led to bimodal size distribution.

Direct addition of the copper precursor at the beginning of the reaction led to the formation of small silica nanoparticles (up to ~ 30 nm determined by TEM) and larger nanoparticles with a $D_{AF4\text{-}DLS}$ of 47 nm. The small formed nanoparticles are also detected in the corresponding AF4 fractogram at an elution time of around 12.5 min (Figure 2.21 a). A homogenous size distribution with only one particle species was determined for copper-labeled NPs prepared by the slow addition of precursor during NP formation. A similar observation was made for SiO_2-Co-EDTA-II-2h NPs with only one detected particle species (Figure 2.21 b) and an increased hydrodynamic diameter of 20 nm compared to

copper-labeled NPs. In contrast, the rare-earth element precursor mixtures, Gd- and Eu-TMS-EDTA, led to the formation of a bimodal distribution. Both TEM and AF4 measurements indicated a large amount of small nanoparticles besides larger NPs.

2.1.3.3. Discussion

Mixing TMS-EDTA with copper ions results in the formation of a copper-TMS-EDTA complex. In aqueous media, $CuCl_2$ dissolved to form the octahedral $[Cu(H_2O)_6]^{2+}$ complex. In the presence of L-Arginine, the amino acid coordinates with the primary amine and the carboxylic group to Cu(II) to form a $[Cu(L\text{-}arg)]^{2+}$ or $[Cu(L\text{-}arg)_2]^{2+}$ complex with two water molecules attached at the remaining coordinating sites in each case [89,90]. Addition of the hexadentate ligand EDTA leads to the formation of the Cu-EDTA complex with also an N2 O4 coordination [91]. Since both ligands form Cu(II) complexes with N2 O4 coordination, both complexes are expected to have a similar absorption wavelength, as detected.

In contrast, copper complexation with TMS-EDTA is characterized by a slight blue-shift. TMS-EDTA possesses only five major binding moieties for metal complexation compared to the hexadentate EDTA ligand: two secondary amines and 3 carboxylic acid groups. The different binding situation compared to EDTA is most-likely causing the slight blue shift. Details of the binding situation have not been reported so far. It would be interesting to further investigate the structure of the formed complex by using other methods, such as NMR or potentiometric titration, in the future.

Primary SiO_2 NPs labeled with copper ions can only be formed in the presence of TMS-EDTA. These results show that an incorporation of the copper ions (present as $[Cu(L\text{-}arg)]^{2+}$ or $[Cu(L\text{-}arg)_2]^{2+}$ complexes) into SiO_2 NPs did not occur when TMS-EDTA was absent. The SiO_2 units do not have an affinity towards copper, which is strong enough to compete with L-Arginine as chelating agent. Unspecific adsorption of copper ions into the SiO_2 structure is unlikely. The $[Cu(L\text{-}arg)_x]$ complexes do not bear a functional group which can be chemically attached to the siloxane structures. Successful incorporation of metal ions into the silica nanoparticles would require stronger chelating agents with functional groups that can attach to the siloxane structure.

TMS-EDTA concentration and the Cu-TMS-EDTA concentration have strong effects on particle formation. An increase of the TMS-EDTA concentration led to decreasing silica concentrations and decreasing particle sizes. The copper concentration plays an important

role, too. Increasing the copper amount by a factor of four at identical TMS-EDTA concentrations (compare batch SiO_2-Cu-EDTA-D with SiO_2-Cu-EDTA-F) led to lower silica concentrations and particle sizes.

As mentioned above, there are mainly three factors influencing the synthesis of the silica particles in this process: the pH, the L-Arginine concentration, and the synthesis temperature [74]. In this thesis, the reaction time, the L-Arginine concentration, and the temperature were identical in all cases. Therefore, the pH might be responsible for the observed deviations. However, the addition of the TMS-EDTA precursor to the L-Arginine concentration did not lead to significant changes in the pH (in both cases pH ~ 10-11). An increase in the pH should also lead to increasing hydrolysis rates, which would show an increased particle formation rather than the observed decrease [74].

Decreasing particle sizes can have two reasons. First, an increase in initial nucleation will lead to a higher number of formed particles combined with a decrease in particle size [75]. Second, the TEOS hydrolysis is reduced during the synthesis. This would lead to a decreased growth of the seed NPs leading to smaller particle sizes.

The first case is more likely to be the explanation for the observed decreasing particles sizes with increasing TMS-EDTA concentration. TMS-EDTA in the aqueous phase likely contributes to the amount of dissolved silica species which will lead to earlier nucleation in combination with a higher number of particles formed compared to the absence of TMS-EDTA. In addition, TMS-EDTA might lead to increased hydrolysis rates by interactions between the TMS-EDTA with silicates species. This does not explain why increasing the copper concentrations (identical TMS-EDTA) led to decreasing silica concentrations and decreased particles number densities.

Syntheses of metal-labeled primary nanoparticles depend on the used metal ions. The DLS and ICP-OES results reveal some differences in the SiO_2 NP formation for transition metals versus lanthanides in the precursor mixture. Whereas all transition metals showed comparable results (similar sizes and labeling rates), using Ce(III) led to smaller particles and lower labeling efficiency. One major difference between transition metals and the lanthanides is the ionic radii and coordination number. The tested transition metal ions have ionic radii of less than 0.7 Å and coordination numbers of up to 6 [92]. The lanthanides have larger ionic radii of about 1.0 Å and prefer higher coordination numbers (minimum of 7) [92]. The different coordination properties presumably lead to different TMS-

EDTA complexes, which might explain the different results. The results thus indicate that the nucleation and particle growth during the synthesis is greatly affected by the formed TMS-EDTA metal complexes. The rare-earth elements likely enhance particle nucleation by increasing and sharpening the supersaturation. Further systematic studies using other metal TMS-EDTA mixtures are necessary to fully understand the particle formation in dependence of the metal cation properties.

The addition rate of the precursor solution for metal-labeling of silica NPs determines secondary nucleation. These results showed that copper labeling by simply adding the precursor mixture in a single injection during shell growth leads to a bimodal distribution. The most likely reason is secondary nucleation (new particle formation) parallel to growth of the existing SiO_2 seeds. Interestingly, secondary nucleation is even increased when copper chloride is added 15-30 minutes after TMS-EDTA is added. On the other hand, less new particles were formed when copper and TMS-EDTA were added together. This supports the hypothesis that the initial nucleation is mediated by both, the presence of TMS-EDTA and the corresponding complexes.

Continuous addition of transition metal TMS-EDTA complexes leads to homogenous shell growth. Slowly increasing the concentration of the complexes during NP formation prevented secondary nucleation. The steady conversion of the injected precursor prevents a critical concentration to be reached to induce new nucleation. In addition, a strong dependence of the applied metal ion was observed. In contrast to the transition metals used, rare-earth metal complexes led to secondary seed nucleation. This is in line with the aforementioned observation of smaller primary particles formed using Ce(III). Rare-earth metal TMS-EDTA complexes increase the nucleation rate leading to smaller particles sizes.

2.1.4. Summary

The synthesis, labeling, and AF4 characterization of silica nanoparticles in a size range of 13-110 nm was investigated.

A biphasic synthesis procedure developed by Hartlen [74] was applied for the synthesis of silica nanoparticles with mean core diameters of 13-92 nm. Synthesized particles were characterized using TEM, DLS, and AF4. The three particle sizing methods were in good agreement except for the largest nanoparticles tested where smaller diameters were de-

tected using AF4. A linear relationship between the retention time and the hydrodynamic diameter confirmed that the synthesized nanoparticles elute according to AF4 theory similar to SiO_2 NPs investigated by Barahona *et al.* [18]. I demonstrated that the prepared silica nanoparticles can be used as a platform for the development of reference particles. Fluorescence and metal labeling were applied to develop tracer nanoparticles with facilitated identification.

Fluorescence labeling of silica nanoparticles using Rhodamine was performed using the Hartlen method and the Stöber synthesis. TEM and AF4 measurements revealed a narrower size distribution for the particles synthesized using the Hartlen method. The synthesized particles showed ideal retention behavior. Distinct differentiation between unlabeled and labeled silica nanoparticles was confirmed using AF4 with online fluorescence measurements.

Incorporation of metal ions into silica nanoparticles (metal labeling) was successfully achieved using a synthesis protocol developed from the Hartlen method. Precursor complexes were formed between TMS-EDTA and the respective metal ions. The precursor complexes were introduced during the biphasic particle synthesis procedure. Formation of the metal-TMS-EDTA complex with Cu(II) as cation was confirmed by optical spectroscopy.

Synthesis of labeled SiO_2 NPs was investigated by varying the metal/TMS-EDTA ratios and concentrations, addition times, and metal ions. Increasing the amount of copper led to decreasing particle sizes. The incorporation of different metals revealed differences between the use of transition metals and lanthanides. Use of transition metal precursor mixtures showed higher labeling efficiency and larger hydrodynamic diameters. Incorporation of metal-TMS-EDTA complexes during seeding growth of unlabeled silica nanoparticles showed that the continuous addition of the metal-TMS-EDTA complexes is beneficial. Compared to in-situ preparation of copper-TMS-EDTA during seeding growth and the direct addition of the precursor mixture at the reaction initiation, controlled addition of the precursor over time prevents the formation of new seeds (secondary nucleation). While this procedure was successful applied for the preparation of copper- and cobalt-labeled nanoparticles, using rare-earth metal TMS-EDTA precursors resulted in secondary nucleation and a bimodal size distribution.

The results indicate that TMS-EDTA (and the respective complexes) affects the nucleation of nanoparticles by sharpening the supersaturation peak as described by Fouilloux *et al.* [93]. A higher and narrower supersaturation peak leads to the formation of a higher number density of smaller nanoparticles. Narrowing of the supersaturation peak can result from (i) decreasing silica solubility or (ii) increasing TEOS hydrolysis rates [93]. The different ionic radii of the transition metals compared to the rare-earth metal ions, and the different coordination numbers might affect both, silica solubility and TEOS hydrolysis. Hence, smaller nanoparticles and secondary nucleation as observed for rare-earth metal containing precursors are expected.

Future studies should include investigations on the leaching out of the metal cations in batch or directly using ICP-MS coupled AF4. In addition, structural studies on the distribution of the incorporated metal-complex in a single particle using high-resolution imaging techniques with elementary analysis are of interest. The central question on why different metal-TMS-EDTA complexes lead to different particle sizes could be investigated using in-situ measurements during NP formation, similar to the investigation by Fouilloux *et al.* [76].

2.2. Gold nanoparticles

2.2.1. Synthesis of aqueous gold nanoparticles

Gold nanoparticles were used as representative metallic nanoparticle system for the investigation and development of metal reference and tracer nanoparticles. Many published protocols for the synthesis of gold nanoparticles involve the reduction of a gold precursor in the presence of a stabilizing ligand [64]. Depending on the synthesis conditions, electrostatically or sterically stabilized nanoparticles with a dispersity of as low as 5 % can be obtained [64]. The most common precursors are tetrachloroauric(III) acid, $HAuCl_4$, and chloro(triphenylphosphine)-gold(I), $AuPPh_3Cl$. Whereas non-polar AuNPs can be produced with excellent dispersity up to a size of approximately 15 nm, aqueous AuNPs are available in a broader size regime of up to 200 nm but usually lack a homogenous morphology [94].

In this thesis, aqueous gold nanoparticles were investigated because they are available in a broad size range. AuNPs with core diameters up to 20 nm were synthesized using either sodium borohydride or sodium citrate as reducing agents for $HAuCl_4$ (Figure 2.22). Sodium borohydride is a strong reducing agent and allows the synthesis of small particles already at room temperature [95]. On the other hand, the citrate reduction method described by Turkevich *et al.* [69] and further developed by Frens *et al.* [70] was applied. This method requires elevated temperatures to produce particles with a narrow size distribution [96].

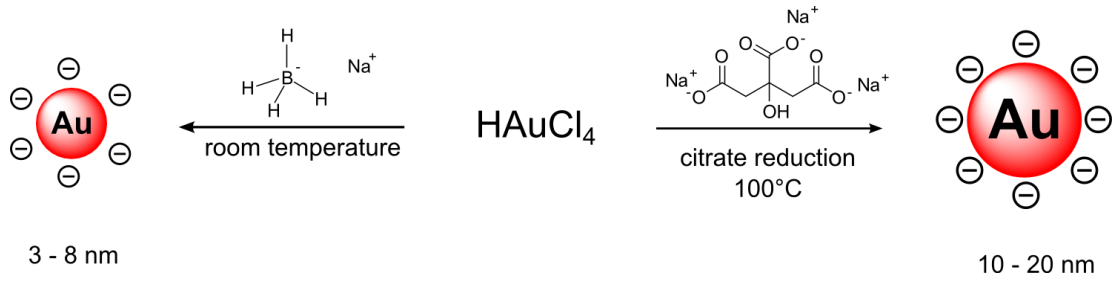

Figure 2.22: Synthesis route for aqueous gold nanoparticles using borohydride and citrate as reducing agents.

Larger AuNPs were fabricated using a seeding growth method by Perrault *et al.* [97]. Citrate coated particles synthesized via the citrate reduction method were used as seeds to grow larger particles in the presence of hydroquinone (Figure 2.23). Hydroquinone is a mild reducing agent which is believed to reduce Au(I) ions only in the presence of Au(0) surfaces [97]. Different particle sizes can be obtained by variation of the seed concentration. Similar to the citrate synthesis, the particles are electrostatically stabilized by the adsorbed citrate ions.

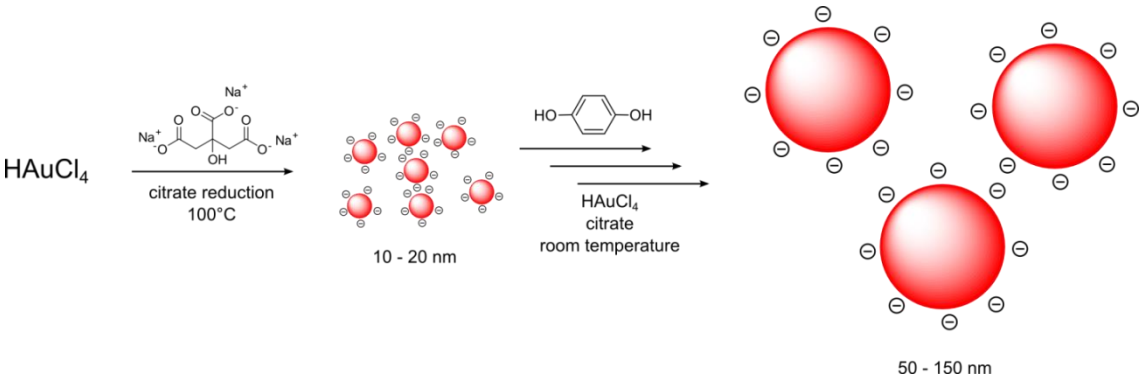

Figure 2.23: Seeding growth of citrate-stabilized gold nanoparticles using hydroquinone as reducing agent.

2.2.1.1. Experimental procedures

Gold nanoparticles with a mean core diameter of 5 nm were prepared by reduction of $HAuCl_4$ according to a previously published procedure [98]. Briefly, 2 mL of a freshly prepared $NaBH_4$ solution (10 mg/mL) was added to 100 mL of a 0.1 mM $HAuCl_4$ solution while stirring at room temperature. The solution turned red within less than 5 minutes. The dispersion was finally filtrated through a 0.2 µm PES syringe filter. The particles were labeled as AuNP-5-BH_4.

Citrate-stabilized gold nanoparticles with mean core diameters < 20 nm were synthesized according to the Frens method [70]. In a typical batch, 72 mg (5 mmol) $HAuCl_4$ was dissolved in 800 mL water and heated to boiling. Then, 28 mL of a 1 % (w/v) sodium citrate solution was added all at once. The solution was kept stirring while heating was maintained for 30 minutes. After cooling down, the dispersion was filtered using a 0.2 µm PES syringe filter. Different batches were synthesized using this protocol (AuNP-16-citrate and AuNP-17-citrate).

Gold nanoparticles with mean core diameters of 79 nm (AuNP-79-citrate) were synthesized using the seeding growth procedure by Perrault *et al.* [97]. Citrate-stabilized gold nanoparticles synthesized by the Frens method were used as gold seeds. First, 200 µL of a 1 % (w/v) sodium citrate solution, 1 mL of a 1 % (w/v) $HAuCl_4$ solution, 97 mL of water, and 1.02 mL seed solution were mixed. The dispersion was then stirred at room temperature and 1 mL of a 0.03 M hydroquinone solution was added at once. A color change was observed within few minutes. After stirring for 18 hours, the dispersion was finally filtered using a 0.2 µm PES syringe filter.

Batch dynamic light scattering was performed on DLS setup 2 (details listed in chapter 5.2). AF4 characterization was performed using a 10 kDa RC membrane and different eluent compositions. AuNP-5-BH_4 and AuNP-17-citrate particles were characterized using a 0.5 mM $NaNO_3$ with 0.005 % (w/v) SDS solution. AF4 measurements of AuNP-79-citrate particles were performed using 0.5 mM $NaNO_3$ solution only. The corresponding flow methods are illustrated in Figure 2.24.

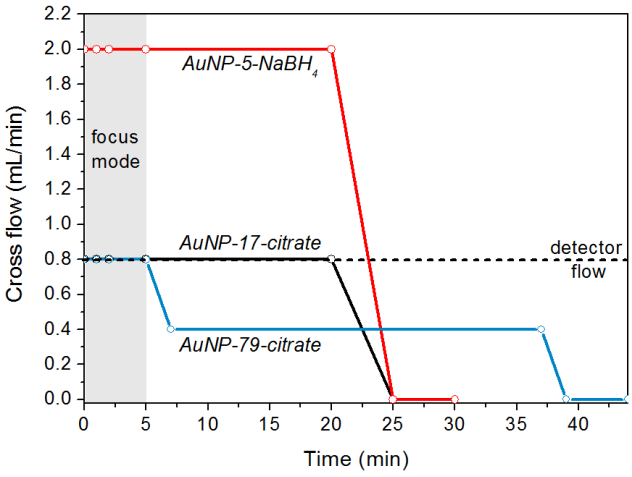

Figure 2.24: Applied flow methods for AF4 characterization of gold nanoparticles.

2.2.1.2. Results

The colloidal characterization of the synthesized gold nanoparticles is summarized in Table 2.10. TEM and SEM images of the synthesized AuNPs are presented in Figure 2.25. Sodium borohydride as reducing agent yielded gold nanoparticles with a mean core diameter of 5 nm and a broad size distribution. AuNPs synthesized by citrate reduction showed a narrow size distribution and a mean core diameter of 17 nm. Seeding growth of citrate-stabilized AuNPs resulted in gold nanoparticles with a mean core diameter of 79 nm.

Table 2.10: Colloidal characterization of synthesized gold nanoparticles.

	$D_{TEM/SEM}$ (nm)	$D_{Batch-DLS}$ (nm)	$D_{AF4-DLS}$ (nm)	Zeta potential (mV)	LSPR band (nm)
AuNP-5-BH_4	5.4 ± 1.0	12.2[a]	n.a.[b]	-36	512
AuNP-17-citrate	16.6 ± 1.1	20.2 ± 3.5	29.3 ± 5.8	-30	518
AuNP-79-citrate	78.8 ± 11.1	82.5 ± 8.6	n.a.[b]	-35	543

[a]High polydispersity prevented accurate determination from the cumulant fit method. [b]No determination with online DLS available. For further information see main text.

The determined hydrodynamic diameter of the citrate-stabilized AuNPs fit well to the determined core diameter via TEM. However, DLS measurements of the borohydride-stabilized particles consistently indicated the presence of larger AuNPs, possibly aggregates. Cumulant analysis of scattering from AuNP-5-BH_4 yielded a mean D_h of 12 nm.

Batch DLS measurements of the particles synthesized by seeding growth were in good agreement with SEM results. The size-dependent position of the LSPR maximum was reflected in a gradual red-shift of the LSPR with increasing size. Mean zeta potential values of -30 to -36 mV confirmed the negative surface charges expected for all particle systems. TEM and SEM images of the synthesized particles confirmed a predominantly spherical particle shape whereas fractions of smaller particles and uneven morphologies were observed for particles prepared by seeding growth.

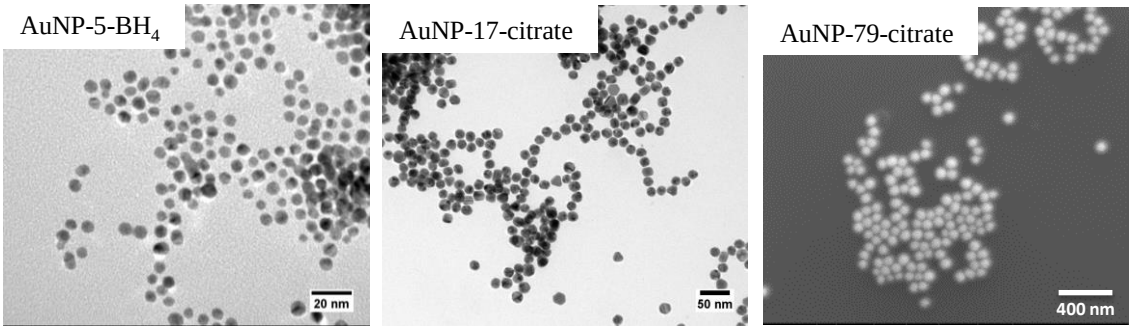

Figure 2.25: TEM and SEM images of synthesized gold nanoparticles.

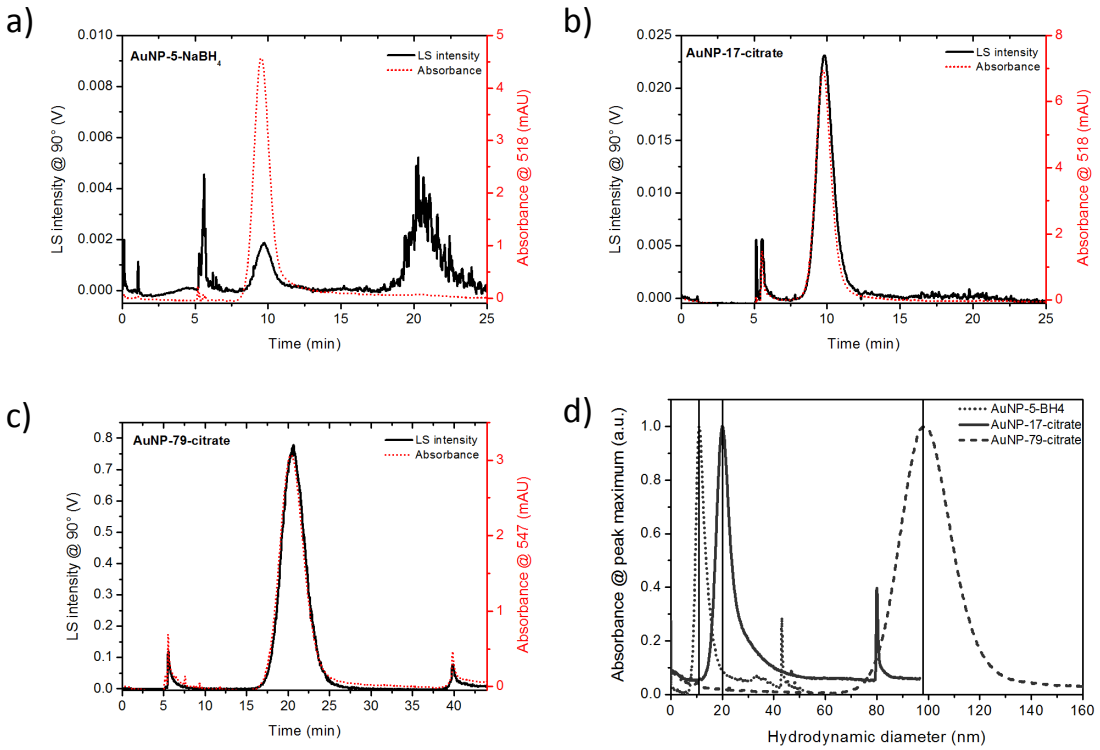

Figure 2.26: AF4 fractograms (black solid line - LS detection, red dotted line - UV-Vis absorption) of a) AuNP-5-BH_4, b) AuNP-17-citrate, c) AuNP-79-citrate NPs, and d) determined size distribution via retention time transformation.

The AF4 fractograms of the AuNP-5-BH_4 nanoparticles (Figure 2.26 a) included a void peak at 5.5 minutes, the main sample peak at 9.8 minutes and a release peak at 21 minutes using light scattering detection. The high release peak may be caused by over-retained or agglomerated AuNPs. Using UV-Vis absorption, only the main sample peak is detected. For AuNP-17-citrate, only the void and the main sample peak was detected by LS and UV-Vis detection (Figure 2.26 b). AF4 measurements of AuNP-79-citrate particles revealed an additional small release peak at an elution time of 40 minutes (Figure 2.26 c).

Online DLS measurements could only be achieved for AuNP-citrate-17 NPs. The scattering intensity for AuNP-5-BH_4 was too low for an accurate determination of D_h. Size determination of AuNP-79-citrate particles resulted in hydrodynamic diameter larger than 300 nm which is above the maximum hydrodynamic radius measurable by DLS in flow mode [99] and not congruent with the batch DLS results. The determined D_h of AuNP-citrate-17 particles showed large deviations from TEM and batch DLS which might be due to the low scattering intensity detected.

The retention time was transformed into the hydrodynamic diameter by calculating the membrane channel height using the D_h of AuNP-17-citrate NPs. The determined size distributions can be found in Figure 2.26 d. The size peak maxima of AuNP-5-BH_4 and AuNP-79-citrate NPs were found to be 11 nm and 97 nm, respectively. A significantly larger value was determined for AuNP-79-citrate NPs compared to batch DLS measurements.

2.2.1.3. Discussion

AF4 characterization of gold nanoparticles with different diameters was achieved via retention time evaluation. The characterization of electrostatically stabilized AuNPs was compared with different methods. DLS and TEM characterization of citrate-stabilized AuNPs with a mean core diameter of 17 nm were in good agreement with online DLS during AF4. Online DLS of borohydride-stabilized gold nanoparticles was not possible because of the low scattering intensity of the gold nanoparticles. Online DLS of AuNPs synthesized by seeding growth (AuNP-79-citrate) led to distorted results (diameters above 300 nm), which may be caused by concentration effects. Another reason might be a too short residence time of the particles to allow proper evaluation scattering signal. The calculated maximum radius for an reliable determination was calculated to be ~ 60 nm [99]. This study reveals some drawbacks of online DLS measurements to determine D_h.

The evaluation of the particle size distributions by transformation of the retention time into the hydrodynamic diameter according to AF4 theory revealed slightly larger D_h than batch DLS. Particle-membrane interactions may have caused shifted retention times which led to an improper determination of the membrane height necessary for D_h calculation. This issue has often been reported for metal nanoparticles [5,16,17,57]. An understanding of the effect of eluent composition and the particle surface on the particle-membrane interactions is required to understand and overcome this observation, and will be discussed in the following sections.

2.2.2. Surface modification of gold nanoparticles

The colloidal stability of nanoparticles plays an important role for reliable FFF characterization. Particle stability is governed by the stabilization mechanisms and the surrounding medium as summarized in chapter 1.4. The stability can be varied by modifying the particle surface. Surface modification of metal nanoparticles is often achieved by specific adsorption of stabilizing ligands onto the particle surface [64]. A high ligand binding affinity is crucial for a reliable particle modification. The affinity to adsorb onto the metal surface can be assessed based on the “hard and soft (Lewis) acids and bases" (HSAB) principle. Stabilizing ligands used for the modification should therefore bear a functional group which determines the attraction between the AuNP surface and the ligand. Gold as a relatively soft metal has increasing affinity with “softer” ions. Thus ligands with primary amines (intermediate “softness”) will be easily replaced by thiolated (soft) ligands [100]. Thiolated ligands are therefore often used for AuNP modification leading to an almost covalent attachment to the NP surface [101].

In this work, different ligand classes were tested for the modification of the synthesized gold nanoparticles in order to provide an adequate range of particles with different properties (Figure 2.27). The goal was to identify suitable ligands which provide AuNPs with enhanced colloidal stability.

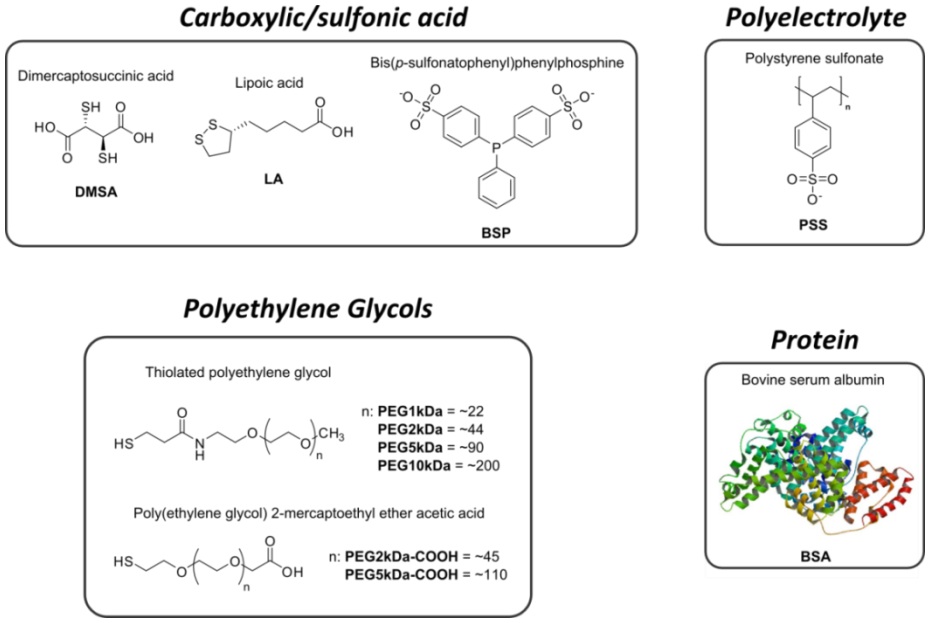

Figure 2.27: Ligands applied for the modification of synthesized AuNPs.

The choice of the ligands was meant to introduce different surface functionalities and ligand classes. Dimercaptosuccinic acid (DMSA), lipoic acid (LA), and bis(*p*-sulfonatophenyl)phenylphosphine (BSP) are well-known short and charged ligands for the stabilization of gold nanoparticles [101,102]. Polystyrene sulfonate (PSS) was chosen as polyelectrolyte, which has also been used for AuNP modification before [103]. These ligands will provide charged electrostatically stabilized AuNPs. Bovine serum albumin (BSA) coated nanoparticles are reported to have a combination of electrostatic and steric stabilization [104]. AuNPs stabilized with polyethylene glycols (PEGs) are characterized by a steric stabilization mechanism which increases with increasing PEG length [105,106].

2.2.2.1. Experimental procedures

Nanoparticle surface modification was performed using different batches of citrate-stabilized gold nanoparticles that were prepared as described in chapter 2.2.1. A general procedure comprised the preparation of a ligand stock solution, the addition of an aliquot to the synthesized AuNPs, shaking or stirring for at least 2 hours, and purification via centrifugation. The amount of added ligand was calculated as a 20-fold excess. The calculation was based on the AuNP surface area (calculated by the core diameter determined by TEM), the AuNP concentration (determined via ICP-OES), and the ligand footprint.

An average ligand footprint of 0.2 nm^2 was assumed based on previously published results on alkylthiol capped gold NPs [107].

Citrate-stabilized gold nanoparticles with a mean core diameter of 16 nm (AuNP-16-citrate) were modified with lipoic acid (LA), dimercaptosuccinic acid (DMSA), Bis(p-sulfonatophenyl)phenylphosphine (BSP), polystyrene sulfonate (PSS), and bovine serum albumin (BSA). To 4.5 mL of citrate-stabilized gold nanoparticles, an aliquot of the ligands stock solution was added at once. The stock solutions were prepared by dissolving the ligands in ultrapure water (BSP, PSS, and BSA) or 0.5 M NaOH solution (DMSA, LA). The respective molar masses (M), mass concentrations (β), and added volumes (V) of the modifying ligands are listed in Table 2.11. Modified NPs were labeled as "AuNP-16-L" where L stands for the respective ligand.

Table 2.11: Molar masses (M), mass concentrations (β) of stock solution, and added volumes (V_{added}) of modifying ligands for the modification of citrate-stabilized gold nanoparticles (D_{TEM} = 16 nm).

Ligand	**DMSA**	**LA**	**BSP**	**PSS**	**BSA**
M (g/mol)	182.2	206.3	534.6	70000	66000
β(stock) (mg/mL)	10	10	10	100	100
V_{added} (µL)	15.1	17.1	44.3	580.2	547.0

Gold nanoparticles with a mean core diameter of 12 nm were surface-modified with thiolated polyethylene glycols (PEG). The PEGylation and characterization procedure were published in *Analytical Chemistry* **2016**, *88*, 10065-10073 [108]. Briefly, aqueous stock solutions of thiolated PEGs were prepared (Table 2.12). Then, 542 µL (20-fold excess) of the respective stock solution was added to 70 mL of citrate-stabilized AuNPs (AuNP-12-citrate) under stirring. A ligand footprint of 0.4 nm^2 was assumed for PEGs [109]. After stirring for 2 hours, the dispersions were purified using centrifugation using PES filter units with a mean cut-off of 100 kDa (Sartorius, Germany) followed by dilution with water and a final filtration through 0.2 µm PES syringe filter membranes.

Table 2.12: Molar masses and mass concentrations of PEG stock solution used for the modification of citrate-stabilized gold nanoparticles (D_{TEM} = 12 nm).

Ligand	PEG1kDa	PEG2kDa	PEG5kDa	PEG10kDa
M (g/mol)	1000	2000	5000	10000
β(stock) (mg/mL)	10	20	50	100

Effects of particle size were tested by modifying the NP surface of AuNP-5-$NaBH_4$, AuNP-17-citrate, and AuNP-79-citrate NPs with BSP and a heterobifunctional (carboxyl- and thiol-terminated) PEG (PEG2kDa-COOH). The respective volume of a 10mg/mL BSP and PEG2kDa-COOH stock solution was added to 2 mL of the as-synthesized dispersions (20-fold excess assuming a ligand footprint of 0.2 nm^2). Purification was performed via centrifugation (3 x 14000 rpm) and redispersion in ultrapure water.

Dynamic light scattering was performed on different setups (see chapter 5.2) as indicated in the respective section. AF4 fractionation was performed using 10 kDa PES membranes. The eluent composition was adjusted using $NaNO_3$ or NH_4NO_3 as electrolytes. The standard flow method A as listed in Table 5.2 was applied (Figure 2.28).

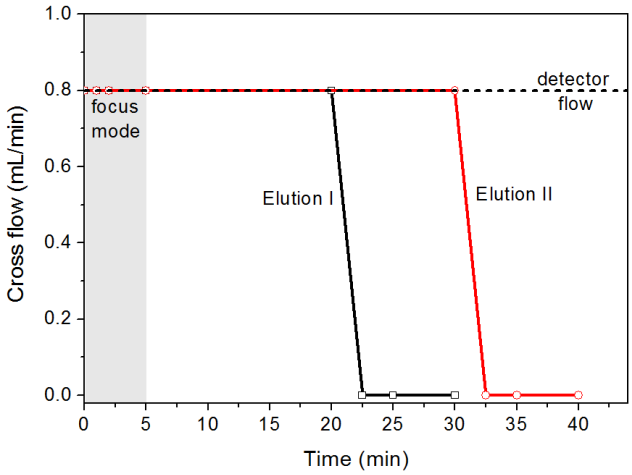

Figure 2.28: AF4 method for the characterization of surface-modified AuNPs (Elution I). Elution profile II was applied for characterization of AuNP-12-PEG10kDa NPs.

2.2.2.2. Results

AuNPs with charged ligands – electrostatic stabilization

The results of the modification of the citrate-stabilized AuNPs (AuNP-16-citrate) with DMSA, LA, BSP, PSS, and BSA are summarized in Table 2.13.

Table 2.13: Results of the colloidal characterization of modified AuNPs with a mean core diameter of 16 nm.

	$D_{\text{Batch-DLS}}$ (nm)[a]	$D_{\text{AF4-DLS}}$ (nm)[c]	Zeta potential (mV)	LSPR (nm)
AuNP-16-citrate	17.6 ± 0.3	19.7 ± 1.2	-36	518
AuNP-16-DMSA	88.4 ± 28.3	28.5 ± 17.3	-41	522 (690)
AuNP-16-LA	18.6 ± 0.8	18.9 ± 1.6	-35	520
AuNP-16-BSP	18.5 ± 0.6	20.3 ± 0.9	-35	522
AuNP-16-PSS	46.5 ± 11.8	21.4 ± 7.6	-41	522
AuNP-16-BSA	47.2[b]	27.6 ± 2.0	-23	526

[a]DLS characterization was performed on setup 2. [b]High polydispersity prevents accurate determination using cumulant fit method. [c]Only the main sample peak was analyzed.

Surface modification with LA and BSP led to a slight increase of D_h as determined by batch DLS. A large increase of the of D_h to 88 nm in the case of DMSA indicated particle agglomeration. PSS and BSA modifications were accompanied with an increase of D_h up to 47 nm. An increase of D_h was expected due to the high molecular weight and larger structure of the polyelectrolyte and the protein. However, since the hydrodynamic diameter of BSA monomer is ~ 3.5 nm [110], an increase of less than 10 nm for a single layer was expected. Thus, particle agglomeration cannot be ruled out. The zeta potential of BSA modified AuNPs increased from -36 mV (AuNP-citrate-16) to -23 mV suggesting a more sterically stabilization and are in good agreement with literature data [111]. The remaining zeta potentials (-35 to -41 mV) were in the same range as for citrate-stabilized NPs (-36 mV). The UV-Vis spectra of the nanoparticles after purification are presented in Figure 2.29.

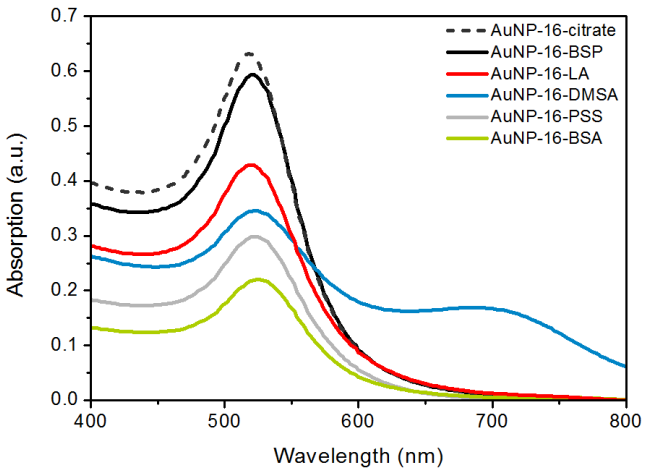

Figure 2.29: UV-Vis spectra of surface-modified AuNPs (D_{TEM} = 16 nm).

Decreasing absorption intensities were observed for all AuNP modifications in the order BSP>LA>DMSA>PSS>BSA. The lowered AuNP concentrations were likely caused during the modification procedure by incomplete redispersion after centrifugation. The UV-Vis spectrum of AuNP-16-DMSA showed a second peak at a wavelength of 690 nm. This second peak indicates nanoparticle agglomeration and supports the results of the batch DLS measurements. The spectra of the other nanoparticle modifications showed only one main peak. AF4 characterization of the AuNPs was carried out to obtain a more detailed size distribution (Figure 2.30).

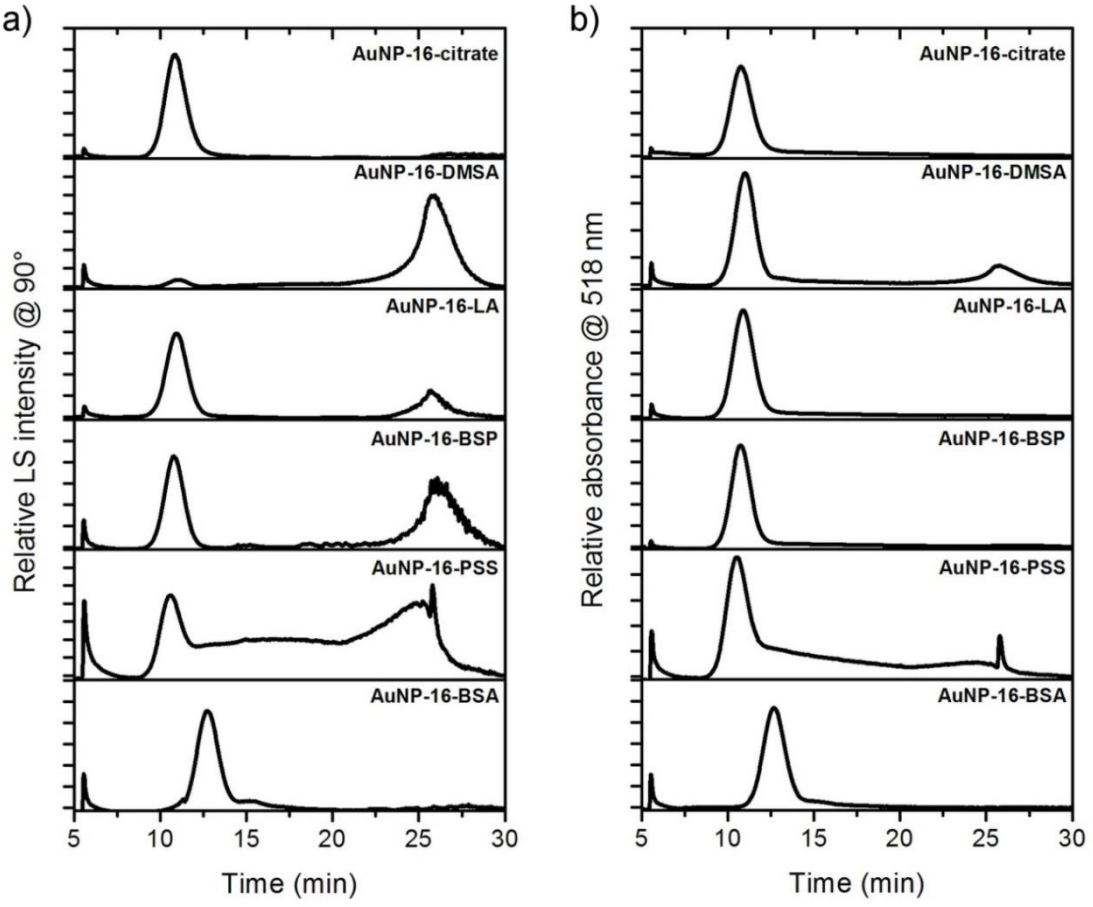

Figure 2.30: AF4 fractograms of modified AuNPs: (a) the relative light scattering (LS) intensity at 90° and (b) the relative absorbance at 518 nm. AF4 was performed on a 10 kDa PES membrane and a 0.5 mM $NaNO_3$ solution as carrier liquid.

The AF4 fractogram of as-synthesized, citrate-stabilized AuNPs was characterized by one main sample peak (10.8 minutes), which was detected using light scattering and UV-Vis absorption. Fractogram of AuNPs modified with DMSA revealed two peaks, the main sample peak at 10.9 minutes, and a large release peak at around 26 minutes. UV-Vis spectra of the release peak showed a peak maximum at 700-710 nm, whereas the main sample

peak consisted of AuNPs with a maximum absorption at 520-525 nm (data not shown here). Hence, the release peak can be associated to agglomerated nanoparticles. For BSP- and LA-modified AuNPs, the sample peak and a release peak was observed using light scattering detection (Figure 2.30 a). The absence of a UV-Vis signal at the corresponding elution time indicates a rather low particle amount (Figure 2.30 b).

The sample peak for PSS-modified NPs with a maximum at an elution time of 10.5 minutes was smeared out unless the cross-flow was turned off. Particles were constantly eluted during the application of the cross-flow field. However, the concentration of the eluted particles decreased with increasing elution time (Figure 2.30, b). UV-Vis spectra recorded at the sample peak maximum and the release peak did not show any difference, which excludes particle agglomeration (data not shown here).

Fractograms of BSA-stabilized particles displayed only one sample peak (12.8 minutes) without the presence of a release peak. A small shoulder was detected at an elution time of 15.3 minutes using LS detection. The small shoulder might result from the adsorption of BSA dimers.

PEGylated AuNPs – steric stabilization

The characterization and AF4 results of the PEGylated AuNPs were published in *Analytical Chemistry* **2016**, *88*, 10065-10073 [108]. A summary of the results is presented in Table 2.14.

Table 2.14: Results of the colloidal characterization of PEGylated AuNPs with a mean core diameter of 12 nm [108].

	$D_{\text{Batch-DLS}}$ (nm)[a]	$D_{\text{AF4-DLS}}$ (nm)	Zeta potential (mV)	LSPR (nm)
AuNP-12-citrate	15.8 ± 4.2	n.a.[b]	-42	519
AuNP-12-PEG1kDa	22.1 ± 9.7	21.1 ± 5.2	-21	526
AuNP-12-PEG2kDa	27.0 ± 9.7	25.7 ± 6.8	-15	524
AuNP-12-PEG5kDa	36.1 ± 11.9	36.2 ± 5.9	-12	524
AuNP-12-PEG10kDa	40.7 ± 14.3	41.9 ± 11.2	-9	522

[a]DLS characterization was performed using DLS setup 1. [b]Scattering intensity too low.

AuNP modification with thiolated PEGs led to AuNPs with decreasing zeta potential and increasing D_h with increasing PEG chain length. A slight shift of the LSPR was also ob-

served due to the different refractive indices of the attached polymers [112]. The AF4 fractograms of the PEGylated AuNPs are presented in Figure 2.31.

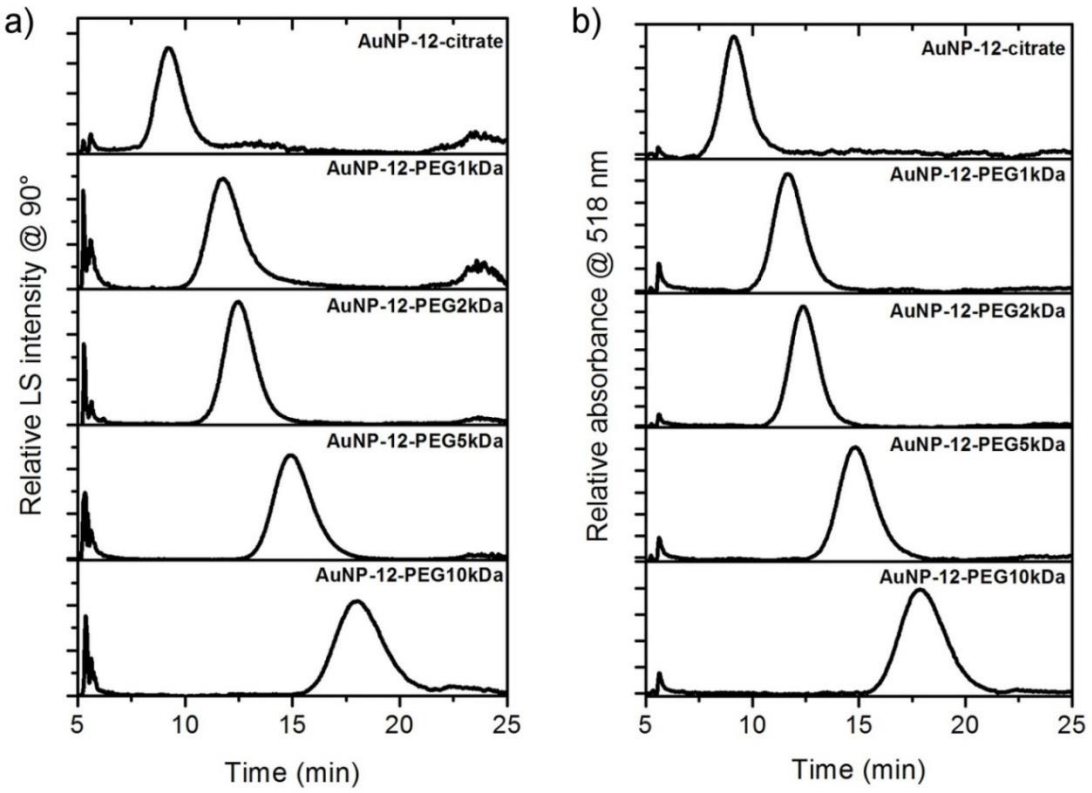

Figure 2.31: AF4 fractograms of PEGylated AuNPs: (a) the relative light scattering (LS) intensity at 90° and (b) the relative absorbance at 518 nm. AF4 was performed on a 10 kDa PES membrane and a 0.5 mM NH_4NO_3 solution as carrier liquid.

A narrow Gaussian-like peak shape was determined for all particles. Increasing retention times with increasing PEG chain length was observed. Online DLS measurements were in good agreement with batch DLS measurements (Table 2.14). For citrate- and PEG1kDa-stabilized AuNPs, a slight release peak at elution times between 22.5 and 25 minutes was detected by light scattering (Figure 2.31, a) but not by UV-Vis absorption (Figure 2.31 b).

Comparison of different AuNP sizes

The effect of particle size on the modification and AF4 characterization was investigated with AuNP-5-$NaBH_4$, AuNP-17-citrate, and AuNP-79-citrate (see chapter 2.2.1). The results of the surface modification with PEG2kDa-COOH and BSP are presented in Table 2.15.

Table 2.15: Results of the colloidal characterization of citrate-, BSP-, and PEG2kDa-COOH-stabilized AuNPs with different sizes.

	$D_{\text{Batch-DLS}}$ (nm)	Zeta potential (mV)	LSPR (nm)[b]
AuNP-5-$NaBH_4$	12.2[a]	-36	518
AuNP-5-BSP	16.8[a]	-20	520
AuNP-5-PEG2kDa-COOH	20.0 ± 4.6	-13	520
AuNP-17-citrate	20.2 ± 3.5	-30	520
AuNP-17-BSP	23.8 ± 5.3	-25	520
AuNP-17-PEG2kDa-COOH	29.2 ± 4.4	-29	520
AuNP-79-citrate	82.5 ± 8.6	-35	546
AuNP-79-BSP	84.2 ± 8.4	-38	548
AuNP-79-PEG2kDa-COOH	81.2 ± 9.2	-39	548

[b]High polydispersity prevents accurate determination of polydispersity using the cumulant fit. [b]LSPR detected via UV-Vis measurements (DAD) during AF4. Spectra at the peak maxima were evaluated.

Batch DLS measurements showed increasing D_h for BSP- and PEG2kDa-COOH-stabilized AuNPs with mean core sizes of 5 nm and 17 nm. For AuNPs with a mean core size of 5 nm, a mean D_h of 17 nm was determined for particles modified with BSP. DLS measurements of these particles did not allow a calculation of the standard deviation because their distribution was too broad. Batch DLS of the respective PEG2kDa-COOH modified NPs revealed a PEG-shell of 3.9 nm. Increasing zeta potentials were detected in the order PEG2kDa-COOH > BSP > BH_4. For AuNP-17-PEG2kDa-COOH NPs, a shell thickness of 4.5 nm was detected. No significant effect on the zeta potential was observed. In contrast, the largest particles investigated showed unaltered D_h regardless of the attached ligand. Also, only minor changes of the zeta potential were detected. Online DLS measurements could not be evaluated because the signals were too weak (AuNP-5 and AuNP-17) or the auto-correlation functions were too distorted (AuNP-79). The AF4 fractograms of the modified AuNPs are depicted in Figure 2.32.

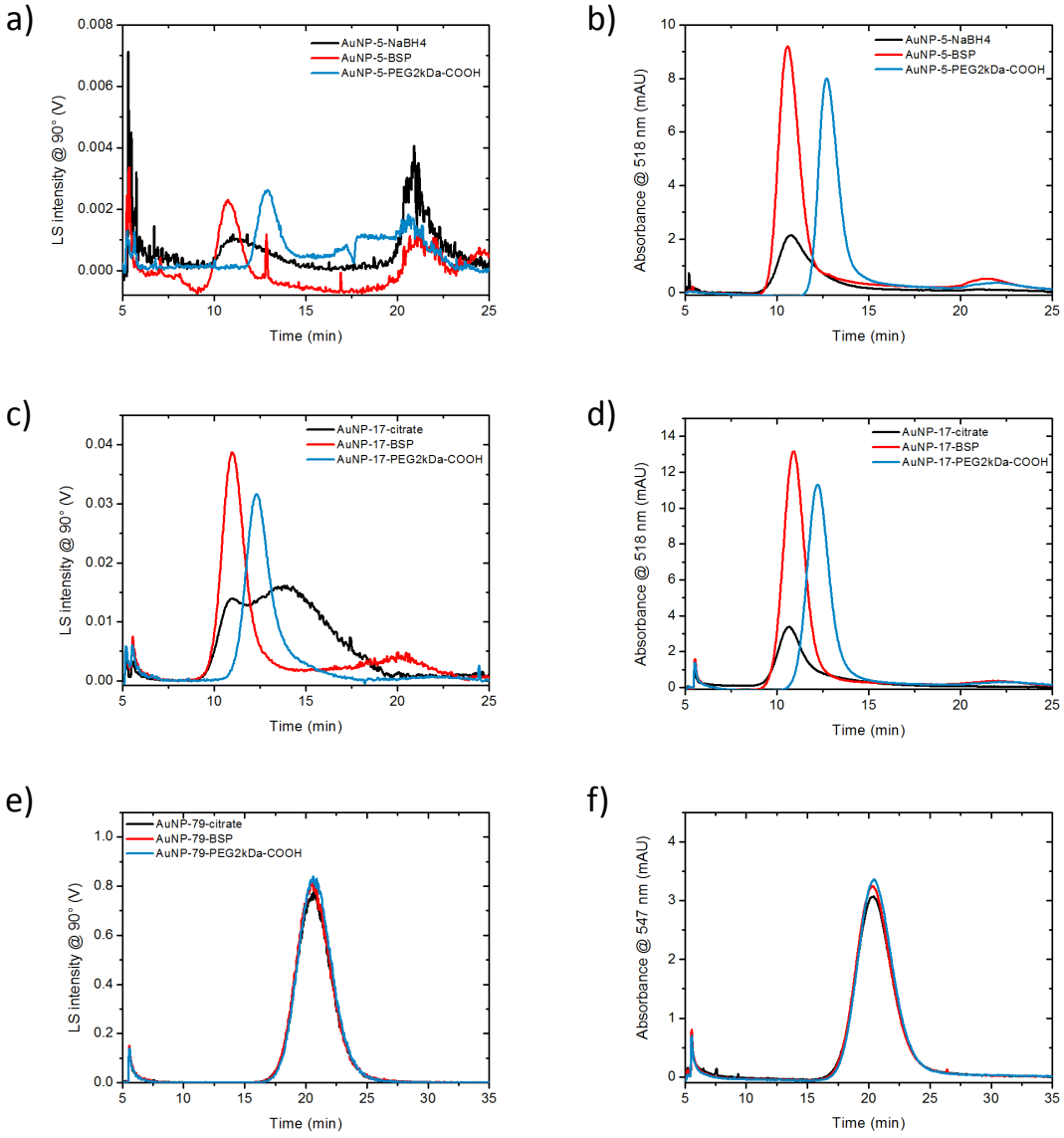

Figure 2.32: AF4 fractograms of citrate- (black), BSP- (red), and PEG2kDa-COOH-stabilized (blue) AuNPs with different sizes using light scattering (LS) (left) and UV-Vis absorption detection (right). A 10 kDa PES membrane and a 0.05 % ammonium nitrate solution.

AF4 fractograms of AuNP-5 NPs were characterized by low light scattering signal (Figure 2.32 a). Using UV-Vis absorbance detection revealed larger and narrower peaks for BSP- and PEG2kDa-COOH-stabilized AuNPs (Figure 2.32 b). An increased retention time for the AuNP-5-PEG2kDa-COOH NPs compared to BH_4- and BSP-stabilized AuNPs was detected. Similar observations were made for AuNP-17 NPs. Citrate-stabilized particles showed agglomeration indicated by a broad shoulder peak (Figure 2.32 c). A corresponding tailing peak using UV-Vis detection was recorded for these AuNPs (Figure 2.32 d). In contrast, when BSP and PEG2kDa-COOH was used for AuNP stabilization, higher and narrower elution peaks were observed using both detection

methods (Figure 2.32 c, d). A slight tailing was observed for the modified AuNPs using light scattering detection, possibly indicating minor agglomeration. AF4 fractograms of AuNP-79 particles did not show any changes in dependence of the stabilizing ligand. A single Gaussian-like sample peak was observed for both detection methods (Figure 2.32 e, f).

2.2.2.3. Discussion

AF4 characterization is well suited for the evaluation of AuNP surface modification. The results of the AF4 characterization of surface-modified AuNPs (AuNP-16 NPs) confirmed that AF4 in combination with a multi-detector approach is a powerful tool for colloidal analysis. Separation of primary AuNPs and agglomerates were successful for partially agglomerated AuNPs. For DMSA-modified AuNPs, agglomeration was observed as shown by the LS detection during AF4. Surface modification of PSS revealed a broadly distributed peak over the whole retention time which is likely caused by over-retained particles due to particle-membrane interactions. All other tested particle modifications were in good agreement with batch DLS measurements. Hence, the success of the surface modification using thiolated PEGs, BSA, LA, and BSP was verified using AF4.

Surface modification strongly influences AF4 characterization. The second major finding was that the surface modification influences the recovery rate and performance of AF4. This was especially observed for BH_4- and citrate-stabilized AuNPs. Particles stabilized with these rather loosely bound ligands showed agglomeration (LS detection) and decreased signal intensities (UV-Vis absorption) compared to particles modified with BSP and PEG2kDa-COOH. Both ligands are known to improve the colloidal stability of AuNPs [106,113]. These results already show that AF4 has a significant effect on nanoparticles with different surface properties. This will be evaluated further in chapter 3.

2.2.3. Silver-labeled gold nanoparticles

The easy detection and surface modification of gold nanoparticles make them ideal nanoparticles samples for FFF. Sample spiking requires labeling to introduce distinct properties that distinguish reference particles from ENPs. In order to achieve this, gold nanoparticles were labeled with gold/silver shells which provide particles with specific optical absorbance that can also be distinguished by ICP-OES and ICP-MS elementary analysis.

There are two approaches to achieve gold-silver nanoparticles: the direct synthesis of gold-silver alloys [114,115,116] or post-synthesis modification [117]. Direct synthesis of bimetallic nanoparticles has been achieved by simultaneous reduction of gold and silver precursors in a one- pot synthesis [116]. The direct synthesis of alloyed particles is usually limited to smaller sizes below a diameter of 30 nm [117]. On the other hand, post-synthesis modification of gold nanoparticles using the seeding growth of silver on the gold nanoparticles' surface allows the fabrication of core-shell like particles [117]. This seeding-growth method leads to a greater range of particle sizes since unmodified gold nanoparticles can be synthesized in a broader size range as shown above.

In this thesis, I have used the post-synthesis modification of gold nanoparticles by adapting the procedure published by Rioux *et al.* [117]. The seeding-growth method was based on the particles growth of citrate-stabilized gold nanoparticles in the size range of 15-20 nm. Using $AgNO_3$ and $HAuCl_4$ mixtures, particles with a different shell composition can be produced. I have adapted this procedure and optimized the conditions to achieve particles with a narrow size distribution which then were applied in AF4. In order to achieve different surface functionalities, thiolated ligands were applied for the surface modification of the obtained particles.

2.2.3.1. Experimental procedures

Citrate-stabilized gold nanoparticles were used as seeds (β(Au) = 44.6 mg/L, labeled as Au-citrate). A total of 72 mg $HAuCl_4$ (5 mmol) were dissolved in 800 mL ultrapure water and subsequently heated to boiling. Then, 28 mL of a 1 % (w/v) sodium citrate solution was added all at once and the solution was kept boiling under vigorous stirring for 30 minutes. After cooling down, the dispersion was used without further purification.

Synthesis parameters such as the precursor/citrate ratio and the thickness of the gold/silver shell were optimized to obtain particles with a narrow size distribution (see Appendix A). A typical seeding growth was performed by diluting 30 mL AuNP seed particles with the same amount of ultrapure water and heating to boiling. Then, the respective amounts of $HAuCl_4$ (25 mM) and $AgNO_3$ (25 mM) were added (Table 2.16). Simultaneously, 1 mL of a sodium citrate solution (104 mM) was added. The solution was kept stirring under boiling for an additional 30 minutes. All particle dispersions were then filtered using a 0.2 µm PES syringe filter after cooling down. No further purification was performed.

Table 2.16: Added amounts (*n*) of $HAuCl_4$ and $AgNO_3$ (both 25 mM) for the seeding growth of different shells on AuNP seeds.

NP batch	Au/Ag ratio	*n*($HAuCl_4$) (µmol)	*n*($AgNO_3$) (µmol)
Au@Au	100/0	10.4	0
Au@AuAg	50/50	5.2	5.2
Au@Ag	0/100	0	10.3

Surface modification of the synthesized NPs was performed using BSP, LA, PEG2kDa, and PEG10kDa. A stock solution of the corresponding ligand was added to 1 mL of the NP solution. A 100-fold excess assuming a ligand footprint of 0.2 nm^2 was used after preliminary tests showed that a 20-fold excess was not sufficient for a successful modification. Purification was performed via centrifugation (3 × 14000 rpm) and redispersion in ultrapure water. LA-modified particles were redispersed and washed with 10 mM NaOH.

Dynamic light scattering was performed on different setups as described in section 5.2. AF4 fractionation was performed on a 10 kDa PES membrane using a 1 mM NH_4NO_3 and 0.005 % SDS solution. The standard flow method A as listed in Table 5.2 was chosen (Figure 2.33).

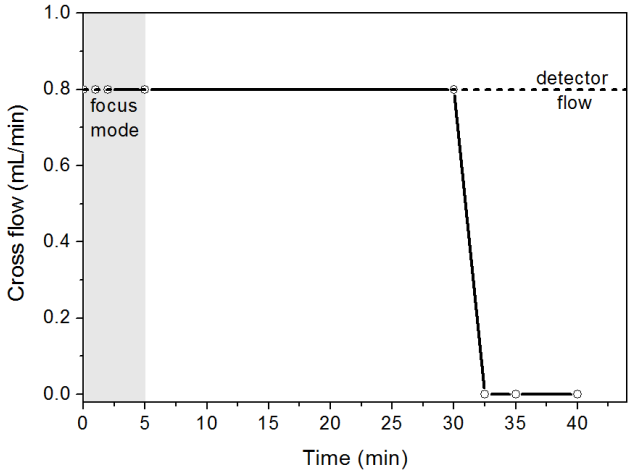

Figure 2.33: The AF4 method used for the characterization of gold/silver NPs.

2.2.3.2. Results

NP synthesis

The results of the testing different synthesis conditions are summarized in Appendix A. Table 2.17 summarizes the results of the NP synthesis.

Table 2.17: Results of the colloidal characterization of silver-labeled AuNPs.

	$D_{\text{Batch-DLS}}$ (nm)	Au/Ag (wt %)	LSPR band (nm)	Zeta potential (mV)
Au-citrate	20.2 ± 1.4	--	519	-25
Au@Au-citrate	25.0 ± 5.3	--	522	-29
Au@AgAu-citrate	24.0 ± 2.0	21.7	496	-36
Au@Ag-citrate	24.4 ± 1.5	74.9	389	-36

The hydrodynamic diameter of the gold nanoparticles increased due to seeding growth. Shell growth using only $HAuCl_4$ (Au@Au-citrate) led to an increase of D_h of 5 nm and a slight red-shift of the LSPR to 521 nm (Figure 2.34). Particle growth using equimolar amounts of $HAuCl_4$ and $AgNO_3$ resulted in an increase of D_h of 4.0 nm. The maximum of the LSPR shifted towards smaller wavelengths, and the peak shape changed. Higher absorption at shorter wavelengths up to 300 nm was observed. Pure $AgNO_3$ to cover AuNPs increased D_h by 4.4 nm. A broad absorption peak was detected at 389 nm. The particles were all negatively charged with mean zeta potential values in the range of -29 to -36 mV.

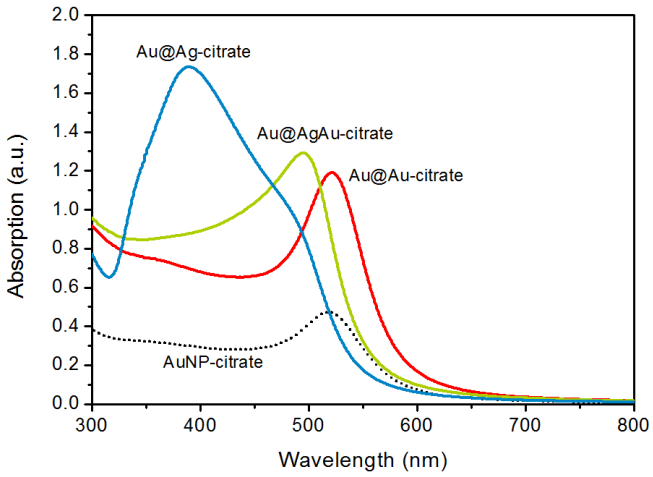

Figure 2.34: UV-Vis spectra of as-synthesized AuNPs and Ag-labeled AuNPs.

TEM and energy-filtered TEM (EFTEM) images are presented in Figure 2.35. Particle morphologies were similar for all three tested variations. EF TEM images confirm the core-shell like structure of the synthesized NPs as described in literature [117].

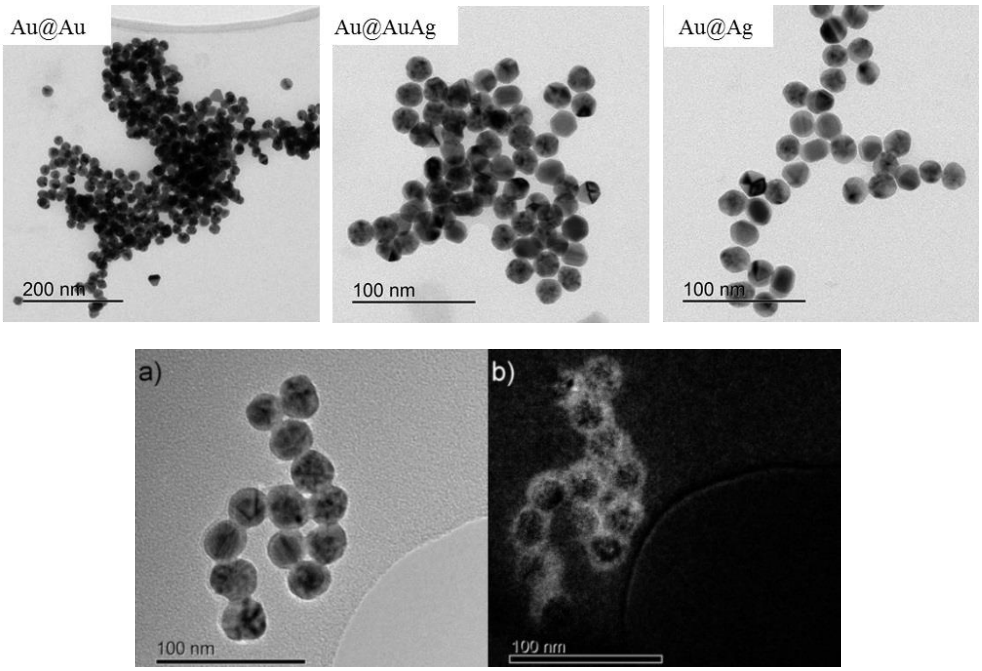

Figure 2.35: Top: TEM images of AuNPs prepared by seeding growth using different Au/Ag ratios. Bottom: Bright field TEM (a) and corresponding Energy-filtered TEM (Ag M4,5 edge at 367 eV) (b) of Au@Ag nanoparticles.

Surface modification

The UV-Vis spectra of the modified NPs are presented in Figure 2.36.

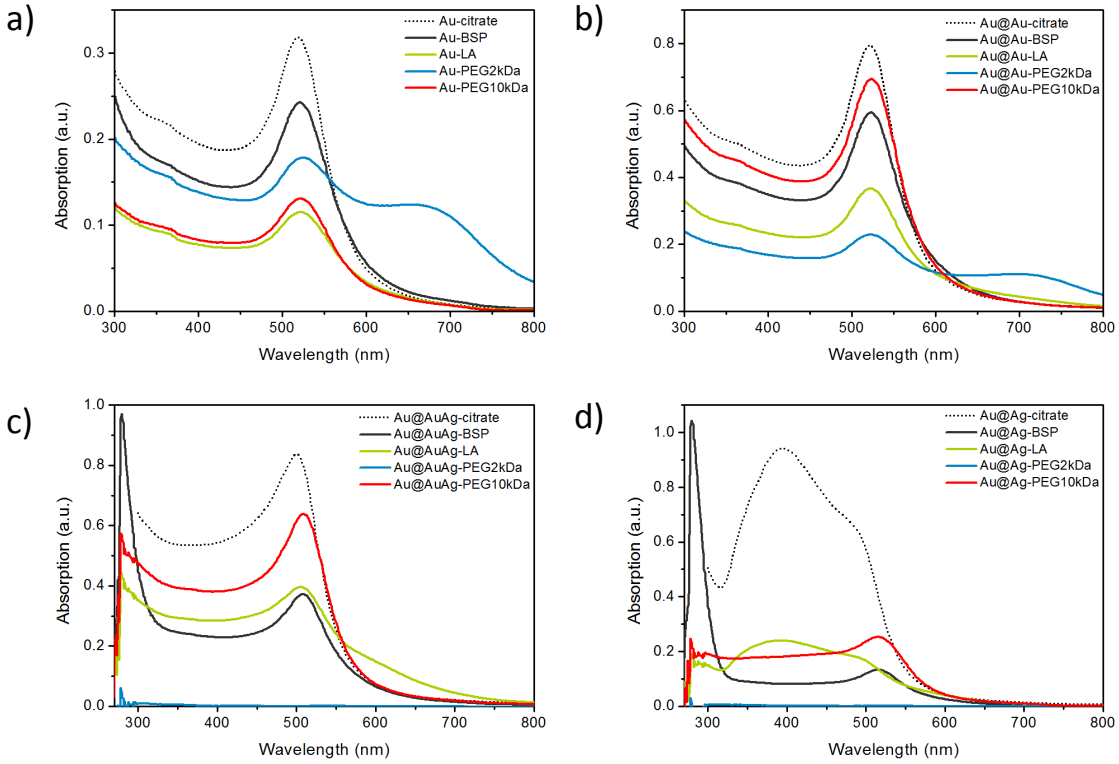

Figure 2.36: UV-Vis absorption spectra of a) Au seed, b) Au@Au, c) Au@AuAg, and d) Au@Ag NPs.

In all cases, a lower absorption compared to the as-synthesized citrate-stabilized nanoparticles was observed that was likely caused by agglomeration and insufficient redispersion of particles. For the Au seed NPs, agglomeration of PEG2kDa-stabilized AuNPs was indicated by the presence of a shoulder at higher wavelengths (Figure 2.36 a). Similar observations were made for the Au@Au NPs showing a second peak for the PEG2kDa-modification. Modification with the other ligands did not show any significant differences.

Ag-labeled AuNPs showed different optical behavior depending on the applied ligand. For Au@AuAg NPs, a clear red shift was detected for the modified particles. LA-stabilized Au@AuAg particles showed a shoulder in the UV-Vis spectra indicating agglomeration. No UV-Vis signal was detected for Au@AuAg particles modified with PEG2kDa. UV-Vis spectra of the BSP-stabilized Au@AuAg NPs revealed an intense sharp peak at 279 nm. Comparable observations were made for A@Ag NPs. LA-modified particles led to decreasing absorption but similar peak shape. Again, no signal was detected for PEG2kDa-stabilized particles. BSP-modification resulted also in a sharp intense peak at 279 nm. Even more surprising was a total change of the spectra with a peak maximum of the LSPR at 516 nm, the same as for Au@Ag-PEG10kDa particles. However, no additional peak was detected below 300 nm. The hydrodynamic diameters determined using batch DLS are presented in Figure 2.37.

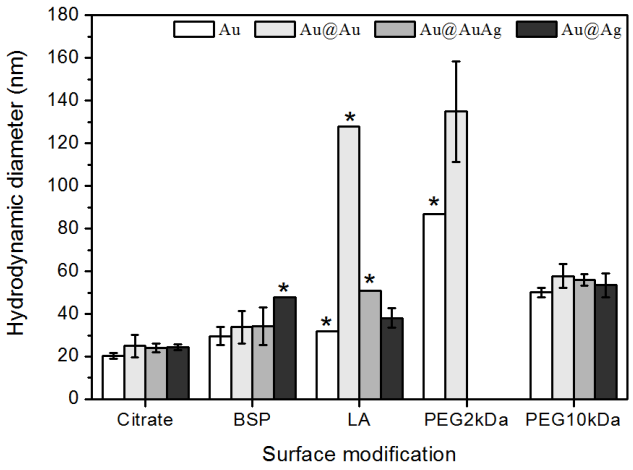

Figure 2.37: Hydrodynamic diameters of surface-modified NPs. Error bars represent one standard deviation. No error bar for the D_h of marked (*) NPs modification were calculated because of too high polydispersity.

Surface modification led to an increase of the D_h in all cases. A slight increase of D_h was observed using BSP as stabilizing ligand. Agglomeration was observed for Au@Ag-BSP

particles. LA-modification led to agglomeration for the Au@Au and Au@AuAg NPs. Surface modification using PEG2kDa led to significant agglomeration in all cases whereas application of the longer PEG led to comparable D_h ranging from 50 to 58 nm.

AF4 investigation

The particle modifications were further tested using AF4 in order to determine the applicability as tracer particles. Figure 2.38 shows the AF4 fractograms of the Au@Au, Au@AuAg, and Au@Ag NPs stabilized with different ligands.

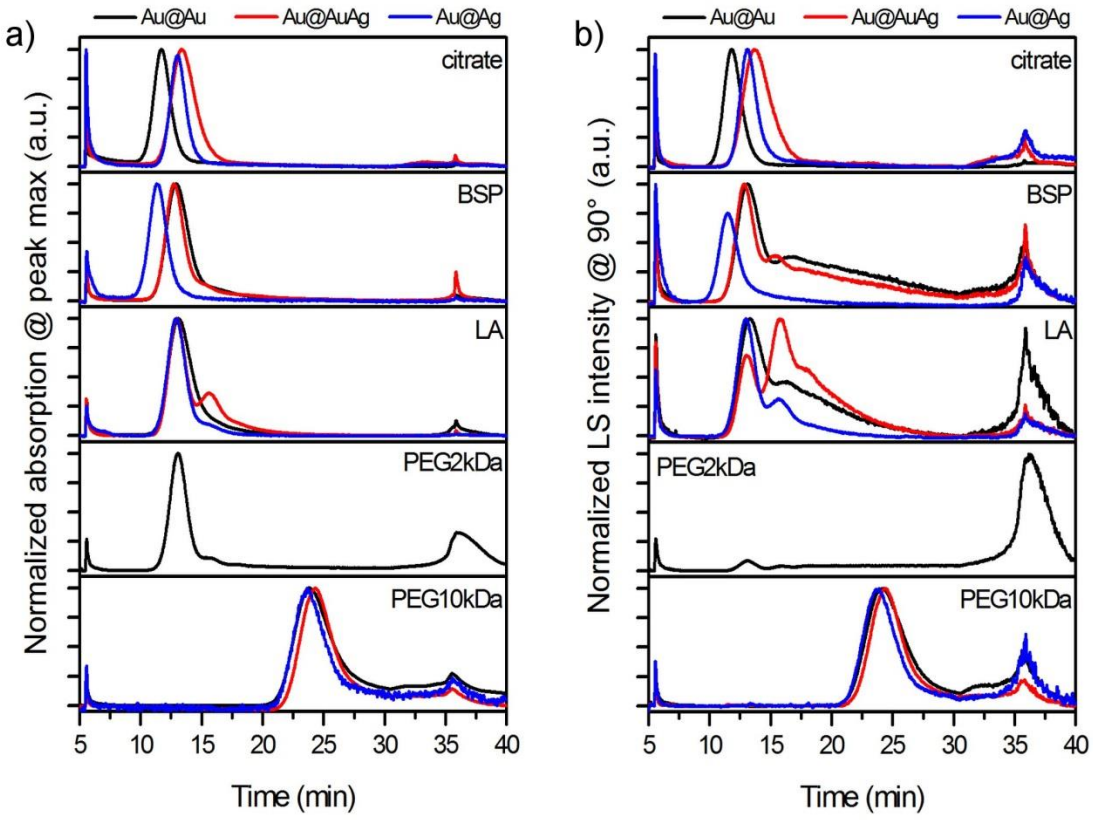

Figure 2.38: Normalized AF4 fractograms of as-synthesized (citrate) and surface-modified Au@Au (black), Au@AuAg (red), and Au@Ag (blue) NPs. AF4 measurements were performed using 1 mM NH_4NO_3 and 0.005 % SDS solution.

AF4 fractograms of citrate-stabilized NPs showed only one main sample peak using both optical absorption and light scattering. Longer retention times were detected for silver-labeled AuNPs. The retention time shifted to shorter elution times for BSP-stabilized Au@AuAg (~ 0.7 minutes) and Au@Ag NPs (~ 1.7 minutes) indicating decreasing particle sizes (Figure 2.38 a). In contrast, Au@Au-BSP NPs were shifted to longer retention times. Light scattering detection revealed a broad shoulder for Au@Au-BSP and

Au@AuAg-BSP NPs that was attributed to agglomerated nanoparticles. A similar observation was made for LA-stabilized AuNPs with more distinct and less broad shoulder peaks detected by light scattering (Figure 2.38 b). Compared to the as-synthesized citrate-stabilized NPs, a retention time shift to larger retention times were only observed for Au@Au NPs whereas the retention time did not change for the silver-labeled NPs.

Au@Au-PEG2kDa NPs showed narrow sample peak with a small shoulder and a large release peak at elution times above 30 minutes. The release peak was caused by agglomerated particles detected by a peak shift in the online UV-Vis spectra to higher wavelengths (data not shown here). Using the larger PEG10kDa as ligand resulted in stable NPs, which was confirmed by the presence of only one sample peak. The increased light scattering intensity and UV-Vis absorption at elution times > 30 minutes are presumably caused by the decreasing cross-flow. The online UV-Vis absorption spectra of the void peak at 5.5 minutes and the corresponding sample peak at peak maximum were plotted for citrate-, LA-, and BSP-stabilized NPs (Figure 2.39).

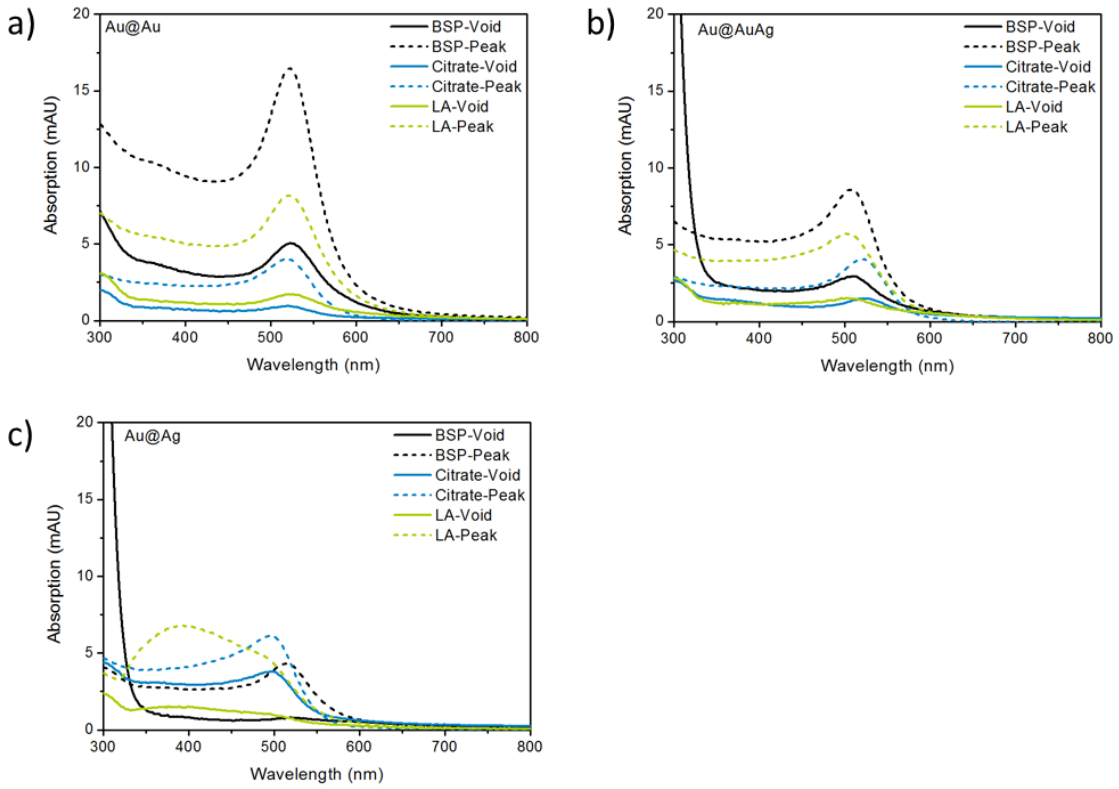

Figure 2.39: Online UV-Vis spectra of as-synthesized citrate- (blue), LA- (green), and BSP- (black) stabilized Au@Au (a), Au@AuAg (b), and Au@Ag (c) NPs. The spectra of the void peak (solid line) and the corresponding sample peak at peak maximum (dashed line) are presented.

Identical peak maxima and shapes were observed for the spectra of the void and sample peaks for all tested Au@Au NP modifications (Figure 2.39 a). AuNPs with silver containing shells revealed some differences. AuNPs covered with a mixed Au-Ag shell (Au@AuAg) and BSP ligands gave different absorption spectra at the void peak and the sample peak. Spectra of the void peak showed increasing absorption below 350 nm whereas the main sample peak exhibited one main peak with a peak maximum at 508 nm. The sample apparently contained two different species. Similar results were obtained for the Au@Ag-BSP NPs with two different UV-Vis absorption spectra obtained for the void peak (peak maximum below 300 nm) and the sample peak (peak maximum at 514 nm).

The most surprising aspect of the data is the significant difference between the batch and the online UV-Vis spectra of the silver-labeled, citrate-stabilized AuNPs where batch UV-Vis of Au@Ag-citrate NPs showed a broad peak at a wavelength of 396 nm. Online measurements revealed a peak at 496 nm with a shape that was similar to the AuNPs. The online and the batch absorption spectra for Au@AuAg-citrate NPs deviated by 20 nm. The identical peak positions of the void and sample peak indicated that the sample contained only one particle species.

2.2.3.3. Discussion

Seeding growth of citrate-stabilized AuNPs using different Au/Ag ratios led to the formation of core/shell like particles with distinct optical properties. A strong dependence of the LSPR on the Ag content in the shell was detected as described in literature [117]. An increase of the Ag content in the surrounding NP shell led to absorption at lower wavelengths which was caused by the electronic properties of the silver atoms. A core-shell like structure was indicated by EFTEM measurements. Increasing the Ag content led to an increase of the extinction coefficient [116] and increased detectability. Labeling of AuNPs via seeding growth using different Au/Ag ratios is a suitable method for the fabrication of particles with distinct optical absorption properties.

AF4 fractionation altered the structure and optical behavior of citrate-stabilized AuNPs with silver-containing shells. The AF4 fractionation of silver-labeled as-synthesized AuNPs led to a change of their optical absorption (peak shifts towards higher wavelengths). Peak shifts to wavelengths of around 520 nm indicate a higher gold content of the NP surface as a consequence of the dissolution of the Ag-containing shell. This result

shows that AF4 fractionation can have a severe impact on particle stability during AF4 fractionation.

Surface modification with BSP promotes dissolution of silver rich shells. NP surface modification using BSP led to the dissolution of the silver-labeled NPs and the formation of a second species that was separated using AF4 measurements. Silver nanoparticles are known for their ligand dependent oxidation and dissolution [118,119]. BSP has a high affinity to silver and is known to oxidize silver [120]. The formed species with a sharp absorption peak at ~ 280 nm is likely attributed to Ag(I)-phosphine complexes.

PEGylation of silver-labeled NPs affects the optical behavior. While PEG2kDa-modification of the NPs led to agglomeration, PEG10kDa allowed successful particle stabilization but also altered the optical properties. The reason for the unsuccessfully PEGylation using thiolated PEG2kDa is unclear. Agglomeration might have been induced due to insufficient stabilization with the smaller PEG chain compared to the larger PEG10kDa ligand. UV-Vis batch measurements revealed a shift of the LSPR to higher wavelengths. This again indicated dissolution of the silver-containing shells. A possible explanation is Ag oxidation. Further measurements have to be performed to prove this hypothesis.

Lipoic acid was the only ligand which successfully retained the optical properties of silver labeled AuNPs, although particles partially agglomerated. The influence of lipoic acid on the stability of silver nanoparticles has not yet been studied in detail. The bidentate binding might lead to an improved stability of Ag-containing shells compared to the monodentate binding of the PEGs. A higher surface coverage might lead to a sufficient passivation of the surface. Particle agglomeration was detected for all tested particles. An optimization of the modification protocol might lead to stable particles with stable optical properties.

2.2.4. Summary

Gold nanoparticles with a mean core diameter of 5 nm and 17 nm were prepared by direct reduction of $HAuCl_4$ using sodium borohydride and sodium citrate, respectively. Seeding growth was performed to obtain particles with a mean core diameter of 79 nm. Characterization using TEM and DLS were in good agreement. Online DLS measurements during AF4 characterization were only applicable for particles with a mean core diameter of

17 nm. Smaller particles could not be measured due to low signal intensities whereas distorted auto-correlation functions were recorded for larger nanoparticles (AuNP-79-citrate). Size determination using AF4 theory showed ideal elution behavior and particle sizes that matched with batch measurements (DLS and TEM).

Surface modification of gold nanoparticles with different stabilizing ligands was performed and evaluated using AF4. Particle modification with DMSA led to agglomerated AuNPs. The polyelectrolyte PSS provided particles with a large increase of the hydrodynamic diameter. AF4 was characterized by a broad peak caused by particle-membrane interactions. LA-, BSP-, and BSA-modified AuNPs were well dispersed as shown by successful AF4 fractionation.

Finally, AuNPs were coated with silver/gold shells to obtain silver-labeled AuNPs. Seeding growth of citrate-stabilized AuNPs with different gold/silver ratios led to the formation of particles with distinct optical absorption properties. Surface modification affected the stability and composition of the formed shells. BSP led to a degradation of the shell due to silver oxidation, which was monitored in batch and using AF4. Particle modification with LA led to partial aggregation but stable shell composition whereas PEG2kDa led to agglomerates which could not be redispersed. Particles modified with PEG10kDa led to stable particle dispersions but also affected the shell by decomposition (likely due to oxidation).

2.3. Colloidal stability of synthesized nanoparticles

The colloidal stability of nanoparticles is an essential prerequisite for reliable nanoparticle analysis using FFF [7,15]. Dilution and concentration by orders of magnitude as well as the shear-type movement in close vicinity to the membrane may cause agglomeration and adsorption phenomena as described above. Agglomeration of nanoparticles occurs when the repulsive interactions are reduced by the change of the solvent (see section 1.4.2). In aqueous samples, the repulsive double-layer interaction is reduced by increasing the ionic strength, which leads to decreasing Debye lengths. Since the adjustment of the ionic strength is often needed in AF4 fractionation, colloidal stability against agglomeration is a key property for NP samples.

In this section, the agglomeration stability of nanoparticles was tested by dispersing the NPs in salt solutions with different ionic strength. Time-dependent DLS measurements

were used to directly monitor the evolution of the hydrodynamic size. For gold nanoparticles, UV-Vis absorbance measurements were used as a complementary technique to observe agglomeration. AuNP agglomeration causes a red shift of the LSPR band to larger wavelengths (red-shift) due to plasmon coupling [121]. As a quantitative measure for particle agglomeration measured by UV-Vis absorbance of gold nanoparticles, several agglomeration indices or ratios are described in literature [103,121,122,123]. I have used a modification of the flocculation parameter described by Whitesides [121] that determines the amount of adsorbed light at higher wavelengths (600-800 nm).

This section reports that the tested silica and gold nanoparticles were stable against agglomeration to an ionic strength of at least of 25 mM. Larger silica NPs sizes were prone to agglomeration at lower ionic strengths compared to smaller silica NPs. Agglomeration of gold NPs was dependent on the surface functionality. Particles with loosely attached citrate ligands showed higher agglomeration tendency compared to the more covalently bound lipoic acid or PEGylated AuNPs. Even in the absence of agglomeration, decreasing particle concentrations were determined for PEG-stabilized AuNPs due to particle adsorption on the cuvette walls.

2.3.1. Experimental procedures

The colloidal stability of gold and silica NPs was tested by dispersing the NPs in sodium nitrate or ammonium nitrate solutions with different concentrations. The electrolytes and their concentrations were matched to the eluent composition during AF4 analysis. Hydrodynamic diameters and the UV-Vis absorbance (for AuNPs only) were detected for at least 12 hours.

Citrate-stabilized gold nanoparticles with a mean core diameter of 16 nm and the respective surface-modified AuNPs (AuNP-16-LA/BSP/PSS/DMSA) were analyzed by dispersing the nanoparticles in $NaNO_3$ solutions. In addition, citrate-stabilized gold nanoparticles with a mean core size of 94 nm (mean zeta potential = -36 mV) synthesized using the method by Perrault *et al.* [97] were also tested. The Rhodamine-labeled silica nanoparticles synthesized by the Hartlen and the Stöber method presented in chapter 2.1.2 were analyzed using the same protocol. The ionic strength was varied between 1 and 250 mM.

The characterization of PEGylated gold nanoparticles was described in a previous publication [108]. Here, ammonium nitrate was used for the adjustment of the ionic strength

(0.5-50 mM). Details about the instruments and procedures are summarized in the supplementary information of [108].

The time-dependent hydrodynamic diameter measurements of gold nanoparticles (D_{TEM} = 16 nm) and silica nanoparticles was performed using a DynaPro PlateReader II (Wyatt Technologies, Dernbach, Germany). Time-dependent UV-Vis measurements were performed using an Infinite M200 PRO multimode microplate reader (Tecan Trading AG, Switzerland). For both characterization methods, a total volume of 120 µL of each sample was analyzed using a 96 well plate (Corning-3880; Corning Life Sciences, Corning, NY). The evaluation of the UV-Vis spectra of AuNPs was based on a Normalized Flocculation Parameter (NFP). The NFP represents the proportion of absorbed light at wavelengths from 600-800 nm [108].

2.3.2. Results

2.3.2.1. Silica nanoparticles

The time-dependent hydrodynamic diameter of Rhodamine-labeled silica nanoparticles at different ionic strengths are illustrated in Figure 2.40.

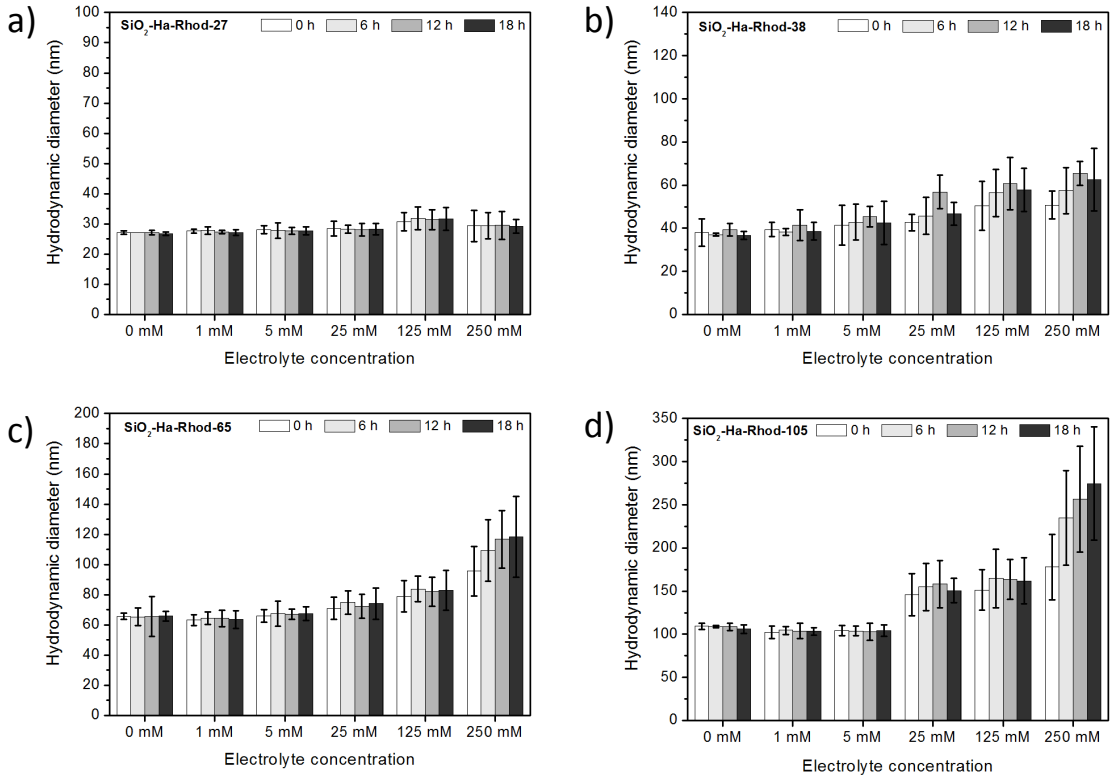

Figure 2.40: Time-dependent hydrodynamic diameters of (a) SiO_2-Ha-Rhod-27, (b) SiO_2-Ha-Rhod-38, (c) SiO_2-Ha-Rhod-65, and (d) SiO_2-Ha-Rhod-105 at different ionic strengths ($NaNO_3$ electrolyte).

The results showed a dependence of the ionic strengths on the particle size and agglomeration stability. The smallest nanoparticles tested, SiO_2-Ha-Rhod-27, did not show a significant increase of D_h up to an ionic strength of 25 mM. A slightly larger D_h combined with an increase of the polydispersity was determined above an ionic strength of 25 mM (Figure 2.40, a). For SiO_2-Ha-Rhod-38, an increase of D_h at an ionic strength of 25 mM was detected. Further increase of the hydrodynamic diameter and the polydispersity with increasing ionic strength was observed.

Similar observations were made for the larger SiO_2 NPs. Silica NPs with a mean core diameter of 38 nm showed slightly larger D_h at I = 25 mM and I = 125 mM but remained constant over time. Only at the highest ionic strength tested (250 mM), D_h increased significantly over time. SiO_2-Ha-Rhod-105 NPs showed a comparable behavior. A more significant increase of D_h directly after addition of the electrolyte was observed but remained unchanged over 18 hours. At a final ionic strength of 250 mM, the hydrodynamic diameter steadily increased.

2.3.2.2. Citrate-stabilized gold nanoparticles

Figure 2.41 summarizes the evolution of the hydrodynamic diameters over time and the corresponding Normalized Flocculation Parameter of citrate-stabilized AuNPs in different ionic strengths. Citrate-stabilized gold nanoparticles with a mean core diameter of 16 nm did not show significant changes at ionic strengths up to 5 mM. At an ionic strength of 25 mM, a slight increase in the hydrodynamic diameter and more significant increase of the NFP indicated initial agglomeration. At higher ionic strengths, AuNP-16-citrate NPs agglomerated immediately after mixing with the salt solution as shown by the large increase of D_h and high constant NFP. AuNP-94-citrate particles showed a similar behavior. The AuNPs were stable up to an ionic strength of 25 mM and rapidly agglomerated at higher ionic strengths which is reflected by great increase in the hydrodynamic diameter and the Normalized Flocculation Parameter.

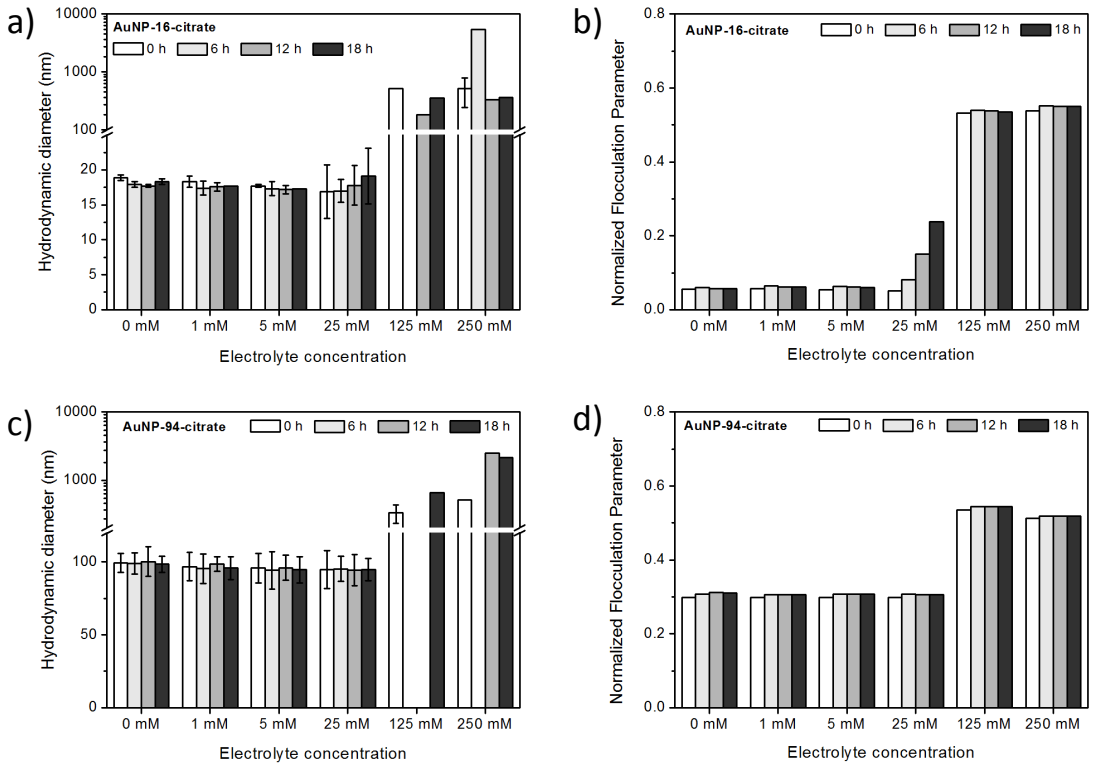

Figure 2.41: Hydrodynamic diameters (a,c) and Normalized Flocculation Parameters (b,d) of citrate-stabilized AuNPs (AuNP-16-citrate: a,b, AuNP-94-citrate: c,d) at different ionic strengths ($NaNO_3$ electrolyte). AuNPs with a mean core diameter of 16 nm (top) and 94 nm (bottom) were tested.

2.3.2.3. Surface-modified gold nanoparticles

Electrostatically stabilized gold nanoparticles

The results of the colloidal stability investigation of the BSP-, LA-, and DMSA-modified AuNPs are presented in Figure 2.42.

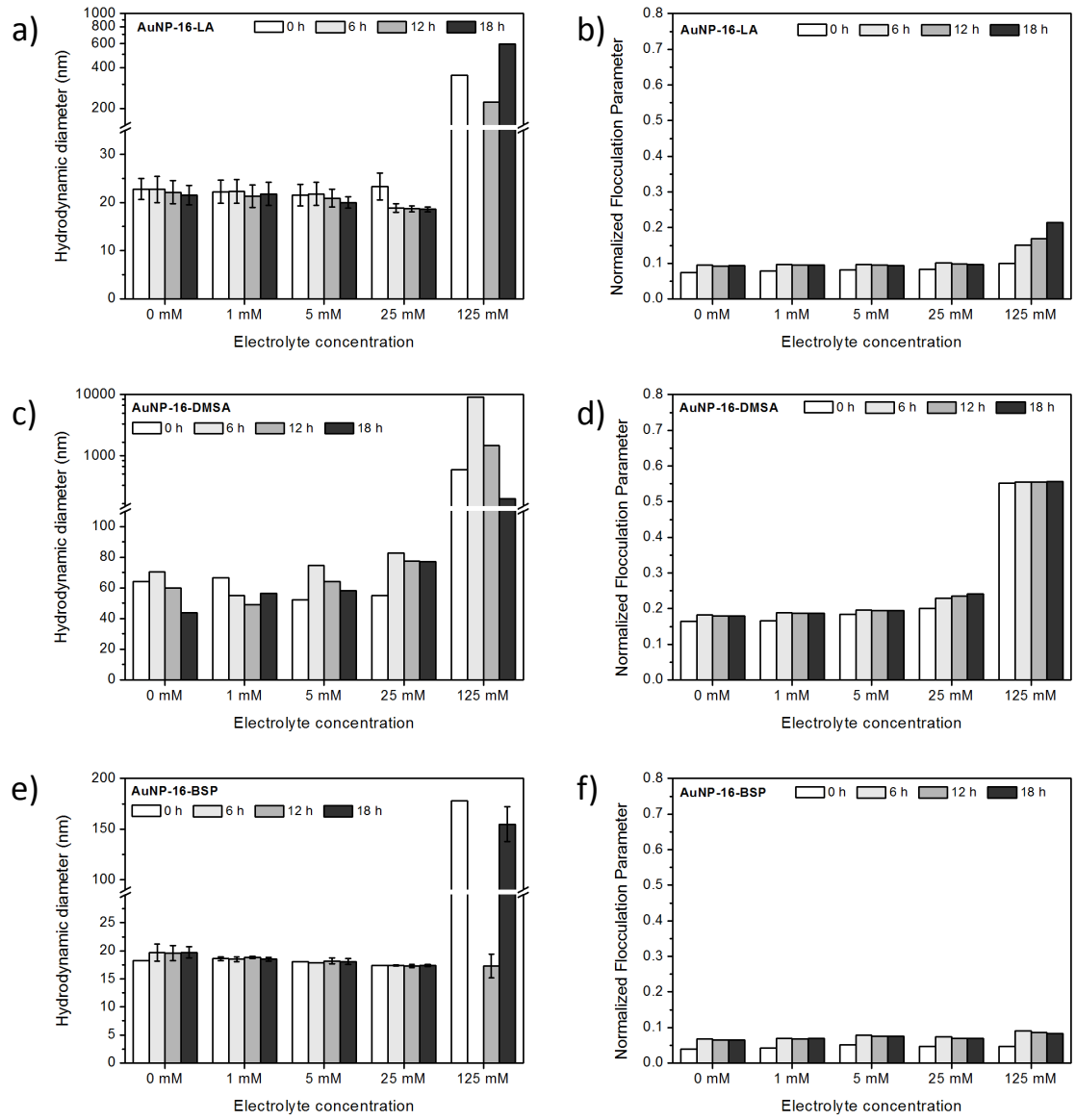

Figure 2.42: Hydrodynamic diameters (a,c,e) and Normalized Flocculation Parameters (b,d,f) of LA-, DMSA-, and BSP-modified AuNPs at different ionic strengths ($NaNO_3$ electrolyte).

The D_h and NFP of AuNP-16-LA particles remained constant up to an ionic strength of 25 mM. At an ionic strength of 125 mM, the increase of D_h above 200 nm and the NFP indicate particle agglomeration. DMSA-stabilized AuNPs showed fluctuating hydrodynamic diameters in the range of 40-80 nm at ionic strengths up to 25 mM. Again, AuNP agglomeration was observed at an ionic strength of 125 mM. For AuNP-16-BSP particles, constant D_h up to an ionic strength of 25 mM was observed. Increasing D_h indicating particle agglomeration was observed at I = 125 mM. The UV-Vis analysis showed only minor changes of the NFP, no particle agglomeration was detected even at the highest ionic strength (125 mM).

The results of the colloidal stability investigation of the PSS- and BSA-modified AuNPs are presented in Figure 2.43.

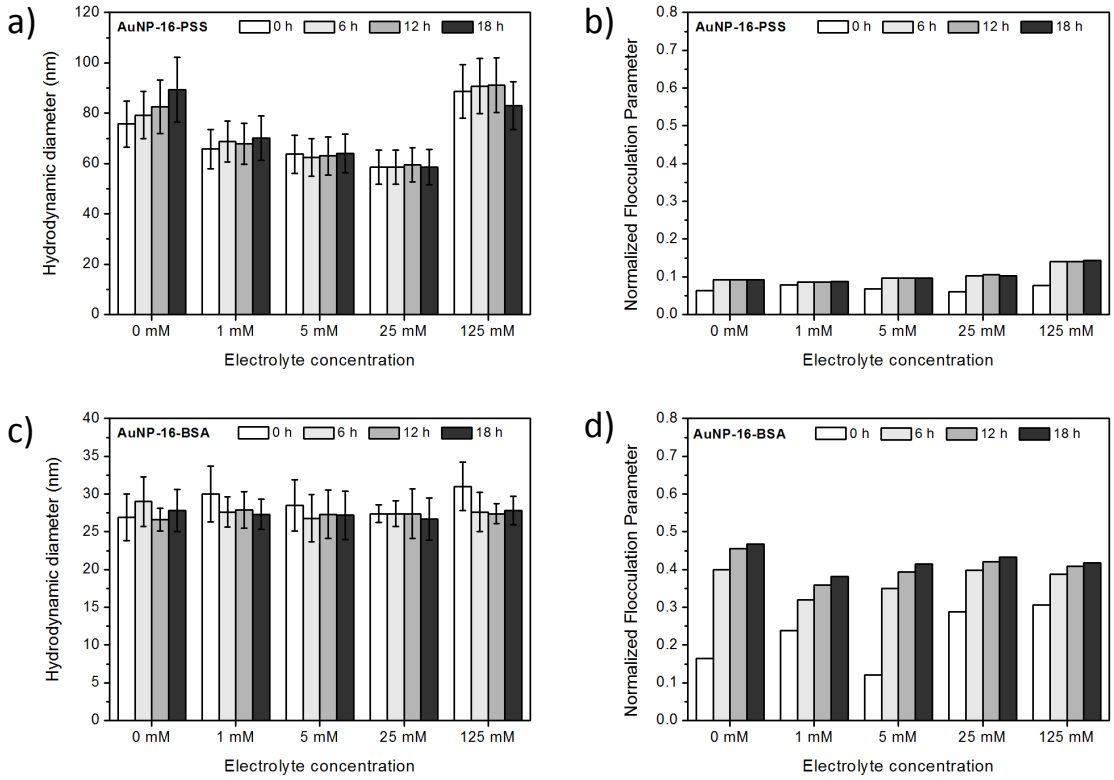

Figure 2.43: Hydrodynamic diameters (a,c) and Normalized Flocculation Parameters (b,d) of PSS- and BSA-modified AuNPs at different ionic strengths ($NaNO_3$ electrolyte).

Hydrodynamic diameter of PSS-modified AuNPs varied between the different ionic strengths tested. The D_h in water slightly increased over time with a final D_h of 90 nm, which is similar to the D_h determined at I = 125 mM. Moderate ionic strength led to a decrease of D_h with a minimum at around 60 nm at I = 25 mM (Figure 2.43 a). A slight increase of the NFP over time in all tested media with a greater increase at I = 125 mM was detected which might indicate minor agglomeration (Figure 2.43 b).

The D_h of BSA-stabilized AuNPs remained constant in the range of 26-29 nm for all ionic strengths tested. UV-Vis evaluation revealed increasing NFP over time for all tested ionic strength indicating particle agglomeration. This result is in stark contrast to the batch DLS measurements where no agglomeration was observed (Figure 2.43 d). An accumulation of the particles at the liquid-solid interface was observed after the measurements. Enrichment of the particles at the well surface is likely the reason for the increases absorption at higher wavelengths caused by LSPR coupling.

Polyethylene glycol modified gold nanoparticles

Time-dependent Normalized Flocculation Parameters of the citrate- and PEG-stabilized AuNPs in water and at I = 50 mM are presented in Figure 2.44. Figure A.4 includes the time-dependent NFPs at I = 0.05 mM and 0.5 mM (see Appendix).

The citrate-stabilized AuNPs were stable up to an ionic strength of 5 mM. At an increased ionic strength of 50 mM, the NFP increased significantly due to particle agglomeration. In the case of PEGylated AuNPs, no change of the NFP was detected and AuNP agglomeration did not occur.

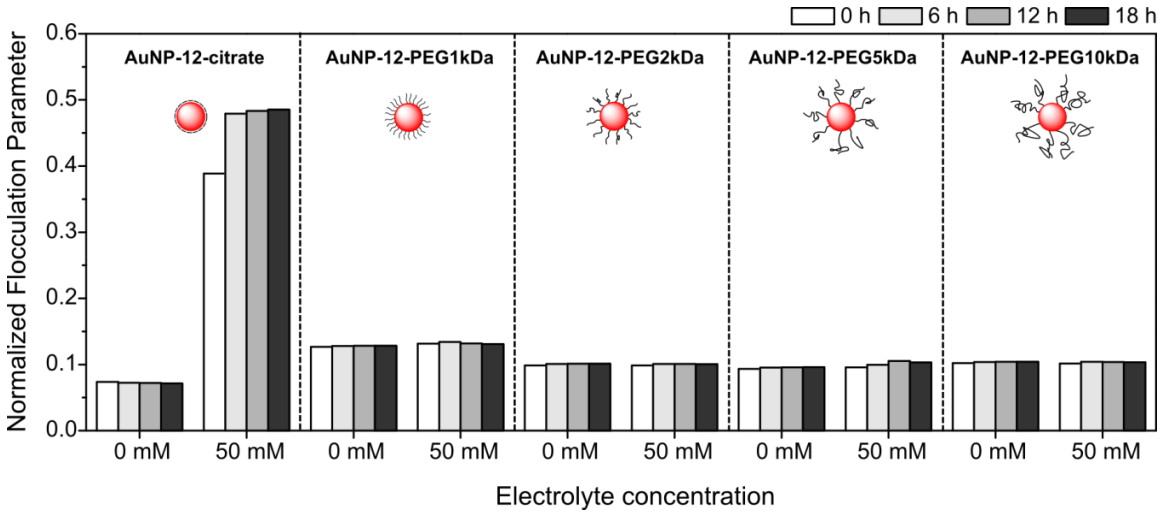

Figure 2.44: Time-dependent Normalized Flocculation Parameter of citrate- and PEG-stabilized gold nanoparticles at different ionic strengths (NH_4NO_3 electrolyte).

Figure 2.45 presents the time-dependent NFPs, normalized absorption at 520 nm, and hydrodynamic diameters at I = 5 mM. The normalized absorption at 520 nm in water and at I = 0.05 mM, 0.5 mM, and 50 mM are presented in Figure A.5 (see Appendix).

UV-Vis absorption spectra indicate particle concentrations and thus sedimentation and adsorption processes inside the cuvette walls. The absorbance at the LSPR peak is proportional to the particle concentration [124].

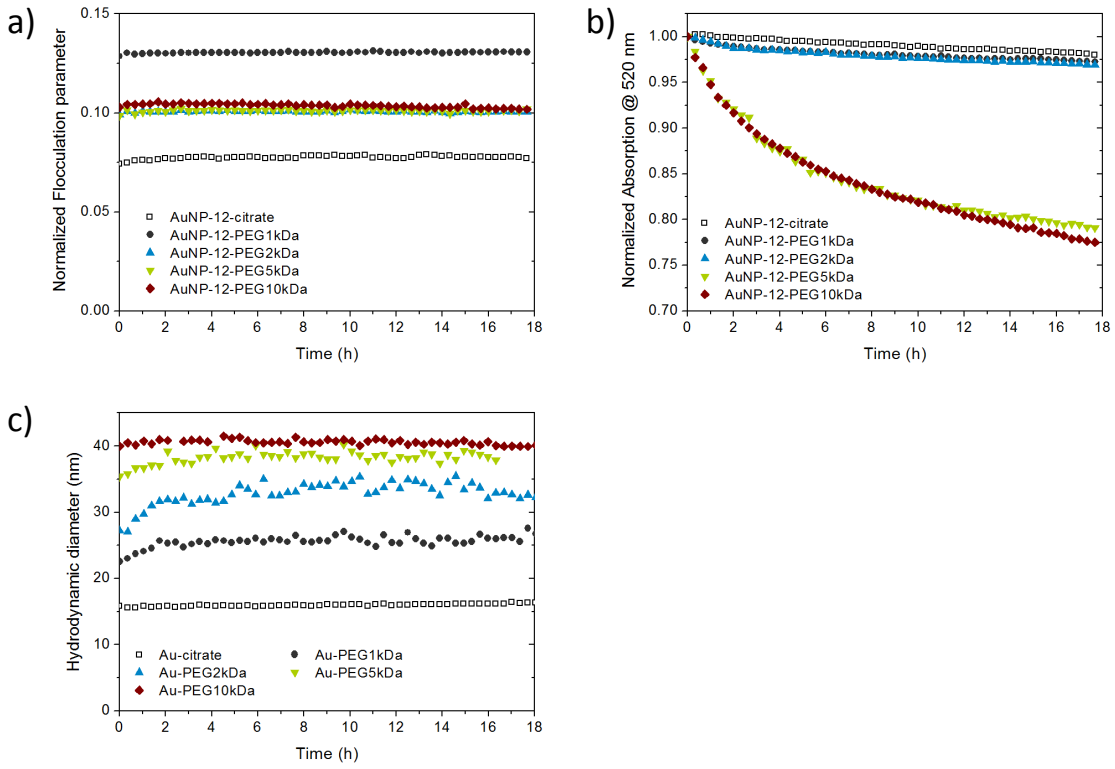

Figure 2.45: Time-dependent Normalized Flocculation Parameter (a), normalized absorption @ 520 nm (b), and hydrodynamic diameter (c) of citrate- and PEG-stabilized gold nanoparticles at I = 5 mM [108].

A sharp decrease of the absorbance of citrate-stabilized AuNPs at I = 50 mM was observed (Figure A.5 a). No significant changes were detected for PEG1kDa- and PEG2kDa-stabilized AuNPs up to an ionic strength of 5 mM and for PEG5kDa- and PEG10kDa-stabilized AuNPs up to I = 0.5 mM (Figure A.5 b-e).At the other ionic strengths, absorbance decreases significantly over time. The comparison between the NFP, the normalized absorbance at 520 nm, and the D_h at I = 5 mM reveals that decreasing particle concentrations are not related to a change in particle size (Figure 2.45). Since a plate reader was used for UV-Vis measurements, sedimentation of agglomerates would have been detected. Only adsorption on the cuvette walls can explain the decreasing particle concentrations.

2.3.3. Discussion

Silica nanoparticles showed size and ionic strength dependent agglomeration stability. Silica NPs with a mean core size of 28 nm did not show increasing D_h in the tested electrolyte solution. On the other hand, an increase of D_h was detected for the largest SiO_2 NPs (D_{TEM} = 105 nm) at I = 25 and 125 mM and remained constant over time. Since no further growth was detected, agglomeration was likely not the reason for this observation.

A strong, continuously increase of D_h for the 105 nm sized particles was detected at I = 250 mM and indicated particle agglomeration. A similar observation was made for 66 nm sized particles showing agglomeration at I = 250 mM. SiO_2 NPs with a mean diameter of 38 nm showed less significant increases of D_h at I = 125 and 250 mM indicating lower agglomeration. The observed agglomeration for larger particles at lower ionic strengths is consistent with experimental data on agglomeration of different NPs, such as AuNPs [125], AgNPs [126], and SiO_2 NPs [127].

Surface modification of gold nanoparticles with ligands having a high gold affinity enhances colloidal agglomeration resistance. This study shows that particle surface modification with ligands that bind more strongly to the gold surface increases the colloidal stability against agglomeration. Whereas citrate-stabilized AuNPs showed initial agglomeration at I = 25 mM, the LA-, BSP-, PSS-, and BSA-modified AuNPs showed no agglomeration or agglomerated at higher ionic strengths. Since the detected zeta potentials were similar for LA- and BSP-modified AuNPs, the electrostatic contribution can assumed to be the same. Therefore, another mechanism has to be the reason for this observation.

Citrate has a lower affinity to gold surfaces than thiolated ligands [128]. Thus, desorption of citrate from the AuNPs surface is more likely than for ligands with higher affinity, which impairs the colloidal stability [101,129]. BSP, BSA, and LA are well known to easily bind to gold surfaces increasing the agglomeration resistance [100,101,104]. These particles showed the highest stability in this study. In the case of BSA, sterically stabilization further contributes to the stability at higher ionic strengths [104]. The mechanism for the higher stability of polyelectrolyte PSS can be attributed to the strong charge effect caused by deprotonated sulfonate groups, which prevents agglomeration even at higher ionic strengths.

Polyethylene glycol modified gold nanoparticles show high agglomeration stability but adsorb to polymer surfaces. Colloidal stability testing did not show any sign of agglomeration for PEGylated AuNPs, even at the highest ionic strength tested (50 mM). Polyethylene glycol stabilized nanoparticles are known for their high colloidal stability against agglomeration [130]. The increased stability is caused by the sterically stabilization of the PEG polymer which is less sensitive to changes of the ionic strength.

A major finding of this study was the decreasing UV-Vis absorption of PEGlyated AuNPs over time at already moderate ionic strengths. This behavior was often contribut-

ed to minor particle agglomeration and settling of the AuNPs out of the light path [131]. DLS measurements and evaluation of the UV-Vis spectra using the Normalized Flocculation Parameter excluded agglomeration and sedimentation to cause the decreasing UV-Vis absorption in this study. I have attributed this observation to particle adsorption on the surfaces of the well plate. These findings are supported by similar investigations that show that polyethylene glycol easily adsorbs on similar materials (polypropylene and polystyrene) [132,133]. My results revealed that PEG attached to nanoparticles surfaces is able to immobilize these particles on plastic walls.

2.3.4. Summary

In this section, the colloidal stability of the synthesized nanoparticles in different ionic strength was evaluated using dynamic light scattering and UV-Vis measurements. Silica nanoparticles showed higher stability against agglomeration than citrate-stabilized gold nanoparticles. Agglomeration of silica nanoparticles depended on the particle size: the smallest particles showed the highest stability against agglomeration. The critical ionic strength to induce agglomeration was determined to be between 25 mM and 125 mM for particles with mean core sizes of 36 nm. Agglomeration of larger particles with mean core sizes of 66 and 105 nm was induced at ionic strengths between 125 mM and 250 mM.

AuNP batch agglomeration strongly depended on the attached ligand. Particles with more covalently attached ligands were less prone for agglomeration compared to citrate-stabilized AuNPs. A difference between electrostatically stabilized particles modified with BSP or LA compared to PEGylated particles was observed. PEGylated AuNPs showed similar stability against agglomeration but were prone to adsorption at the well surfaces at already moderate ionic strengths (I = 5 mM). The adsorption depends on the PEG length and the ionic strength: Adsorption increased with increasing PEG length and increasing ionic strength.

This chapter has described the preparation of well-characterized reference nanoparticles with different sizes and properties. In the next section, I will present the investigation of nanoparticles loss mechanisms during AF4 by using the obtained reference nanoparticles and correlating their properties to respective loss mechanisms.

3. Particle losses during flow field-flow fractionation

Loss of nanoparticle samples during AF4 characterization is a critical limitation that has recently gained increasing attention due to the growing number of nanoparticle investigations using AF4. Several factors that contribute to particle losses make the identification of particle loss mechanisms a complex issue (see chapter 1.4). Here, I present a systematic study of the loss mechanisms of nanoparticles with well-defined particles and characterization protocols to separate different contributions.

I will focus on the effect of the particle surface properties from different stabilizing ligands. Electrostatically and sterically stabilized gold nanoparticles bearing different surface functionalities were investigated as representative metal nanoparticles. Fluorescent labeled silica nanoparticles were employed as representative metal oxide particles. Eluent compositions with different ionic strengths were tested. Relative sample recovery was determined online during FFF using the optical absorption of the particles. Absolute recoveries were determined offline via elementary analysis or fluorescent measurements of collected nanoparticle fractions. The results were combined to derive a more general NP loss mechanism for different particle types.

The stabilizing mechanism had a great influence on the particle loss mechanism. Sterically stabilized particles were lost by adsorption on the separation membrane at higher ionic strength. Electrostatically stabilized particles were lost by both agglomeration and adsorption. Gold nanoparticles with weakly attached ligands suffered large non-membrane- and membrane-related losses. Gold nanoparticles with strongly attached ligands showed fewer losses (membrane- and non-membrane-related). Silica nanoparticles were more robust. They also suffered membrane-related losses but less non-membrane-related losses. However, particle losses were lower than for citrate-stabilized AuNPs.

3.1. Methods

3.1.1. Nanoparticles

Losses of nanoparticles with different surface modifications and core composition were investigated by testing the synthesized nanoparticles presented in the previous chapter. Citrate-stabilized gold nanoparticles were modified with different ligands in order to vary the particles surface composition and functionalities. Different batches were used for the investigation, which were thoroughly characterized in batch beforehand. The specific characteristics such as zeta potential and TEM results are presented in the respective chapter. Particle losses of silica nanoparticles during AF4 characterization were examined using Rhodamine-labeled nanoparticles. Rhodamine-labeled silica nanoparticles were used for the determination of sample losses since the fluorescence detection enhances the sensitivity and supply additional detection signal.

3.1.2. Flow field-flow fractionation setup

A standard Flow-FFF system coupled to different detectors was used. The instrument configuration is described in the experimental section (chapter 5.2). The AF4 setup was operated using a short channel in which a precut ultrafiltration membrane was inserted. The flow path of the system is illustrated in Figure 3.1. After sample injection, the sample is separated in the channel and sequentially passes different detectors: UV-Vis variable wavelength detector (VWD) or diode array detector (DAD), and a fluorescence detector. The detected wavelengths were adjusted to fit the particles' optical properties which were detected offline in advance. Multi-angle light scattering (MALS) and dynamic light scattering were applied to detect the light scattering intensity and the hydrodynamic diameter of the particles, respectively. Fractions were collected either with a fraction collector, or by collecting the samples manually. Refractive index detection was not used in this study.

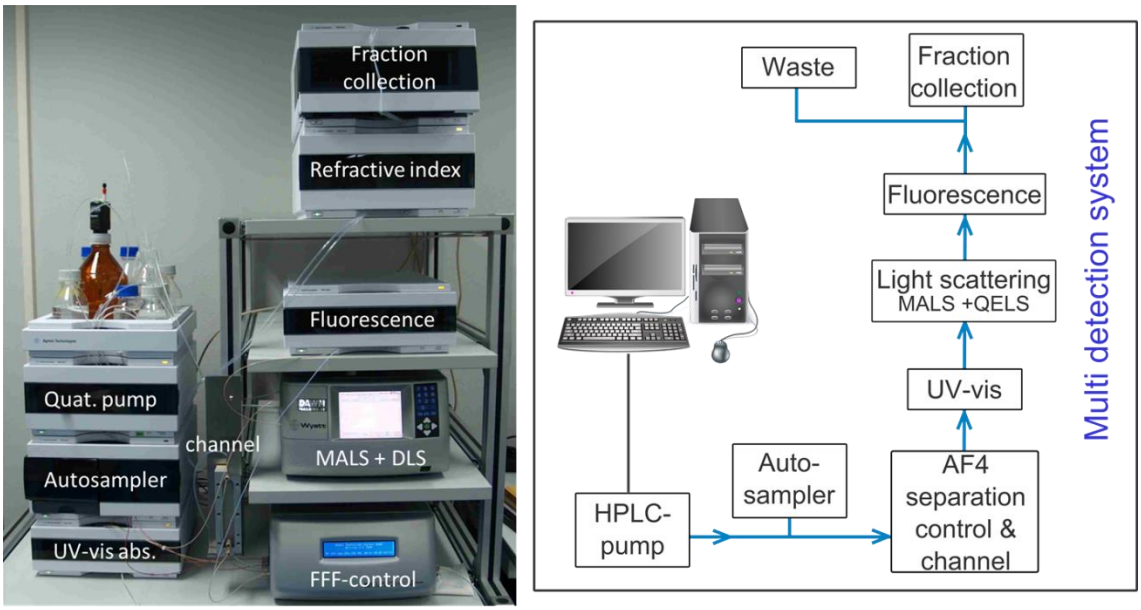

Figure 3.1: FFF setup used in this thesis. The system is comprised of standard LC components. Liquid flow is controlled by the flow control unit with connected separation channel and subsequent multi detection system.

3.1.3. Recovery determination

The relative and absolute sample recoveries were determined using absorption and fluorescence detection as well as elementary analysis. Relative recoveries were based on the online optical absorption. Gold nanoparticle concentrations were determined by online UV absorbance detection (wavelength matched to the respective LSPR position). Rhodamine-labeled silica nanoparticles were detected and quantified using fluorescence detection.

The calculation of relative and absolute recoveries were determined as described in a previous publication and briefly described in the following [108]. A reference run with identical flow rates and method parameters but without the application of a cross-flow was used as the reference and set to 100 %. The relative recovery calculated as

$$Relative\ Recovery = \frac{peak\ area_{fractogram}}{peak\ area_{reference}} \tag{7}$$

Two different reference values were determined:

a) Reference peak area channel: the calibration run was performed under standard conditions but without the application of a cross-flow.

b) Reference peak area tubing: the calibration run was performed with a PEEK tubing (1.2 mm inner diameter) instead of the separation channel under otherwise standard conditions but without cross-flow.

The relative recoveries presented here are in relation to a reference peak area determined by particle elution through the separation channel unless otherwise stated. Absolute recoveries of gold nanoparticles were determined by ICP-OES analysis of collected particles (all fractions united) using the following equation:

$$Absolute\ Recovery = \frac{Au\ mass_{collected}}{Au\ mass_{injected}} \quad (8)$$

The absolute recoveries of Rhodamine-labeled silica nanoparticles were determined by offline fluorescence detection of collected fractions using equation 9:

$$Absolute\ Recovery = \frac{Fluorescence_{\ collected}}{Fluorescence_{\ injected}} \quad (9)$$

A differentiation between non-membrane- and membrane-related losses was achieved by comparison of different flow paths and detection signals. Non-membrane-related losses were identified by comparing the MALS, UV-Vis or fluorescence signals of the reference runs in dependence of the ionic strength (no cross-flow applied). Under the assumption that recovery is maximal when using ultrapure water, statements about relative losses compared to ultrapure water were made. Membrane-related losses were identified by calculation of the relative recovery ratios.

3.2. Losses of gold and silica nanoparticles

The goal of this investigation was to detect the material influence on sample losses during AF4 characterization. Nanoparticle recoveries of silica and gold nanoparticles were detected at different ionic strengths. The adjustment of the ionic strength represents a major system-based influence parameter on particle losses [7,13].

3.2.1. Experimental procedures

Rhodamine-labeled silica nanoparticles (SiO_2-Ha-Rhod-27) and citrate-stabilized gold nanoparticles (AuNP-16-citrate) (chapters 2.1.2 and 2.2.1) were introduced to AF4 in this

set of experiments. The detailed properties of the used nanoparticles are summarized in Table 2.3 and Table 2.13. Particle elution through the separation device without the application of a cross-flow was used to assess non-membrane-related losses in dependence of different ionic strengths. Absolute recoveries of Rhodamine-labeled silica nanoparticles using ultrapure water and 5 mM ammonium nitrate solution as eluent were determined by offline fluorescence measurements of collected fractions. A volume of 30 µL of the SiO_2 dispersion (β(Si) = 3166 mg/L) was injected, which corresponds to approximately $1.1 \cdot 10^{13}$ particles. A total volume of 3 mL was collected. Each measurement was performed in triplicates. A calibration curve was determined by volumetric dilution of the original dispersion in the respective solvent and offline fluorescence measurements.

Membrane-related losses were quantified using flow method A (Table 5.2). The ionic strength was adjusted using sodium nitrate as eluent. For the fractionation of citrate-stabilized gold nanoparticles (AuNP-16-citrate) a volume of 20 µL was injected, which corresponds to approximately $2.6 \cdot 10^{10}$ particles (β(Au) = 53 mg/L). Fractionation of Rhodamine-labeled silica NPs was performed using a volume of 15 µL (~$5.5 \cdot 10^{12}$ particles). For both particle types, the reference runs used the separation channel without a cross-flow. The measurements consisted of three reference runs (no cross-flow applied) and three fractionation runs (cross-flow applied) using the corresponding eluent composition. Between the reference and fractionation runs, water was injected in order to rinse the analyzing system.

3.2.2. Results

3.2.2.1. Non-membrane-related losses

The integrated UV-Vis absorbance peak areas of citrate-stabilized gold nanoparticles and Rhodamine-labeled silica nanoparticles are presented in Figure 3.2.

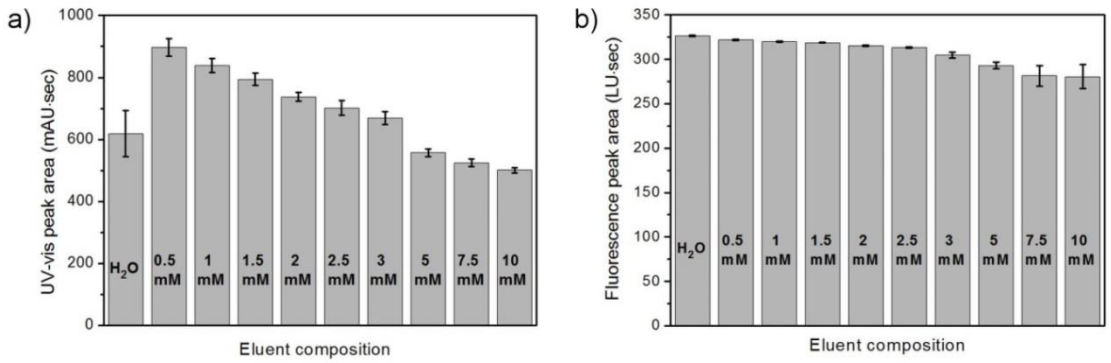

Figure 3.2: Integrated peak areas of reference runs of (a) AuNP-16-citrate NPs (UV-Vis detection at 518 nm, AU = Absorption Units) and (b) SiO_2-Ha-Rhod-27 NPs (fluorescence detection at 573 nm, LU = Luminescence Units) at different ionic strengths ($NaNO_3$ electrolyte).

Increasing ionic strengths led to decreasing peak areas in both cases. This corresponds to decreasing particle concentrations since the optical properties of the gold and silica NPs did not change noticeably at different ionic strengths (tested off-line). Lower NP concentrations were detected for citrate-stabilized gold nanoparticles, when ultrapure water was used as eluent (Figure 3.2 a). The lowest ionic strength tested (0.5 mM) already led to decreased particle losses. The reason for the higher particle losses in water is unclear but was observed for different particle batches and different salts throughout the whole study. At an ionic strength of 10 mM, the optical absorption decreased to only 56 % compared to the use of 0.5 mM. The observation of system-based losses of citrate-stabilized gold nanoparticles is in agreement with other reports [17,23,36].

Rhodamine-labeled silica nanoparticles showed similar but significantly lower decrease of signal intensities with increasing ionic strengths. In contrast to the citrate-stabilized AuNPs, using ultrapure water as eluent resulted in the highest signal detected. The difference between the use of water (highest peak area detected) and 10 mM $NaNO_3$ (lowest peak area detected) was only 14 %. The absolute recoveries of Rhodamine-labeled silica nanoparticles were detected in water and at an ionic strength of 5 mM by batch fluorescence measurements of the collected fractions. Figure 3.3 presents the detected corresponding online and batch fluorescence measurements.

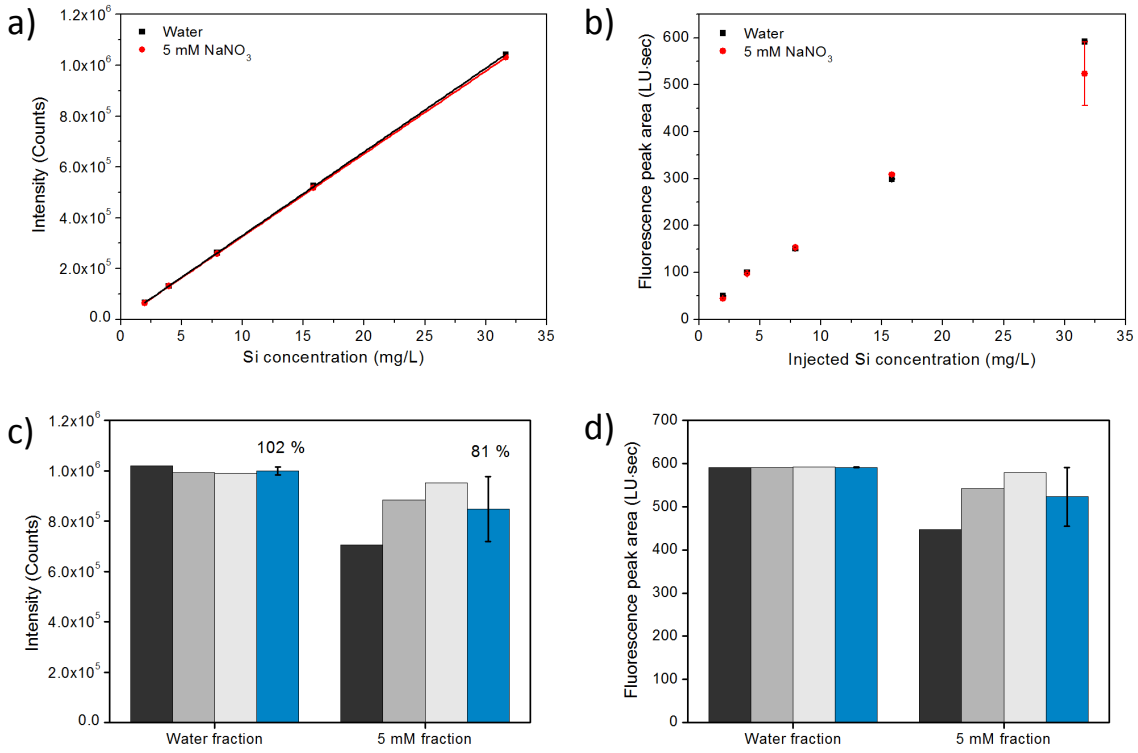

Figure 3.3: Determination of absolute recoveries of SiO_2-Ha-Rhod-27 NPs: (a) Fluorescence calibration curves (batch) and (b) corresponding fluorescence peak areas (online); (c) fluorescence intensities (batch) and (d) corresponding fluorescence peak areas (online) of collected fractions using ultrapure water and 5 mM ammonium nitrate solution. Blue bars represent the average of three measurements.

Identical fluorescence intensities of the silica NPs diluted with ultrapure water and 5 mM ammonium nitrate solution confirm an equal optical behavior at the tested ionic strength (Figure 3.3 a). Comparing the online fluorescence peak areas in water and at an ionic strength of 5 mM showed no differences up to an injected Si-concentration of 15 mg/L (Figure 3.3 b). At higher salt concentrations, decreasing fluorescence signals were determined. No particle losses were detected when ultrapure water was used (Figure 3.3 c). At an ionic strength of 5 mM, an average absolute recovery of 81 % was detected. A similar trend was observed for the online fluorescence measurements (Figure 3.3 d).

3.2.2.2. Membrane-related losses

The AF4 fractograms (light scattering signals) of citrate-stabilized gold nanoparticles obtained at different ionic strength are presented in Figure 3.4.

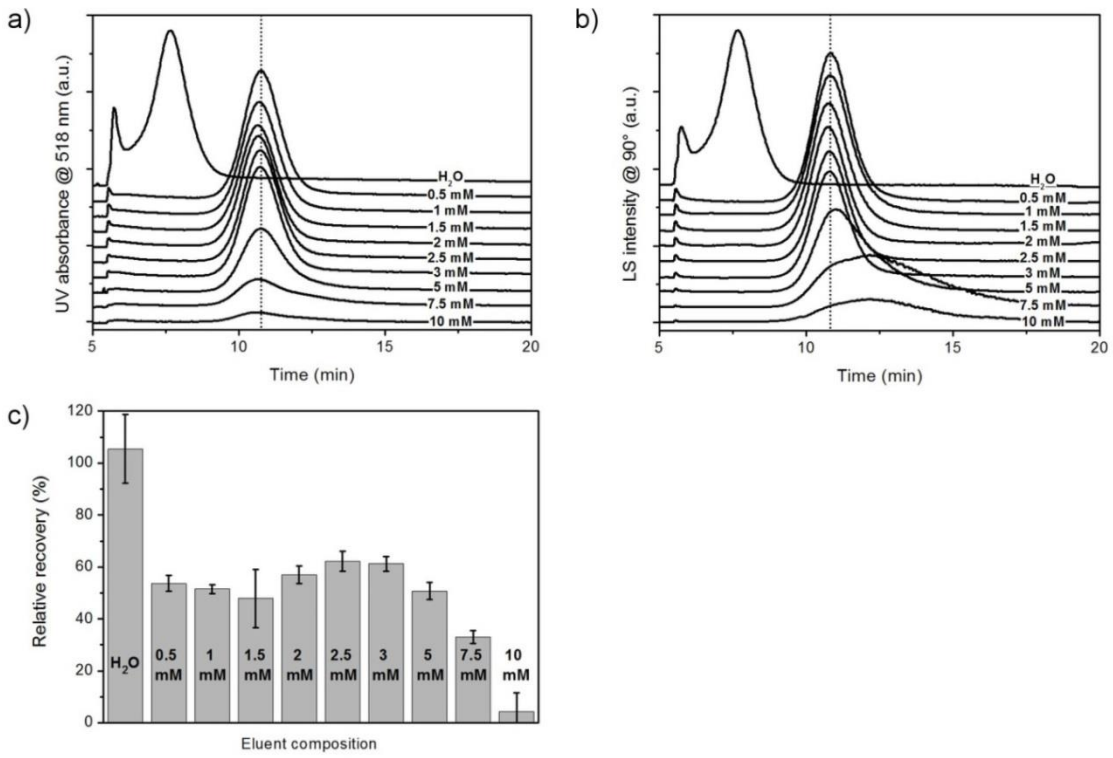

Figure 3.4: AF4 fractograms (a,b) and relative recoveries (c) of AuNP-16-citrate particles at different ionic strengths ($NaNO_3$ electrolyte).

Citrate-stabilized AuNPs showed a significant shift of the retention time between water and a low ionic strength of 0.5 mM. The closer approach towards the membrane allowed the particles to undergo sufficient relaxation. Constant retention times were observed between 0.5 and 3 mM. Band broadening and decreasing peak areas were observed above an ionic strength of 3 mM. Decreasing light scattering intensities and peak shifts to longer retention times were observed indicating particle agglomeration above ionic strengths of 3 mM (Figure 3.4 b). The relative recovery was the highest when using ultrapure water, varied between 33-62 % up to an ionic strength of 7.5 mM, and dropped to below 10 % at I = 10 mM.

The AF4 fractograms of Rhodamine-labeled silica nanoparticles are presented in Figure 3.5.

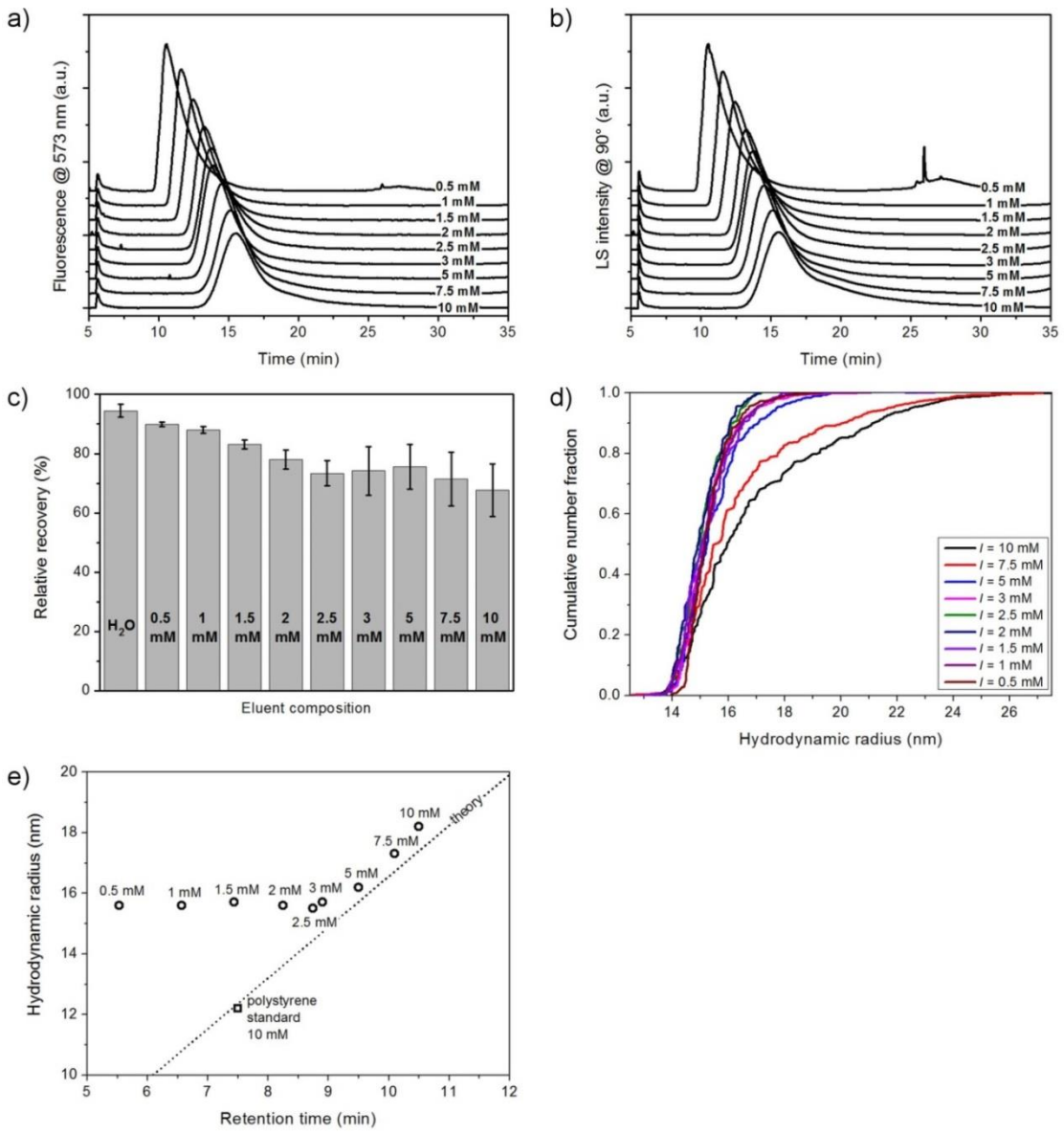

Figure 3.5: AF4 fractograms (a,b), relative recoveries (c), cumulative number fraction (d), and retention time analysis (e) of SiO2-Ha-Rhod-27 NPs at different ionic strengths.

Increasing the ionic strengths led to a steady shift of the retention times (Figure 3.5 a,b,e). The main sample peak was shown in all AF4 fractograms. A small peak detected at an elution time of ~26 minutes using an ionic strength of I = 0.5 mM was likely caused by particle species desorbed from the membrane (Figure 3.5 b). A plot of the hydrodynamic radius vs the retention time showed pre-elution of silica nanoparticles up to an ionic strength of 3 mM, which is likely caused by overloading effects. At higher ionic strengths, retention time shifts are close to the theoretical value. Fluorescence and light scattering detection revealed peak broadening at ionic strengths of 7.5 mM and 10 mM (Figure 3.5 a,b). An increase of D_h and broadening of the distribution was confirmed by

cumulative number distribution plot (Figure 3.5 d). Relative recoveries were highest using ultrapure water as eluent (95 %) and decreased with increasing ionic strength to 74 % at I = 2.5 mM. Further increase of the ionic strength led to minor decrease with a final relative recovery of 68 % when using an ionic strength of 10 mM.

3.2.3. Discussion

Non-membrane-related particle losses are caused by adsorption on internal surfaces. System-based losses at higher ionic strengths can either be caused by particle adsorption inside the flow system or particle aggregation and consecutive alteration of the detected (size-dependent) signals. Especially in the case of gold nanoparticles, the detected UV-Vis absorbance depends strongly on the particle size [124]. The results of the absolute recovery determination of the Rhodamine-labeled silica NPs support the assumption that the system-based losses are caused by internal adsorption. Since the results from online fluorescence measurements and batch determination fit well, and the optical behavior did not change at the different ionic strengths, agglomeration can be excluded as loss mechanism.

Non-membrane-related particle losses of silica nanoparticles are less influenced by ionic strength than losses of citrate-stabilized gold nanoparticles. The experiments revealed that both nanoparticle systems showed increasing particle losses with increasing ionic strengths but with different magnitudes. Citrate-stabilized AuNPs showed high system-based losses due to particle adsorption inside the analyzing system as described in reference [108]. Rhodamine-labeled silica NPs were less affected by the ionic strength. Particle elution through PEEK tubing yielded high absolute recoveries in water and particle losses of 19 % when adjusting the ionic strength to 5 mM. Comparing the results of SiO_2 NPs and citrate-stabilized gold NPs reveals that internal adsorption is less critical for SiO_2 NPs. Only at the highest concentration injected, system-based particle losses were detected at an ionic strength of 5 mM.

Silica nanoparticles are less prone to adsorption on the separation membrane during AF4 fractionation. Low recoveries and high membrane-related losses in the range of 38 % (I = 2.5 mM) to more than 90 % (I = 10 mM) were found for citrate-stabilized AuNPs. At the highest ionic strength tested (I = 7.5 and 10 mM), citrate-stabilized gold nanoparticles agglomerated. Silica NPs agglomerated at ionic strengths of 7.5 mM and 10 mM. Although the particle losses induced during fractionation increased with increasing ionic

strength from less than 5 % (ultrapure water) to 38 % (I = 10 mM), the recoveries were still relatively high compared to that of AuNPs. Gold and silica nanoparticle have to be compared with caution: the tested particle systems varied in size, leading to different particle-membrane distances. Different particle numbers were injected to compensate the different detector responses of silica and gold nanoparticles. Further research should be undertaken to investigate the size and concentration dependencies by using a mass-sensitive detector such as ICP-MS that enables a comparison of different NPs at identical concentrations.

AF4 fractionation influences the agglomeration behavior of nanoparticles. A finding of this study is the NP agglomeration induced during fractionation. Peak broadening indicated a broadening of the size distribution for both particles systems at relatively moderate ionic strengths (I = 7.5-10 mM). In both cases, an increase of D_h was the reason for peak broadening. A red-shift of the LSPR was detected at higher ionic strengths for AuNPs indicating NP agglomeration (data not shown here). For SiO_2 NPs, the cumulative number distribution also indicated particle agglomeration. These findings are in contrast to the colloidal stability testing, where no agglomeration was observed even at much higher ionic strengths. Thus, the fractionation conditions have a severe impact on the particle stability.

3.3. Effect of stabilizing ligand on gold nanoparticle losses

The nanoparticle surface is key for colloidal stability. Nanoparticle losses during FFF characterization are influenced by the surface functionality of which charge and hydrophilicity are believed to be the most important features [8,10]. This study assesses the effect of the surface functionalization on NP losses during AF4. The modified AuNPs described in chapter 2.2.2 were used for the loss investigation. AuNPs were classified according to their stabilization mechanism in electrostatically and polymerically stabilized AuNPs. The ligand affinity and the stabilization mechanism turn out to play an important role and cause different loss mechanisms.

3.3.1. Experimental procedures

AF4 measurements

AuNPs with different core diameters and surface modifications were used for the analysis of gold nanoparticle losses. Details about the synthesis and colloidal characterization are presented in chapter 2.2. LA- (AuNP-16-LA), BSP- (AuNP-16-BSP), and BSA- (AuNP-16-BSA) stabilized AuNPs with a mean core diameter of 16 nm were analyzed in AF4 under identical conditions. AF4 characterization was performed using a 10 kDa PES membrane in a short channel. An injection volume of 20 µL was used in flow method A (Table 5.2). The ionic strength was adjusted with $NaNO_3$ as electrolyte. The measurement sequence consisted of three reference runs (no cross-flow applied) and three fractionation runs (cross-flow applied) using the corresponding eluent composition. Between the reference and fractionation runs, water was injected in order to rinse the analyzing system.

PEGylated nanoparticles (AuNP-12-PEG1kDa/2kDa/5kDa/10kDa, chapter 2.2.) were analyzed using a 10 kDa PES membrane. The ionic strength was adjusted using NH_4NO_3 as electrolyte. Flow program A was used as specified in the instrumental section (Table 5.2). For fractionation of Au-PEG10kDa particles, the elution phase with constant cross-flow was maintained for 25 minutes. The absolute recovery of citrate- and PEG5kDa-stabilized AuNPs was determined by ICP-OES analysis of collected fractions.

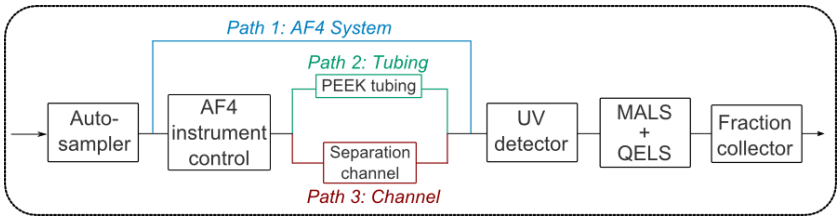

Figure 3.6: Applied flow paths for AuNP fraction collection and subsequent ICP-OES analysis.

Different elution paths were investigated as shown in Figure 3.6. In path 1, the fractionation system was circumvented by connecting the autosampler directly to the UV-detector with PEEK tubing. The fractionation channel was replaced in path 2 by PEEK tubing. Path 3 contained the complete setup as used for AF4 fractionation. Particle elution using path 3 was performed with (fractionation) and without (reference) the application of a cross-flow.

Membrane adsorption tests

Two membrane adsorption tests were performed in order to estimate the particle adsorption on the ultrafiltration membranes [108]. A simulation of the focusing process was performed using a simple membrane adsorption test. A filter holder (PP, Swinnex®) with a mounted 10 kDa PES membrane was placed after the UV detector. The adsorption tests consisted in the injection of AuNP-12-citrate and AuNP-12-PEG5kDa NPs (identical concentrations) and pushing the AuNPs against the filter for 5 minutes at the same cross-flow density used in the separation experiments ($6.5 \cdot 10^{-6}$ m/s). The membrane was immediately removed, rinsed with ultrapure water, and dried at room temperature. SEM characterization was carried out to detect adsorbed AuNPs.

The second membrane adsorption test was performed by drop-casting AuNP solution onto ultrafiltration membrane followed by SEM analysis. First, ultrafiltration membranes were soaked in ultrapure water (15 minutes), after which the surface was dried at room temperature. Then, 10 µL of AuNP solutions (30 mg/L) were diluted with 10 µL of an electrolyte solution (NH_4NO_3) of different ionic strengths, after which 10 µL of the final AuNP electrolyte solution was drop-casted on the membrane (settling time of 1 min). The surface was then gently rinsed with ultrapure water and dried at room temperature. Optical images and SEM images were taken to image adsorbed AuNPs.

3.3.2. Results

3.3.2.1. Electrostatically stabilized gold nanoparticles

The AF4 fractograms using UV-Vis and light scattering detection (Figure 3.7 a, b) show a peak shift of ~4.5 minutes from water to I = 0.5 mM. Increasing the ionic strength further to I = 10 mM did not influence the retention time. Small release peaks were observed when using ultrapure water, 0.5 mM, and 1.0 mM sodium nitrate solution as eluent, which might indicate membrane saturation (Figure 3.8 b). Symmetrical peaks without band broadening were observed for all I.

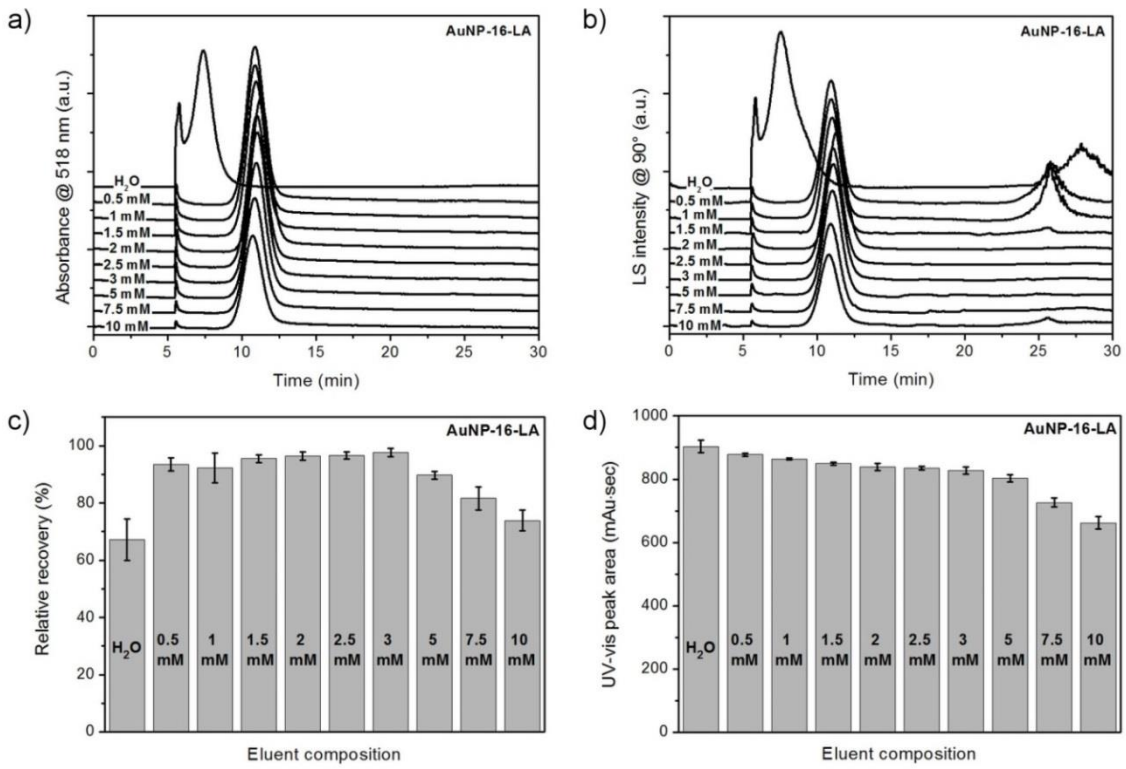

Figure 3.9: AF4 fractograms (a, b), corresponding relative recoveries (c), and peak areas of the reference runs (d) of LA-stabilized AuNPs at different ionic strengths ($NaNO_3$ electrolyte).

The peak areas of the reference runs decreased slightly by 9 % of the peak are in water with increasing ionic strength (3 mM) (Figure 3.10 d). A more pronounced decrease was observed up to 73 % of the original peak area when increasing the ionic strength further (I = 10 mM). The relative recoveries were low (67 %) when using ultrapure water but remained high (93-98 %) up to I = 3 mM. Increasing the ionic strength to 5 mM, 7.5 mM, and 10 mM led to decreasing relative recoveries of 90 %, 82 %, and 74 %, respectively.

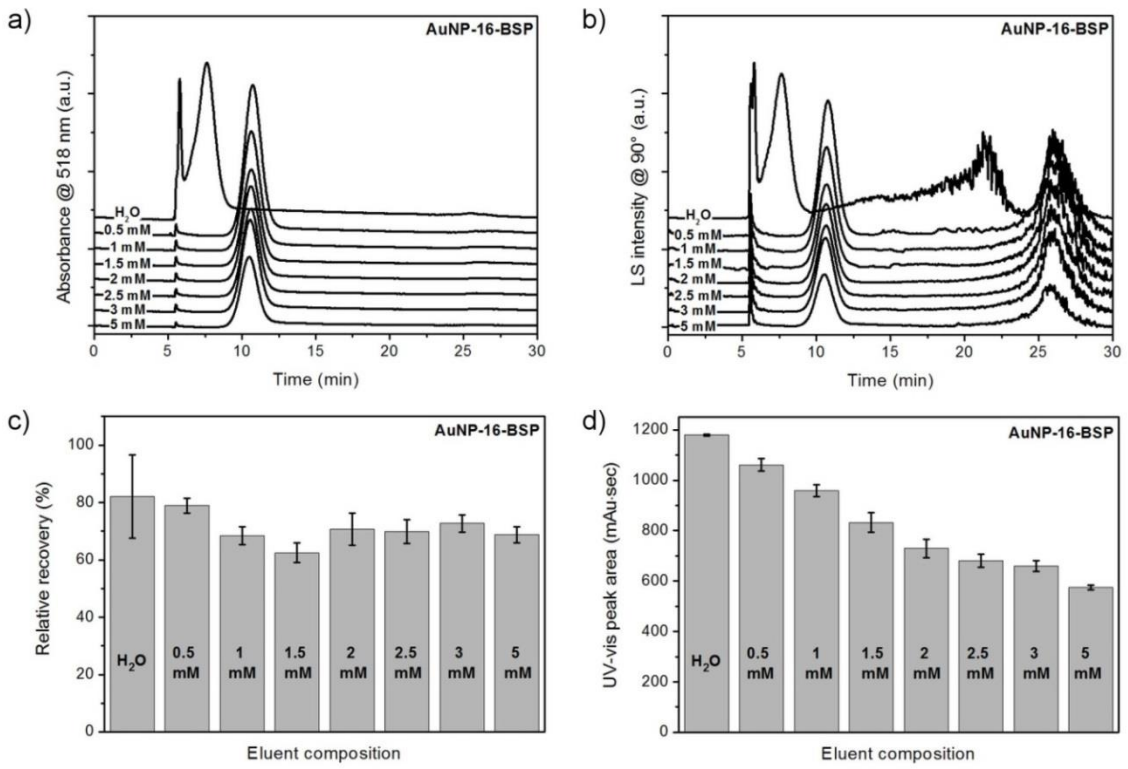

Figure 3.11: AF4 fractograms (a, b), corresponding relative recoveries (c), and peak areas of the reference runs (d) of BSP-stabilized AuNPs at different ionic strengths ($NaNO_3$ electrolyte).

The AF4 fractograms of BSP-stabilized AuNPs (Figure 3.11 a, b) showed a similar peak shift as the LA-modified AuNPs when adjusting the ionic strength compared to the use of ultrapure water only (Figure 3.11 a, b). No peak broadening (LS and UV-Vis detection) was observed throughout the ionic strengths tested (I = 5 mM). In contrast to citrate- and LA-stabilized AuNPs, significant release peaks were observed for all tested media. The reason for this observation is unclear. Desorption of reversibly adsorbed AuNPs or agglomeration might be an explanation. Since no UV-Vis peak was detected at the corresponding elution time the amount of adsorbed or agglomerated AuNPs is rather low (Figure 3.11 a). Peak areas of the reference runs steadily decreased by approximately 10 % with increasing ionic strength (up to I = 2.0 mM) and finally lowered to 49 % (at I = 5.0 mM) (Figure 3.11 d). The relative recoveries varied between 82 % (water) and 62 % (I = 1.5 mM) but no clear trend was observed (Figure 3.11 c). Significant system-based losses occurred for BSP-stabilized AuNPs at moderate ionic strengths (up to I = 2.0 mM).

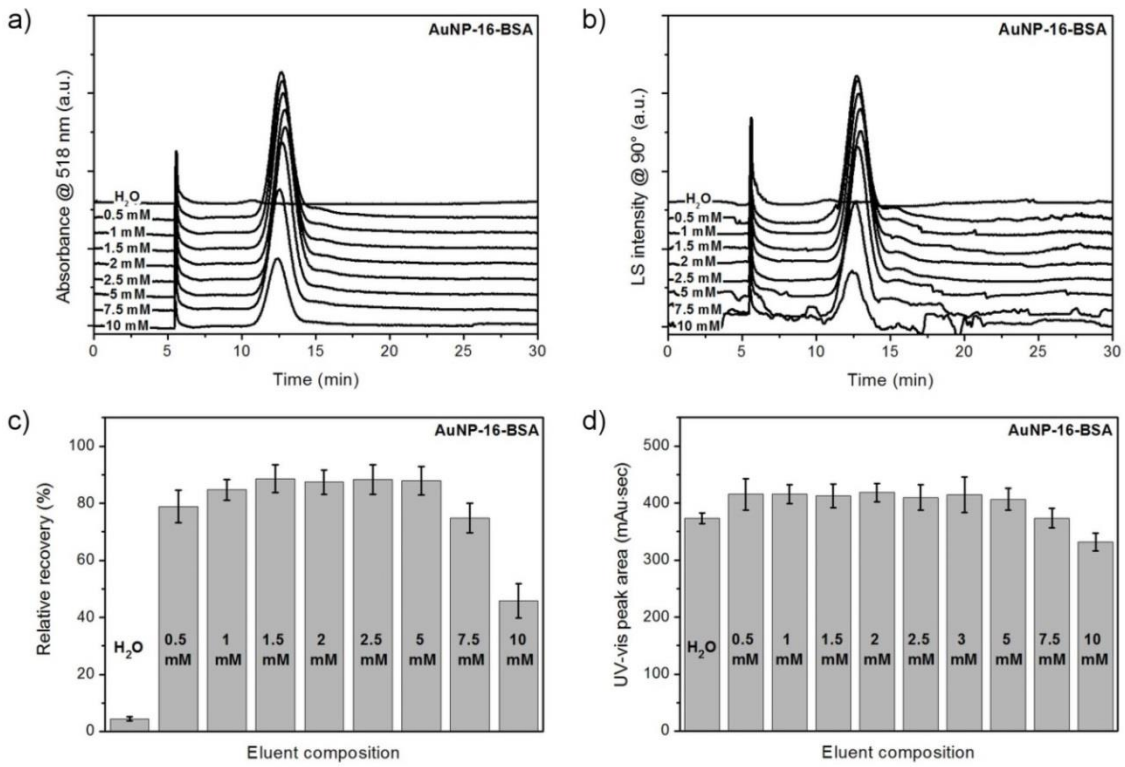

Figure 3.12: AF4 fractograms (a, b), corresponding relative recoveries (c), and peak areas of the reference runs (d) of BSA-stabilized AuNPs at different ionic strengths ($NaNO_3$ electrolyte).

Fractionation of BSA-coated AuNPs (Figure 3.12 a, b) using water as eluent led to almost complete particle loss due to adsorption (very low UV and LS signals). The main sample peak emerged at elution times of 12.5 minutes when adjusting the ionic strength. Constant peak shapes and retention times were observed at all tested ionic strengths. Relative recoveries were in the range of 79 % to 88 % at ionic strengths up to I = 5 mM after which the recoveries dropped to 75 % (I = 7.5 mM) and 46 % (I = 10 mM) (Figure 3.12 c). Increasing background signals were observed with increasing ionic strengths (Figure 3.12 b). Peak areas of the reference runs were constant at ionic strengths between 0.5 mM and 5.0 mM (Figure 3.12 d). Lower peak areas were detected in water and at higher ionic strengths indicating the ionic strength dependency.

3.3.2.2. Polyethylene glycol modified gold nanoparticles

Parts of this chapter were published in *Analytical Chemistry* **2016**, *88*, 10065-10073 [108].

Membrane-related losses

A retention time shift of the particles was observed for all tested NPs when using ammonium nitrate solution instead of ultrapure water (Figure 3.13). Citrate-stabilized AuNPs showed similar retention times when using a salt concentration of 0.05 mM and 0.5 mM. Further increase of the ionic strength to 5 mM led to complete particle loss (no signals in UV-Vis and LS detection). Particle agglomeration was observed when using ultrapure water as eluent.

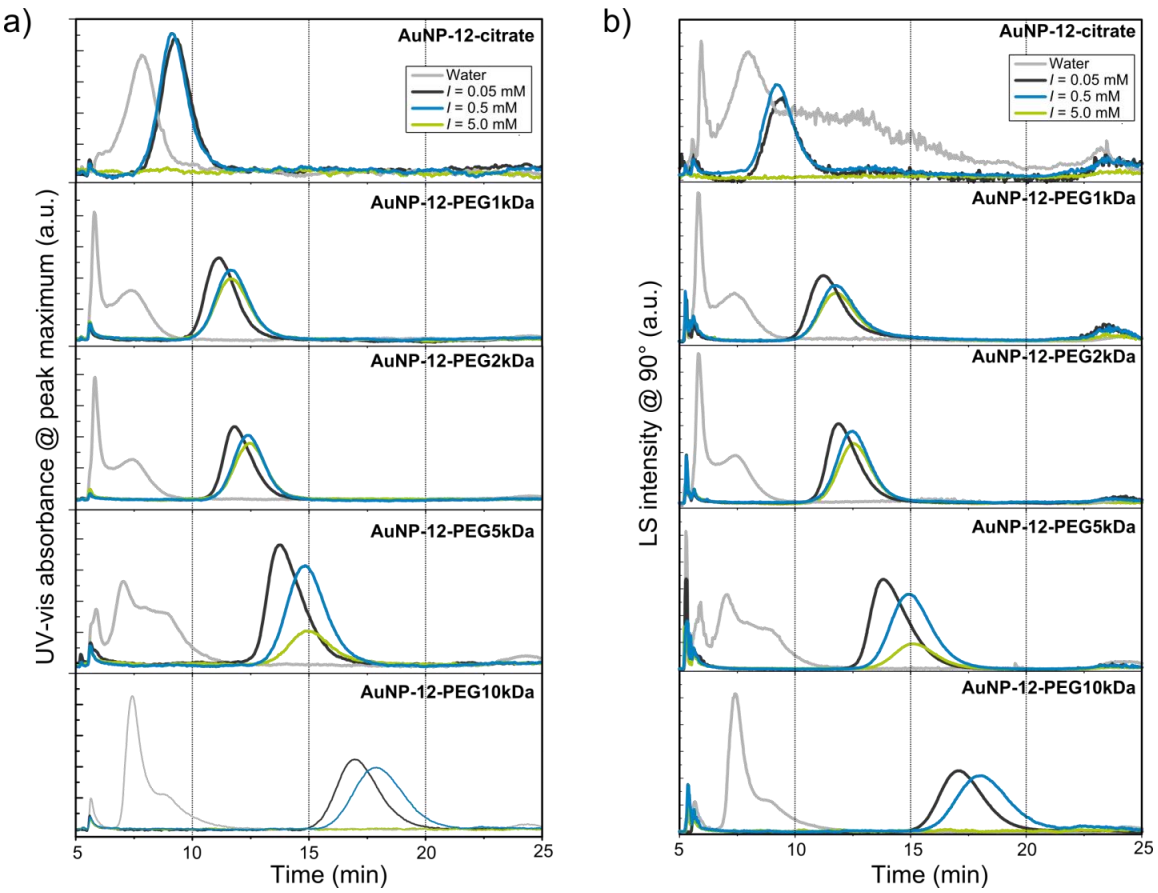

Figure 3.13: AF4 fractograms of citrate- and PEG-stabilized AuNPs at different ionic strengths using a) UV-Vis detection at peak maximum and b) LS detection at 90° [108].

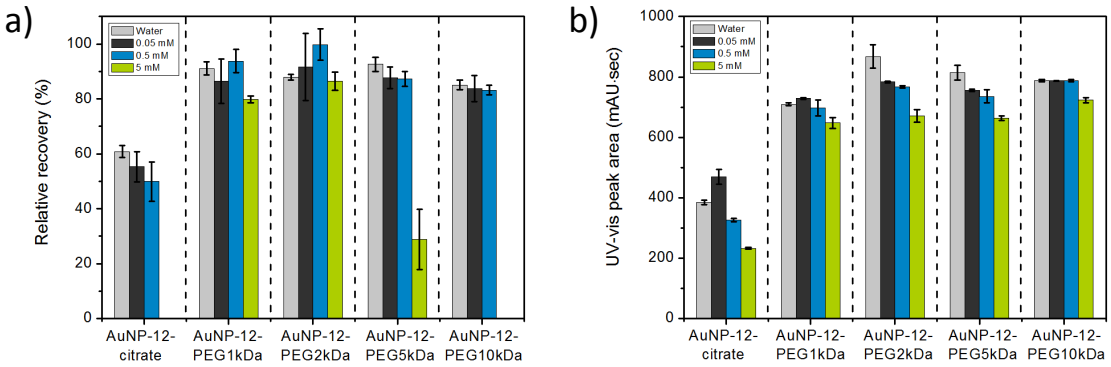

Figure 3.14: Relative AuNP recoveries after (a) fractionation and (b) peak areas of particle elution through PEEK tubing at different ionic strengths (NH_4NO_3 electrolyte) [108].

PEGylated AuNPs showed similar behavior with retention time shifts up to an ionic strength of 0.5 mM. For PEG1kDa- and PEG2kDa-stabilized AuNPs, minor decreases of the signal intensities (UV-Vis and LS detection) were observed when increasing the ionic strength from 0.5 mM to 5 mM. Signal intensities of AuNP-12-PEG5kDa and AuNP-12-PEG10kDa particles were significantly reduced with complete loss of PEG10kDa-stabilized AuNPs at I = 5 mM. No agglomeration was observed for all tested AuNPs during AF4 characterization when adjusting the ionic strength.

Relative recoveries of citrate-stabilized AuNPs gradually decreased from 61 % (water) to 50 % (I = 0.5 mM) with increasing ionic strength (Figure 3.14, a). At I = 5 mM, complete particle loss was detected as indicated by the fractogram. Relative recoveries of PEGylated particles were significantly larger and varied from 83 % to 100 % for ionic strengths up to 0.5 mM. Increasing the ionic strength to 5 mM led to a minor decrease of the relative recoveries of 6 % and 5 % for PEG1kDa- and PEG2kDa-stabilized AuNPs, respectively. Large decreases of 58 % were observed for AuNP-12-PEG5kDa particles as well as complete particle loss of PEG10kDa-stabilized AuNPs. SEM images of the membrane adsorption test in flow are shown in Figure 3.15.

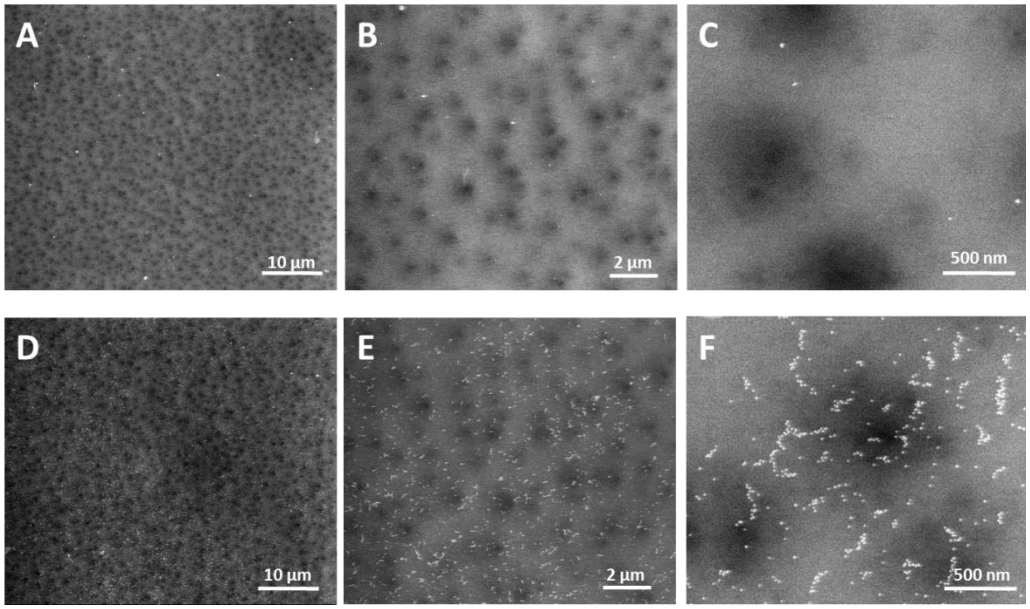

Figure 3.15: SEM images of membrane adsorption test in flow [108]. Membrane adsorption of AuNP-12-citrate (A-C) and AuNP-12-PEG5kDa (D-F) at I = 5 mM was tested.

In the case of citrate-stabilized AuNPs, only few particles were detected (Figure 3.15 A-C). Many AuNP-12-PEG5kDa NPs adsorbed on the ultrafiltration membrane (Figure 3.15 D-F). Similar observations were made when particle adsorption on the membrane was tested by drop-casting experiments (Figure 3.16 and Figure 3.17). Optical images of the ultrafiltration membranes after adsorption testing showed dark blue spots at ionic strengths above 25 mM for citrate-stabilized AuNPs (Figure 3.16, top). Agglomeration of citrate-stabilized particles was induced under these conditions leading to a settling of agglomerates on the membrane. In contrast, red spots were observed for PEG5kDa-stabilized AuNPs already at low ionic strengths (I = 1 mM) indicating that significant particle adsorption already occurred under these conditions (Figure 3.16, bottom). SEM images of the tested ultrafiltration membrane (I = 5 mM) confirmed a higher particle number density of PEG5kDa-stabilized AuNPs adsorbed on the ultrafiltration membrane (Figure 3.17).

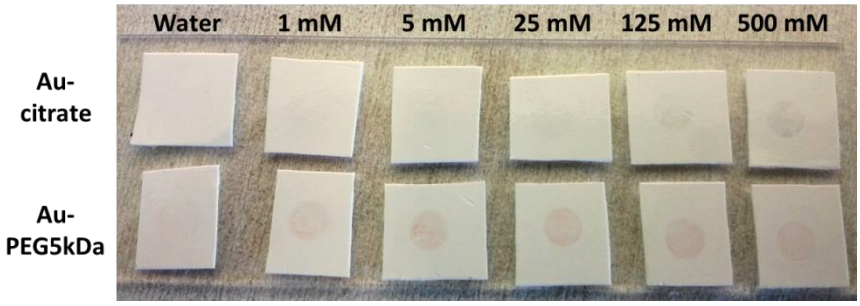

Figure 3.16: Optical images of particles adsorbed drop-casting experiments using AuNP-12-citrate and AuNP-12-PEG5kDa AuNPs [108]. Agglomeration and adsorption of citrate-stabilized AuNPs at ionic strengths above 25 mM was observed. Adsorption of AuNP-12-PEG5kDa was already observed at an ionic strength of 1 mM as shown by the red spots.

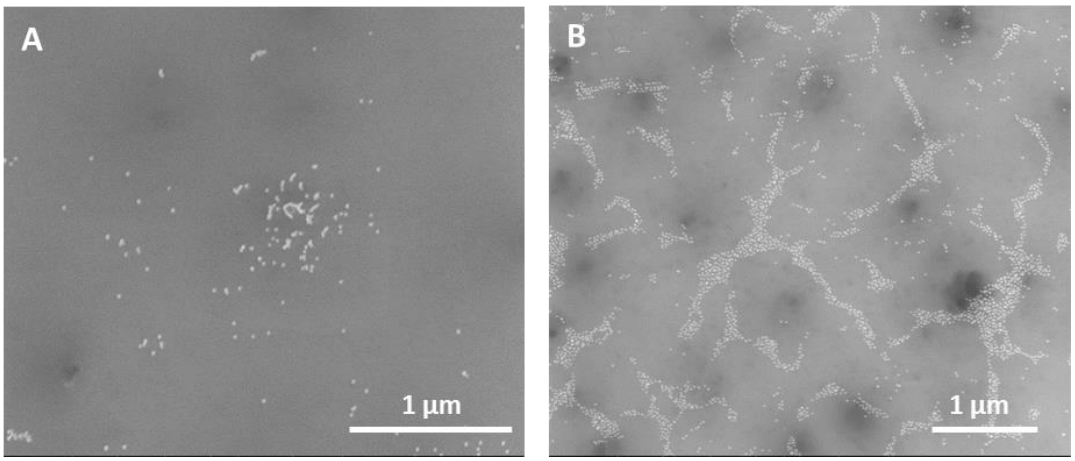

Figure 3.17: SEM images of membrane adsorption test at I = 5 mM (drop-casting) [108]. Few adsorbed AuNP-12-citrate NPs were detected (A) whereas many AuNP-12-PEG5kDa particles adsorbed on the membrane.

Non-membrane-related losses

Evaluating the peak areas of the reference runs revealed increasing system-based losses with increasing ionic strength except for AuNP-12-citrate and AuNP-12-PEG1kDa particles (Figure 3.14 b). For these particles, the highest peak areas were detected at the lowest ionic strength tested (0.05 mM). Peak areas of the remaining particles dropped by 23 % (AuNP-12-PEG2kDa), 19 % (AuNP-12-PEG5kDa), and 9 % (AuNP-12-PEG10kDa).

The absolute system-based losses of citrate- and PEG5kDa-stabilized AuNPs were determined by ICP-OES analysis. Bypassing different parts of the setup (see Figure 3.6) allowed the identification of specific loss places. The results are presented in Figure 3.18.

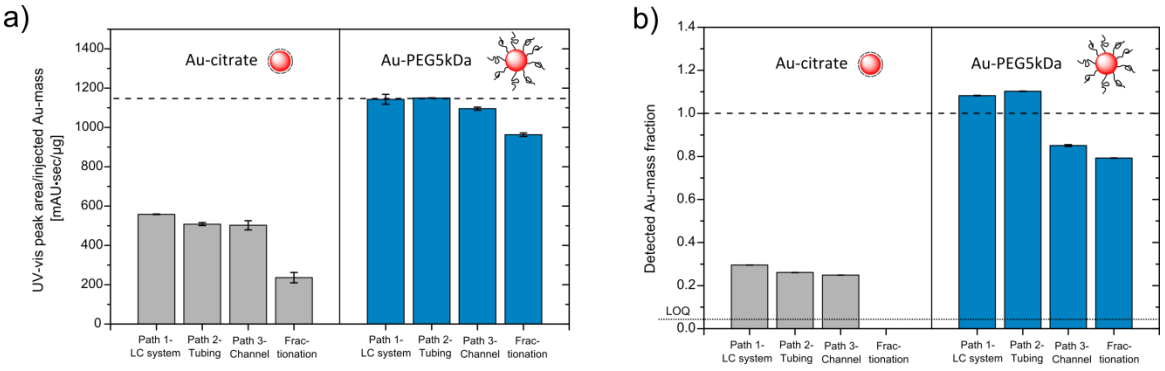

Figure 3.18: a) Normalized UV-Vis peak areas and b) detected Au mass fractions of citrate- and PEG5kDa-stabilized AuNPs eluted through PEEK tubing using different flow paths [108].

Elementary analysis revealed high losses of citrate-stabilized AuNPs almost independent of the elution path (Figure 3.18 b, path 1-3). No particles were detected in the collected AuNPs fraction when a cross-flow was applied (fractionation). AuNP-12-PEG5kDa particles showed no losses when eluted through elution paths 1 and 2. Elution through the separation channel without (path 3) and with (fractionation) the application of a cross-flow led to minor particle losses of 15 % and 21 %, respectively.

The comparison of the online UV-Vis peak areas and the offline ICP-OES results indicates losses that occurred before and after the UV-Vis detector. Since no losses were determined for AuNP-12-PEG5kDa on elution path 1, the peak area was set as a reference. For citrate-stabilized AuNPs, the evaluation revealed losses of 51−56% before and 15-18 % after reaching the UV detector. In the case of PEG5kDa-stabilized AuNPs, smaller losses of only 4 % (elution path 3) and 16 % (fractionation) before, and 11% (elution path 3) and 5% (fractionation) after reaching the UV detector were observed.

3.3.3. Discussion

Ligands with strong affinity to the AuNP surface prevent particle losses by decreasing particle degradation during AF4 characterization. The comparison of citrate-, BSP-, and LA-modified AuNPs indicate a correlation between the binding affinity of the ligand and NP losses during fractionation. Citrate-stabilized particles suffered large system-based and membrane-related losses with a strong ionic strength dependency. BSP as ligand with a more covalently bound character increased membrane-related recoveries as well as the colloidal stability, and no agglomeration was detected. A clear influence of the ionic strength on the reference runs indicated system-based losses through particle adsorption. The highest AuNP recoveries were detected when LA was used as modifying agent. A

dependence of the ionic strength was also observed but was less pronounced. At ionic strengths above 3 mM, system-based and membrane-based relative losses increased for LA-modified AuNPs due to adsorption but without any agglomeration.

The colloidal stability testing in batch already indicated differences between the modified particles, which were attributed to the different binding affinities of the stabilizing ligands. The affinity of the ligands increases in the order of citrate < BSP < LA [100]. The different colloidal stabilities may be linked not only to the agglomeration behavior in batch and during AF4 but also to adsorption. The loss of stabilizing ligand during AF4 fractionation may cause a lowering of repulsive particle-surface interactions, which would favor adsorption on the ultrafiltration membrane and also internal surfaces. I believe that the degradation of the stabilizing ligand shell underlies the main loss mechanism for AuNPs stabilized with weakly adsorbed ligands. A similar explanation for the adsorptive loss of citrate-stabilized AuNPs was proposed by Mudalige *et al.* [26].

PEGylated AuNPs suffer losses by bridging adsorption. The most striking result to emerge from the data is that AuNPs stabilized with large PEG chains showed strong membrane adsorption at higher ionic strengths. The higher losses of PEGylated particles at higher ionic strengths were exclusively due to adsorption on the separation membrane and not on internal surfaces. The higher adsorption rate on the membrane than on other internal surfaces can be caused by mainly two factors. First, the different surface properties of the surface materials (PEEK tubing vs. PES membrane) cause different interactions most likely due to charge effects. Second, the residence time of the particles at the surfaces is significantly different. Particles are rapidly eluted through the PEEK tubing, whereas the contact on the membrane is significantly larger during fractionation. The second factor is likely contributing in a larger extend since particle losses due to adsorption were also found on other materials such as polypropylene and polystyrene cuvettes as shown at the colloidal stability measurements in chapter 2.3.

The bridging adsorption mechanism strongly depends on the ionic strength (Figure 3.19). At low ionic strengths, electrostatic repulsion prevents adsorption of the charged PEGylated particles. Increasing the ionic strength will lead to decreasing screening lengths and an approach of the particles towards the membrane until the ligand shell can get into contact with the membrane (Figure 3.19, bottom). The PEG-membrane interactions will then determine whether "bridging adsorption" occurs. Because of the increasing

chain length and higher chain mobility, longer PEG chains can bridge a larger gap between particles and the membrane.

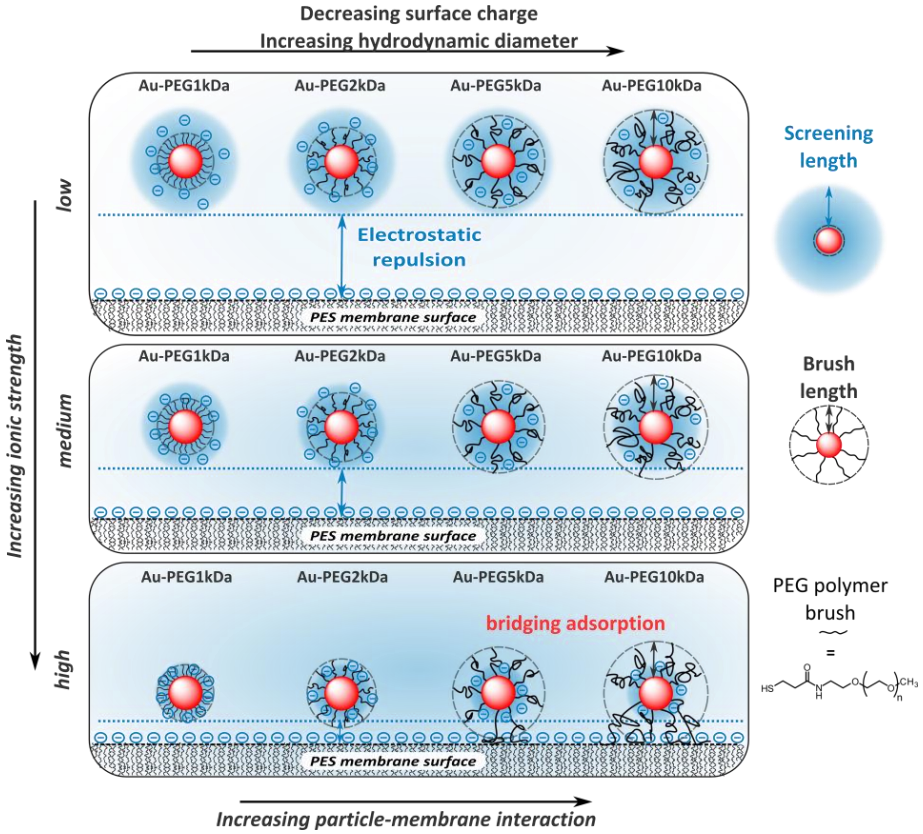

Figure 3.19: Proposed particle loss mechanism of PEGylated AuNPs. Increasing ionic strength will lead to increasing particle losses of particles stabilized with large polymer shells due to bridging adsorption [108].

Similar bridging mechanisms have been previously used to explain adsorption of polymerically stabilized particles on surfaces. The effect of PEG size of ferritin particles and the ionic strength on the particle adsorption on silica surfaces was reported by Tsukamoto *et al.* [134]. Increased adsorption of polymer-coated silver NPs on uncoated silica surfaces over silver nanoparticles was reported by Lin *et al.* [43]. The authors explain this phenomenon by a bridging mechanism of the polymer shell, which connects the particles with the surface.

3.4. Spiking of river water

Asymmetrical flow-field flow fractionation can fractionate samples with complex matrices, such as natural inorganic or organic nanoparticles extracted from river water or soils [7]. The particle composition and its surface properties determine the influence of other sample contents on the colloidal properties. Several studies have shown that natural or-

ganic matter readily adsorb on nanoparticles [36,53,59,135]. The adsorption of natural organic matter depends strongly on the stabilizing ligand [136,137,138]. Reference or tracer nanoparticles with different surface modifications have be tested in the respective matrices in order to identify a suitable particles system. As a proof-of-concept, surface-modified AuNPs were used as tracer nanoparticles to spike river water, which was analyzed using AF4. There are two primary aims of this study: 1. To investigate the stability of the modified AuNPs in a complex matrix. 2. To ascertain AF4 fractionation behavior of the AuNPs dispersed in a complex matrix. River water was chosen since particle containing river water samples have already been investigated using AF4 [7]. Sample preparation is usually straight forward since only the separation of large substances via centrifugation or filtration is necessary [139].

3.4.1. Experimental procedures

Gold nanoparticles with a mean core diameter of 17 nm stabilized by citrate, BSP, or PEG2kDa-COOH were chosen for this study. The synthesis and modification of AuNP-17-citrate, AuNP-17-BSP, and AuNP-17-PEG2kDa-COOH particles was presented in section 2.2.2. A river water sample was taken from the Saar river on March 22nd at the "Daarler" bridge in Saarbrücken, Germany. The sample was stored in the dark (4 °C). A conductivity of 1167 µS/cm (equivalent to an ionic strength of ~19 mM, calculated according to DIN 38404-C10R3) and a pH of 8.14 were determined. The AuNPs were concentrated by centrifugation of 1.5 mL AuNP and dispersion and redispersion in 300 µL ultrapure water (β(Au) = 120-140 mg/L). Then, 50 µL of the particles were mixed with 950 µL river water, filtered using a 0.2 µm and a 5.0 µm syringe filter (RC). Particles were incubated for 1 hour before characterization.

Colloidal analysis was performed using UV-Vis absorption and AF4. UV-Vis spectra were recorded using an Infinite M200 PRO multimode microplate reader (Tecan Trading AG, Switzerland). AF4 fractionation was performed using a precut 10 kDa PES ultrafiltration membrane and a 0.5 mM $NaNO_3$ as carrier solution. Flow method A (Table 5.2) was modified by using a focus flow of 2 mL/min and a decreasing cross-flow (2 mL/min to 0 mL/min in 15 minutes) (Figure 3.20).

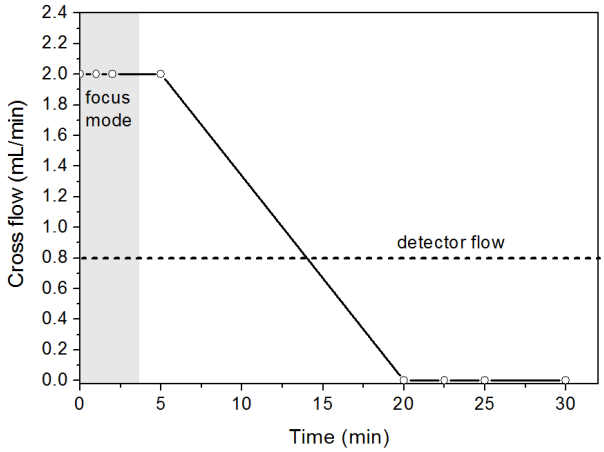

Figure 3.20: Applied flow methods for AF4 characterization of AuNPs dispersed in river water.

3.4.2. Results

Citrate- and BSP-stabilized AuNPs showed a broad shoulder peak with a maximum absorption of around 690 nm indicating nanoparticle agglomeration (Figure 3.21). The UV-Vis spectra of AuNP-17-PEG2kDa-COOH NPs did not show any differences for the tested media. The river water sample with the dispersed PEG2kDa-COOH-stabilized AuNPs was analyzed by AF4. The fractograms are shown in Figure 3.22. All fractograms displayed a void peak and one main sample peak. AF4 fractogram of the nanoparticles dispersed in water showed the highest peak. In the case of the spiked river water samples, smaller peaks were detected. Retention times were identical for all tested samples. No signs of agglomeration were observed. AF4 characterization of the pure river water without added NPs did not result in any distinct peak (Figure 3.22, blue trace).

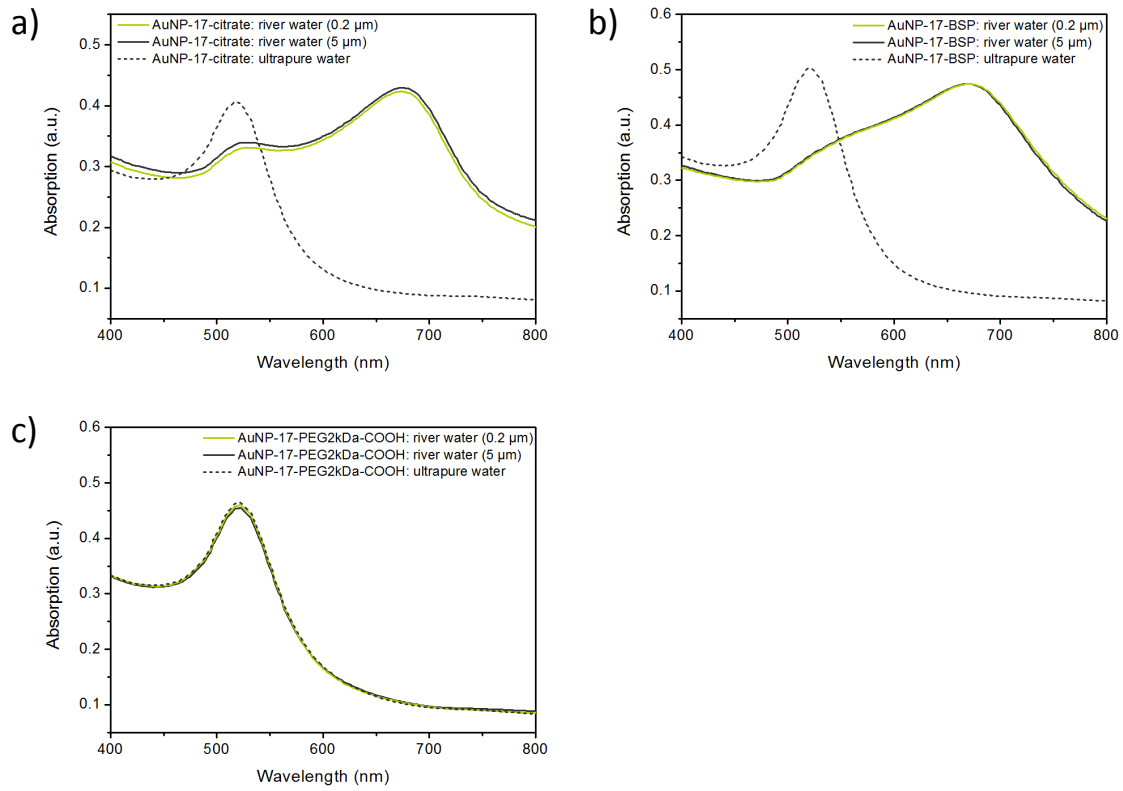

Figure 3.21: UV-Vis spectra of (a) AuNP-17-citrate, (b) AuNP-17-BSP, and (c) AuNP-17-PEG2kDa-COOH NPs. AuNPs were dispersed in ultrapure water (dotted line), 0.2 µm filtered (green) or 4.5 µm filtered (black) river water. A red shift of the LSPR for citrate-and BSP-stabilized AuNPs in river water indicate particle agglomeration.

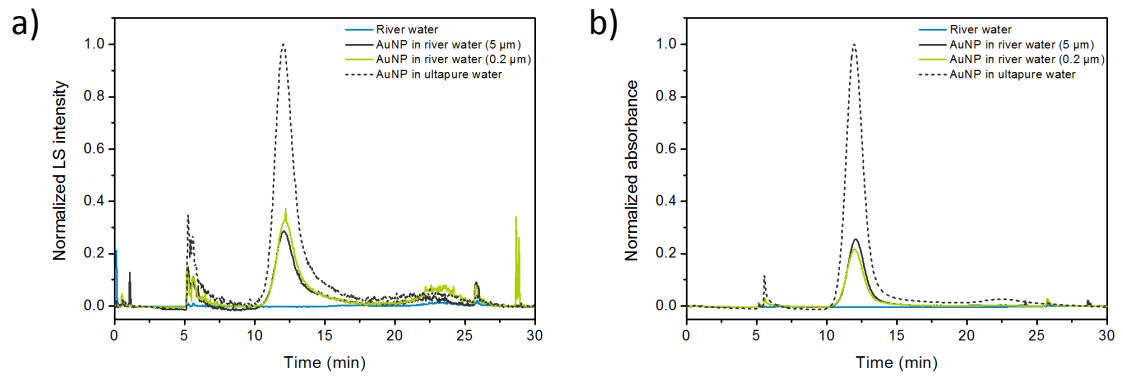

Figure 3.22: AF4 fractograms of river water (blue) and AuNP-17-PEG2kDa-COOH NPs dispersed in ultrapure water (dotted), 0.2 µm filtered (green) or 5 µm filtered (black) river water. Light scattering intensity (a) and UV-Vis absorbance @518 nm (b) were normalized to the highest peak.

The integrated peak areas of the reference run (no cross-flow applied) and fractionation measurements (cross-flow applied) are shown in Figure 3.23.

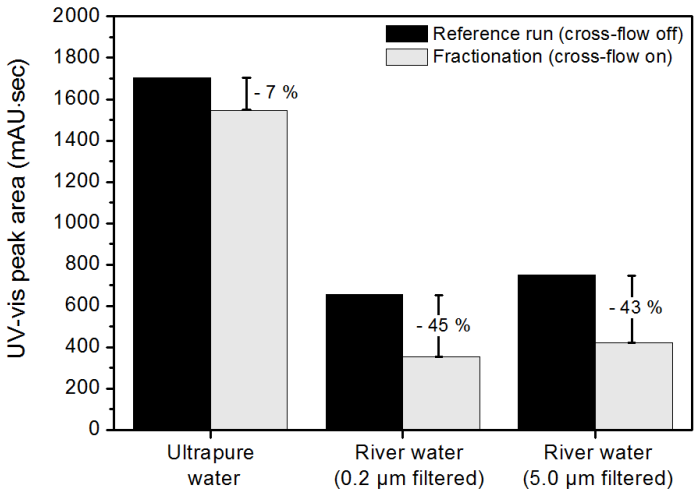

Figure 3.23: Integrated UV-Vis peak areas of AuNP-17-PEG2kDa-COOH dispersed in different media. Black bars: Reference run without the application of a cross-flow. Grey bars: Fractionation (cross-flow applied).

Compared to the AuNPs dispersed in ultrapure water (relative recovery of 93 %), decreasing signals were detected for the river water samples. In the reference runs, 60 % less particles and relative losses of 43-45 % due to fractionation (membrane-related) were detected for the river water samples.

3.4.3. Discussion

Successful sample spiking of river water depends on the stabilizing ligand. The results from batch UV-Vis measurements confirmed that the particle surface properties is essential for successful sample spiking. The electrostatically stabilized citrate- and BSP-modified AuNPs agglomerated when mixed with the river water. In contrast, the more sterically stabilized AuNP-17-PEG2kDa-COOH particles were not affected by the river water matrix. The agglomeration can be caused by (i) dissolved salts in the river water which lowered the repulsive electrostatic interactions, (ii) dissolved species, such as natural organic matter (NOM), adsorbing on the nanoparticle surface [102] or (iii) a combination of both (adsorption of dissolved species and subsequent flocculation) [136]. The determined ionic strength (~ 19 mM) was below the critical ionic strength that causes agglomeration for citrate- and BSP-stabilized AuNPs (see chapter 2.3). A combination of adsorption of dissolved species onto the electrostatically stabilized particles and subsequent flocculation caused by the presence of divalent cations may be the reason for the observed agglomeration [136]. The PEGylated particles were sufficiently stabilized at

higher ionic strength and less affected by NOM adsorption [140]. Therefore, PEGylated AuNPs represent a suitable reference system for sample spiking.

River water samples spiked with PEGylated AuNPs suffered significant losses during AF4. The AF4 measurements showed that the applied AuNP-17-PEG2kDa-COOH tracer particles were successfully recovered. However, substantial particle losses were observed during the reference runs as well as the fractionation runs. Since no signs of agglomeration were observed (retention time shift, LS signals), particle losses have to be caused by adsorption on surfaces. The increased ionic strength in the river water likely causes bridging adsorption to occur. There are several possible adsorption places possible, namely (i) the sample vial, (ii) internal surfaces of the analyzing system, and (iii) the separation membrane.

The lower signals of the reference runs (no cross-flow) can be explained by adsorption on the sample vial and internal surfaces. Although the UV-Vis spectra (Figure 3.21 c) showed that the particles had initially identical concentrations, particle adsorption inside the sample vial over time cannot completely be excluded. Electron microscopy images and the previous reported results already showed that substantial losses can also occur due to adsorption on internal surfaces (see also Appendix C).

During fractionation (cross-flow on), a higher amount of AuNPs dispersed in river water were adsorbed on the membrane (Figure 3.23). It can be concluded that the river water matrix has a severe effect on the membrane adsorption of the PEGylated AuNPs. A possible explanation is increased adsorption during the focusing step, in which not only the particles but also the matrix components are driven to the membrane. Although small matrix components can pass the membrane, an effect on the particle-membrane interactions can still occur.

3.5. Summary

This investigation of nanoparticle losses of different nanoparticles has shown that the particle surface chemistry is the central property influencing the loss mechanisms.

The comparison of silica and citrate-stabilized gold nanoparticles has revealed lower particle losses for silica NPs. AF4 fractionation at different ionic strengths showed that silica nanoparticles are less prone to adsorb on internal surfaces. At higher ionic strength moderate particle losses at the separation membrane were detected. Agglomeration of the gold

(citrate-stabilized) and silica nanoparticles was observed at lower ionic strengths (above 5 mM) than in batch measurements (above 25 mM). This confirms that the AF4 conditions reduce particle stability affecting analyses results.

In chapter 3.3, ligand-dependent particle losses during AF4 were determined by comparison of surface-modified AuNPs. This study has found that the type and affinity of the ligand determines the loss mechanisms. Loosely bound citrate-stabilized AuNPs showed overall lower recoveries caused by losses due to membrane adsorption and on internal surfaces. The high losses are likely induced by particle degradation and loss of the stabilizing ligands under AF4 conditions. Surface modification of the ligands with BSP, LA, and BSA led to mainly electrostatically stabilized AuNPs, which showed increasing recovery rates. The best results were obtained with LA, probably because of its high affinity to the gold surface. The strongly binding LA prevents particle degradation enabling high colloidal stability. A major finding was the adsorption of PEGylated AuNPs on the membrane surface depending on ligand length and ionic strength. Larger PEG shells adsorb via a bridging adsorption mechanism. At low ionic strength levels, excellent relative recoveries were observed.

Finally, the spiking of river water was performed in order to test the suitability and AF4 performance of modified AuNPs in a complex matrix. Citrate- and BSP-stabilized AuNPs (core diameter 17 nm) could not be redispersed in river water whereas PEG2kDa-COOH-stabilized AuNPs were not affected. AF4 fractionation of the spiked river water samples revealed a significant matrix effect, increasing particle losses due to adsorption on internal surfaces and the separation membrane.

4. Conclusion and Outlook

4.1. Conclusions

In this thesis, I developed nanoparticles which can be used as reference nanoparticles during flow field-flow fractionation and identified particle loss mechanisms of different stabilized nanoparticles during AF4 characterization. The performance of gold and silica reference nanoparticles was tested by investigating the different requirements stated in the introduction. Each nanoparticle system has drawbacks that can be overcome by the various strategies investigated in this thesis.

The foundation of the systematic approach for the development of suitable reference particles was the availability of nanoparticles with a *narrow size distribution and different properties (size, surface chemistry, charge)*. I achieved this goal by synthesizing well-defined nanoparticles using reliable synthesis procedures. By comparing different sizing techniques (batch DLS and TEM) with online DLS during AF4 measurements and AF4 theory, I showed that the particles can successfully be used for channel calibration, a key requirement to obtain particle size distributions in AF4. Surface modification of gold nanoparticles with diverse ligand classes resulted in nanoparticles with different stabilization mechanisms (electrostatically, sterically, and electrosterically), agglomeration and adsorption properties.

In the next step, *reliable particle identification* with standard setups and detectors was achieved by labeling silica nanoparticles with fluorescence dye or metal ions. Differentiation between fluorescently labeled and unlabeled silica NPs was successfully achieved using online fluorescence detection during AF4 measurements. I developed a one-pot synthesis of metal-labeled silica nanoparticles with enhanced identification due to their adaptable composition (metal/Si ratio). The optically already characteristic gold nanoparticles were further labeled by coating with silver/gold shells with varying compositions. Silver incorporation into the surrounding shell led to specific optical absorption as well as a different elemental composition of the nanoparticles. Surface modification revealed that the silver containing shell degraded depending on the attached ligand, especially during field-flow fractionation. This study proved that the applied nanoparticles are well suited as reference particles to investigate NP losses.

The particle loss mechanisms during field-flow fractionation were investigated by evaluation of particle losses in dependence of the stabilizing ligand. I found that minor losses of silica nanoparticles were detected at moderate ionic strengths whereas citrate- (electrostatically) stabilized gold nanoparticles were prone to losses throughout the whole study. It was shown that these losses were attributed to adsorption on the membrane and inside the analyzing system at already low ionic strengths (~1 mM). In addition, particle agglomeration was observed for citrate-stabilized gold nanoparticles at higher ionic strengths. Modification with ligands that strongly bind to the gold surface resulted in decreased particle losses. A major finding was high losses of highly stable PEGylated AuNPs at low ionic strengths. I identified the governing loss mechanism of sterically stabilized NPS to be a polymer shell mediated bridging adsorption. This adsorption mechanism was shown to depend on the polymer thickness and the ionic strength. Taken together, these findings suggest that particle losses are enhanced by particle degradation due to weakly adsorbed ligands or mediated by ligand-dependent interactions. The study of particle losses contributed to the design of NPs with minimized losses.

River water spiking with differently stabilized gold nanoparticles revealed that PEGylation was suitable to inhibit agglomeration of particles, allowing successful dispersion. The AF4 characterization revealed a negative effect of the river water matrix on particle recoveries but did not show an effect on particle sizing. This proof-of-concept study, although limited by the lack of a comprehensive method optimization, revealed that directed particle modification is a valuable key for the fabrication of reference particles.

The dissertation succeeded in providing a general insight into particle loss mechanisms during FFF characterization, their governing factors, and strategies to overcome them. It reveals that losses depend on the type of ligand and strongly depend on the eluent composition. A deliberate design of reference particles should always include consideration of the sample matrix elements and FFF method parameters.

4.2. Outlook

The development of an optimized FFF methodology requires further assessment of the effects of instrumental parameters, such as membrane and internal surface coatings, on the particle losses and stabilities in FFF characterization. I believe that there are two major concepts for future developments towards an optimized FFF approach.

First, FFF instruments may be optimized by combining suitable materials and FFF parameters for the analysis of a specific type of ENP. This is of interest when the particle properties, such as the colloidal stability or surface charges, are known and do not differ significantly for each sample. These instruments are fitted for use in quality assurance or regulatory institutions which often only monitor a specific number of analytes.

The second concept would allow a broad range of NPs to be tested and includes a pre-evaluation of sample properties and an adapted choice of FFF parameters. If a given set of properties are known, the FFF setup may be adjusted prior to analysis by using specialized carrier solutions, membranes and in-situ modification. For example, if sterically stabilized particles are analyzed, FFF modification with a polymer that minimizes particle-membrane interactions may be performed in combination with a suitable membrane and carrier liquid. A database established by a systematic investigation of FFF parameters and different reference particles as presented in this thesis would greatly facilitate FFF optimization.

Concerning the development of metal-labeled silica nanoparticles, more research is needed to better understand their formation and the effect of the metal ion. Increasing the metal-content and developing multi-element labeling with a broad set of elements would be a great benefit. The application of such “fingerprint” particles for sample spiking can be expanded to additional analytical techniques that are able to determine the elemental composition.

Another possible area of future research would be to investigate the effect of fractionation conditions on particle degradation in more detail. As shown multiple times in this thesis, there is a huge difference of particle stabilities in batch and during fractionation that are yet knot fully understood. Monitoring the leaching of isotopically labeled ligands and atoms during different fractionation steps would allow a more comprehensive understanding of such degradation processes.

5. Materials and instrumentation

5.1. Chemicals

All aqueous samples and eluents were prepared using ultrapure water (>18 MΩ) (Milli-Q water purification system type Advantage A10 and ELIX 20, Millipore Corp., USA). Chloroauric acid was prepared according to standard synthesis procedure [141, pp. 1057-1058]. The following chemicals were used as purchased without further purification.

Table 5.1: List of chemicals used in this study.

Compound	Purity	Abbreviation	Supplier
Ammonium nitrate	p.a.	--	Sigma-Aldrich
Sodium nitrate	p.a.	--	Merck
Silver nitrate	99.9 %	--	ABCR
α-Lipoic acid	98 %	LA	Sigma-Aldrich
Albumin, monomer bovine	≥ 97 %	BSA	Sigma-Aldrich
Polystyrene sulfonate (M_w ~ 70,000)	--	PSS	Sigma-Aldrich
Bis(p-sulfonatophenyl)phenylphosphine dihydrate dipotassium salt	97 %	BSP	Sigma-Aldrich
Trisodium citrate dihydrate	p.a.	--	Merck
Tetraetyhlorthosilicate	--	TEOS	Sigma-Aldrich
N-(trimethoxysilylpropyl) ethylenediaminetriacetic acid	45 %	TMS-EDTA	ABCR
Copper(II) chloride dihydrate	--	--	Riedel de Hän
Gadolinium(III) chloride hexahydrate	--	--	Sigma-Adlrich
Europium(III) chloride hexahydrate	99.99 %	--	Sigma-Aldrich
Cobalt(II) chloride hexahydrate	--	--	Fluka
Sodium dodecyl sulfate	≥ 99%	SDS	Sigma-Aldrich
poly(ethylene glycol) methyl ether thiol (average Mn = 1.000)	--	PEG1kDa	Sigma-Aldrich
O-(2-mercaptoethyl)-O-methylpolyethylene glycol (average Mn = 2.000, 5.000, 10.000)	--	PEG2kDa PEG5kDa PEG10kDa	Sigma-Aldrich

5.2. Instrumentation

Flow field-flow fractionation was carried out on a Wyatt Eclipse DUALTEC system (Wyatt Technology Europe, Dernbach, Germany) coupled to an Agilent Technologies high-performance liquid chromatography system (Agilent Technologies 1260 infinity series, Waldbronn, Germany). The different components and the flow path are presented in Figure 3.1. A quaternary pump with integrated degassing system (G1311B) supplied the liquid flow. The aqueous carrier solutions used during measurement sequences were prepared on-line by adjusting the amount of the respective solvents. All samples were injected using an autosampler with a stainless steel injection needle and a 100 µL sample loop (G1329B). The separation channel was connected to different detectors. Optical absorption was monitored using a variable wavelength ultraviolet/visible detector (G1314F) or a Diode Array Detector (G1315C). The detection wavelengths were set according to the maximum absorption of the respective sample. For examples, AuNPs absorption was detected at the surface plasmon resonance absorption maximum of the particle analyzed. NPs without distinctive UV-Vis absorption such as unlabeled silica nanoparticles were analyzed using a detection wavelength of 280 nm. A fluorescence detector (G1321B) was used for the detection of Rhodamine-labeled SiO_2 NPs (λ_{exc} = 553 nm, λ_{em} = 573 nm). Fractions from AF4 measurements were collected with an Analytical-Scale Fraction Collector (G1364C).

Online light scattering was conducted by a DAWN HELEOS II light scattering instrument (Wyatt Technology, Dernbach, Germany) with internal QELS (dynamic light scattering) registered by a detector at an angle of 149° (WyattQELS, Wyatt Technology, Dernbach, Germany; laser wavelength = 658 nm).

AF4 measurements were performed on a short channel (inlet-to-outlet length 17.4 cm) and a 350 µm Mylar spacer. Ultrafiltration membranes with a mean cut-off of 10 kDa (PES or RC) were used. PES membranes were purchased from Wyatt (Wyatt Technology, Dernbach, Germany) or Microdyn-Nadir (PES, Nadir® UP010, Microdyn-Nadir GmbH, Wiesbaden, Germany) and if necessary cut to fit prior to use. RC membranes were purchased from Wyatt. The membrane was rinsed with ultrapure water and further conditioned for 1 h with the corresponding eluent. In a typical measurement sequence, changing the eluent composition was accompanied by a blank run injecting ultrapure water in order to equilibrate the system.

Collected QELS data were analyzed for hydrodynamic diameter **(online DLS, $D_{AF4\text{-}DLS}$)** using the Astra V software (Cumulant fit, Version 5.3.4.20, Wyatt Technology). UV-Vis peak areas were integrated using Agilent Chemstation Version B.04.03 (Agilent Technologies, Waldbronn, Germany).

The presented hydrodynamic diameters were determined by calculating the mean D_h out of each determined hydrodynamic diameter for each slice. The standard deviation is given as a measure of the polydispersity.

Different flow methods were used depending on the respective sample properties, such as size and size distribution. In general, the method consisted of four different steps:

1. Elution including a one minute elution and focus step prior to the actual focusing procedure for baseline and flow rate stabilization.
2. Sample injection and focusing for at least 3 minutes (Focus + Inject).
3. Sample elution using a cross-flow field.
4. Elution and inject step at zero force field at the end of the measurement for flushing the whole system including the sampler prior to the next injection.

The following AF4 methods were used unless otherwise stated:

Table 5.2: Flow method A.

Start time (min)	End time (min)	Duration (min)	Mode	Cross-flow start (mL/min)	Cross-flow end (mL/min)
0.00	1.00	1.00	Elution	0.80	0.80
1.00	2.00	1.00	Focus	0.80	0.80
2.00	5.00	3.00	Focus + Inject	0.80	0.80
5.00	20.00	15.00[a]	Elution	0.80	0.80
20.00	22.50	2.50	Elution	0.80	0.00
22.50	25.00	2.50	Elution	0.00	0.00
25.00	30.00	5.00	Elution + Inject	0.00	0.00

[a]Duration was extended for larger NPs as stated in the respective section.

Table 5.3: Flow method B used for the characterization of unlabeled silica nanoparticles. Detector flow was set to 0.8 mL/min.

Start time (min)	End time (min)	Duration (min)	Mode	Cross-flow start (mL/min)	Cross-flow end (mL/min)
0.00	0.30	0.30	Elution	0.00	0.00
0.30	2.30	2.00	Elution	1.00[a]	1.00[a]
2.30	3.30	1.00	Focus	1.00[a]	1.00[a]
3.30	5.30	2.00	Focus + Inject	1.00[a]	1.00[a]
5.30	6.30	1.00	Focus	1.00[a]	1.00[a]
6.30	31.30	25.00	Elution	1.00[a]	0.00
31.30	36.30	5.00	Elution + Inject	0.00	0.00

[a]Silica NPs with mean core diameter < 20 nm were fractionated using a cross-flow of 1.50 mL/min.

Table 5.4: Flow method C used for the characterization of citrate-stabilized AuNPs (AuNP-79-citrate). Detector flow was set to 0.8 mL/min.

Start time (min)	End time (min)	Duration (min)	Mode	Cross-flow start (mL/min)	Cross-flow end (mL/min)
0.00	0.50	0.50	Elution	0.00	0.00
0.50	1.50	1.00	Focus	1.00	1.00
1.50	3.50	2.00	Focus + Inject	1.00	1.00
3.50	4.50	1.00	Focus	1.00	1.00
4.50	24.50	20.00	Elution	1.00	0.00
24.50	29.50	5.00	Elution + Inject	0.00	0.00

Table 5.5: Flow method D used for the characterization of Rhodamine-labeled silica nanoparticles.

Start time (min)	End time (min)	Duration (min)	Mode	Cross-flow start (mL/min)	Cross-flow end (mL/min)
0.00	1.00	1.00	Elution	1.00	1.00
1.00	2.00	1.00	Focus	1.00	1.00
2.00	7.00	5.00	Focus + Inject	1.00	1.00
7.00	37.00	30.00	Elution	1.00	0.00
37.00	39.50	2.50	Elution	0.00	0.00
39.50	44.50	5.00	Elution + Inject	0.00	0.00

Zeta potential of the NPs was measured using a Zetasizer Nano ZSP (Malvern Instruments Ltd., Herrenberg, Germany). The samples were measured in 1.0 mM ammonium nitrate solution (unless stated otherwise) to ensure a sufficient conductivity. Standard disposable zeta-cuvettes with electrodes were used at a temperature of 20 °C.

Dynamic light scattering (DLS) in batch (**batch DLS,** $D_{\text{Batch-DLS}}$) was used for the determination of the hydrodynamic diameters. Two different setups were used throughout this study.

Setup 1: Zetasizer Nano ZSP (Malvern Instruments Ltd., Herrenberg, Germany). The instrument was operated in 173° backscatter mode (laser wavelength = 633 nm). Samples were measured using disposable cuvettes with a volume of 3 mL at a temperature of 20 °C.

Setup 2: DynaPro PlateReader II (Wyatt Technologies, Dernbach, Germany). A total volume of 120 µL was measured at a temperature of 20 °C. The scattered light intensity was monitored at an angle of 158° (laser wavelength = 830 nm).

In both cases, the z-average diameter derived from cumulant analysis was used for the determination of the hydrodynamic diameter. The standard deviation or the polydispersity index (PDI) was given as an indication of polydispersity (see also ISO 13321:1996).

Transmission UV-Vis spectra were recorded on a Cary 300 UV-Visible spectrophotometer (Varian Inc, USA) using disposable UV cuvettes. Transmission UV-Vis spectra for testing the colloidal stability of AuNPs were performed using an Infinite M200 PRO multimode microplate reader (Tecan Trading AG, Switzerland). A background measurement using ultrapure water was subtracted in each case.

Fluorescence spectroscopy of Rhodamine-labeled silica nanoparticles was performed on a FluoroMax-3 (Jobin Yvon GmbH, Germany) using disposable cuvettes with a minimum volume of 3 mL. The excitation wavelength was set to 553 nm and the emission was monitored from 563 nm to 800 nm.

Transmission electron microscopy (TEM) was done on a JEM-2100(HR) or a JEM2011 TEM (Jeol, Germany). Particle solutions were drop- casted on a carbon-coated copper grid and dried at air. TEM images were analyzed using the FIJI software [142] in order to determine the particles' core diameter (D_{TEM}) and the size distribution.

Scanning electron microscopy (SEM) was performed on a Quanta 400 ESEM (FEI, Germany). Membrane analysis was performed by removing the membrane from the separation channel, washing with ultrapure water, and drying in air. SEM was then performed in low vacuum mode to limit charging. Image analysis was performed using the FIJI software [142].

Elemental analysis was performed using inductively coupled plasma optical emission spectrometry (ICP-OES) and inductively coupled plasma mass spectrometry (ICP-MS). ICP-OES was conducted with an Ultima2 ICP-OES (Horiba Jobin Yvon, Unterhaching, Germany).

Appendix

A. Synthesis optimization of silver-labeled gold nanoparticles

The optimized conditions for the synthesis of silver-labeled gold nanoparticles were determined by variation of different parameters:

- precursor/citrate ratio,
- thickness of shell growth,
- ligand modification.

Nanoparticle synthesis was carried out following the procedure described in chapter 2.2. Briefly, 5 mL AuNP seed (β(Au) = 44.6 mg/L, labeled here as AuNP-seeds) particles were diluted with 25 mL ultrapure water. Then, the respective amount of $HAuCl_4$ (25 mM) and $AgNO_3$ (25 mM) were simultaneously added with 1 mL of a sodium citrate solution with different concentrations. The solution was kept stirring under boiling for further 30 minutes. All particle dispersions were then filtered using a 0.2 µm PES syringe filter (Roth) after cooling down. No further purification was performed. Particle characterization included UV-Vis spectroscopy and DLS measurements (DLS setup 1).

First, the seeding growth of citrate-stabilized gold nanoparticles using different citrate/$HAuCl_4$ (cit/Au) and citrate/$AgNO_3$ in the range of 1 to 20 was tested to identify the optimal condition. The ratio was adjusted by varying the used citrate concentration while remaining the $HAuCl_4$ concentration constant. The corresponding UV-Vis spectra and size distributions are depicted in Figure A.1. Table A.1 and Table A.2 summarize the determined particle properties.

The determined particle sizes and UV-Vis absorption data suggest that there is an optimum for the citrate/$HAuCl_4$ ratio in the range of 5-10. A ratio of 5 seems to be sufficient for complete shell formation after which saturation occurs and a mean shell thickness of around 4.2 nm is remained which is close to the theoretical calculated value of 5 nm. In addition, the particles' polydispersity is in the same range as for the seed particles when using cit/Au ratios of 5-10.

Table A.1: Results of the colloidal characterization of AuNP seeding growth with varying citrate/$HAuCl_4$ ratios.

Citrate/ $HAuCl_4$	$D_{Batch\text{-}DLS}$ (nm)	PDI	LSPR band (nm)
AuNP-seeds	17.2	0.054	517
1	23.3	0.157	525
2.5	22.9	0.210	523
5	26.0	0.050	520
7.5	26.1	0.067	521
10	26.0	0.052	521
20	25.5	0.130	522
20 dropwise)	25.7	0.100	523

Table A.2: Results of the colloidal characterization of AuNP seeding growth with varying citrate/$AgNO_3$ ratios.

Citrate/ $AgNO_3$	$D_{Batch\text{-}DLS}$ (nm)	PDI	LSPR band (nm)
AuNP-seeds	17.2	0.054	517
1	27.4	0.057	396
2.5	27.1	0.023	392
5	26.8	0.040	391
7.5	27.4	0.092	391
10	26.9	0.064	391
20	26.3	0.045	392
20, dropwise	25.9	0.058	390

Lower cit/Au ratios led to smaller particle sizes with increasing polydispersity although the UV-Vis spectra look similar to the particles obtained with cit/Au ratios of 5-10. Increasing the cit/Au ratio to 20 led to slightly smaller particle sizes again and increased polydispersity. The lower absorption intensity of the LSPR band may be caused by enhanced agglomeration and precipitation or the formation of particle seeds. Dropwise addition of the reactants showed even less absorption intensities. A too high citrate concentration might also lead to increased seed formation and smaller particles sizes.

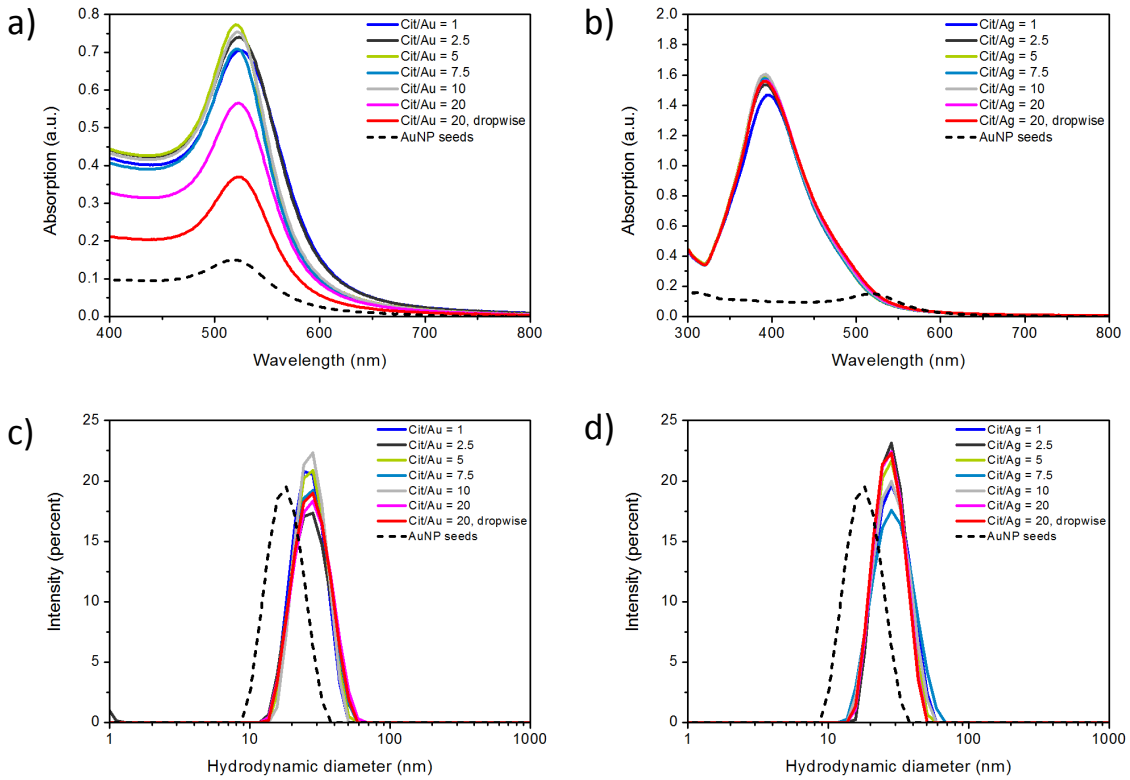

Figure A.1: UV-Vis spectra (a,b) and hydrodynamic size distribution (c,d) of AuNPs covered with gold and silver shells prepared by seeding growth with different citrate/precursor ratios.

In the case of seeding growth with $AgNO_3$ as precursor, the citrate/AgNO3 ratio has lees effect on the shell thickness (Table A.2). The determined mean particle sizes from DLS measurements and the polydispersity are similar for all tested ratios. Only at a citrate/$AgNO_3$ ratio of 20 and in the case of the dropwise addition, slightly smaller particle sizes were obtained. A clear shift of the LSPR band to lower wavelengths is detected where no significant differences between the different citrate/$AgNO_3$ ratios were observed (Figure A.1 b). Compared to the seeding growth with gold, an increment in the optical absorption is obvious. The Ag-coated AuNPs absorb nearly twice as much light compared to the larger AuNPs obtained via $HAuCl_4$ seeding growth. For further experiments, a citrate/precursor ratio of 10 was remained.

Next, the maximum gold and silver shell thickness which can be achieved in a single seeding growth step was examined by varying the added amount of $HAuCl_4$ and $AgNO_3$. The results are summarized in Table A.3. UV-Vis spectra and corresponding hydrodynamic size distributions are depicted in Figure A.2.

Table A.3: Results of the colloidal characterization of AuNP seeding growth with varying gold and silver shell thicknesses. The theoretical shell thickness was calculated assuming a complete conversion of added precursors, $HAuCl_4$ and $AgNO_3$

Batch	Theoretical shell thickness (nm)	$D_{Batch\text{-}DLS}$ (nm)	PDI	LSPR band (nm)
AuNP-seeds	--	17.2	0.054	517
Au@Au-3	3	18.8	0.044	519
Au@Au-6	6	22.6	0.055	520
Au@Au-9	9	24.4	0.051	521
Au@Au-12	12	26.7	0.045	521
Au@Au-15	15	29.2	0.04	521
Au@Au-18	18	24.5	0.053	521
Au@Au-21	21	20.1	0.057	520
Au@Ag-1	1	19.9	0.056	512
Au@Ag-2	2	20.9	0.079	505
Au@Ag-3	3	22.0	0.142	497
Au@Ag-4	4	22.8	0.078	383
Au@Ag-5	5	23.4	0.097	387
Au@Ag-6	6	23.8	0.186	391
Au@Ag-7	7	25.2	0.083	393

An increase of the hydrodynamic diameter was determined with increasing theoretical shell thicknesses of 15 nm. A decrease of the NP diameter with further increasing the $HAuCl_4$ amount was detected. Secondary seed formation is the likely reason for this observation. This can also be concluded from the UV-Vis spectra which show a slight red-shift of the LSPR from 517 nm for the seed AuNPs to 521 nm for theoretical shell thicknesses of 9-18 nm. Using the highest $HAuCl_4$ concentration corresponding to a theoretical shell thickness of 21 nm, the LSPR band maximum was detected at 520 nm. However, a low and unaltered PDI was detected for all batches. It was concluded that for the growth of a gold shell on AuNPs under the chosen conditions, a maximum shell thickness of 15 nm should not be exceeded in order to avoid secondary seed formation.

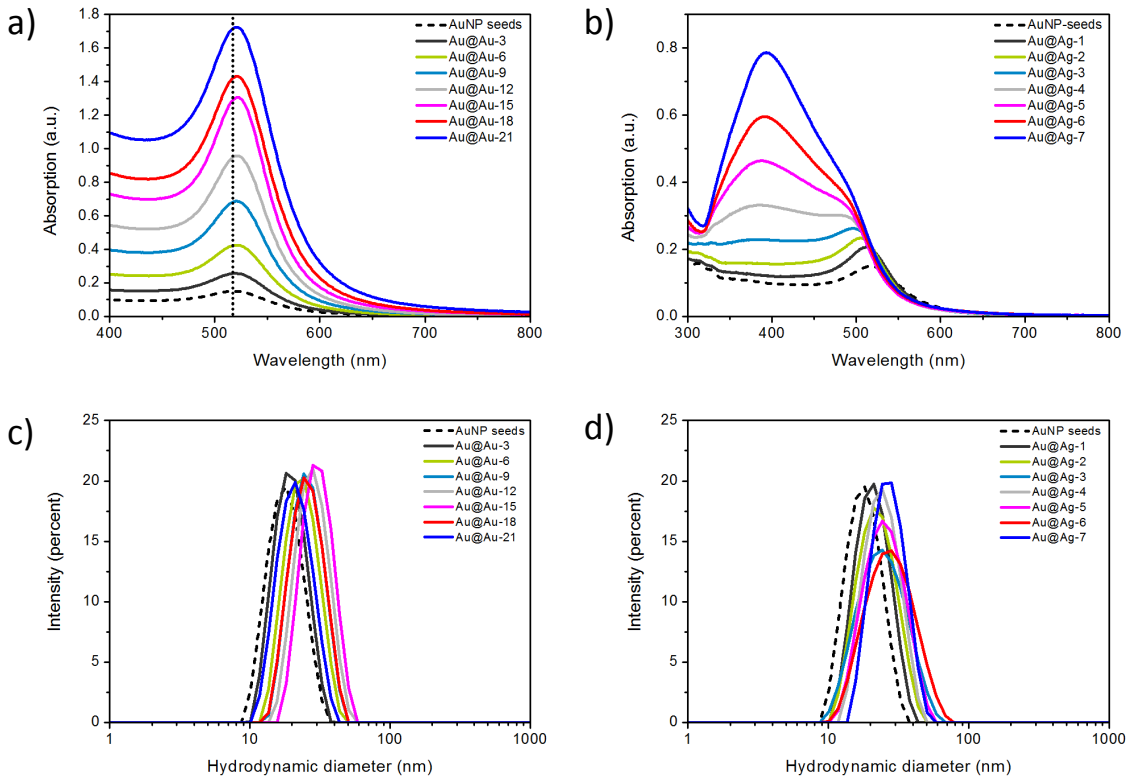

Figure A.2: UV-Vis spectra (a,b) and hydrodynamic size distribution (c,d) of AuNPs covered with different gold and silver shell thicknesses.

Testing the possible shell thickness of silver shells on AuNPs in a more narrow range (1-7 nm) showed increasing hydrodynamic diameter with increasing $AgNO_3$ addition. The LSPR band showed a large blue-shift until a theoretical shell thickness of 4 nm after which a slight shift to higher wavelengths was observed. This also might be explained by secondary seed formation. The PDI varied between 0.056 and 0.186. No clear trend was observed. However, further investigation, such as TEM will allow further conclusions about whether secondary seeding was responsible for these observations or not. Due to the size sensitivity of the scattered light intensity, DLS is not suitable to detect smaller NPs in the presence of large NPs.

For the development of silver-labeled AuNPs, a maximum shell thickness of 5 nm was chosen. Different precursor mixtures were tested to investigate the change of the optical absorption. UV-Vis spectra and hydrodynamic size distributions are shown in Figure A.3. A summary of the results can be found in Table A.4.

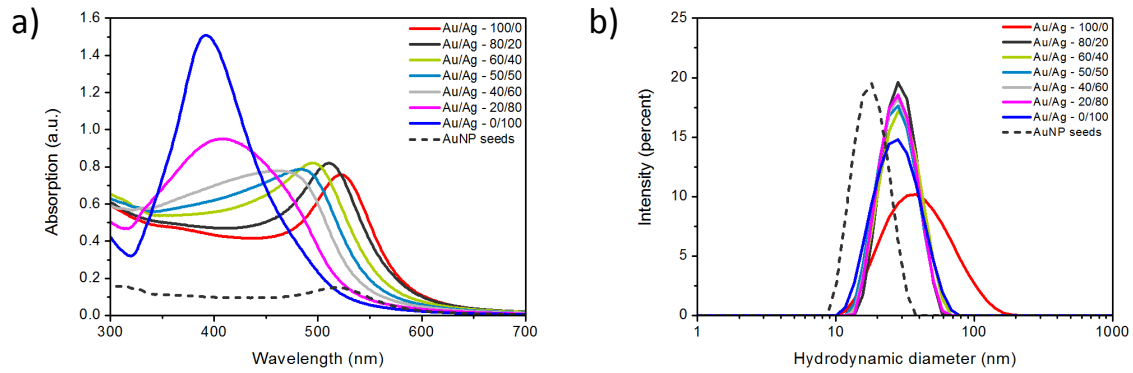

Figure A.3: UV-Vis spectra (a) and hydrodynamic size distribution (b) of AuNPs covered with shells of different gold/ silver ratios. A theoretical thickness of 5 nm was adjusted.

Table A.4: Results of the colloidal characterization of AuNP seeding growth with varying gold/silver shells.

Au/Ag ratio	D_h (nm)	PDI	LSPR band (nm)
Au-seeds	17.2	0.054	517
100/0	34.5	0.228	522
80/20	26.5	0.122	510
60/40	26.6	0.134	495
50/50	26.0	0.089	484
40/60	26.5	0.094	460
20/80	25.9	0.127	408
0/100	25.0	0.152	392

A gradual blue-shift with increasing Ag content was observed (Figure A.3). This shows the tunability of the optical properties by fabrication of different Ag/Au shells. Furthermore, the increased surface plasmon resonance absorption intensity is only observed at higher silver contents above 60 % but is accompanied with increasing PDI. The results form DLS suggest that there is an optimum composition at equimolar amounts of silver and gold (lowest PDI).

In summary, seeding growth of AuNPs with different shell thicknesses and compositions were fabricated and analyzed by DLS and UV-Vis spectroscopy. The optimized conditions were found to be: a citrate/precursor ratio of 10, shell thicknesses below 5 nm, and the use of equimolar amounts of $AgNO_3$ and $HAuCl_4$ for the formation of mixed shells.

B. Additional results on nanoparticle agglomeration of PEGylated gold nanoparticles

This section provides additional data on time-dependent Normalized Flocculation Parameters and normalized absorbance of citrate- and PEG-stabilized gold nanoparticles.

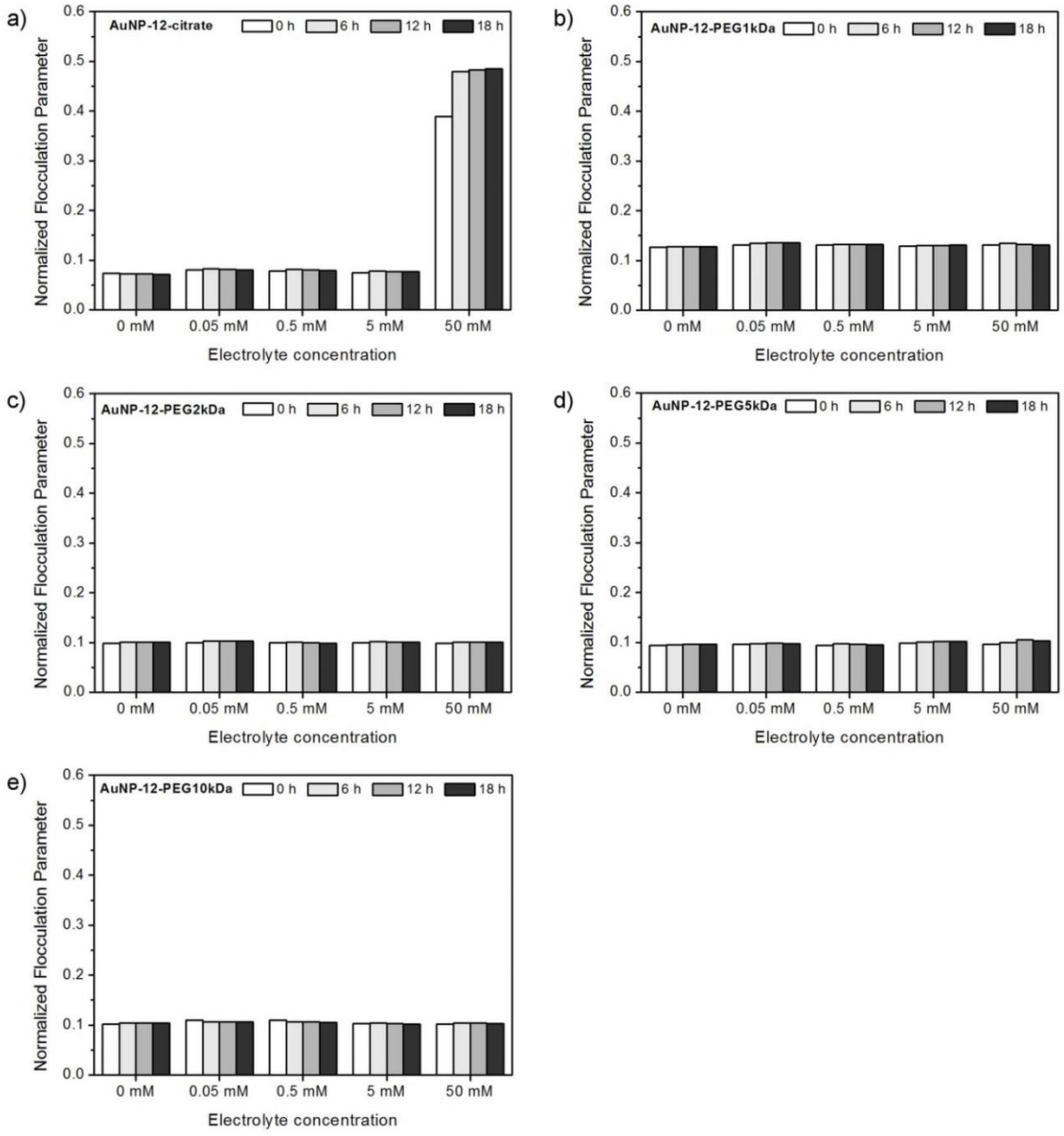

Figure A.4: Time-dependent Normalized Flocculation Parameter of citrate- and PEG-stabilized gold nanoparticles at different ionic strengths (NH_4NO_3 electrolyte).

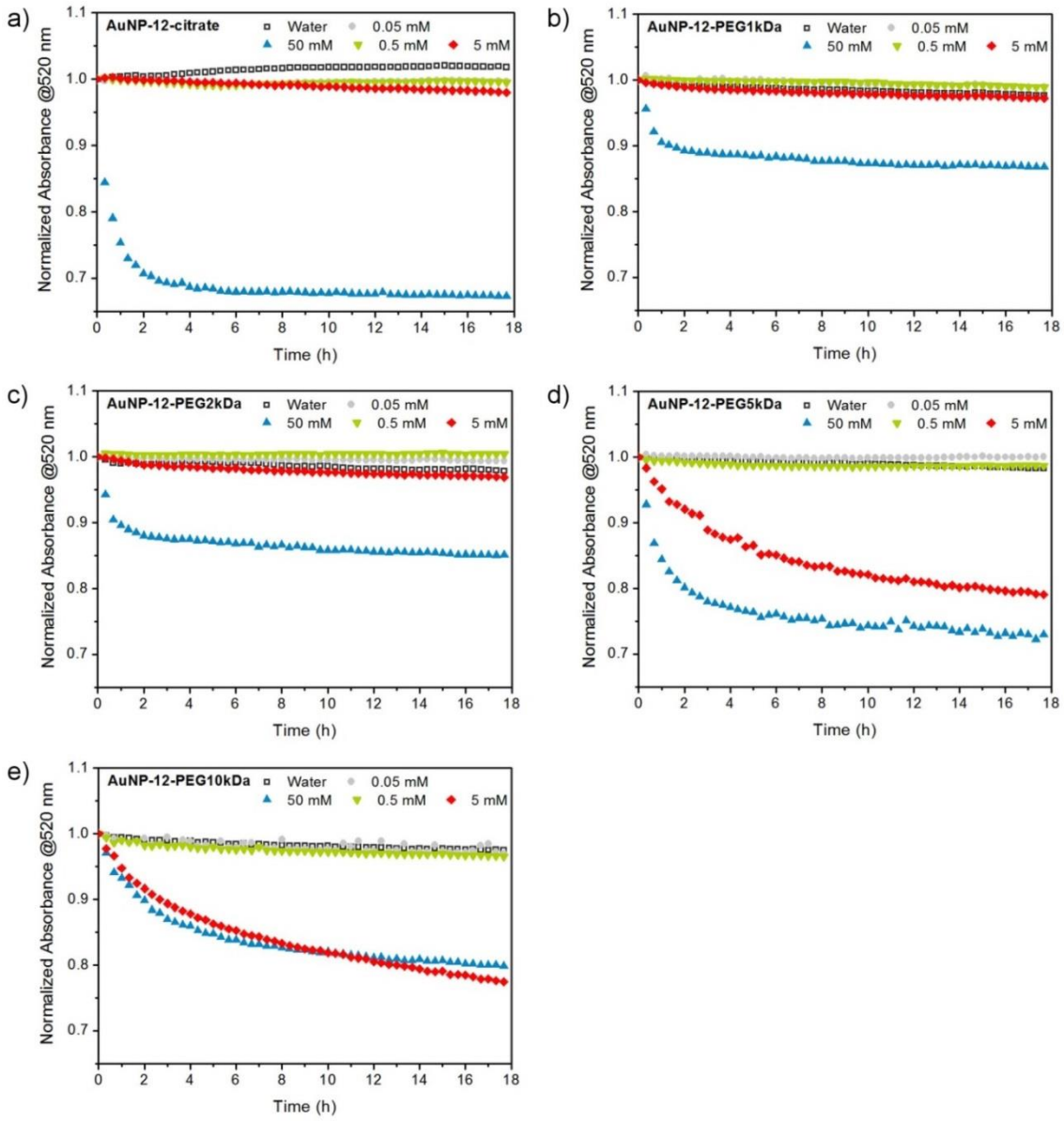

Figure A.5: Time-dependent normalized absorbance of citrate- and PEG-stabilized gold nanoparticles at different ionic strengths (NH_4NO_3 electrolyte) (image adapted from ref [108]).

C. Particle adsorption on internal surfaces

Additional SEM images of surfaces inside the analyzing system are presented in this chapter. Figure A.6 presents the SEM images of sliced PEEK tubings, which were used for 2 years. Comparison of the images obtained by secondary (A-C) and backscattered (D-F) electron detection allows the identification of silica nanoparticles and gold nanoparticles (the only NP samples tested with this tubing).

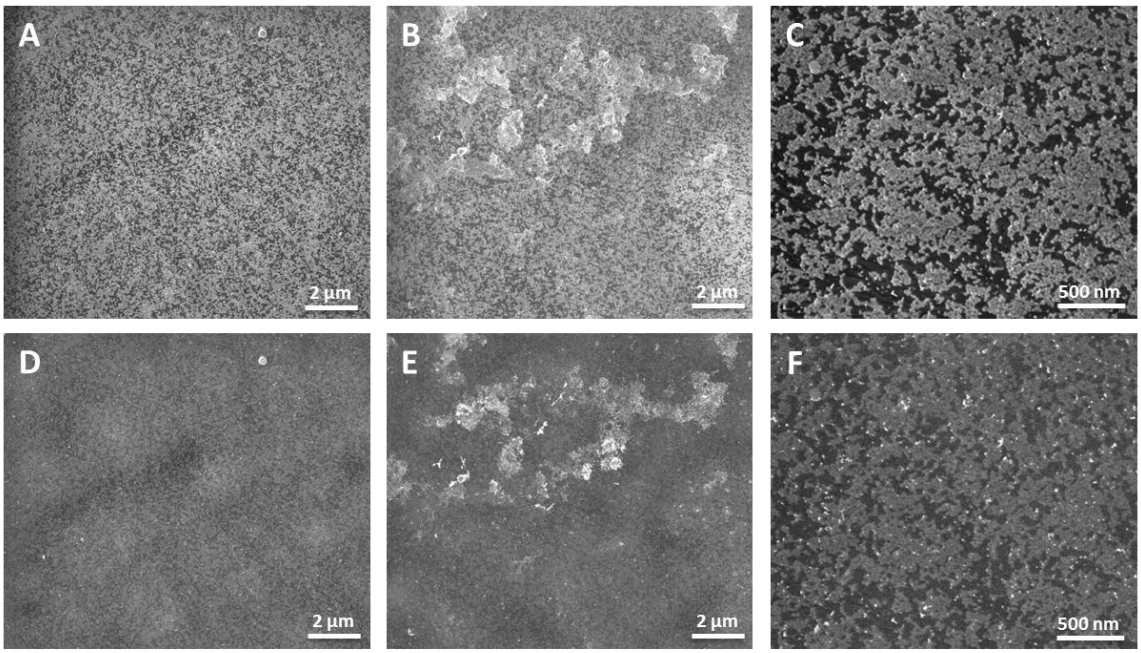

Figure A.6: SEM images (A-C: secondary electron detection, D-F: backscattered electron detection) of PEEK tubings covered with different nanoparticles.

Figure A.7 presents the SEM images of the injector valves rotor seal. The bright spots and corresponding EDX spectra confirm the presence of adsorbed gold nanoparticles.

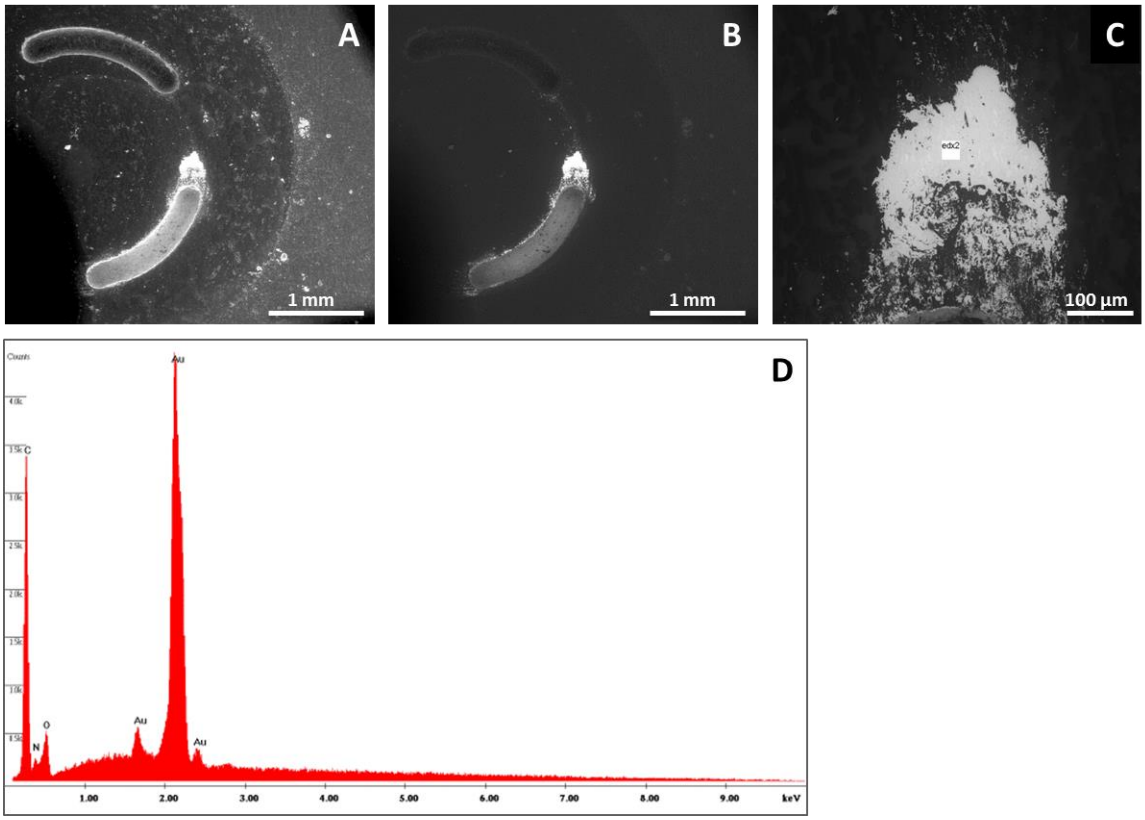

Figure A.7: SEM images (A-C) and corresponding EDX spectrum (D) of the injector valve rotor seal. (A: secondary electron detection, B and C: backscattered electron detection.)

Bibliography

[1] Commission Recommendation of 18 October 2011 on the definition of nanomaterial. *Official Journal of the EU* **2011**, *L 275-38*.

[2] Brown, S. C.; Boyko, V.; Meyers, G.; Voetz, M.; Wohlleben, W. Toward Advancing Nano-Object Count Metrology: A Best Practice Framework. *Environmental Health Perspectives* **2013**, *121*, 1282-1291.

[3] Wohlleben, W. Validity range of centrifuges for the regulation of nanomaterials: from classification to as-tested coronas. *Journal of Nanoparticle Research* **2012**, *14*, 1-18.

[4] Tiede, K.; Boxall, A. B. A.; Tiede, D.; Tear, S. P.; David, H.; Lewis, J. A robust size-characterisation methodology for studying nanoparticle behaviour in 'real' environmental samples, using hydrodynamic chromatography coupled to ICP-MS. *Journal of Analytical Atomic Spectrometry* **2009**, *24*, 964-972.

[5] Cho, T.; Hackley, V. Fractionation and characterization of gold nanoparticles in aqueous solution: asymmetric-flow field flow fractionation with MALS, DLS, and UV–Vis detection. *Anal Bioanal Chem* **2010**, *398*, 2003-2018.

[6] Baalousha, M.; Lead, J. *Characterization of nanomaterials in complex environmental and biological media*; Elsevier: Amsterdam, Netherlands, 2015.

[7] Kammer, F. v. d.; Legros, S.; Hofmann, T.; Larsen, E. H.; Loeschner, K. Separation and characterization of nanoparticles in complex food and environmental samples by field-flow fractionation. *TrAC Trends in Analytical Chemistry* **2011**, *30*, 425-436.

[8] Ulrich, A.; Losert, S.; Bendixen, N.; Al-Kattan, A.; Hagendorfer, H.; Nowack, B.; Adlhart, C.; Ebert, J.; Lattuada, M.; Hungerbuhler, K. Critical aspects of sample handling for direct nanoparticle analysis and analytical challenges using asymmetric field flow fractionation in a multi-detector approach. *Journal of Analytical Atomic Spectrometry* **2012**, *27*, 1120-1130.

[9] Sotebier, C. A.; Bierkandt, F. S.; Rades, S.; Jakubowski, N.; Panne, U.; Weidner, S. M. Sample loss in asymmetric flow field-flow fractionation coupled to inductively coupled plasma-mass spectrometry of silver nanoparticles. *Journal of Analytical Atomic Spectrometry* **2015**, *30*, 2214-2222.

[10] Bendixen, N.; Losert, S.; Adlhart, C.; Lattuada, M.; Ulrich, A. Membrane–particle interactions in an asymmetric flow field flow fractionation channel studied with titanium dioxide nanoparticles. *Journal of Chromatography A* **2014**, *1334*, 92-100.

[11] Schimpf, M. E.; Caldwell, K.; Giddings, J. C. *Field-Flow Fractionation Handbook*; Wiley: New York, 2000.

[12] Williams, S. K. R.; Runyon, J. R.; Ashames, A. A. Field-Flow Fractionation: Addressing the Nano Challenge. *Analytical Chemistry* **2010**, *83*, 634-642.

[13] Gigault, J.; Pettibone, J. M.; Schmitt, C.; Hackley, V. A. Rational strategy for characterization of nanoscale particles by asymmetric-flow field flow fractionation: A tutorial. *Analytica Chimica Acta* **2014**, *809*, 9-24.

[14] Giddings, J. C. A New Separation Concept Based on a Coupling of Concentration and Flow Nonuniformities. *Separation Science* **1966**, *1*, 123-125.

[15] Wahlund, K.-G. Flow field-flow fractionation: Critical overview. *Journal of Chromatography A* **2013**, *1287*, 97-112.

[16] Gigault, J.; Hackley, V. Observation of size-independent effects in nanoparticle retention behavior during asymmetric-flow field-flow fractionation. *Anal Bioanal Chem* **2013**, *405*, 6251-6258.

[17] Hagendorfer, H.; Kaegi, R.; Traber, J.; Mertens, S. F. L.; Scherrers, R.; Ludwig, C.; Ulrich, A. Application of an asymmetric flow field flow fractionation multi-detector approach for metallic engineered nanoparticle characterization – Prospects and limitations demonstrated on Au nanoparticles. *Analytica Chimica Acta* **2011**, *706*, 367-378.

[18] Barahona, F.; Geiss, O.; Urbán, P.; Ojea-Jimenez, I.; Gilliland, D.; Barrero-Moreno, J. Simultaneous Determination of Size and Quantification of Silica Nanoparticles by Asymmetric Flow Field-Flow Fractionation Coupled to ICPMS Using Silica Nanoparticles Standards. *Analytical Chemistry* **2015**, *87*, 3039-3047.

[19] Meermann, B.; Wichmann, K.; Lauer, F.; Vanhaecke, F.; Ternes, T. A. Application of stable isotopes and AF4/ICP-SFMS for simultaneous tracing and quantification of iron oxide nanoparticles in a sediment-slurry matrix. *Journal of Analytical Atomic Spectrometry* **2016**, *31*, 890-901.

[20] Nischwitz, V.; Goenaga-Infante, H. Improved sample preparation and quality control for the characterisation of titanium dioxide nanoparticles in sunscreens

using flow field flow fractionation on-line with inductively coupled plasma mass spectrometry. *Journal of Analytical Atomic Spectrometry* **2012**, *27*, 1084-1092.

[21] BIPM, I., IFCC, ILAC, IUPAC, IUPAP, ISO, OIML,. In *JCGM 200:2012*, 2012.

[22] Tsuzuki, T. *Nanotechnology Commercialization*; Pan Stanford Publishing: Singapore, 2013.

[23] Schmidt, B.; Loeschner, K.; Hadrup, N.; Mortensen, A.; Sloth, J. J.; Bender Koch, C.; Larsen, E. H. Quantitative Characterization of Gold Nanoparticles by Field-Flow Fractionation Coupled Online with Light Scattering Detection and Inductively Coupled Plasma Mass Spectrometry. *Analytical Chemistry* **2011**, *83*, 2461-2468.

[24] Zattoni, A.; Rambaldi, D. C.; Reschiglian, P.; Melucci, M.; Krol, S.; Garcia, A. M. C.; Sanz-Medel, A.; Roessner, D.; Johann, C. Asymmetrical flow field-flow fractionation with multi-angle light scattering detection for the analysis of structured nanoparticles. *Journal of Chromatography A* **2009**, *1216*, 9106-9112.

[25] López-Heras, I.; Madrid, Y.; Cámara, C. Prospects and difficulties in TiO2 nanoparticles analysis in cosmetic and food products using asymmetrical flow field-flow fractionation hyphenated to inductively coupled plasma mass spectrometry. *Talanta* **2014**, *124*, 71-78.

[26] Mudalige, T. K.; Qu, H.; Sánchez-Pomales, G.; Sisco, P. N.; Linder, S. W. Simple Functionalization Strategies for Enhancing Nanoparticle Separation and Recovery with Asymmetric Flow Field Flow Fractionation. *Analytical Chemistry* **2015**, *87*, 1764-1772.

[27] Meermann, B. Field-flow fractionation coupled to ICP–MS: separation at the nanoscale, previous and recent application trends. *Anal Bioanal Chem* **2015**, *407*, 2665-2674.

[28] Meermann, B.; Fabricius, A.-L.; Duester, L.; Vanhaecke, F.; Ternes, T. Fraction-related quantification of silver nanoparticlesvia on-line species-unspecific post-channel isotope dilution in combination with asymmetric flow-field-flow fractionation (AF4)/sector field ICP-mass spectrometry (ICP-SF-MS). *Journal of Analytical Atomic Spectrometry* **2014**, *29*, 287-296.

[29] Gigault, J.; Hackley, V. A. Differentiation and characterization of isotopically modified silver nanoparticles in aqueous media using asymmetric-flow field flow fractionation coupled to optical detection and mass spectrometry. *Analytica Chimica Acta* **2013**, *763*, 57-66.

[30] Pálmai, M.; Szalay, R.; Bartczak, D.; Varga, Z.; Nagy, L. N.; Gollwitzer, C.; Krumrey, M.; Goenaga-Infante, H. Total synthesis of isotopically enriched Si-29 silica NPs as potential spikes for isotope dilution quantification of natural silica NPs. *Journal of Colloid and Interface Science* **2015**, *445*, 161-165.

[31] Majedi, S. M.; Lee, H. K. Recent advances in the separation and quantification of metallic nanoparticles and ions in the environment. *TrAC Trends in Analytical Chemistry* **2016**, *75*, 183-196.

[32] Burns, A.; Sengupta, P.; Zedayko, T.; Baird, B.; Wiesner, U. Core/Shell Fluorescent Silica Nanoparticles for Chemical Sensing: Towards Single-Particle Laboratories. *Small* **2006**, *2*, 723-726.

[33] Pinho, S. L. C.; Faneca, H.; Geraldes, C. F. G. C.; Delville, M.-H.; Carlos, L. D.; Rocha, J. Lanthanide-DTPA grafted silica nanoparticles as bimodal-imaging contrast agents. *Biomaterials* **2012**, *33*, 925-935.

[34] Dubascoux, S.; Von Der Kammer, F.; Le Hécho, I.; Gautier, M. P.; Lespes, G. Optimisation of asymmetrical flow field flow fractionation for environmental nanoparticles separation. *Journal of Chromatography A* **2008**, *1206*, 160-165.

[35] Schachermeyer, S.; Ashby, J.; Kwon, M.; Zhong, W. Impact of carrier fluid composition on recovery of nanoparticles and proteins in flow field flow fractionation. *Journal of Chromatography A* **2012**, *1264*, 72-79.

[36] Meisterjahn, B.; Neubauer, E.; Von der Kammer, F.; Hennecke, D.; Hofmann, T. Asymmetrical flow-field-flow fractionation coupled with inductively coupled plasma mass spectrometry for the analysis of gold nanoparticles in the presence of natural nanoparticles. *Journal of Chromatography A* **2014**, *1372*, 204-211.

[37] Evans, D. F.; Wennerström, H. *The Colloidal Domain: Where Physics, Chemistry, Biology, and Technology Meet*, Second ed.; Wiley: New York, 1999.

[38] Elimelech, M.; Gregory, J.; Jia, X.; Williams, R. A. *Particle Deposition and Aggregation: Measurement, Modelling and Simulation*; Butterworth-Heinemann: Woburn, 1998.

[39] Myers, D. *Surfaces, Interfaces, and Colloids*, Second ed.; John Wiley & Sons, Inc.: New York, 1999.

[40] Israelachvili, J. N. *Intermolecular and Surface Forces*, Third ed.; Academic Press: San Diego, 2011.

[41] Linse, P.; Wennerstrom, H. Adsorption versus aggregation. Particles and surface of the same material. *Soft Matter* **2012**, *8*, 2486-2493.

[42] Chellam, S.; Wiesner, M. R. Particle transport in clean membrane filters in laminar flow. *Environmental Science & Technology* **1992**, *26*, 1611-1621.

[43] Lin, S.; Cheng, Y.; Liu, J.; Wiesner, M. R. Polymeric Coatings on Silver Nanoparticles Hinder Autoaggregation but Enhance Attachment to Uncoated Surfaces. *Langmuir* **2012**, *28*, 4178-4186.

[44] von der Kammer, F.; Ferguson, P. L.; Holden, P. A.; Masion, A.; Rogers, K. R.; Klaine, S. J.; Koelmans, A. A.; Horne, N.; Unrine, J. M. Analysis of engineered nanomaterials in complex matrices (environment and biota): General considerations and conceptual case studies. *Environmental Toxicology and Chemistry* **2012**, *31*, 32-49.

[45] Giddings, J. C.; Caldwell, K. D. Field-flow fractionation: choices in programmed and nonprogrammed operation. *Analytical Chemistry* **1984**, *56*, 2093-2099.

[46] Hartmann, R. L.; Williams, S. K. R. Flow field-flow fractionation as an analytical technique to rapidly quantitate membrane fouling. *Journal of Membrane Science* **2002**, *209*, 93-106.

[47] Kassalainen, G.; Williams, S. K. In *Field-Flow Fractionation in Biopolymer Analysis*, Williams, S. K. R.; Caldwell, K. D., Eds.; Springer Vienna, 2012, pp 23-36.

[48] Bolea, E.; Jiménez-Lamana, J.; Laborda, F.; Castillo, J. R. Size characterization and quantification of silver nanoparticles by asymmetric flow field-flow fractionation coupled with inductively coupled plasma mass spectrometry. *Anal Bioanal Chem* **2011**, *401*, 2723-2732.

[49] Loeschner, K.; Navratilova, J.; Legros, S.; Wagner, S.; Grombe, R.; Snell, J.; von der Kammer, F.; Larsen, E. H. Optimization and evaluation of asymmetric flow field-flow fractionation of silver nanoparticles. *Journal of Chromatography A* **2013**, *1272*, 116-125.

[50] Isaacson, C. W.; Bouchard, D. Asymmetric flow field flow fractionation of aqueous C60 nanoparticles with size determination by dynamic light scattering and quantification by liquid chromatography atmospheric pressure photo-ionization mass spectrometry. *Journal of Chromatography A* **2010**, *1217*, 1506-1512.

[51] Schimpf, M. E.; Caldwell, K.; Giddings, J. C.; Wiley: New York, 2000, pp 325-343.

[52] Geiss, O.; Cascio, C.; Gilliland, D.; Franchini, F.; Barrero-Moreno, J. Size and mass determination of silver nanoparticles in an aqueous matrix using asymmetric flow field flow fractionation coupled to inductively coupled plasma mass spectrometer and ultraviolet–visible detectors. *Journal of Chromatography A* **2013**, *1321*, 100-108.

[53] Cumberland, S. A.; Lead, J. R. Particle size distributions of silver nanoparticles at environmentally relevant conditions. *Journal of Chromatography A* **2009**, *1216*, 9099-9105.

[54] Gigault, J.; Cho, T.; MacCuspie, R.; Hackley, V. Gold nanorod separation and characterization by asymmetric-flow field flow fractionation with UV–Vis detection. *Anal Bioanal Chem* **2013**, *405*, 1191-1202.

[55] Gigault, J.; Nguyen, T.; Pettibone, J.; Hackley, V. Accurate determination of the size distribution for polydisperse, cationic metallic nanomaterials by asymmetric-flow field flow fractionation. *J Nanopart Res* **2014**, *16*, 1-10.

[56] Poda, A. R.; Bednar, A. J.; Kennedy, A. J.; Harmon, A.; Hull, M.; Mitrano, D. M.; Ranville, J. F.; Steevens, J. Characterization of silver nanoparticles using flow-field flow fractionation interfaced to inductively coupled plasma mass spectrometry. *Journal of Chromatography A* **2011**, *1218*, 4219-4225.

[57] Hagendorfer, H.; Kaegi, R.; Parlinska, M.; Sinnet, B.; Ludwig, C.; Ulrich, A. Characterization of Silver Nanoparticle Products Using Asymmetric Flow Field Flow Fractionation with a Multidetector Approach – a Comparison to Transmission Electron Microscopy and Batch Dynamic Light Scattering. *Analytical Chemistry* **2012**, *84*, 2678-2685.

[58] Kavurt, U. B.; Marioli, M.; Kok, W. T.; Stamatialis, D. Membranes for separation of biomacromolecules and bioparticles via flow field-flow fractionation. *Journal of Chemical Technology & Biotechnology* **2015**, *90*, 11-18.

[59] Baalousha, M.; Manciulea, A.; Cumberland, S.; Kendall, K.; Lead, J. R. Aggregation and surface properties of iron oxide nanoparticles: Influence of ph and natural organic matter. *Environmental Toxicology and Chemistry* **2008**, *27*, 1875-1882.

[60] Bouby, M.; Geckeis, H.; Geyer, F. W. Application of asymmetric flow field-flow fractionation (AsFlFFF) coupled to inductively coupled plasma mass spectrometry (ICPMS) to the quantitative characterization of natural colloids and synthetic nanoparticles. *Anal Bioanal Chem* **2008**, *392*, 1447-1457.

[61] Baalousha, M.; Stolpe, B.; Lead, J. R. Flow field-flow fractionation for the analysis and characterization of natural colloids and manufactured nanoparticles in environmental systems: A critical review. *Journal of Chromatography A* **2011**, *1218*, 4078-4103.

[62] Runyon, J. R.; Ulmius, M.; Nilsson, L. A perspective on the characterization of colloids and macromolecules using asymmetrical flow field-flow fractionation. *Colloids and Surfaces A: Physicochemical and Engineering Aspects* **2014**, *442*, 25-33.

[63] Funk, W.; Dammann, V.; Donnevert, G.; Ianelli, S.; Ianelli, E.; Gray, A. *Quality Assurance in Analytical Chemistry*, Second ed.; Wiley-VCH Verlag GmbH & Co. KGaA: Weinheim, 2006.

[64] Daniel, M.-C.; Astruc, D. Gold Nanoparticles: Assembly, Supramolecular Chemistry, Quantum-Size-Related Properties, and Applications toward Biology, Catalysis, and Nanotechnology. *Chemical Reviews* **2004**, *104*, 293-346.

[65] Tang, L.; Cheng, J. Nonporous silica nanoparticles for nanomedicine application. *Nano Today* **2013**, *8*, 290-312.

[66] Ribeiro, T.; Raja, S.; Rodrigues, A. S.; Fernandes, F.; Farinha, J. P. S.; Baleizão, C. High performance NIR fluorescent silica nanoparticles for bioimaging. *RSC Advances* **2013**, *3*, 9171-9174.

[67] Dekkers, S.; Krystek, P.; Peters, R. J. B.; Lankveld, D. P. K.; Bokkers, B. G. H.; van Hoeven-Arentzen, P. H.; Bouwmeester, H.; Oomen, A. G. Presence and risks of nanosilica in food products. *Nanotoxicology* **2011**, *5*, 393-405.

[68] Li, Z.; Barnes, J. C.; Bosoy, A.; Stoddart, J. F.; Zink, J. I. Mesoporous silica nanoparticles in biomedical applications. *Chemical Society Reviews* **2012**, *41*, 2590-2605.

[69] Turkevich, J.; Stevenson, P. C.; Hillier, J. A study of the nucleation and growth processes in the synthesis of colloidal gold. *Discussions of the Faraday Society* **1951**, *11*, 55-75.

[70] Frens, G. Controlled Nucleation for Regulation of Particle-Size in Monodisperse Gold Suspensions. *Nature-Physical Science* **1973**, *241*, 20-22.

[71] Daniel, M.-C.; Astruc, D. Gold Nanoparticles: Assembly, Supramolecular Chemistry, Quantum-Size-Related Properties, and Applications toward Biology, Catalysis, and Nanotechnology. *Chemical Reviews* **2003**, *104*, 293-346.

[72] Iler, R. K. *The Chemistry of Silica: Solubility, Polymerization, Colloid and Surface Properties and Biochemistry of Silica*; Wiley: New York, 1979.

[73] Stöber, W.; Fink, A.; Bohn, E. Controlled growth of monodisperse silica spheres in the micron size range. *Journal of Colloid and Interface Science* **1968**, *26*, 62-69.

[74] Hartlen, K. D.; Athanasopoulos, A. P. T.; Kitaev, V. Facile Preparation of Highly Monodisperse Small Silica Spheres (15 to >200 nm) Suitable for Colloidal Templating and Formation of Ordered Arrays. *Langmuir* **2008**, *24*, 1714-1720.

[75] Yokoi, T.; Sakamoto, Y.; Terasaki, O.; Kubota, Y.; Okubo, T.; Tatsumi, T. Periodic arrangement of silica nanospheres assisted by amino acids. *Journal of the American Chemical Society* **2006**, *128*, 13664-13665.

[76] Fouilloux, S.; Taché, O.; Spalla, O.; Thill, A. Nucleation of Silica Nanoparticles Measured in Situ during Controlled Supersaturation Increase. Restructuring toward a Monodisperse Nonspherical Shape. *Langmuir* **2011**, *27*, 12304-12311.

[77] Atchison, N.; Fan, W.; Brewer, D. D.; Arunagirinathan, M. A.; Hering, B. J.; Kumar, S.; Papas, K. K.; Kokkoli, E.; Tsapatsis, M. Silica-Nanoparticle Coatings by Adsorption from Lysine–Silica-Nanoparticle Sols on Inorganic and Biological Surfaces. *Angewandte Chemie International Edition* **2011**, *50*, 1617-1621.

[78] van Blaaderen, A.; Vrij, A. Synthesis and characterization of colloidal dispersions of fluorescent, monodisperse silica spheres. *Langmuir* **1992**, *8*, 2921-2931.

[79] Beija, M.; Afonso, C. A. M.; Martinho, J. M. G. Synthesis and applications of Rhodamine derivatives as fluorescent probes. *Chemical Society Reviews* **2009**, *38*, 2410-2433.

[80] Verhaegh, N. A. M.; Vanblaaderen, A. Dispersions of Rhodamine-Labeled Silica Spheres - Synthesis, Characterization, and Fluorescence Confocal Scanning Laser Microscopy. *Langmuir* **1994**, *10*, 1427-1438.

[81] Wang, L.; Wang, K. M.; Santra, S.; Zhao, X. J.; Hilliard, L. R.; Smith, J. E.; Wu, J. R.; Tan, W. H. Watching silica nanoparticles glow in the biological world. *Analytical Chemistry* **2006**, *78*, 646-654.

[82] Tavernaro, I.; Cavelius, C.; Peuschel, H.; Kraegeloh, A. Bright fluorescent silica-nanoparticle probes for high-resolution STED and confocal microscopy. *Beilstein Journal of Nanotechnology* **2017**, *8*, 1283-1296.

[83] Hermanson, G. T. *Bioconjugate Techniques*; Academic Press: Amsterdam, 2013.

[84] Baalousha, M.; Lead, J. R. Rationalizing Nanomaterial Sizes Measured by Atomic Force Microscopy, Flow Field-Flow Fractionation, and Dynamic Light Scattering: Sample Preparation, Polydispersity, and Particle Structure. *Environmental Science & Technology* **2012**, *46*, 6134-6142.

[85] Shaffer, T. M.; Harmsen, S.; Khwaja, E.; Kircher, M. F.; Drain, C. M.; Grimm, J. Stable Radiolabeling of Sulfur-Functionalized Silica Nanoparticles with Copper-64. *Nano Letters* **2016**, *16*, 5601-5604.

[86] Dupont, D.; Brullot, W.; Bloemen, M.; Verbiest, T.; Binnemans, K. Selective Uptake of Rare Earths from Aqueous Solutions by EDTA-Functionalized Magnetic and Nonmagnetic Nanoparticles. *ACS Applied Materials & Interfaces* **2014**, *6*, 4980-4988.

[87] Santra, S.; Bagwe, R. P.; Dutta, D.; Stanley, J. T.; Walter, G. A.; Tan, W.; Moudgil, B. M.; Mericle, R. A. Synthesis and characterization of fluorescent, radio-opaque, and paramagnetic silica nanoparticles for multimodal bioimaging applications. *Advanced Materials* **2005**, *17*, 2165-2169.

[88] Shaffer, T. M.; Wall, M. A.; Harmsen, S.; Longo, V. A.; Drain, C. M.; Kircher, M. F.; Grimm, J. Silica Nanoparticles as Substrates for Chelator-free Labeling of Oxophilic Radioisotopes. *Nano Letters* **2015**, *15*, 864-868.

[89] Yamauchi, O.; Odani, A. Stability constants of metal complexes of amino acids with charged side chains - Part I: Positively charged side chains (Technical Report). *Pure and Applied Chemistry* **1996**, *68*, 469-496.

[90] Albourine, A.; Petit-Ramel, M.; Thomas-David, G.; Vallon, J.-J. Complexes binaires et ternaires du cuivre(II) avec la 1-canavanine et la 1-arginine examinés par potentiométrie, spectrophotométrie visible et dichroïsme circulaire. *Canadian Journal of Chemistry* **1989**, *67*, 959-966.

[91] Martell, A. E.; Plumb, R. C. Complexes of Various Metals with Ethylenediaminetetraacetic Acid. *The Journal of Physical Chemistry* **1952**, *56*, 993-996.

[92] Shannon, R. Revised effective ionic radii and systematic studies of interatomic distances in halides and chalcogenides. *Acta Crystallographica Section A* **1976**, *32*, 751-767.

[93] Fouilloux, S.; Daillant, J.; Thill, A. Single step synthesis of 5–30 nm monodisperse silica nanoparticles: Important experimental parameters and modeling. *Colloids and Surfaces A: Physicochemical and Engineering Aspects* **2012**, *393*, 122-127.

[94] Niu, J.; Zhu, T.; Liu, Z. One-step seed-mediated growth of 30-150 nm quasispherical gold nanoparticles with 2-mercaptosuccinic acid as a new reducing agent. *Nanotechnology* **2007**, *18*.

[95] Aihara, N.; Torigoe, K.; Esumi, K. Preparation and Characterization of Gold and Silver Nanoparticles in Layered Laponite Suspensions. *Langmuir* **1998**, *14*, 4945-4949.

[96] Minh, T.; Rebekah, D.; Madeline, T.; Sonal, P. Effect of citrate ratio and temperature on gold nanoparticle size and morphology. *Materials Research Express* **2016**, *3*, 105027.

[97] Perrault, S. D.; Chan, W. C. W. Synthesis and surface modification of highly monodispersed, spherical gold nanoparticles of 50-200 nm. *Journal of the American Chemical Society* **2009**, *131*, 17042-17043.

[98] Selvakannan, P. R.; Mandal, S.; Phadtare, S.; Pasricha, R.; Sastry, M. Capping of Gold Nanoparticles by the Amino Acid Lysine Renders Them Water-Dispersible. *Langmuir* **2003**, *19*, 3545-3549.

[99] Technology, W., Technical Note 12781: Maximum Rh Measurable by DLS in Flow Mode.

[100] Liu, K.; Zheng, Y.; Lu, X.; Thai, T.; Lee, N. A.; Bach, U.; Gooding, J. J. Biocompatible Gold Nanorods: One-Step Surface Functionalization, Highly Colloidal Stability, and Low Cytotoxicity. *Langmuir* **2015**, *31*, 4973-4980.

[101] Sperling, R. A.; Parak, W. J. Surface modification, functionalization and bioconjugation of colloidal inorganic nanoparticles. *Philosophical Transactions of the Royal Society A: Mathematical, Physical and Engineering Sciences* **2010**, *368*, 1333-1383.

[102] Schmid, G. Large clusters and colloids. Metals in the embryonic state. *Chemical Reviews* **1992**, *92*, 1709-1727.

[103] Wu, Z.; Liang, J.; Ji, X.; Yang, W. Preparation of uniform Au@SiO2 particles by direct silica coating on citrate-capped Au nanoparticles. *Colloids and Surfaces A: Physicochemical and Engineering Aspects* **2011**, *392*, 220-224.

[104] Brewer, S. H.; Glomm, W. R.; Johnson, M. C.; Knag, M. K.; Franzen, S. Probing BSA Binding to Citrate-Coated Gold Nanoparticles and Surfaces. *Langmuir* **2005**, *21*, 9303-9307.

[105] Rahme, K.; Nolan, M. T.; Doody, T.; McGlacken, G. P.; Morris, M. A.; O'Driscoll, C.; Holmes, J. D. Highly stable PEGylated gold nanoparticles in water: applications in biology and catalysis. *RSC Advances* **2013**, *3*, 21016-21024.

[106] Liu, T.; Thierry, B. A Solution to the PEG Dilemma: Efficient Bioconjugation of Large Gold Nanoparticles for Biodiagnostic Applications using Mixed Layers. *Langmuir* **2012**, *28*, 15634-15642.

[107] Smith, A. M.; Marbella, L. E.; Johnston, K. A.; Hartmann, M. J.; Crawford, S. E.; Kozycz, L. M.; Seferos, D. S.; Millstone, J. E. Quantitative Analysis of Thiolated Ligand Exchange on Gold Nanoparticles Monitored by 1H NMR Spectroscopy. *Analytical Chemistry* **2015**, *87*, 2771-2778.

[108] Jochem, A.-R.; Ankah, G. N.; Meyer, L.-A.; Elsenberg, S.; Johann, C.; Kraus, T. Colloidal Mechanisms of Gold Nanoparticle Loss in Asymmetric Flow Field-Flow Fractionation. *Analytical Chemistry* **2016**, *88*, 10065-10073.

[109] Wuelfing, W. P.; Gross, S. M.; Miles, D. T.; Murray, R. W. Nanometer Gold Clusters Protected by Surface-Bound Monolayers of Thiolated Poly(ethylene glycol) Polymer Electrolyte. *Journal of the American Chemical Society* **1998**, *120*, 12696-12697.

[110] Yohannes, G.; Wiedmer, S. K.; Elomaa, M.; Jussila, M.; Aseyev, V.; Riekkola, M.-L. Thermal aggregation of bovine serum albumin studied by asymmetrical flow field-flow fractionation. *Analytica Chimica Acta* **2010**, *675*, 191-198.

[111] Dewald, I.; Isakin, O.; Schubert, J.; Kraus, T.; Chanana, M. Protein Identity and Environmental Parameters Determine the Final Physicochemical Properties of Protein-Coated Metal Nanoparticles. *The Journal of Physical Chemistry C* **2015**, *119*, 25482-25492.

[112] Ghosh, S. K.; Pal, T. Interparticle Coupling Effect on the Surface Plasmon Resonance of Gold Nanoparticles:â€‰ From Theory to Applications. *Chemical Reviews* **2007**, *107*, 4797-4862.

[113] Han, X.; Goebl, J.; Lu, Z.; Yin, Y. Role of Salt in the Spontaneous Assembly of Charged Gold Nanoparticles in Ethanol. *Langmuir* **2011**, *27*, 5282-5289.

[114] Liu, S.; Chen, G.; Prasad, P. N.; Swihart, M. T. Synthesis of Monodisperse Au, Ag, and Au–Ag Alloy Nanoparticles with Tunable Size and Surface Plasmon Resonance Frequency. *Chemistry of Materials* **2011**, *23*, 4098-4101.

[115] Zheng, N.; Fan, J.; Stucky, G. D. One-step one-phase synthesis of monodisperse noble-metallic nanoparticles and their colloidal crystals. *Journal of the American Chemical Society* **2006**, *128*, 6550-6551.

[116] Link, S.; Wang, Z. L.; El-Sayed, M. A. Alloy Formation of Gold–Silver Nanoparticles and the Dependence of the Plasmon Absorption on Their Composition. *The Journal of Physical Chemistry B* **1999**, *103*, 3529-3533.

[117] Rioux, D.; Meunier, M. Seeded Growth Synthesis of Composition and Size-Controlled Gold–Silver Alloy Nanoparticles. *The Journal of Physical Chemistry C* **2015**, *119*, 13160-13168.

[118] Mulvaney, P.; Linnert, T.; Henglein, A. Surface chemistry of colloidal silver in aqueous solution: observations on chemisorption and reactivity. *The Journal of Physical Chemistry* **1991**, *95*, 7843-7846.

[119] Ho, C.-M.; Yau, S. K.-W.; Lok, C.-N.; So, M.-H.; Che, C.-M. Oxidative Dissolution of Silver Nanoparticles by Biologically Relevant Oxidants: A Kinetic and Mechanistic Study. *Chemistry – An Asian Journal* **2010**, *5*, 285-293.

[120] Yang, J.; Lee, J. Y.; Too, H.-P.; Valiyaveettil, S. A Bis(p-sulfonatophenyl)phenylphosphine-Based Synthesis of Hollow Pt Nanospheres. *The Journal of Physical Chemistry B* **2006**, *110*, 125-129.

[121] Weisbecker, C. S.; Merritt, M. V.; Whitesides, G. M. Molecular Self-Assembly of Aliphatic Thiols on Gold Colloids. *Langmuir* **1996**, *12*, 3763-3772.

[122] Zhang, X.; Servos, M. R.; Liu, J. Ultrahigh Nanoparticle Stability against Salt, pH, and Solvent with Retained Surface Accessibility via Depletion Stabilization. *Journal of the American Chemical Society* **2012**, *134*, 9910-9913.

[123] Volkert, A. A.; Subramaniam, V.; Ivanov, M. R.; Goodman, A. M.; Haes, A. J. Salt-Mediated Self-Assembly of Thioctic Acid on Gold Nanoparticles. *ACS Nano* **2011**, *5*, 4570-4580.

[124] Shang, J.; Gao, X. Nanoparticle counting: towards accurate determination of the molar concentration. *Chemical Society Reviews* **2014**, *43*, 7267-7278.

[125] Frens, G. Particle size and sol stability in metal colloids. *Kolloid-Zeitschrift und Zeitschrift für Polymere* **1972**, *250*, 736-741.

[126] Afshinnia, K.; Sikder, M.; Cai, B.; Baalousha, M. Effect of nanomaterial and media physicochemical properties on Ag NM aggregation kinetics. *Journal of Colloid and Interface Science* **2017**, *487*, 192-200.

[127] Liu, Y.; Tourbin, M.; Lachaize, S.; Guiraud, P. Silica Nanoparticle Separation from Water by Aggregation with AlCl3. *Industrial & Engineering Chemistry Research* **2012**, *51*, 1853-1863.

[128] Thai, T.; Zheng, Y.; Ng, S. H.; Mudie, S.; Altissimo, M.; Bach, U. Self-Assembly of Vertically Aligned Gold Nanorod Arrays on Patterned Substrates. *Angewandte Chemie International Edition* **2012**, *51*, 8732-8735.

[129] Zhu, T.; Vasilev, K.; Kreiter, M.; Mittler, S.; Knoll, W. Surface Modification of Citrate-Reduced Colloidal Gold Nanoparticles with 2-Mercaptosuccinic Acid. *Langmuir* **2003**, *19*, 9518-9525.

[130] Karakoti, A. S.; Das, S.; Thevuthasan, S.; Seal, S. PEGylated Inorganic Nanoparticles. *Angewandte Chemie International Edition* **2011**, *50*, 1980-1994.

[131] Stein, B.; Zopes, D.; Schmudde, M.; Schneider, R.; Mohsen, A.; Goroncy, C.; Mathur, S.; Graf, C. Kinetics of aggregation and growth processes of PEG-stabilised mono- and multivalent gold nanoparticles in highly concentrated halide solutions. *Faraday Discuss* **2015**.

[132] Curry, D.; Scheller, H.; Lu, M.; Mkandawire, M.; Servos, M. R.; Cui, S.; Zhang, X.; Oakes, K. D. Prevention of doxorubicin sorptive losses in drug delivery studies using polyethylene glycol. *RSC Advances* **2015**, *5*, 25693-25698.

[133] Liu, B.; Huang, P.-J. J.; Zhang, X.; Wang, F.; Pautler, R.; Ip, A. C. F.; Liu, J. Parts-per-Million of Polyethylene Glycol as a Non-Interfering Blocking Agent for Homogeneous Biosensor Development. *Analytical Chemistry* **2013**, *85*, 10045-10050.

[134] Tsukamoto, R.; Godonoga, M.; Matsuyama, R.; Igarashi, M.; Heddle, J. G.; Samukawa, S.; Yamashita, I. Effect of PEGylation on Controllably Spaced Adsorption of Ferritin Molecules. *Langmuir* **2013**, *29*, 12737-12743.

[135] Delay, M.; Dolt, T.; Woellhaf, A.; Sembritzki, R.; Frimmel, F. H. Interactions and stability of silver nanoparticles in the aqueous phase: Influence of natural organic matter (NOM) and ionic strength. *Journal of Chromatography A* **2011**, *1218*, 4206-4212.

[136] Stankus, D. P.; Lohse, S. E.; Hutchison, J. E.; Nason, J. A. Interactions between Natural Organic Matter and Gold Nanoparticles Stabilized with Different Organic Capping Agents. *Environmental Science & Technology* **2011**, *45*, 3238-3244.

[137] Yin, Y.; Shen, M.; Tan, Z.; Yu, S.; Liu, J.; Jiang, G. Particle Coating-Dependent Interaction of Molecular Weight Fractionated Natural Organic Matter: Impacts on the Aggregation of Silver Nanoparticles. *Environmental Science & Technology* **2015**, *49*, 6581-6589.

[138] Philippe, A.; Schaumann, G. E. Interactions of Dissolved Organic Matter with Natural and Engineered Inorganic Colloids: A Review. *Environmental Science & Technology* **2014**, *48*, 8946-8962.

[139] Beckett, R.; Nicholson, G.; Hart, B. T.; Hansen, M.; Calvin Giddings, J. Separation and size characterization of colloidal particles in river water by sedimentation field-flow fractionation. *Water Research* **1988**, *22*, 1535-1545.

[140] Tejamaya, M.; Römer, I.; Merrifield, R. C.; Lead, J. R. Stability of Citrate, PVP, and PEG Coated Silver Nanoparticles in Ecotoxicology Media. *Environmental Science & Technology* **2012**, *46*, 7011-7017.

[141] Brauer, G. *Handbook of Preparative Inorganic Chemistry*, Second ed.; Academic Press: New York, 1965.

[142] Schindelin, J.; Arganda-Carreras, I.; Frise, E.; Kaynig, V.; Longair, M.; Pietzsch, T.; Preibisch, S.; Rueden, C.; Saalfeld, S.; Schmid, B.; Tinevez, J.-Y.; White, D. J.; Hartenstein, V.; Eliceiri, K.; Tomancak, P.; Cardona, A. Fiji: an open-source platform for biological-image analysis. *Nat Meth* **2012**, *9*, 676-682.